Dissertation zur Erlangung des Doktorgrades
der Fakultät für Chemie und Pharmazie
der Ludwig-Maximilians-Universität München

– Illuminating New Frontiers – Innovative Synthesis and Characterization of Nitridophosphate-Based Materials for Solid-State-Lighting

Reinhard Michael Pritzl
aus
Mallersdorf-Pfaffenberg, Deutschland

2024

Erklärung

Diese Dissertation wurde im Sinne von §7 der Promotionsordnung vom 28. November 2011 von Herrn Prof. Dr. Wolfgang Schnick betreut.

Eidesstattliche Versicherung

Diese Dissertation wurde eigenständig und ohne unerlaubte Hilfsmittel erarbeitet

München, den 07.11.2024

_____

Reinhard Michael Pritzl

Dissertation eingereicht am:	07.11.2024
1. Gutachter:	Prof. Dr. Wolfgang Schnick
2. Gutachter:	Prof. Dr. Hubert Huppertz
Mündliche Prüfung am:	16.12.2024

I am a firm believer, that without speculation there is no good & original observation.

Charles Darwin

Letter to A. R. Wallace 1857

Vorwort

An dieser Stelle möchte ich zunächst die Möglichkeit nutzen, mich bei den vielen Menschen zu bedanken, ohne die diese Arbeit nicht möglich gewesen wäre.

An erster Stelle gilt mein aufrichtiger Dank meinem Doktorvater, Herrn Prof. Dr. Wolfgang Schnick, für die Chance, meine Dissertation unter seiner Betreuung anfertigen zu dürfen. Die zahlreichen Fachgespräche, wertvollen Ratschläge, die bereitgestellten Mittel und die Freiheit, das Forschungsthema nach meinen eigenen Vorstellungen zu gestalten, bildeten die perfekte Grundlage, um meinem wissenschaftlichen Forscherdrang nachzugehen.

Ebenso bedanke ich mich bei Herrn Prof. Dr. Hubert Huppertz, der sich bereit erklärt hat, das Zweitgutachten zu übernehmen. In diesem Zusammenhang möchte ich auch ein großes Dankeschön für die Ausrichtung des Obergurgl-Seminars für Festkörperchemie aussprechen. Es bot mir mehrmals die großartige Möglichkeit, meine Forschung in einem familiären Umfeld zu präsentieren, zu diskutieren und fachlich einzuordnen.

Mein Dank gilt ferner den Professoren Johrendt, Markic, Klapötke und Karaghiosoff, die sich freundlicherweise bereit erklärt haben, als Mitglieder der Prüfungskommission meiner mündlichen Verteidigung zu fungieren.

Ein besonderer Dank geht an Dr. Sebastian Wendl und Dr. Sebastian Vogel, die mich zu Beginn meiner Zeit im Arbeitskreis Schnick unterstützt und mich in die Arbeit an der Hochdruckpresse sowie in der Röntgenstrukturanalyse eingearbeitet haben. Insbesondere dir, Sebi, gilt mein tiefster Dank: Während meiner Zeit als F-Praktikant habe ich nicht nur viel gelernt, sondern auch meine Begeisterung für Nitridophosphate entdeckt. Du bist einer der Hauptgründe, warum ich mich der Festkörperchemie verschrieben habe.

Herrn Dr. Tobias Giftthaler danke ich für seine Unterstützung während meiner Masterarbeit und darüber hinaus. Du hattest stets ein offenes Ohr, sei es für fachliche Fragen oder einfach für ein Gespräch. Deine reflektierte Sichtweise auf verschiedenste Themen hat mich sowohl wissenschaftlich als auch menschlich sehr geprägt und bereichert.

Herzlichen Dank an Dr. Simon Kloß, Dr. Stefan Rudel und PD Dr. Constantin Hoch, deren Türen immer für mich offen standen. Speziell dir Simon ein großes Dankeschön, dass du mir den Zugang zum Arbeitskreis durch den HiWi-Job erleichtert hast. Frau Dr. Lisa Gamperl danke ich für die

vielen inspirierenden und konstruktiven Gespräche, sei es auf fachlicher oder privater Ebene. Dank dir habe ich auch eine neue Wertschätzung für American Football entwickelt. Unsere gemeinsamen Projekte schätze ich sehr, auch wenn sie nicht immer den gewünschten Erfolg brachten. Ich glaube weiterhin an ein BLA aus der Hochdruckpresse!

Ein großes Dankeschön gilt meinen internen und externen Kooperationspartnern. Besonders bedanke ich mich bei Herrn Dr. Peter J. Schmidt von der Firma Lumileds für die erfolgreiche Zusammenarbeit und seine Unterstützung im Bereich Lumineszenz. Die Diskussionen und Anregungen in unseren Meetings haben mein Verständnis entscheidend vertieft und die Qualität vieler meiner Projekte in diesem Bereich erheblich verbessert. Herzlichen Dank auch an (Prof. und Dr. in spe) Kristian Witthaut. Deine Überlegungen bei einer Tasse Kaffee und deine DFT-Rechnungen haben mein Forschungsthema maßgeblich bereichert. Vielen Dank auch an Frau Dr. Monika Pointner für die fachliche Unterstützung bei den STEM-Messungen, die insbesondere einem meiner Projekte sehr zugutekamen. Herrn Dr. Marwin Dialer danke ich für die zahlreichen bereichernden Diskussionen – auch wenn wir nicht immer einer Meinung waren, fanden wir am Ende oft zu einem gemeinsamen Ergebnis. Deine Perspektiven haben meine Arbeit sehr bereichert. In diesem Kontext möchte ich auch Herrn Florian Engelsberger meinen tiefen Dank aussprechen, gerade auf der Zielgerade warst du eine enorme Hilfe und Bereicherung.

Mein Dank gilt auch meinen Praktikanten Nepomuk Korber, Nadine Fahle, Nina Prinz und Leopold Blahusch, deren Unterstützung und Neugier für die Festkörperchemie unter extremen Bedingungen wertvolle Beiträge zu meinen Forschungsprojekten geleistet haben. Gemeinsam haben wir einige schöne Ergebnisse erzielt.

Meinen Freunden und Kollegen Dr. Sophia Wandelt, Thanh Chau, Dr. Sebastian Ambach, Mirjam Zipkat, Thaddäus Koller, Georg Krach und Jennifer Steinadler danke ich für die vielen gemeinsamen Stunden im Labor und darüber hinaus. Abschließend möchte ich mich bei allen anderen Mitgliedern der Arbeitskreise Schnick, Johrendt, Hoch und Lotsch für die großartige Zeit hier im zweiten Stock bedanken.

Ein herzliches Dankeschön gilt meinen Freunden in der Heimat sowie jenen, die ich erst in München kennenlernen durfte. Mona und Robert, ich bin wirklich froh euch zu meinen Freunden zählen zu dürfen, auch wenn der Umzug nach Ismaning schmerzt. Speziell danke ich Dr. Sebastian Reiner und Lisa Seidl – wer hätte gedacht, dass du mich hier doch noch überholst, Sebastian?! Und dass ihr beide jetzt in Dänemark gelandet seid, überrascht mich immer noch. Einfach nur Danke – ich bin mir sicher, ohne euch hätte ich das Studium nicht durchgestanden.

Zum Schluss möchte ich mich bei allen Menschen bedanken, die ich zu meiner Familie zähle: Danke an Claudia, Raimondo und Gianina, dass ihr mich so herzlich in euren Kreis aufgenommen habt. Mein größter Dank geht an dich Ami, dass du immer mein Rückhalt daheim bist, auch in den schwierigsten Momenten. Dein offenes Ohr für die wirren Gedanken in meinem Kopf ist mein Anker in all dem Chaos.

Und zu guter Letzt: Ein riesiges Danke an Mama & Papa, Christine & Andi (und natürlich die Kleinen)! Ohne eure unerschütterliche Unterstützung und die Ratschläge, die ich stets daheim bekomme, wäre ich nicht der Mensch, der ich heute bin.

Natürlich vergisst man bei solchen Danksagungen immer jemanden. Ich hoffe, ihr nehmt es mir nicht übel – aber wer mich kennt, weiß, das war natürlich pure Absicht!

Nach den vielen Dankesworten, möchte ich nun ein paar Zeilen verwenden um diese Arbeit in das richtige Licht zu rücken. Da hoffentlich einige Menschen in Zukunft diese Dissertation lesen werden, möchte ich es mir nicht nehmen lassen in Anlehnung einer Buchweisheit „*Happiness can be found, even in the darkest of times, if one only remembers to turn on the light*“, diese Dissertation mit einem positiven Gedanken zu beginnen. Die Entwicklung von Phosphoren für pc-LEDs ist nicht nur ein technischer notwendiger Schritt, sondern auch im wahrsten Sinne des Wortes, die Möglichkeit Licht in unsere Welt zu bringen. In dieser Arbeit werden die verschiedensten Aspekte der Synthese neuartiger Nitridophosphate untersucht, mit dem Ziel, eine Grundlage für innovative Materialien mit Potential in modernen LED-Technologien zu schaffen.

Meinem persönlichen Anreiz sei damit genug gewürdigt, und so möchte ich abschließend mit einem weiteren Zitat aus derselben Bücherreihe enden:

„LUMOS“

Reinhard Pritzl

Table of Contents

1 Introduction

1.1 The Imperative of Innovation – Prospects for a Bright Future?

Since the earliest days of humanity, innovation and technological advancement have shaped civilization. A key aspect of technical progress is our ability to understand materials and their properties. Materials science forms the foundation for many technological breakthroughs, marking significant epochs in human history: the Stone, Bronze, and Iron Ages, each characterized by advances in materials technology. In recent centuries consistent growth in new technologies and functional materials is observable, facing the epochal challenges of civilization.[1,2] Nowadays, environmental pollution and climate change are big threats that are countered by research of new functional materials that significantly reduce the global material and energy consumption.[3-7]

One sector with significant energy-saving potential is artificial lighting, where even small improvements can lead to substantial reductions in energy consumption. The replacement of approximately 35% of incandescent and discharge lamps by phosphor-converted light-emitting diodes (pc-LEDs) has already made a remarkable impact, resulting in estimated global energy savings of 185 TWh per year. If the current replacement rate is maintained, this value could increase to around 450 TWh per year by 2035.[8,9] Incandescent bulbs convert only about 5% of the energy they consume into visible light, dissipating the majority as heat. In contrast, pc-LEDs efficiencies ranging from 40% to 70% are significantly higher, while also being able to display nearly the entire visible spectrum.[10-12] The US Department of Energy (DOE) estimates an additional energy saving potential of around 20% through further developments in pc-LED technology.[9] One of these development options is to improve the quality of the light sources by making them more efficient and by improving color rendering, the ability to reproduce color of objects like illuminated by the sun. The necessity of improving color rendering of pc-LEDs can be humorously summarized by a remark from the former US President Donald Trump: “[...]*most importantly, the light's no good. I always look orange*[...]*”*, a claim that clearly does not justice to the quality of these well-established light sources.[13] One of the current research focuses is therefore on the development of new ceramic light converters (so-called phosphors), the centerpieces of pc-LEDs (Figure 1.1), which convert UV and blue light into different colors of the visible spectrum. These phosphors can be used to influence the correlated color temperature (*CCT*) and the color rendering index (*CRI*) of a pc-LED to achieve the best possible lighting properties for the respective application.[14]

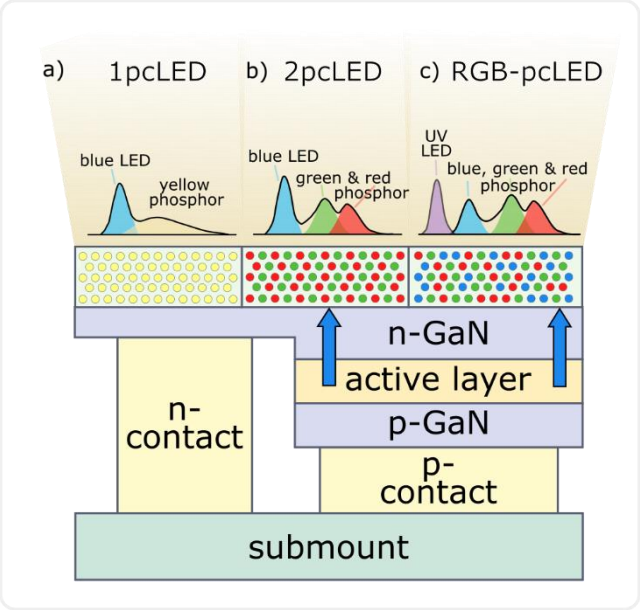

Figure 1.1. Schematic illustration of state-of-the-art white Light-Emitting Diode (wLED) devices. a) wLED device combining blue LED chip with yellow phosphor (1pc-LED). b) wLED device combining blue LED chip with green and red phosphors (2pc-LED). c) wLED device combining ultraviolet LED chip with blue, green & red phosphors (RGBpc-LED). This illustration was adapted from Pust *et al.*[15,16]

The widespread use of LEDs in products such as televisions, smartphone flashlights and automotive headlights demonstrates the impact of chemical research on sustainable lighting technologies. Next to these established LED applications, the research focuses on more specialized applications, such as Human Centric Lighting.[17,18] The principle idea here is an interior lighting concept that adapts the lighting to a natural daylight pattern. This also allows for a needs-based, infinitely adjustable color temperature and illuminance, positively impacting people by enhancing concentration, mood, recovery, and more. However, full-spectrum lighting is essential to ideally simulate natural light. This is currently achieved by GaN UV chip with green, cyan, and red-emitting phosphors. Cyan-emitting phosphors are added to fill the blue to green region of the visible spectrum (470–520 nm, so-called cyan gap) to achieve higher *CRI* values.[19,20] Another point that offers potential for improvement is the development of phosphors with narrow-band red emission with little to no infrared spill-over.[21] However, the discovery, development, and optimization of (novel) narrow-band emitting phosphors is challenging and leaves room for further advancement.

In order to understand the fundamental possibilities for developing phosphor materials, it is essential to clarify the principles of Solid-State Luminescence (*SSL*). Most commercially available *SSL* phosphors consist of host structures, such as anionic networks balanced by cations, doped with guest activator ions, such as Eu^{2+}.[22,23] Activator ions absorb high energy UV and blue

light, whereby electrons enter an excited state. In case of Eu^{2+}, electrons are excited from a 4*f* ground state to a 5*d* level. These excited electrons can return to the ground state by releasing energy, either radiatively or non-radiatively, emitting light of certain color. Due to vibrational relaxation processes, the emitted photons have lower energies and longer wavelengths than the absorbed photons, leading to different colors (Figure 1.2). This is termed as red-shift, also known as down-conversion or phosphor-conversion (since the processes occur within the phosphor material).[23]

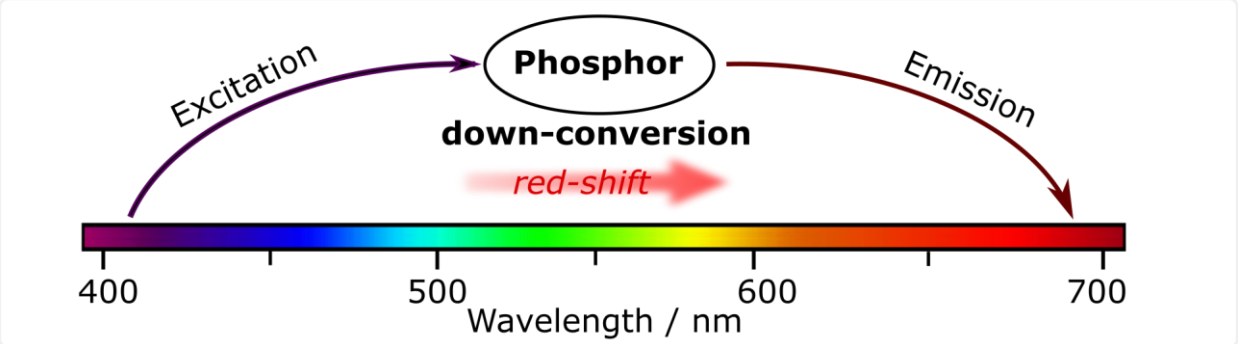

Figure 1.2. Schematic illustration of the down-conversion process in phosphor materials. The emission color was selected as red for clarity reasons.

The energetic difference between excitation and emission is referred to as Stokes shift, described by Equation (1.1).[24]

$$E_{\text{Stokes}} = 2\,S \cdot \hbar\omega \tag{1.1}$$

with S = Huang-Rhys parameter
$\hbar$ = Dirac constant
ω = angular vibration frequency

The Huang-Rhys parameter S is a measure for the strength of the electron-phonon coupling and thus depends on the rigidity of the host lattice (high rigidity ≙ small value for S). ω corresponds to the phonon frequencies and therefore depends on the atomic weight of the host structure atoms (atoms with high molar mass ≙ small value for ω). From these considerations, it can be concluded that small Stokes shifts are associated with rigid host structures incorporating atoms with high molar masses.[25,26]

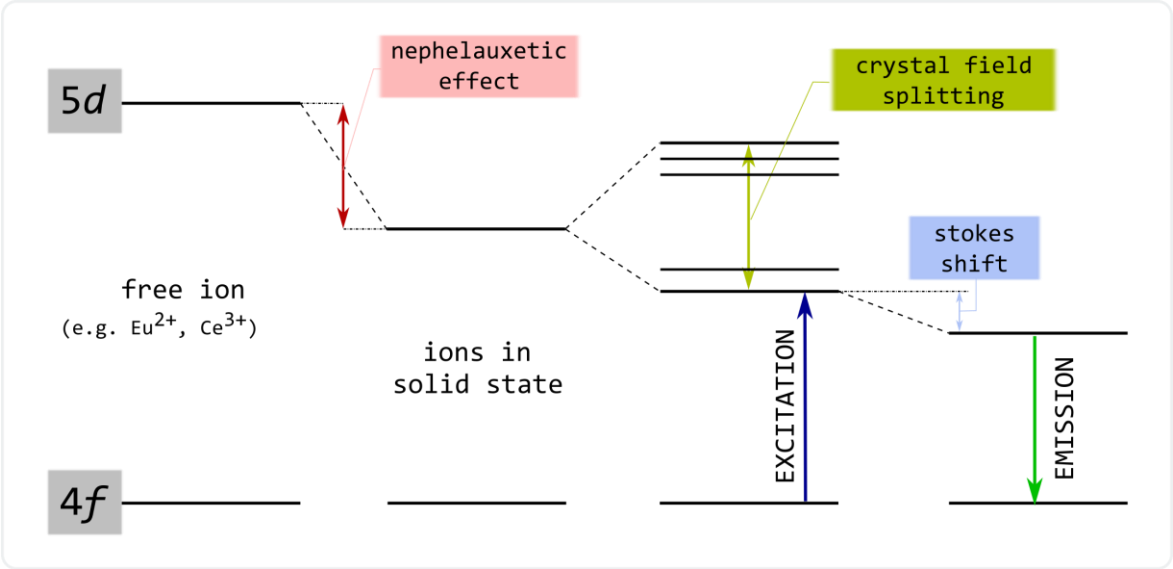

Figure 1.3. Schematic energy diagram of Eu^{2+}: The energy difference between $4f^7$ ground state and $4f^6 5d^1$ excited state is reduced through the host lattice (nephelauxetic effect, crystal field splitting and stokes shift).

The energy of the 5*d* orbitals of Eu^{2+} is reduced compared to a free activator ion, due to the influence of the ligands in its immediate environment. This reduction in energy, named nephelauxetic (cloud expanding) effect, is related to covalency as d-d electron repulsion is diminished through bond formation and thus dependent on type of ligand.[27] In addition, the local arrangement of ligands exerts an influence on the energetic splitting of the 5*d* orbitals. Depending on the coordination number (*CN*), geometry, symmetry, and distances ("bond lengths") to the activator ion, different splitting patterns of the degenerate 5*d* orbitals occur, which are known as crystal field splittings (Figure 1.3).[28] Based on the previous considerations, it is evident that the energetic positions of the 5*d* levels are highly sensitive to the local environment of the activator ion. Consequently, the emission properties, including the spectral position and shape of the emission band, are effected as well.[27,29] This sensitivity offers significant potential for tailoring specific emission properties for desired applications by altering the local environment of the activator ion in the host lattice.

This implies the following strategies for the preparation of novel phosphor materials based on a classification by Sohn *et al.*[30]

a) Tuning: Slight modification of the host lattices of well-known phosphors according to the aforementioned aspects (e.g. substitution and co-doping)
b) Mimicking: Replicating the crystal structures of well-known host lattices with other elements (e.g. silicate vs. phosphate)

c) Identification: Identifying suitable host lattices with well-known crystal structures for activator incorporation
d) Design/Development: Creating novel host-structures for doping (e.g. new structure types and new substance classes)

The primary focus of this work lies on the development of novel potential host structures (d) rather than their optimization, as well as on the development of innovative approaches for synthesis of these materials. Therefore, the following chapter are dedicated to providing an outline of the substance classes dealt with during this thesis, offering a structural overview and methodological insights into their preparation.

1.2 Nitridophosphates: A Substance Class on the Road to Glory?

In recent years, the lighting sector has been fundamentally revolutionized by the substance class of nitrides (N^{3-}), including nitridosilicates, nitridoaluminates, and nitridophosphates.[15,31,32] Nitridophosphate-based compounds, in particular, have attracted considerable attention in the development of new phosphors for modern *SSL*, as Eu^{2+}-doped representatives are capable of emitting across the entire visible spectrum (Figure 1.4).[31, 33–36]

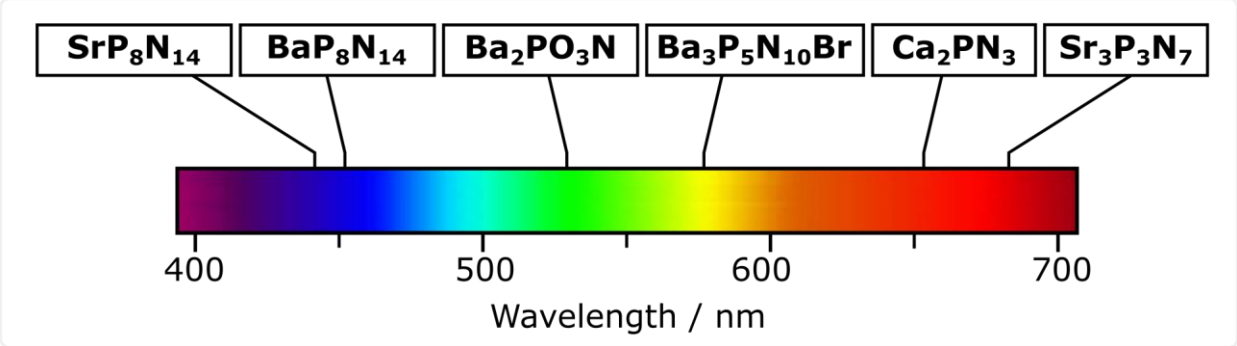

Figure 1.4. Illustration of the emission maxima positions of selected Eu^{2+}-doped nitridophosphate-based compounds under UV to blue light irradiation within the visible spectral range.[31,33–36]

The term “nitridophosphate-based” refers not only to pure nitridophosphates but also to P/N compounds where nitride ions are partially substituted by oxide ions (O^{2-}; oxonitridophosphates), halide ions (e.g. Cl^-; nitridophosphate halides), or functionalized by imide groups (NH^{2-}, imidonitridophosphates). The additional variation of the anionic P/N framework through the incorporation of further network forming cations (*NFC*) such as silicon (Si^{4+}), boron (B^{3+}) and

beryllium (Be^{2+}) in nitridosilicate phosphates, boron- and beryllium phosphorus nitrides is also considered in this context.[37–39]

One of the main reasons for the exceptional emission range of nitridophosphate-based compounds is their great structural diversity. As previously outlined in Chapter 1.1, a desired fundamental change in emission typically necessitates a significant change in the host lattice or, more precisely, the activator ion environment. The high potential for structural diversity of nitridophosphate-based compounds can be easily understood by considering the relationship to oxosilicates. The element combination in nitridophosphates (P/N) is isoelectronic to that of oxosilicates (Si/O), which is the most abundant and structurally diverse class of minerals on Earth.[40] Consequently, similar structural motifs are expected and indeed observed. Comparable to the SiO_4 tetrahedra, which represent the fundamental building unit (*FBU*) in oxosilicates, $P(N/O)_4$ tetrahedra are the predominant *FBU*s in nitridophosphates.

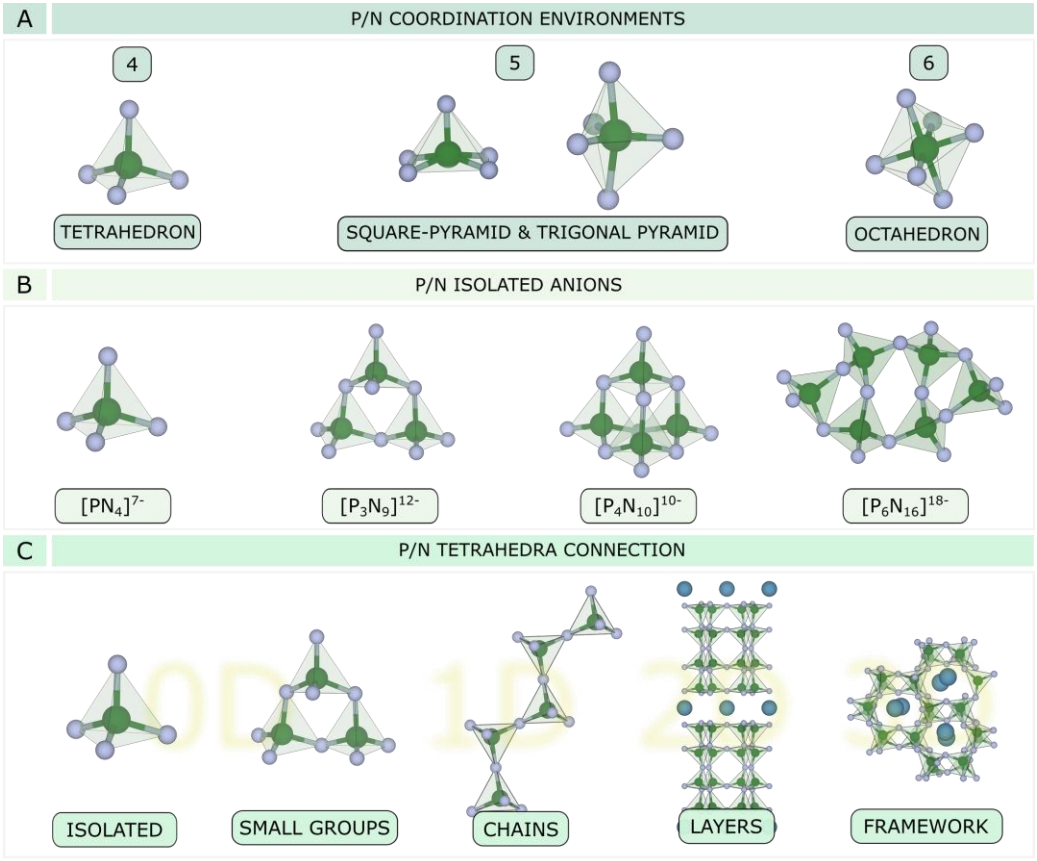

Figure 1.5. Structural motifs in nitridophosphate-based compounds (imido-, oxo- and pure nitridophosphates and nitridophosphate oxides). A) Coordination environments of P^{+V} in nitrides (*CN* = 4–6); B) isolated P/N anions; C) Connection possibilities of PN_4 tetrahedra: isolated, small groups, chains, layers and frameworks.[31,41–51]

Additionally, the same coordination numbers (*CN*) for Si and P are observed under increased pressure (*CN* = 5, trigonal bipyramids and square pyramids; *CN* = 6, octahedra; Figure 1.5a).[42,52–54] The connection of these *FBU*s in nitridophosphates leads to new, similar, as well as homeotypic and isotypic structure types. The degree of condensation κ, defined as the ratio of tetrahedral centers (T) to ligand atoms (L) reflects how the respective *FBU*s are typically present. From highly condensed 3D networks (e.g. $Rb_3P_6N_{11}$), over 2D layers (e.g. in SrP_8N_{14}), 1D chains (e.g. in $Sr_3P_3N_7$), pre-ordered anionic unis (e.g. cyclic $[P_3N_9]^{12-}$ anions in $Li_{12}P_3N_9$ or adamantane-type $[P_4N_{10}]^{10-}$ anions in α-/β-$Li_{10}P_4N_{10}$), to isolated $[PN_4]^{7-}$ anions (e.g. in $Ho_3[PN_4]O$), various structural motifs are observed (Figure 1.5b&c).[36,41,48,55-58] In addition to these similarities to the oxosilicates, nitridophosphates have further characteristics, including the ability for threefold coordinated $N^{[3]}$ atoms (e.g. in *AE*P_8N_{14}).[56] This allows κ values greater than ½, the upper-limit of oxosilicates, illustrated by the binary parent compound SiO_2, in which all-side vertex-sharing tetrahedra occur. Consequently, the theoretical structural diversity should be much greater than that observed in oxosilicates. The rare occurrence of edge-sharing tetrahedra in nitridophosphates, which can be observed e.g. in α-P_3N_5, lends further weight to this hypothesis, given that the electrostatics conditions in oxosilicates precludes this possibility.[59] So far, it has only been discussed in the literature for edge-shared SiO_4 tetrahedra in the example of fibrous SiO_2, although there is disagreement among experts to its plausibility.[60] With all these structural features, nitridophosphates theoretically exhibit even greater structural flexibility than oxosilicates. A review of the literature reveals that, although a significant number of nitridophosphate-based compounds have been investigated (primarily in the last three decades), their quantity is far behind that of silicates.[61] A color-coded periodic table of elements (Figure 1.6) illustrating electropositive elements *M* already stabilized in nitridophosphate-based compounds, prior the beginning of this thesis. This naturally raises the question of why research into nitridophosphates only began more recently. As nitridophosphates are a purely synthetic class of compounds, the most obvious reason is the complexity of their synthesis. This will be discussed in more detail in the following chapter, along with a brief overview of the methods used in this dissertation.

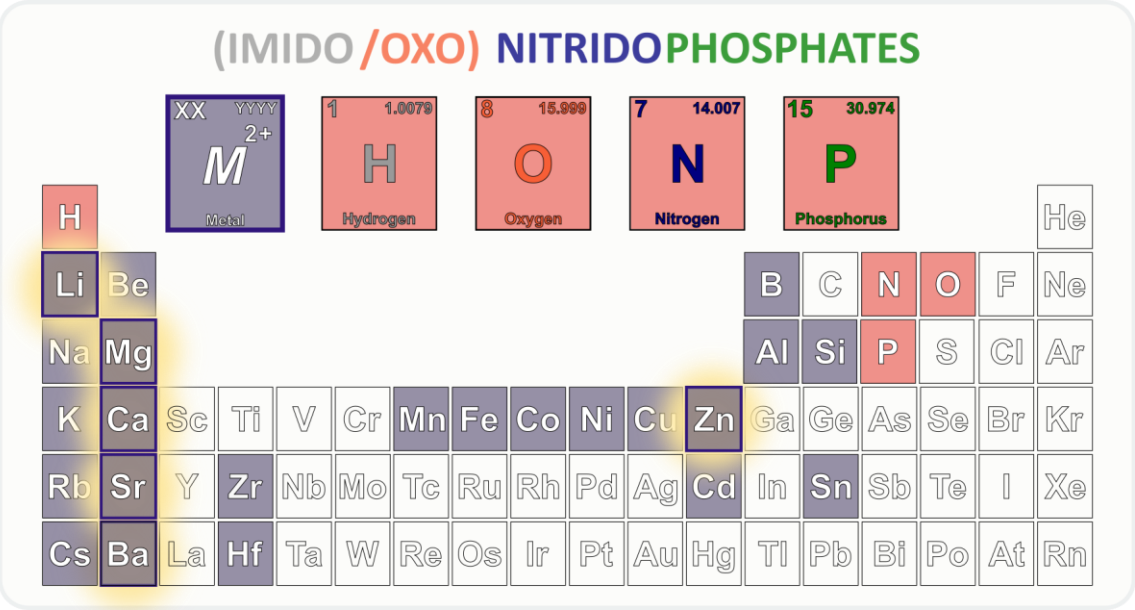

Figure 1.6. Periodic Table of the Elements displaying all electropositive elements (purple) stabilized in imido-, oxo- & pure nitridophosphates prior to this dissertation. For clarity, rare-earth elements were excluded from this representation. The highlighted elements are in special focus of this thesis.

1.3 High-Pressure: State of the Art Techniques for Nitridophosphate Synthesis

The central challenge in nitride synthesis in general and therefore as well in nitridophosphate synthesis is the omnipresent competition with oxygen. While oxygen (O_2), a diradical (nominal double bond) with a bonding energy of 498 kJ·mol^{-1}, can be already activated at moderate temperatures, nitrogen (N_2) with its N≡N triple bond (941 kJ·mol^{-1}) is significantly more stable.[61] Furthermore, oxygen can be easily reduced to O^{2-} (first electron affinity EA_0 = −1.46 eV), while the formation of nitride ions N^{3-} are unfavorable (first electron affinity EA_0 = +0.07 eV).[62] This positive electron affinity makes N^{3-} ions sensitive towards oxidation as they are only stabilized by their direct coordination environments. Therefore, most naturally occurring minerals are oxides while nitrides are exceedingly rare, typically formed only under oxygen-free conditions (e.g. in meteorites).[63-67] Consequently, the main challenges in preparing nitridophosphates lies in preventing oxidation of nitride anions as well as excluding the competitive oxidation by oxygen. This can be achieved by strictly excluding moisture and air, employing inert-gas techniques such as the Schlenk line or glove boxes. However, even in the absence of external oxygen, oxidation can still occur during nitridophosphate synthesis, leading to the elimination of N_2 and a reduction of P^{+V} to P^{+III} or even P^0. One frequently mentioned

example in literature is the decomposition of the thermally labile precursor P_3N_5, which decomposes at around 850 °C (Eq. 1.2).

$$P_3^{+V}N_5^{-III} \xrightarrow{850\ °C} 3\ P^{+III}N^{-III} + N_2^{\pm 0} \xrightarrow{\geq 850\ °C} 3\ P^{\pm 0} + 5/2\ N_2^{\pm 0} \quad (1.2)$$

This temperature is significantly below the crystallization temperature of most nitridophosphates, in particular the higher-condensed ones with $\kappa \geq ½$, which typically require elevated temperatures for bond cleavage and reformation.[59] For this purpose, different synthetic strategies have been developed, either aiming to increase the decomposition temperatures or to decrease the crystallization temperatures.[61] For example, molecular approaches, such as the preparations of disordered P_3N_5 or $SiPN_3$, aim to lower the crystallization temperature through the careful selection of reactive precursors.[68,69] In many of these reactions, the starting materials decompose, and the resulting gas phases gradually increase the reaction pressure. According to *Le Chatelier`s* principle, an increase in pressure raises the decomposition temperature, as the elimination of N_2 is suppressed. Consequently, the application of pressure during these reactions has become a common practice. Various high-pressure synthesis methods have proven effective in this context and are outlined below in ascending order of pressure. The pressure range can vary from several bars in (pressure) ampoules (ambient pressure (AP)), up to 2000 bar in autoclaves or hot isostatic presses (medium pressure (MP)) up to tens of thousands bar (high pressure (HP)) of piston-cylinders ($\leq$ 6 GPa = 60 kbar), belt modules ($\leq$ 10 GPa = 100 kbar) and large volume presses ($\geq$ 100 GPa = 1 Mbar)*, while the maximum static pressures were reported for diamond anvil cells ($\leq$ 1000 GPa = 1 million bar).[70-76] In recent years, it has been demonstrated that maximum pressures are not always required for nitridophosphate synthesis, as long as appropriate synthesis routes and precursors are chosen, as reviewed by Kloß *et al*.[61] Figure 1.7 provides an illustration of the feasible pressure and temperature ranges for the established techniques used in nitridophosphate synthesis.

The compounds prepared during this dissertation were synthesized by using “high” medium-pressure methods and “moderate” high-pressure methods. This methods were used to ensure sufficient pressure to stabilize the products, while also keeping in mind the potential for a simplified transition to industrial standards. Therefore, the hot isostatic press (HIP) and large volume press (LVP) are outlined separately.

* Using the multianvil setup, high-end pressures of approx. 110 GPa are achievable, routine experiments are typically performed below 25 GPa[76]

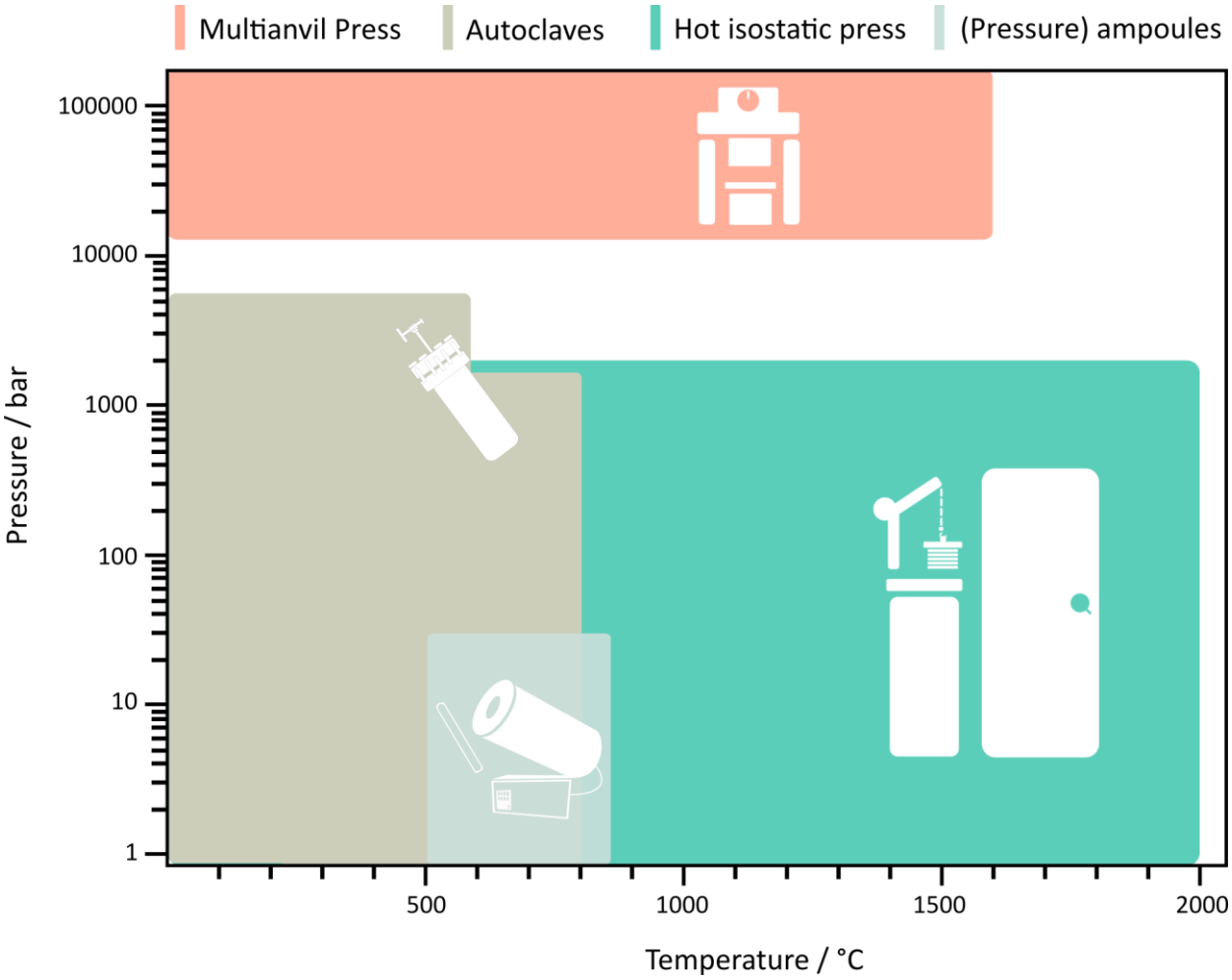

Figure 1.7. Illustration of the *p*-*T* range of established pressure-techniques for nitridophosphate synthesis. Shown techniques: Ampules (gray), hot isostatic press (cyan), autoclaves (olive) and large volume press (red); adapted from Wendl *et al.*[78]

The focus is first on the method with lower of the two synthesis pressures and consequently on the HIP. Hot isostatic pressing plays an important role in material science, especially in the development and manufacturing of novel ceramics and metals. High temperature and high gas pressures are applied to densify powders, consolidate cold-pressed or pre-sintered casts or create fully dense materials. The main advantages of the HIP are the aggregate state of the gaseous pressure medium, and the possibility to operate the parameter pressure (*p*) and temperature (*T*) simultaneously. This helps to eliminate voids in the products and to achieve uniform density throughout the material.[79,80] Particularly in sectors such as aerospace or the automotive industry, where the reliability of material is of crucial importance, hot isostatic pressing enables the production of components for the use in critical and highly stressed applications.[81] While hot isostatic pressing is primarily associated with the aforementioned densification of ceramics and metals, it can also be used to carry out chemical reactions. For instance, the synthesis of

nitridosilicates on a large scale is increasingly realized using the HIP technique.[82-84] The pioneering work of Wendl *et al.*, which demonstrated the great potential of hot isostatic pressing for nitridophosphate synthesis, increasingly brought this class of materials more and more into the industrial focus. Besides the possibility of greater product quantities, three fundamental aspects for synthesis have been demonstrated:

a) Pressure-medium N_2 can serve as reactant[35]
b) Red phosphorus (P_{red}) can be used as a cheap starting material[35]
c) The high pressure conditions considered necessary for many nitridophopshates are not absolutely essential[85]

These insights served as a starting point to prepare quaternary (lowly condensed) nitridophosphate-based compounds in the scope of this thesis.

The basic setup and functional principle of the HIP is briefly described. The HIP (AIP6-30H) used in this work (Figure 1.7) is roughly classified into control unit, pressure booster, main compressor and pressure vessel. This allowed to apply maximum working pressures of up to 200 MPa (all the syntheses were carried out under N_2 atmosphere, whereby Ar was used for purging).

Figure 1.7. HIP (AlP6-30H, American Isostatic Presses Inc., Columbus, USA). Left top: Pressure booster (Maximator, DLE-5-30-2); center: Pressure vessel with crane for lifting the threaded lid and coolant lines; right: control cabinet (control electronics, valves, pumps and main compressor).

The fundamental component of the HIP is the pressure vessel, whose schematic structure is depicted in Figure 1.8.

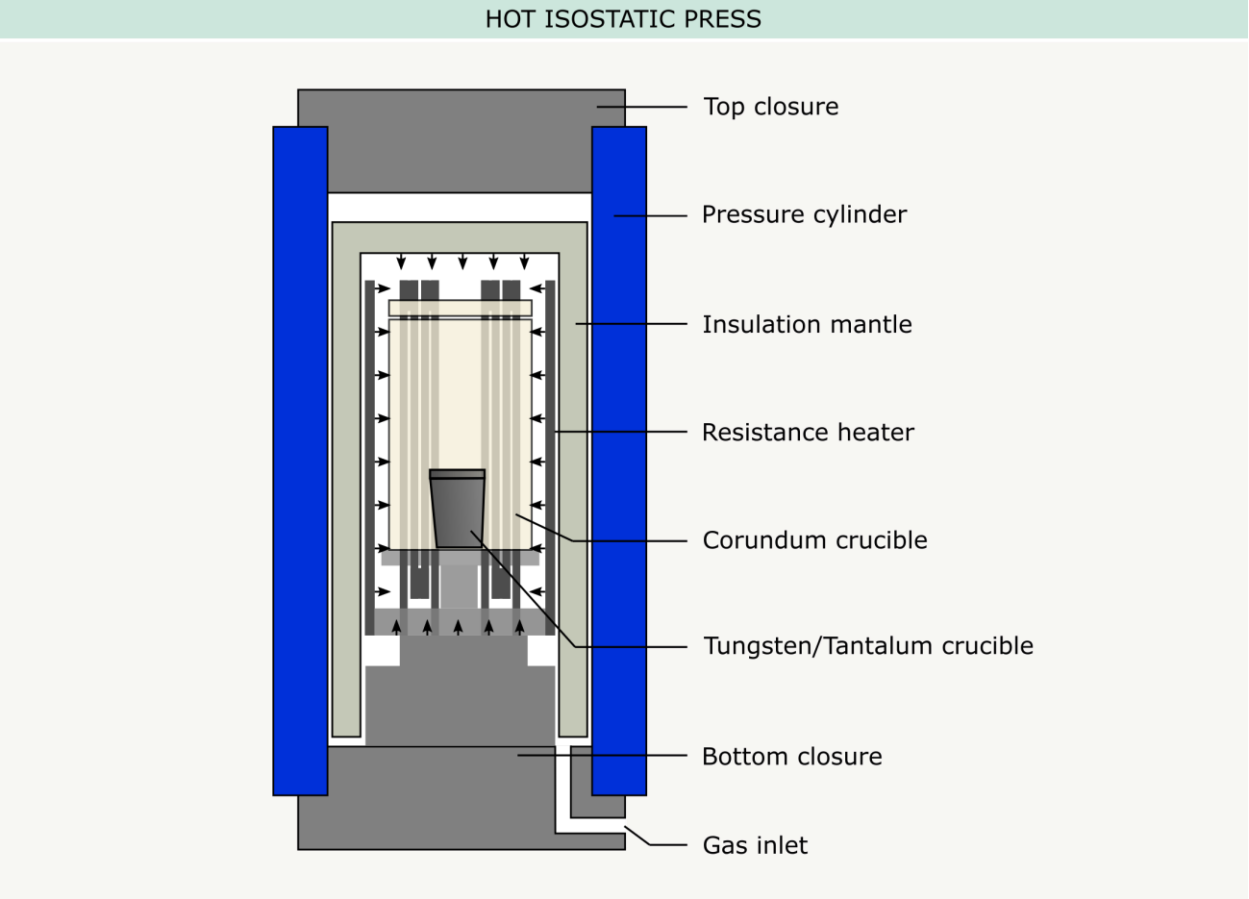

Figure 1.8. Schematic drawing of the pressure vessel of the HIP.

A larger corundum crucible can be inserted into the pressure vessel and used as reaction container. However, for the synthesis of nitrides/nitridophosphates it is recommended to additionally use separate metal crucibles (e.g. W, Ta, Nb) inside the corundum container to avoid direct contact of the nitride reactants with the oxidic surface. Subsequently, the container is positioned between the carbon fiber-reinforced heating elements for resistance heating. After purging the atmosphere with inert gas, an operation pre-pressure is set by the pressure booster in order that the main compressor may be operated. The required intermediate-pressure is selected depending on the desired final pressure of the synthesis. Upon increasing the intermediate-pressure threshold, the sample is heated to the target temperature, through which point the final pressure of 200 MPa is reached. After maintaining these conditions for the intended duration (10–20 h), the reaction chamber is cooled down to 20 °C, and the pressure is released.

In contrast to the medium-pressure approach via HIP synthesis, modern high-pressure syntheses are typically performed using Kawai-type multianvil presses (KMAP).[86] This static high-pressure technology was developed by mineralogists and geophysicists aiming to understand processes within the Earth's interior. KMAPs routinely achieve pressures of up to 25 GPa, enabling the study of pressure conditions corresponding to depths of the uppermost lower earth mantle (~700 km), where phase transformations in rock-forming minerals take place.[75,86,87] Naoto Kawai and Shichi Endo developed in the 1960`s a splitsphere apparatus which serves the basis for today's KMAP technology.[87]

Figure 1.9. Large-volume press using the Kawai-type multianvil setup (Voggenreiter, Mainleus, Germany; with modified Walker-type modules).

The key feature of a KMAP is a two-stage compression system, which generates quasi-hydrostatic pressure through synchronously compression of an octahedral pressure medium through eight cubic second-stage anvils that are compressed by six first-stage anvils. Within this thesis, two identically constructed LVPs (Voggenreiter, Mainleus, Germany) with modified Walker-type modules were used for this purpose (shown in Figure 1.9).[88] In this setup, the uniaxial pressure, generated by the LVP, is initially distributed to six first-stage steel anvils, which creates a cubic compression space. The second-stage anvils are eight cubes made of tungsten carbide (WC) with truncated edges (Figure 1.10a).

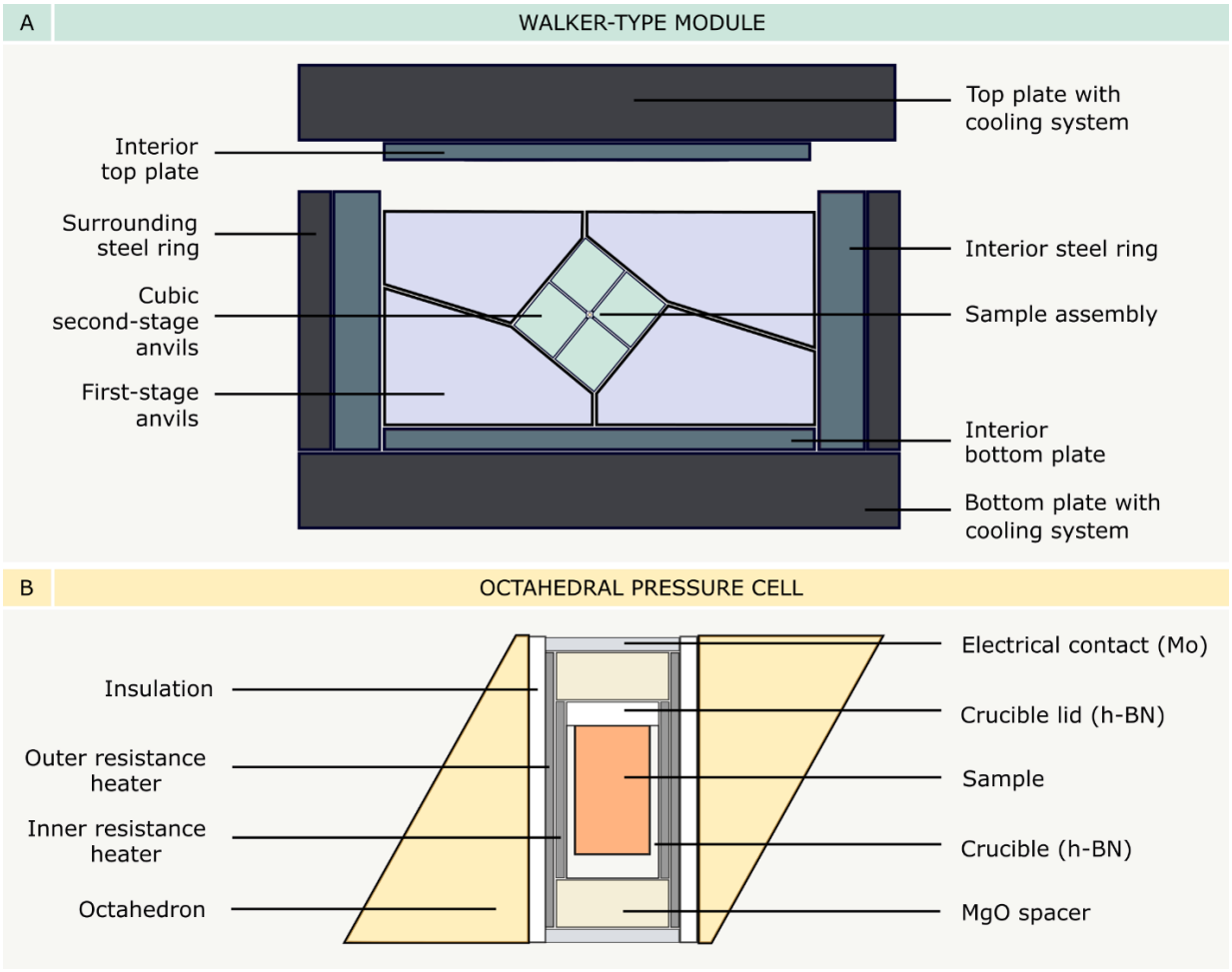

Figure 1.10. a) Schematic drawing of a Walker-type module with six first stage steel anvils and the cubic second stage tungsten carbide anvils, which form an octahedral compression space for the sample assembly. b) Octahedral pressure cell (sample assembly) with resistance heaters and sample crucible.[89]

These in turn create the cavity for and compress the octahedral pressure cell, which contains the sample and resistance heating furnace system. A more detailed guide to the used setup and assembly preparation is given in Chapters 2–4, the Supporting Information and the literature.[89,90]

The internationally common terminology for assembly sizes is the octahedron edge length (*OEL*) to truncated edge length (*TEL*). Typical assembly sizes are 25/17, 18/11, 14/8 and 10/5 (*OEL/TEL*), whereby higher synthesis pressures can be achieved by reducing the size of the assemblies according to the general equation for pressure:

$$p = F/A \tag{1.3}$$

The maximum pressure achievable by the assemblies 18/11, 14/8 and 10/5 is about 10 GPa, 16 GPa and 25 GPa, respectively. Within this thesis, only the assembly size 18/11 was used in

order to obtain larger sample quantities for characterization and to bring the potential novel nitridophosphates directly closer to a possible application due to the lower synthesis pressure required. Consequently, syntheses were carried out down to a minimum pressure of 3 GPa, whereby below this pressure threshold the setup becomes unstable and the potential for technical problems (blowouts) is increased. During synthesis, the resistance heating using graphite furnaces allows maximum temperatures of approximately 1600 °C. The cross-section of the octahedral pressure cell, which shows the individual parts such as graphite furnaces, insulating jacket (ZrO_2), pressure medium (MgO) and sample crucible (h-BN), is shown in Figure 1.10b.

1.4 Scope of this Thesis

This dissertation aims to explore the synthesis and characterization of new imido-, oxo- and pure nitridophosphates and nitridophosphate oxides of known P : N/O ratio, achieved through the deliberate introduction of additional network forming cations (*NFC*) or counter cations (*CC*). Established methods and synthesis routes for nitridophosphate synthesis were utilized alongside completely novel approaches.

Chapter 2 and 3 focus on established high-pressure/high-temperature (HP/HT) synthesis methods for the preparation of nitridophosphate-based compounds, aiming to incorporate Mg^{2+} not only as *CC* (chapter 2) but also as *NFC* (chapter 3):

Chapter 2

From Framework to Layers Driven by Pressure –

The Monophyllo-Oxonitridophosphate β-$MgSrP_3N_5O_2$ and Comparison to its α-Polymorph

Chapter 2 describes the discovery and characterization of the new high-pressure modification β-$MgSrP_3N_5O_2$ and presents an alternate synthesis route for the targeted preparation of the literature-known oxonitridophosphate α-$MgSrP_3N_5O_2$. In both cases, Mg^{2+} ions act as *CC* which are not suitable for Eu^{2+} doping. Therefore, the distinct luminescence properties are attributed to the Eu^{2+} occupation of the respective Sr^{2+} sites and are discussed in detail.

Chapter 3

Tunable Narrow-Band Cyan-Emission of Eu^{2+}-doped Nitridomagnesophosphates $Ba_{3-x}Sr_x[Mg_2P_{10}N_{20}]:Eu^{2+}$ (x = 0–3)

Chapter 3 presents the solid solution series $Ba_{3-x}Sr_x[Mg_2P_{10}N_{20}]:Eu^{2+}$ as the first representatives of alkaline earth metal nitridomagnesophosphates. In addition to the structural characterization, the impact of Mg^{2+} as an additional *NFC* in nitridophosphates was examined. The relationship between the crystal structures and the resulting narrow-band emissions in the cyan spectral region is explored.

Chapters 4 to 7 focus on novel synthetic strategies for the preparation of imido-, oxo- and pure nitridophosphates or nitridophosphate oxides, aiming to expand the synthesis route portfolio for nitridophosphate-based compounds:

Chapter 4

$ZnH_2P_4N_8$: Case Study on Topochemical Imidonitridophosphate High-Pressure Synthesis

Chapter 4 deals with the synthesis of the imidonitridophosphate $Zn_xH_{4-2x}P_4N_8$ (x = 0.5, 0.85, 1) through a high-pressure defunctionalization route applied to the phosphorus nitride imide high-pressure polymorph β-HPN_2. The enhanced structural control, achieved by preserving the anionic P/N structure, was investigated through partial defunctionalization and incorporation of Zn^{2+}. Solid-state MAS NMR experiments provide insights into the real structure and allow conclusions on the topochemical reaction mechanism.

Chapter 5

$CaLi_2PN_3$ – A Quaternary Chain-Type Nitridophosphate by Medium-Pressure Synthesis

Chapter 5 discusses the first quaternary lithium alkaline earth nitridophosphate $CaLi_2PN_3$. In addition to established synthesis routes, a novel double salt approach is introduced, which combines structural motifs from the low-pressure compound Ca_2PN_3 and the high-pressure compound Li_4PN_3 to form a novel compound through medium-pressure synthesis.

Chapter 6

Adamantane-Type Nitridophosphate Phosphors $AE_xLi_{10-2x}P_4N_{10}:Eu^{2+}$ via Medium-Pressure Ion-Exchange Reactions

Chapter 6 discusses the first representatives of adamantane-type alkaline earth nitridophosphates with the generalized sum formula $AE_xLi_{10-2x}P_4N_{10}$ (x(Ca) = 2, 2.7, 4 and x(Sr) = 3). All four compounds were prepared through a simplified ion-exchange reaction under medium-pressure conditions starting from the nitridophosphate-based Li^+ ion conductor $Li_{10}P_4N_{10}$. Besides their structural elucidation, the luminescence properties upon doping with Eu^{2+} are investigated. The subsequent discussion on the applicability of one of the representatives as a red-emitting phosphor for warm white LEDs is supported by simulations of the resulting spectra of the w-LED device incorporating this phosphor.

Chapter 7

Trigonal Planar $[PN_3]^{4-}$ Anion in the Nitridophosphate Oxide $Ba_3[PN_3]O$

Chapter 7 discusses the discovery and investigation of $Ba_3[PN_3]O$, a nitridophosphate oxide featuring unprecedented isolated trigonal planar $[PN_3]^{4-}$ anions, which were obtained during the exploration of nitridophosphates using red phosphorus as a non-preorganized starting material. Various analytical methods allowed not only to successfully verify the presence of this novel anion in the crystal structure for the first time but also allows to provide first benchmark values for these.

1.5 References

[1] Deutsches Patent- und Markenamt DMPA, *Patentanmeldungen,* **2024**, https://www.dpma.de/dpma/veroeffentlichungen/statistiken/patente/ (Date: 16.10.2024).

[2] Statista, *Anzahl von Patentanmeldungen in Deutschland von 2001 bis 2023*, **2024**, https://de.statista.com/statistik/daten/studie/2203/umfrage/entwicklung-der-anzahl-von-patentameldungen-in-deutschland-seit-1997/ (Date: 16.10.2024).

[3] S.L. Lewis, A.M. Maslin, *Nature* **2015**, *519*, 171.

[4] Deutsche Meteorologische Gesellschaft Deutsches Klima-Konsortium, Deutscher Wetterdienst, Extremwetterkongress Hamburg, Helmholtz-Klima-Initiative,

klimafakten.de, *Was wir heute übers Klima wissen - Basisfakten zum Klimawandel, die in der Wissenschaft unumstritten sind*, **2021**.

[5] Deutsche Akademie der Naturforscher Leopoldina e. V., *Klimawandel: Ursachen, Folgen und Handlungsmöglichkeiten*, **2021**.

[6] N. Armaroli, V. Balzani, *Angew. Chem. Int. Ed.* **2006**, *18*, 52.

[7] D.A. King, *Science* **2004**, *303*, 176.

[8] D. MacIsaac, G. Kanner, G. Anderson, *Phys. Teach.* **1999**, *37*, 520.

[9] P. Morgan, M. Hansen, N. Bardsley, G.D. Thomson, K. Gordon, A. Wilkerson, K. Lee, V. Nubbe, S. Donnelly, *2022 Solid-State Lighting R&D Opportunities*, **2022.**

[10] Y. Narukawa, J. Narita, T. Sakamoto, T. Yamada, H. Narimatsu, M. Sano, T. Mukai, *Phys. Status Solidi A*, **2007**, *206*, 2087.

[11] P. Mottier in *LED for Lighting Applications*, V*ol. 134*, John Wiley & Sons, Hoboken (USA), **2010.**

[12] D. MacIsaac, G. Kanner, G. Anderson, *Phys. Teach.* **1999**, *37*, 520.

[13] P. Helsel, NBC NEWS, *Trump: I look orange, but so do you because of energy-efficient light bulbs*, **2019**, https://www.nbcnews.com/politics/politics-news/trump-i-look-orange-so-do-you-because-energy-efficient-n1054021 (Date: 16.10.2024).

[14] J. McKittrick, L.E. Shea-Rohwer, *J. Am. Ceram. Soc.* **2014**, *97*, 1327.

[15] P. Pust, P.J. Schmidt, W. Schnick. *Nat. Mater.* **2015**, *14*, 454.

[16] D. Cupkova, E. Kajati, J. Mocnej, P. Papcun, J. Koziorek, I. Zolotova, *Int. J. Distrib. Sens. Netw.* **2019**, *15*, 1.

[17] K. W. Houser, T. Esposito, *Front. Neurol.* **2021**, *12*, 1.

[18] C. Dou, F. Zhao, S. Liu, Z. Song, Q. Liu, *Inorg. Chem. Front.* **2023**, *10*, 2430.

[19] K. Han, J. Jin, X. Zhou, Y. Duan, M. V. Kovalenko, Z. Xia, *Adv. Mater.* **2024**, *36*, 2313247.

[20] S. Schmiechen, H. Schneider, P. Wagatha, C. Hecht, P.J. Schmidt, W. Schnick, *Chem. Mater.* **2014**, *26*, 2712.

[21] C.C. Lin, R.-S. Liu, *J. Phys. Chem. Lett.* **2011**, *2*, 1268.

[22] L. Wang, R.J. Xie, T. Suehiro, T. Takeda, N. Hirosaki, *Chem. Rev.* **2018**, *118*, 1951.

[23] M. de Jong, L. Seijo, A. Meijerink, F.T. Rabouw, *Phys. Chem. Chem. Phys.* **2015**, *17*, 16959.

[24] G. Blasse, A. Bril, *Philips Tech. Rev.* **1970**, *31*, 304.

[25] G. Blasse, B.C. Grabmaier, *Luminescent Materials*, Springer, Berlin, Heidelberg (Germany), **1994**.

[26] R.-J. Xie, Y. Q. Li, N. Hirosaki, H. Yamamoto, *Nitride Phosphors and Solid-State Lighting*, Taylor & Francis, Boca Raton (USA), **2011**.

[27] N. C. George, K. A. Denault, R. Seshadri, *Annu. Rev. Mater. Res.* **2013**, *43*, 481.

[28] A. Kitai in *Materials for Solid State Lighting and Displays*, John Wiley & Sons, West Sussex (UK), **2017**.

[29] W. B. Park, S. P. Singh, K.-S. Sohn, *J. Am. Chem. Soc.* **2014**, *136*, 2363.

[30] S. Wendl, L. Eisenburger, P. Strobel, D. Günther, J.P. Wright, P.J. Schmidt, O. Oeckler, W. Schnick, *Chem. Eur. J.* **2020**, *26*, 7292

[31] L. Wang, R.-J. Xie, T. Suehiro, T. Takeda, N. Hirosaki, *Chem. Rev.* **2018**, *118*, 1951.

[32] S. Wendl, M. Mallmann, P. Strobel, P.J. Schmidt, W. Schnick, *Eur. J. Inorg. Chem.* **2020**, 841.

[33] A. Marchuk, S. Wendl, N. Imamovic, F. Tambornino, D. Wiechert, P.J. Schmidt, W. Schnick, *Chem. Mater.* **2015**, *27*, 6432.

[34] S. Wendl, S. Mardazad, P. Strobel, P.J. Schmidt, W. Schnick, *Angew. Chem. Int. Ed.* **2020**, *59*, 18240.

[35] M. Mallmann, S. Wendl, P. Strobel, P.J. Schmidt, W. Schnick, *Chem. Eur. J.* **2020**, *26*, 6257.

[36] M. Dialer, K. Witthaut, T. Bräuniger, P.J. Schmidt, W. Schnick, *Angew. Chem. Int. Ed.* **2024**, *63*, e202401419.

[37] G. Krach, J. Steinadler, K. Witthaut, W. Schnick, *Angew. Chem. Int. Ed.* **2024**, *63*, e202404953.

[38] S. Vogel, A.T. Buda, W. Schnick, *Angew. Chem. Int. Ed.* **2018**, *57*, 13202.

[39] F. Liebau, *Structural Chemistry of Silicates*, Springer, Berlin (Germany), **1985**.

[40] E.-M. Bertschler, C. Dietrich, T. Leichtweiß, J. Janek, W. Schnick, *Chem. Eur. J.* **2018**, *24*, 196.

[41] D. Baumann, W. Schnick, *Angew. Chem. Int. Ed.* **2014**, *53*, 14490.

[42] S. J. Ambach, M. Pointner, S. Falkai, C. Paulmann, O. Oeckler, W. Schnick, *Angew. Chem. Int. Ed.* **2023**, *62*, e202303580.

[43] D. Laniel, F. Trybel, A. Néri, Y. Yin, A. Aslandukov, T. Fedotenko, S. Khandarkhaeva, F. Tasnádi, S. Chariton, C. Giacobbe, E. Lawrence Bright, M. Hanfland, V. Prakapenka, W. Schnick, I. A. Abrikosov, L. Dubrovinsky, N. Dubrovinskaia, *Chem. Eur. J.* **2022**, *28*, e202201998.

[44] S. Vogel, M. Bykov, E. Bykova, S. Wendl, S.D. Kloß, A. Pakhomova, S. Chariton, E. Koemets, N. Dubrovinskaia, L. Dubrovinsky, W. Schnick, *Angew. Chem. Int. Ed*. **2019**, *58*, 9060.

[45] M. M. Pointner, C. Ceniza, L. Nusser, K. Witthaut, F. Wolf, M. Weidemann, L. Eisenburger, A. Moewes, O. Oeckler, W. Schnick, *Angew. Chem. Int. Ed.* **2024**, *63*, e202411441.

[46] W. Schnick, J. Luecke, *J. Solid State Chem.* **1990**, *87*, 101.

[47] E.-M. Bertschler, R. Niklaus, W. Schnick, *Chem. Eur. J.* **2017**, *23*, 9592.

[48] E.-M. Bertschler, C. Dietrich, J. Janek, W. Schnick, *Chem. Eur. J*. **2017**, *23*, 2185.

[49] F. J. Pucher, F. W. Karau, J. Schmedt auf der Günne, W. Schnick, *Eur. J. Inorg. Chem.* **2016**, 1497.

[50] F. J. Pucher, A. Marchuk, P. J. Schmidt, D. Wiechert, W. Schnick, *Chem. Eur. J.* **2015**, *21*, 6443.

[51] K. Landskron, H. Huppertz, J. Senker, W. Schnick, *Angew. Chem. Int. Ed.* **2001**, *40*, 2643.

[52] L. Gorelova, A. Pakhomova, G. Aprilis, Y. Yin, D. Laniel, B. Winkler, S. Krivovichev, I. Pekov, N. Dubrovinskaia, L. Dubrovinsky, *Inorg. Chem. Front.* **2022**, *9*, 1735.

[53] E. Bykova, M. Bykov, A. Černok, J. Tidholm, S.I. Simak, O. Hellman, M.P. Belov, I.A. Abrikosov, H.-P. Liermann, M. Hanfland, V.B. Prakapenka, C. Prescher, N. Dubrovinskaia, L. Dubrovinsky, *Nat. Commun.* **2018**, *9*, 4789.

[54] K. Landskron, W. Schnick, *J. Solid State Chem.* **2001**, *156*, 390.

[55] S. Wendl, W. Schnick, *Chem. Eur. J.* **2018**, *24*, 15889.

[56] W. Schnick, U. Berger, *Angew. Chem. Int. Engl*. **1991**, *30*, 830.

[57] S. D. Kloß, N. Weidmann, W. Schnick, *Eur. J. Inorg. Chem.* **2017**, 1930.

[58] S. Horstmann, E. Irran, W. Schnick, *Angew. Chem. Int. Ed. Engl.* **1997**, *36*, 1873.

[59] A. Weiss, A. Weiss, *Z. Anorg. Allg. Chem.* **1954**, *276*, 95.

[60] S. D. Kloß, W. Schnick, *Angew. Chem. Int. Ed.* **2019**, *58*, 7933.

[61] E. Riedel, C. Janiak in *Anorganische Chemie*, *Vol. 8*, De Gruyter, Berlin (Germany), New York (USA), **2011**.

[62] A. E. Rubin, *Am. Min.* **1997**, *82*, 1001.

[63] M. R. Lee, S. S. Russell, J. W. Arden, C. T. Pillinger, *Meteoritics* **1995**, *30*, 387.

[64] F. A. Bannister, *Mineral. Mag. J. Mineral. Soc.* **1941**, *26*, 36.

[65] H. P. Nielsen, V. F. Buchwald, *Proc. Lunar Planet. Sci.* **1981**, *12B*, 1343.

[66] H. J. Axon, J. Kinder, C. W. Haworth, J. W. Horsfield, *Mineral. Mag.* **1981**, *44*, 107.

[67] A. Stock, H. Grüneberg, *Ber. Dtsch. Chem. Ges*. **1907**, *40*, 2573.

[68] H.-P. Baldus, W. Schnick, J. Lücke, U. Wannagat, G. Bogedain, *Chem. Mater.* **1993**, *5*, 845.

[69] N. L. Loh, K.Y. Sia, *J. Mater. Process. Technol.* **1992**, *30*, 45.

[70] T. M. M. Richter, R. Niewa, *Inorganics* **2014**, *2*, 29.

[71] J. Häusler, W. Schnick, *Chem. Eur. J.* **2018**, *24*, 11864.

[72] P.W. Mirwald, I.C. Getting, G.C. Kennedy, *J. Geophys. Res*. **1975**, *80*, 1519.

[73] H.T. Hall, *Rev. Sci. Instrum.* **1960**, *31*, 125.

[74] D. Yamazaki, E. Ito, T. Yoshino, N. Tsujino, A. Yoneda, X. Guo, F. Xu, Y. Higo, K. Funakoshi, *Phys. Earth Planet. Inter.* **2014**, *228*, 262.

[75] L. Dubrovinsky, S. Khandarkhaeva, T. Fedotenko, D. Laniel, M. Bykov, C. Giacobbe, E. Lawrence Bright, P. Sedmak, S. Chariton, V. Prakapenka, A.V. Ponomareva, E.A. Smirnova, M.P. Belov, F. Tasnádi, N. Shulumba, F. Trybel, I.-A. Abrikosov, N. Dubrovinskaia, *Nature*, **2022**, *605*, 274.

[76] T. Ishi, Z. Liu, T. Katsura, *Engineering*, **2019**, *5*, 434.

[77] S. Wendl, *Dissertation*, Ludwig-Maximilians-Universität München (Germany) **2022**.

[78] M.H. Bocanegra-Bernal, *J. Mater. Sci.* **2004**, *39*, 6399.

[79] H.V. Atkinson, S. Davies, *Metall. Mater. Trans. Sect. A*, **2000**, *31*, 2981.

[80] B. Sreenu, R. Sarkar, S.S. Satheesh Kumar, S. Chatterjee, G. Appa Rao, *J. Mater. Sci. Eng. A*, **2020**, *797*, 140254.

[81] H. Watanabe, N. Kijima, *J. Ceram. Soc. Jpn.* **2009**, *117*, 115.

[82] H. Watanabe, M. Imai, N. Kijima, *J. Am. Ceram. Soc.* **2009**, *92*, 641.

[83] H. Watanabe, N. Kijima, *J. Alloys Compd.* **2009**, *475*, 434.

[84] S. Wendl, M. Zipkat, P. Strobel, P.J. Schmidt, W. Schnick, *Angew. Chem. Int. Ed.* **2021**, *60*, 4470.

[85] N. Kawai, M. Togaya, A. Onodera, *Proc. Jpn. Acad.* **1973**, *49*, 623.

[86] N. Kawai, S. Endo, *Rev. Sci. Instrum.* **1970**, *41*, 1178.

[87] D. Walker, M. A. Carpenter, C. M. Hitch, *Am. Miner.* **1990**, *75*, 1020.

[88] D. Walker, *Am. Miner.* **1991**, *76*, 1092.

[89] H. Huppertz, *Z. Kristallogr. – Cryst. Mater.* **2004**, *219*, 330.

2 From Framework to Layers Driven by Pressure – The Monophyllo-Oxonitridophosphate β-$MgSrP_3N_5O_2$ and Comparison to its α-Polymorph

Published in: *Chem. Eur. J.* **2023**, *29*, e202301218.

Authors: Reinhard M. Pritzl, Nina Prinz, Philipp Strobel, Peter J. Schmidt, Dirk Johrendt, and Wolfgang Schnick

DOI: https://doi.org/10.1002/chem.202301218

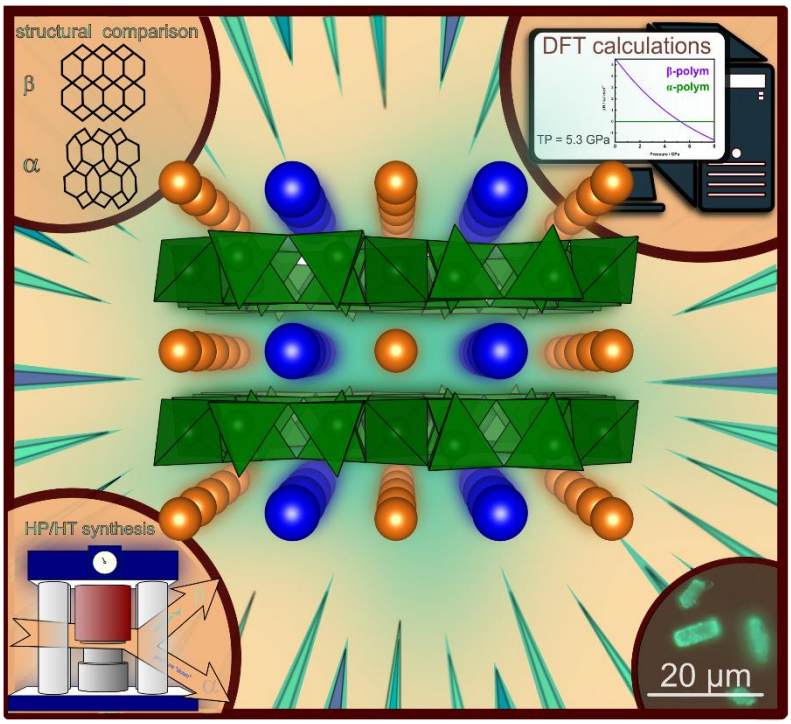

Abstract. Oxonitridophosphates exhibit the potential for broad structural diversity, making them promising host-compounds in phosphor-converted light-emitting diode applications. The novel monophyllo-oxonitridophosphate β-$MgSrP_3N_5O_2$ was obtained by using the high-pressure multianvil technique. The crystal structure was solved and refined based on single-crystal X-ray diffraction data and confirmed by powder X-ray diffraction. β-$MgSrP_3N_5O_2$ crystallizes in the orthorhombic space group *Cmme* (no. 67, a = 8.8109(6), b = 12.8096(6), c = 4.9065(3) Å, Z = 4) and has a structure related to that of $Ba_2CuSi_2O_7$. DFT calculations were performed to investigate the phase transition from α- to β-$MgSrP_3N_5O_2$ and to confirm the latter as the corresponding high-pressure polymorph. Furthermore, the luminescence properties of Eu^{2+} doped samples of both

polymorphs were investigated and discussed, showing blue and cyan emission, respectively (α-$MgSrP_3N_5O_2$; λ_{max} = 438 nm, *fwhm* = 46 nm/2396 cm^{-1}; β-$MgSrP_3N_5O_2$; λ_{max} = 502 nm, *fwhm* = 42 nm/1670 cm^{-1}).

2.2 Introduction

Oxonitridophosphates such as AE_2PO_3N (*AE* = Ca, Sr, Ba) or $Sr_3P_6O_6N_8$ were recently discussed as potential host compounds in phosphor-converted light-emitting diode applications.[1-3] Such mixed-anion compounds often crystallize in various structure types owing to increased flexibility of formal charges through substitution of N^{3-} by O^{2-}. This is useful for tuning the luminescence properties, since a fundamental change in emission usually requires a change in the host lattice or, more importantly, of the activator environment. In contrast to that the doping concentration affects emission only slightly.[4,5] Thus, there is great incentive to explore oxonitridophosphates, since the isoelectronic relationship of P/N to Si/O is expected to result in a similar structural diversity and therefore a variety for host structures as known for silicates. This structural similarity is evident from the oxonitride parent compound PON, which exhibits a number of SiO_2 analogous high-pressure/ high-temperature (HP/HT) modifications.[6,7] Theoretically, there are several strategies to generate new host lattices in the compound class of oxonitridophosphates. One possibility of fundamentally changing the host structure is to modify the degree of condensation κ (i.e. the atomic ratio of the central atoms (P) : ligands (N/O)). Another one is to change the ligand ratio at an existing κ, since oxygen is usually twofold crosslinked and nitrogen can be triply- or even fourfold-connected in nitridic compounds.[8] Hence, O/N substitution theoretically allows for a by far higher number of charge balanced compositions with different cation ratio *CR* = counter cation : network cation, at a constant κ. This affects significantly the physical properties, such as stability due to a more covalent character of P–N-bonds.[9] Within the context of luminescent materials engineering, increased electron density in between activator ion and ligand leads to a stronger nephelauxetic effect.[10] However, only a few oxonitridophosphates have been investigated so far. Primarily, this is due to the challenging synthesis originating from the low thermal stability of phosphorus nitrides (e.g. P_3N_5) and the difficulty of controlled oxygen incorporation. [11-13] The so-called “azide approach“ has proven to be successful for the synthesis of numerous nitridophosphates under high-pressure. Adding PON as an oxygen source has also shown this route to be suitable for oxonitridophosphate synthesis.[14] The thermolysis of the azide leads to an increase of the N_2 partial pressure in the reaction crucible and, according to *Le*

Chatelier, to a suppression of the decomposition of the phosphorus (oxo)nitrides.[3,15] Another successful approach is the combination of "nitride and mineralizer-route". This strategy has been revived and modified recently by Eisenburger *et al.* for synthesis of transition metal oxonitridophosphates, starting from binary nitride precursors like ScN and TiN by adding NH_4F as activation reagent.[16,17] Based on this, a combination of both nitride and azide approaches, appears to be a promising method to synthesize new oxonitridophosphates, as exemplified by the synthesis of $MgSrP_3N_5O_2$. The latter was obtained starting from stoichiometric amounts of Mg_3N_2, $Sr(N_3)_2$, PON and P_3N_5, as well as NH_4Cl as mineralizer, performed under HP/HT conditions (6 GPa, approx. 1270 K).[14] With a degree of condensation $\kappa = 3/7$, $MgSrP_3N_5O_2$ contains a condensed anionic 3D network structure. Contrary, a number of related isoelectronic nitrides, oxonitrides and oxides show layered structure types for $\kappa = 3/7$ (e.g. $RE_2P_3N_7$ (*RE* = La, Ce, Pr, Nd, Sm, Eu, Ho, Yb), $RE_2Si_3O_3N_4$ (*RE* = La, Nd, Sm, Gd, Dy, Ho, Er, Yb), $AE_3P_6O_6N_8$ (*AE* = Sr, Ba), $Ca_2MgSi_2O_7$ and $SrHoAl_3O_7$) .[3,18-22] This observation was our starting point to search for a corresponding layered polymorph of $MgSrP_3N_5O_2$. In this contribution, we report on the synthesis and structure elucidation of the novel β-polymorph of $MgSrP_3N_5O_2$. DFT calculations were performed to investigate the phase transition from α- to β-$MgSrP_3N_5O_2$ and to confirm the latter as the corresponding high-pressure polymorph. In the context of phosphor research, the obtained products were characterized and the luminescence properties of Eu^{2+} doped samples were investigated, compared and related to each other.

2.2 Results and Discussion

As described in literature α-$MgSrP_3N_5O_2$ can be prepared by a HP/HT reaction at 6 GPa and approx. 1270 K using a hydraulic multianvil press starting from Mg_3N_2, $Sr(N_3)_2$, amorphous a-PON, and P_3N_5 according to Equation 2.1: [14]

$$Mg_3N_2 + 3\ Sr(N_3)_2 + 6\ \text{a-PON} + P_3N_5 \rightarrow 3\ \alpha\text{-}MgSrP_3N_5O_2 + 8\ N_2 \qquad (2.1)$$

We found out, that replacing a-PON by P_4O_{10} enables the synthesis of crystallographically phase-pure α-$MgSrP_3N_5O_2$ at 3 GPa and temperatures up to 1670 K (Equation 2.2), which was confirmed by Rietveld refinement of powder X-ray diffraction data (Figure S2.1, Table S2.1, Supporting Information).

$$5\ Mg_3N_2 + 15\ Sr(N_3)_2 + 3\ P_4O_{10} + 11\ P_3N_5 \rightarrow 15\ \alpha\text{-}MgSrP_3N_5O_2 + 40\ N_2 \qquad (2.2)$$

P_4O_{10} is less condensed (κ = 2/5) therefore more reactive than PON (κ = 1/2). Moreover, under these synthesis conditions, it is present in liquid form and thus acts as a flux.[23] Using cristobalite type cri-PON instead of a-PON and increasing the reaction pressure to 7 GPa, the HP modification β-$MgSrP_3N_5O_2$ can be prepared as main phase. However, the preparation of β-$MgSrP_3N_5O_2$ starting from P_4O_{10} at these reaction pressures was not possible. Highest yields can be achieved by using MgO and cri-PON as oxygen sources (according to Equation 2.3).

$$3\ MgO + 3\ Sr(N_3)_2 + 3\ \text{cri-PON} + 2\ P_3N_5 \rightarrow 3\ \beta\text{-}MgSrP_3N_5O_2 + 8\ N_2 \qquad (2.3)$$

The title compounds were isolated as air- and moisture-stable grayish solids. After washing with de-ionized water, crystals with edge lengths up to 20 µm were obtained (Figure S2.2).

2.2.2 Crystal Structure of β-$MgSrP_3N_5O_2$

The crystal structure of β-$MgSrP_3N_5O_2$ was solved and refined based on single-crystal X-ray diffraction data in the orthorhombic space group *Cmme* (no. 67) with lattice parameters a = 8.8109(6), b = 12.80960(6) and c = 4.9065(3) Å. The crystallographic data are given in Table 2.1, Wyckoff positions, atomic coordinates, anisotropic displacement parameters, as well as interatomic distances and angles are given in Tables S2.3 – S2.5. Additional solid-state ^{31}P MAS NMR spectroscopy experiments support the structure solution (Figure S2.3). In the spectrum two signals with an intensity ratio of 2:1 are observed, which can be assigned to the two crystallographic sites (P1: Wyckoff 8*m*; P2: Wyckoff 4*b*). The chemical shifts δ_1= 10.4 and δ_2= 5.4 ppm (Figure S2.4) are in a typical range for oxonitridophosphates.[24, 25] The nitrogen content was determined by CHNS elemental analysis (Tables S2.6). For SEM-EDX measurements (Table S2.2) only the atomic cation ratios were considered (Sr/Mg/P), since partial hydrolysis during water treatment falsifies both the anion and total atomic values. Both, measured cationic values as well as ratios agree well with the theoretical ones. Based on the obtained structure model, a Rietveld refinement based on powder X-ray diffraction data was carried out to check the sample for phase purity and phase content (Figure 2.1, Table S7). Additional reflections of an unknown minor side phase are marked with asterisks in Figure 2.1.

Table 2.1. Crystallographic data from single-crystal refinement of β-$MgSrP_3N_5O_2$.

Formula	**β-$MgSrP_3N_5O_2$**
Crystal system	Orthorhombic
Molecular weight / $g \cdot mol^{-1}$	306.89
Space group	*Cmme* (no. 67)
Lattice parameters / Å	a = 8.8109(6)
	b = 12.8096(6)
	c = 4.9065(3)
Cell volume / $Å^3$	553.77(6)
Formula units per cell	4
Calculated density / $g \cdot cm^{-3}$	3.681
μ / mm^{-1}	10.660
T_{min} / T_{max}	0.8908 / 1.0000
Radiation	Mo-K_α (λ = 0.71073 Å)
Temperature / K	293(2)
F(000)	584
Θ range / °	$2.806 < \Theta < 43.069$
Total no. of reflections	6716
Independent reflections (>2σ)	582 (526)
Refined parameters	37
R_{int}; R_σ	0.0552; 0.0206
$R1$ (all data); $R1$ ($F^2>2\sigma(F^2)$)	0.0317; 0.0270
$wR2$ (all data); w$R2$ ($F^2>2\sigma(F^2)$)	0.0597; 0.0582
Goodness of fit	1.061
$\Delta\rho_{max}$; $\Delta\rho_{min}$ / $e \cdot Å^{-3}$	0.664; −0.968

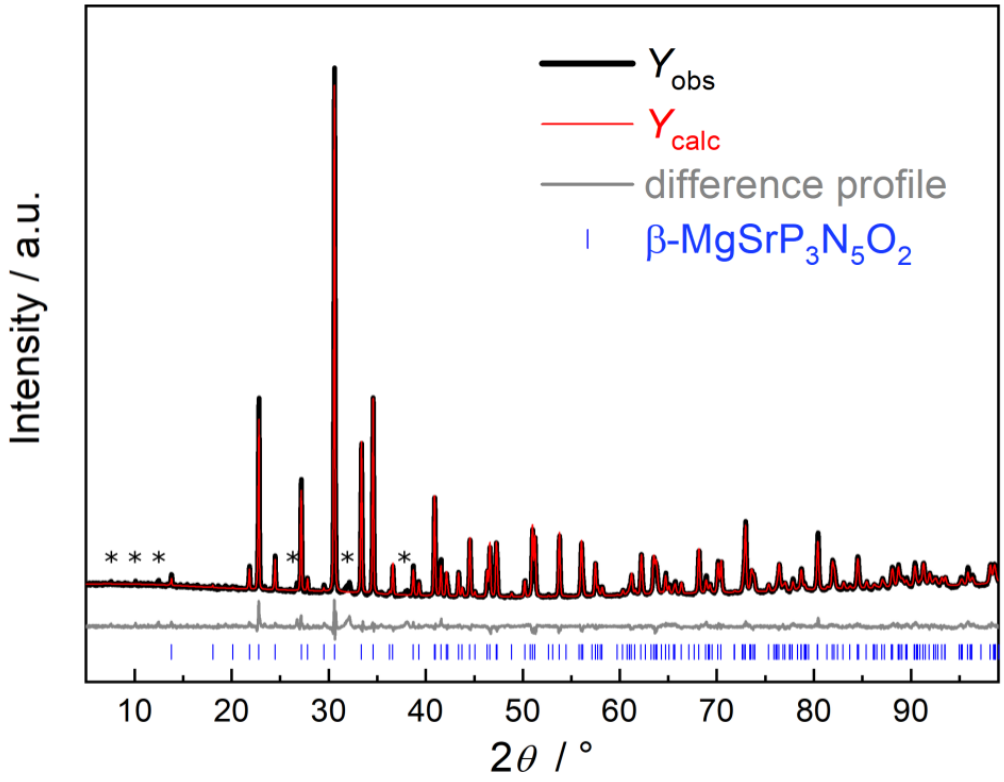

Figure 2.1. Rietveld refinement based on PXRD data of β-$MgSrP_3N_5O_2$ with experimental data (black line), calculated diffraction pattern (red line), corresponding difference profile (gray line) and related Bragg reflections (vertical blue bars). Reflections of an unknown byproduct are marked with asterisks.

In contrast to many textbook examples, a pressure-driven reduction in the dimensionality of the anionic partial structure is observed in the case described here.[26-28] α-$MgSrP_3N_5O_2$ forms a 3D framework structure, whereby β-$MgSrP_3N_5O_2$ prepared under higher pressure can be classified as a monophyllo-oxonitridophosphate following silicate nomenclature, which consists of monolayers of $P(O,N)_4$ tetrahedra and thus has a two-dimensional structure. According to the nomenclature introduced by Liebau, *vierer* and *sechser* rings of condensed $P(O,N)_4$ tetrahedra occur in both polymorphs (Figure 2.2). In the case of α-$MgSrP_3N_5O_2$ additional *achter* rings connect *vierer* and *sechser* rings, resulting in the 3D arrangement.[29]

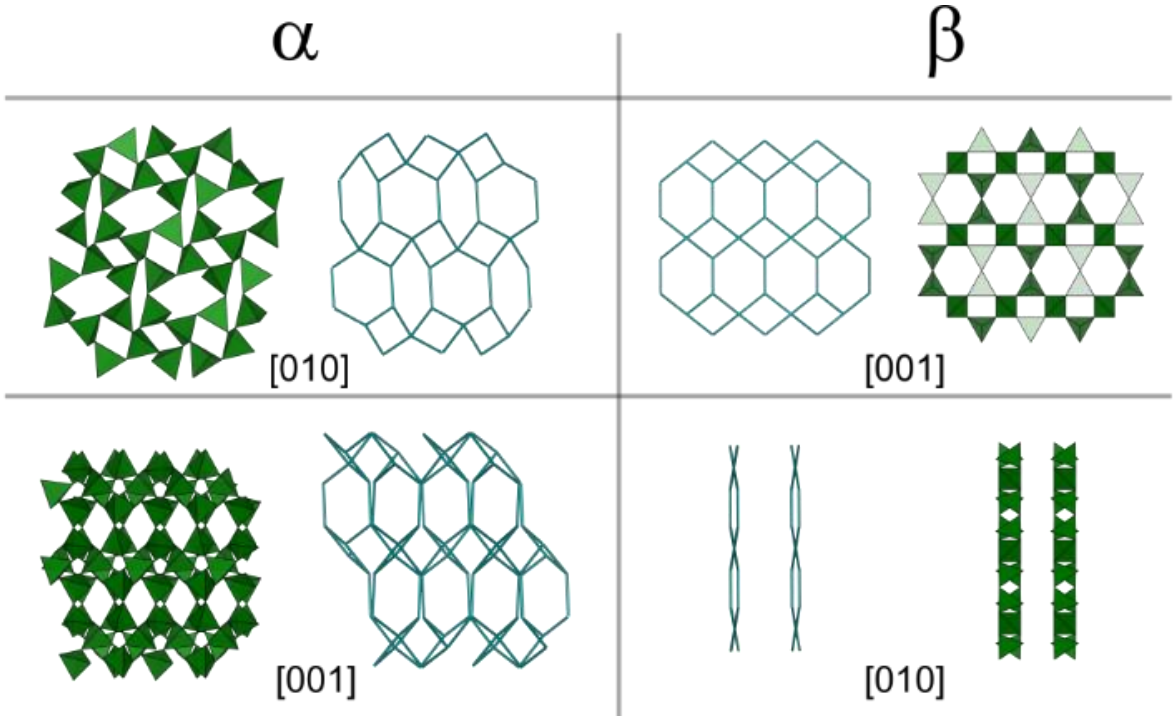

Figure 2.2. Comparison of the anionic $P(O,N)_4$ motifs of both $MgSrP_3N_5O_2$ polymorphs (left side α-type, right side β-type) with respective topological representation. Each connection line in the topological representation exemplifies a P–N–P bond. Top: sechser and vierer rings viewed along [010] (α-type) and [001] (β-type); bottom: framework structure (α-type) viewed along [001] versus layers (β-type) along [010].[30]

Further information about the crystal structure of the α-type see Pucher *et al*.[14] In β-$MgSrP_3N_5O_2$ the anionic $P(O,N)_4$ tetrahedra layer exhibits two different P sites. Respective Q^3-type PON_3 tetrahedra (O terminally bound) and all-side vertex sharing Q^4-type PN_4 tetrahedra (all N bridging) occur in an atomic ratio of 2:1.This stands in good agreement to Pauling`s 2nd rule, where the N atoms prefer the bridging positions, while the O atoms are terminally bound to P.[31-33] The Rietveld refinement as well as lattice energy calculations (MAPLE), bond valence sums (BVS) and charge distribution (CHARDI) calculations (Tables S2.8 and S2.9) support the unambiguous assignment of O an N in the structure model.[34-38] The resulting topology of the anionic framework specified by the point symbol $\{4.6^2\}_2\{4^2.6^2.8^2\}$ (calculated with TOPOS), has been assigned once for nitridophosphate based compounds in bex-*RE*P_3N_7 (topological symbol defined by *Reticular Chemistry Structure Resource* (RCSR)).[39,40]

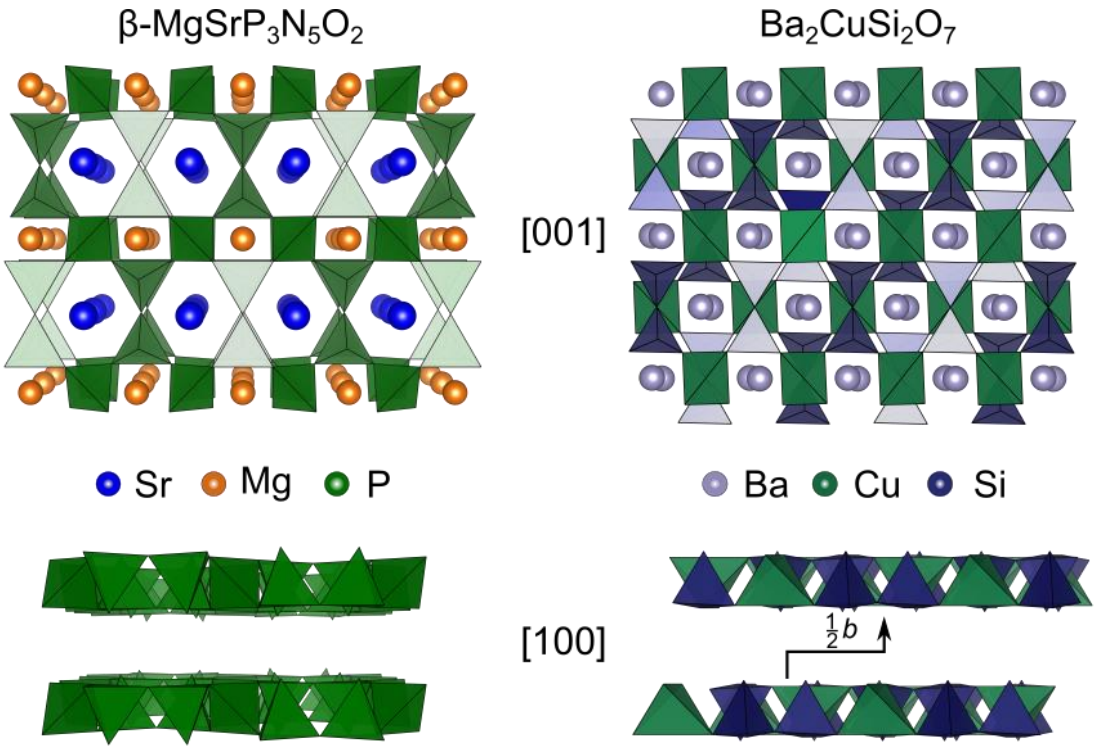

Figure 2.3. Comparison of the structures of β-$MgSrP_3N_5O_2$ (left side) and $Ba_2CuSi_2O_7$ (right side) along [001] as well as [100]. Here, both stacking and displacement along the *c* translation are visualized.[30]

The monolayers in bex-*RE*P_3N_7, which crystallizes in the $Ba_2CuSi_2O_7$ structure type, are shifted one-half of a *b*-translation against each other, whereas in β-$MgSrP_3N_5O_2$ the monolayers are stacked congruently (Figure 2.3).[41,42] Therefore, the layered structure expected for $\kappa = 3/7$ represents a hitherto unprecedented structure type*. The anionic layers of β-$MgSrP_3N_5O_2$ are separated by Sr^{2+} and Mg^{2+} ions in the interstitial spaces of different ring-types created by the $P(N,O)_4$ tetrahedra connection pattern. Sr^{2+} ions prefer the larger *sechser* ring positions, and Mg^{2+} cations prefer the smaller *vierer* ring positions, due to their differing ionic radii (Figures 2.3 and 2.4).[29,43]

* According to recent findings, the mineral johachidolite ($CaAl[B_3O_7]$) represents the structural prototype.

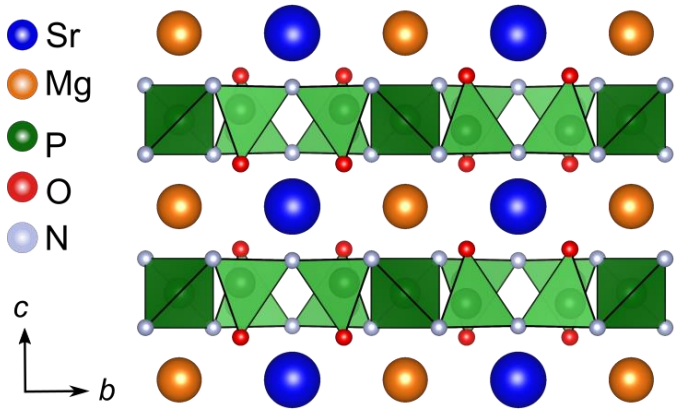

Figure 2.4. Mg (orange) and Sr (blue) cations separated through anionic oxonitridophosphate layers, view along [100].[30]

Thereby, Mg occupies a single crystallographic site located in a slightly compressed octahedron. This is due to the occupation of the axial octahedral corners by O and the equatorial ones by N. This is noticeable by the axial Mg–O bond lengths of 2.117(3) Å, which are slightly shorter than the equatorial Mg–N bond lengths with 2.1845(19) Å (Figure 2.5). Sr is surrounded by four O and six N atoms, in a pentagonal antiprismatic coordination. The Sr–N (2.680(3)–2.8402(19) Å) and Sr–O (2.9071(15) Å) distances are in the same range as reported for other strontium oxonitridophosphates (e.g. Sr_2PO_3N and $Sr_3P_6O_6N_8$) and correspond well with the sum of the ionic radii. [3,43,44]

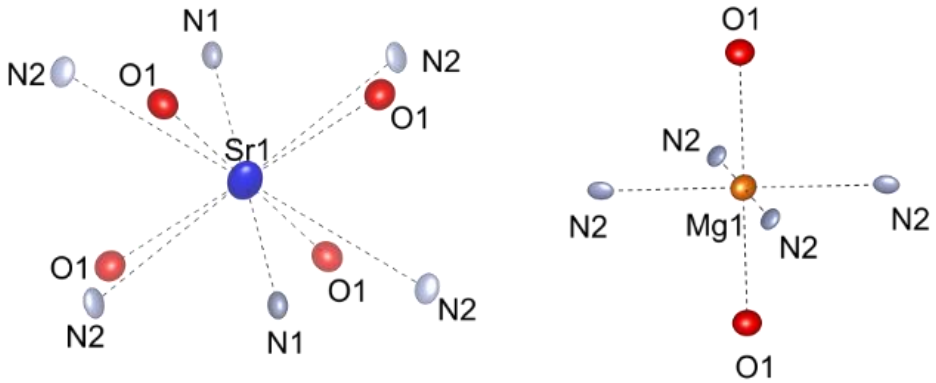

Figure 2.5. Coordination of Sr and Mg atoms in β-$MgSrP_3N_5O_2$. Sr atom is illustrated in blue, Mg atom in orange, O atoms in red, and N atoms in gray (displacement parameters with 95% probability.[30]

2.2.3 Density Functional Theory Calculations

The comparison of the α- and β-polymorphs shows several indications that β-$MgSrP_3N_5O_2$ is a high-pressure phase of α-$MgSrP_3N_5O_2$. The β-type is synthesized at higher pressures, exhibits a smaller cell volume (553.77(6) $Å^3$ versus 562.06(10) $Å^3$) while maintaining $Z = 4$ (= higher density), and shows a higher coordination at the Sr site (*CN* = 10 versus *CN* = 9, Figure 2.8) which is consistent with Neuhaus' pressure-coordination rule.[45] To confirm the assumed high-pressure phase transition correlation from α- to β-$MgSrP_3N_5O_2$, additional ab initio DFT calculations were performed. The structure optimization was obtained through relaxation of atom positions and cell parameters. The energy-volume curves were computed by simulating a synthesis pressure up to 8 GPa. The enthalpy as a function of pressure is depicted in Figure 2.6, as extracted from the energy-volume curves evaluated with the Universal Equation of States.[46] The enthalpy difference as a function of pressure shows an energetic favoring of β-$MgSrP_3N_5O_2$ compared to the α-type for a pressure above 5.3 GPa. The intersection of both curves herein indicates a possible phase transition, which, however, has not been observed experimentally as yet.

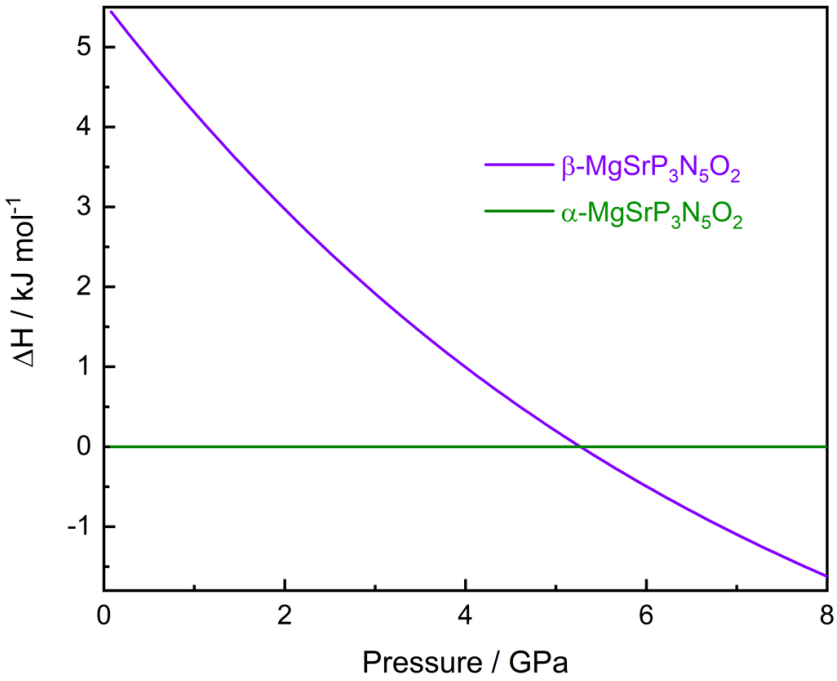

Figure 2.6. Enthalpy-pressure diagram obtained by fitting the Universal Equation of States from Energy-Volume diagram for the α- and β-polymorph.

2.2.4 UV/Vis Reflectance Spectroscopy

To characterize the optical properties an undoped sample of β-$MgSrP_3N_5O_2$ was investigated by diffuse reflectance spectroscopy (Figure S2.4). For determination of the optical band gap, the Kubelka-Munk function $F(R) = (1-R)^2/2R$, where R represents the reflectance, was used to convert the reflectance spectrum into a pseudo-absorption spectrum.[47] Via Tauc plot (plot of hν versus $(F(R)\cdot h\nu)^{1/n}$), an approximately linear region is evident for n =1/2, which indicates a direct band gap (Figure 2.7).[48] By applying a tangent to the inflection point in this range and determination of the intersection with the abscissa, a band gap of about 5.1 eV was estimated.

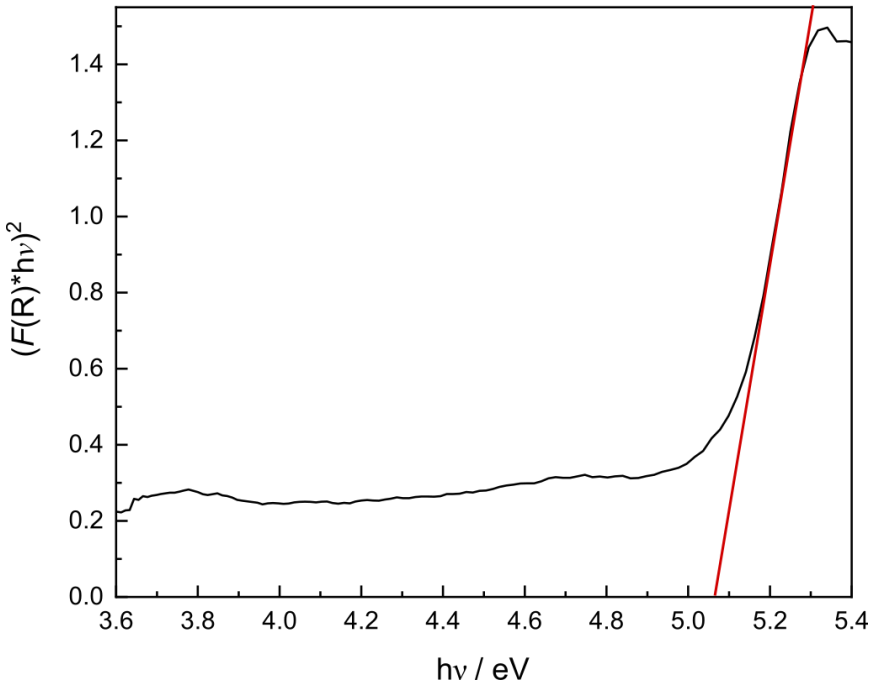

Figure 2.7. Tauc plot of non-doped β-$MgSrP_3N_5O_2$ (black line) with a tangent at the inflection point (red line).

2.2.5 Photoluminescence Properties

To investigate luminescence properties of both modifications, samples were prepared by addition of $EuCl_2$ as dopant to the starting mixtures (approx. 3 mol% Eu^{2+} with respect to Sr^{2+}). Upon irradiation with UV light ($\lambda_{exc.}$ = 420 nm) α-$MgSr_{0.97}P_3N_5O_2$:$0.03Eu^{2+}$ shows blue emission with a maximum at 438 nm and a full width at half-maximum (*fwhm*) of 46 nm/2396 cm^{-1}. In contrast, β-$MgSr_{0.97}P_3N_5O_2$:$0.03Eu^{2+}$ shows a strong cyan emission with 502 nm and *fwhm* = 42 nm/1620 cm^{-1} (Figure 2.9). The observed luminescence can be explained by comparing the cationic coordination spheres. In both cases, only one luminescence signal is

evident, which is consistent with the presence of one crystallographic Sr site, and the ionic radii indicate that Eu^{2+} occupies preferably only Sr^{2+} sites rather than Mg^{2+} sites. [3,49] In α-$MgSrP_3N_5O_2$, Sr is reported to be coordinated by a doubly capped pentagonal bipyramid (see Figure 2.8).[14]

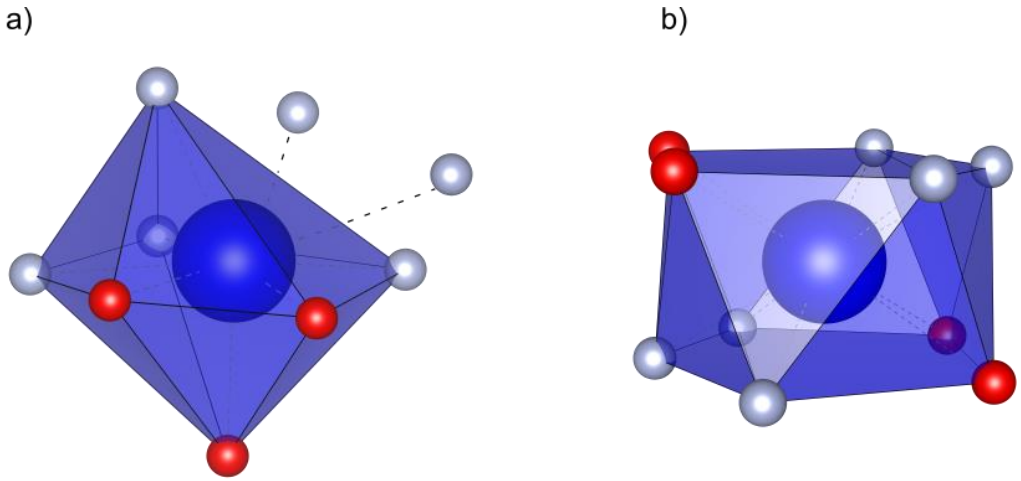

Figure 2.8. Coordination of the Sr site in α-$MgSrP_3N_5O_2$ (a) and β-$MgSrP_3N_5O_2$ (b). Sr atoms are illustrated in blue, O atoms in red and N atoms in gray.[30]

Therefore, the coordination number (*CN*) is 7+2 (3×O and 6×N). In contrast, in β-$MgSrP_3N_5O_2$ Sr exhibits a pentagonal antiprismatic coordination (*CN* = 10; 4×O and 6×N). Sr is in both polymorphs located at the Wyckoff position 4*e*. However, the site in β-$MgSrP_3N_5O_2$ exhibits a higher symmetry (2/*m* versus 1). This contributes to a narrowing of the emission band, caused by a reduction of the lattice relaxation around the activator ion in its excited state due to the higher site symmetry, which can be seen in the reduction of the full width at half maximum from 46 nm/2396 cm^{-1} (α-$MgSr_{0.97}P_3N_5O_2$:$0.03Eu^{2+}$) to 42 nm/1620 cm^{-1} (β-$MgSr_{0.97}P_3N_5O_2$:$0.03Eu^{2+}$).[50-52] This can be explained by symmetry-induced smaller bond length variance in β-$MgSrP_3N_5O_2$, which is $\sigma^2 = 0.0069$ (symmetry-related three different Sr–N/O distances; Table S2.5) versus $\sigma^2 = 0.048$ (nine different Sr–N/O distances) in α-$MgSrP_3N_5O_2$.[53] Furthermore, the observed redshift (λ_{max} = 438 nm (α-type) to λ_{max} = 502 nm (β-type)) can be attributed to the nephelauxetic effect as well as ligand field splitting, whereby essentially the former was considered here (see Figure 2.9). Consideration of the closest ligands of the first coordination sphere of the activator ion (< 2.85 Å Eu^{2+}–N/O distance) may serve as explanation: In the α-type, only three nitrogen atoms and two oxygen atoms are located in close proximity (see Figure 2.10 a), while in the β-type, six nitrogen atoms coordinate most closely (Figure 2.10 b).

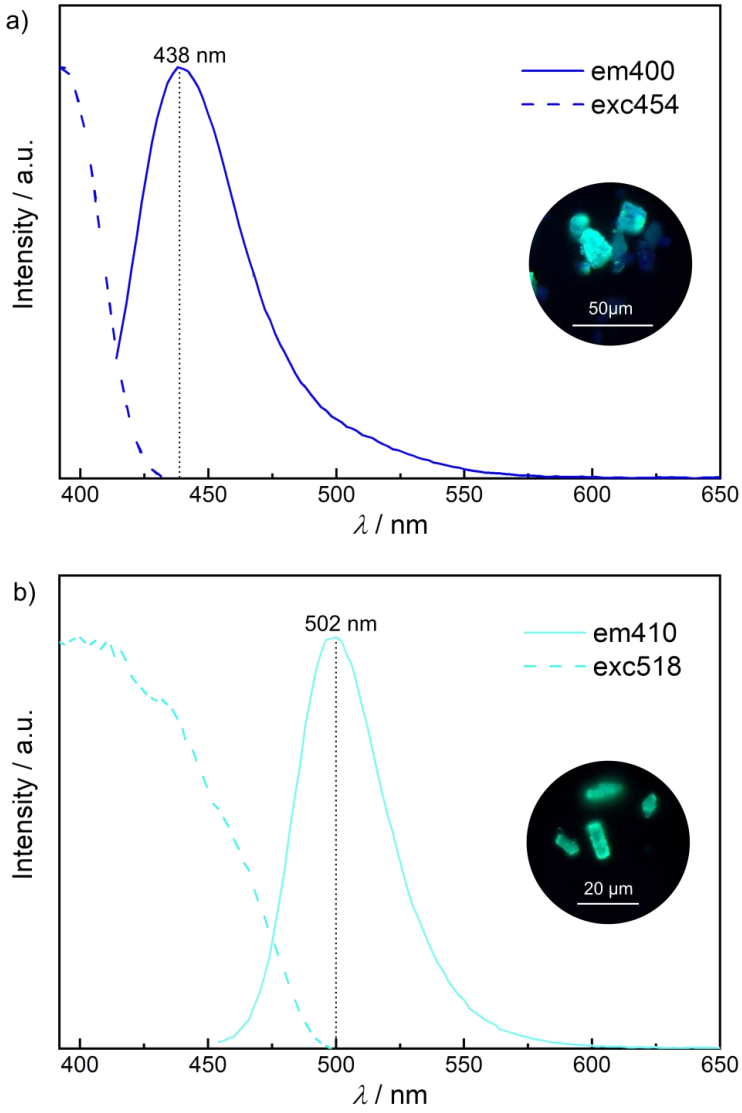

Figure 2.9. Excitation (dashed line) and emission spectra (continuous line) of α-$MgSr_{0.97}P_3N_5O_2$:$0.03Eu^{2+}$ (a) and β-$MgSr_{0.97}P_3N_5O_2$:$0.03Eu^{2+}$ (b), inset: micrograph of luminescent particles.

The smaller electronegativity of nitrogen compared to oxygen leads to an increased covalency of the Eu–N bond, which results in an energetic lowering of the Eu^{2+} 5*d* levels and therefore a reduction of the 4*f*-5*d* transition energy. [54,55] The higher nitrogen content in the first coordination sphere of Eu^{2+} in β-$MgSr_{0.97}P_3N_5O_2$:$0.03Eu^{2+}$ should lead to an enhanced nephelauxetic effect and thus to a stronger reduction of the 4*f*-5*d* transition energy, which leads to the observed red-shift of both, lowest lying absorption and emission bands. A classification of both compounds as (oxo)nitridophosphate based phosphors shows that α-$MgSr_{0.97}P_3N_5O_2$:$0.03Eu^{2+}$ exhibits emission

comparable to $SrSiP_3N_7:Eu^{2+}$ (λ_{max} = 430 nm, *fwhm* = 53 nm/2731 cm^{-1}), while β-$MgSr_{0.97}P_3N_5O_2:0.03Eu^{2+}$ represents the most narrow cyan emitting (oxo)nitridophophate based phosphor known so far, compared to other (oxo)nitridophosphate based phosphors such as $Ca_2PO_3N:Eu^{2+}$ (λ_{max} = 525 nm, *fwhm* ≈ 4025 cm^{-1}).[2,56]

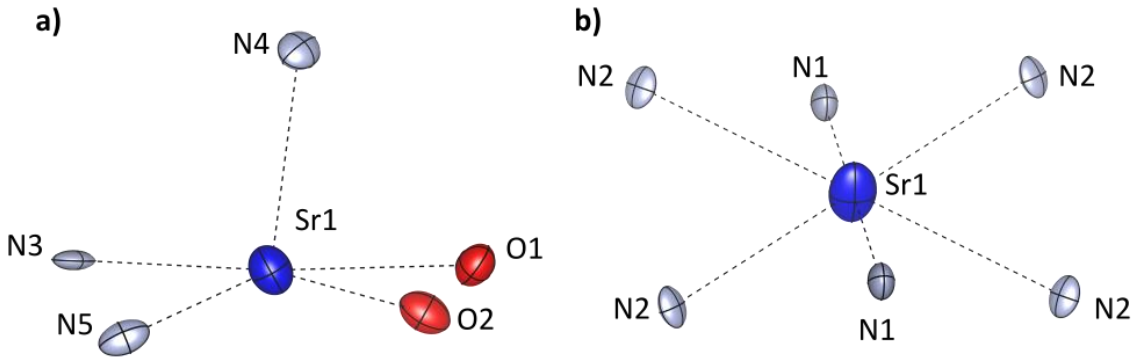

Figure 2.10. Next neighbor coordination of the activator site (O/N distances ≤ 2.85 Å to Sr) in both polymorphs. Sr atoms in blue, O atoms in red, N atoms in gray (displacement parameters with 95% probability). a) Sr site in α-$MgSrP_3N_5O_2$, b) Sr site in β-$MgSrP_3N_5O_2$.

2.2.6 Conclusion

In this contribution, we have reported on synthesis and structural investigation of the high-pressure polymorph β-$MgSrP_3N_5O_2$ as well as a comparison to its low-pressure α-modification $MgSrP_3N_5O_2$ and the structurally similar silicate $Ba_2CuSi_2O_7$. DFT calculations revealed an energetic preference of the β-polymorph at elevated pressure, a possible transition from α- to β-$MgSrP_3N_5O_2$ at 5.3 GPa and confirm the latter as the corresponding high-pressure polymorph. In addition, an alternative synthesis protocol for α-$MgSrP_3N_5O_2$ was developed. Luminescence properties of Eu^{2+}-doped samples of both polymorphs were investigated. The different luminescence behavior was compared and explained. For a more detailed consideration, MO calculations could be performed on both compounds in subsequent work.[57] In terms of a potential application, β-$MgSrP_3N_5O_2$ fills the so called cyan gap (480–520 nm) that commonly occurs in phosphor-converted white light-emitting diodes (pc-wLED).[58,59]. Based on the luminescence properties of the literature known α-polymorph, the subject of subsequent work could be the fundamental investigation of known alkaline earth (oxo)nitridophosphates with respect to their luminescence behavior when doped with Eu^{2+}. In summary, we were able to synthesize and structurally elucidate a novel oxonitridophosphate by comparing structural motifs of literature

known compounds with $\kappa = 3/7$. A possible approach to explore further (oxo)nitridophosphates could be to focus on other compounds that share the same degree of condensation however exhibit completely different structural behavior (e.g. 3D vs. layers, chains vs. isolated units).

2.4 Experimental Section

2.4.1 Preparation of Starting Materials

Synthesis of P_3N_5: In accordance to Stock and Grüneberg semicrystalline phosphorus(V) nitride was prepared through ammonolysis of P_4S_{10} (approx.. 7.0 g, Sigma-Aldrich 99.99%) with ammonia (Air Liquide, 5.0) at 850 °C in a fused silica boat, placed in a quartz tube.[60] To ensure anhydrous conditions, the apparatus (including the fused silica boat) was pre-heated for 5 h at 1000°C under reduced pressure (10^{-3} mbar). Subsequently, the silica boat was loaded with P_4S_{10} in an argon counterflow. The apparatus was saturated with NH_3 for 4 h (constant flow of approx. 3.6 L h^{-1}), heated with a rate of 5 °C min^{-1} to 850 °C, held for 4 h and cooled to ambient temperature with a rate of 5 °C min^{-1}. After flushing the apparatus with Ar for 1 h (in order to remove remaining NH_3) the product was obtained as orange colored grains. P_3N_5 was identified by powder X-ray diffraction, FTIR spectroscopy and CHNS analysis.

Synthesis of cri-PON: Cristobalite type phosphorus oxonitride was synthesized by a modified solid-state reaction of stoichiometric amounts of P_3N_5 and P_4O_{10} according to Kingma *et al.* using a hot isostatic press (HIP, AlP6-30H, American Isostatic Presses, Inc., Columbus, Ohio, USA).[61] The synthesis was carried out under N_2 (99.9%) atmosphere at 100 MPa and 780 °C. For this purpose, the starting materials were ground in an agate mortar and filled into a W crucible, which was placed in an Al_2O_3 over-vessel. The assembly was transferred into the HIP and the apparatus was purged three times. Then a pressure booster (Maximator, DLE-5-30-2) was used to build up the necessary pre-pressure for operating the main-compressor. The pressure was increased to 50 MPa at 20 °C, followed by heating the sample up to 780 °C (heating-rate: 5 °C min^{-1}), resulting in a final pressure of 100 MPa. The reaction condition was maintained for 10 h and subsequently allowed to cool down to 20 °C (cooling-rate: 5 °C min^{-1}) before releasing the remaining pressure manually. The product was obtained as a grayish sinter cake, which was investigated for phase purity by powder X-ray diffraction and CHNS analysis.

Synthesis of $Sr(N_3)_2$: Strontium azide was synthesized by an ion exchange reaction of $SrCO_3$ (Sigma Aldrich, 99.995%) with aqueous HN_3 using a cation exchanger (Amberlyst 15) according Suhrmann *et al.*.[62, 63] HN_3, formed by passing an aqueous solution of NaN_3 (Acros Organics, 99%, extra pure) through the cation exchanger, was carefully dropped into an aqueous suspension of the carbonate until the eluate exhibited pH neutrality. Residues of the carbonate respectively impurities of the starting materials were filtered off and the solvent was removed by rotation evaporation. The product was obtained as crystalline colorless needles, which were investigated for phase-purity by powder X-ray diffraction. **Caution:** HN_3 is explosive in dry form and highly poisonous, special care is mandatory.

2.4.4 Preparation of α-/β-$MgSrP_3N_5O_2$:

The oxonitridophosphate polymorphs α-/β-$MgSrP_3N_5O_2$ were synthesized via high-pressure high-temperature synthesis using a 1000 t press with a modified Walker-type multianvil apparatus.[64-66] Both products were synthesized from stoichiometric amounts of P_3N_5, $Sr(N_3)_2$, Mg_3N_2, cri-PON respectively P_4O_{10}. Doping of both compounds was carried out by partial substitution of Sr^{2+} with Eu^{2+} (approx. 3 mol%) by using $EuCl_2$. Owing to the air-sensitivity, the starting materials were handled in an Ar-filled glovebox (Unilab, MBraun, Garching, O_2 < 1 ppm, H_2O < 0.1 ppm), ground in an agate mortar and transferred into a cylindrical h-BN crucible (HeBoSint® S100, Henze, Kempten, Germany) and closed by a h-BN cap. The latter was placed in an octahedron ($MgO:Cr_2O_3$ (5%), edge length 18 mm, Ceramic Substrates & Components, Isle of Wight, UK), which was drilled through and loaded with a ZrO_2 sleeve (Cesima Ceramics, Wust-Fischbeck, Germany), which contains graphite tubes (Schunk Kohlenstofftechnik GmbH, Gießen, Germany) as electrical resistance furnaces. As pressure media Co-doped (7%) WC cubes (Hawedia, Marklkofen, Germany) with truncated edges (edge length 11 mm) were used. This elaborate design results in a homogeneous pressure transfer to the sample. Additional information regarding this high-pressure setup may be found in the literature. [67,68] The related synthesis conditions can be found in the synthesis part of Results and Discussion.

2.4.5 Scanning Electron Microscopy (SEM) with Energy-Dispersive X-ray Spectroscopy (EDX):

Studies of morphology and chemical compositions of the title compounds were performed on a dualbeam Helios Nanolab G3 UC (FEI, Hillsboro) with an X-Max 80 SDD EDX detector (Oxford Instruments, Abingdon). For this purpose, analysis samples were fixed on carbon adhesive pads.

2.4.6 Solid-State Magic Angle Spinning (MAS) NMR Spectroscopy:

^{31}P NMR spectra were collected with a DSX AVANCE spectrometer (Bruker) with a magnetic field of 11.7 T. The β-$MgSrP_3N_5O_2$ sample was filled into a rotor with a diameter of 2.5 mm, which was mounted on a commercial MAS probe (Bruker). The sample was rotated at a rotation frequency of 20 kHz. The obtained data were analyzed using device-specific software.

2.4.7 Single-Crystal X-ray Diffraction (SCXRD):

A Bruker D8 Quest diffractometer with Mo-Kα radiation (λ = 0.71073 Å) was used for data collection. SADABS was used for absorption correction.[69] The crystal structure was solved by direct methods (SHELXT) and refined by full-matrix least square methods (SHELXL).[70] Deposition number CSD-2236964 contains the supplementary crystallographic data for this paper. The data are provided free of charge by the joint Cambridge Crystallographic Data Centre and Fachinformationszentrum Karlsruhe Access Structures service (http://www.ccdc.cam.ac.uk/structures).

2.4.8 Powder X-ray Diffraction (PXRD):

Powder X-ray measurements were performed by using a STOE STADI P diffractometer with Cu-$K_{\alpha 1}$ radiation (λ = 1.5406 Å), Ge(111) monochromator and Mythen 1 K detector in modified Debye–Scherrer geometry. The samples were sealed in a glass capillary (0.3 mm, Hilgenberg GmbH). The obtained data were Rietveld refined using TOPAS.[71]

2.4.9 Quantum-Chemical Calculations:

Periodic density-functional theory (DFT) calculations were performed using the Vienna ab initio simulation package (VASP).[72] Core and valence electrons were separated using projector-augmented waves (PAW).[73] Generalized-gradient approximation as described by Perdew, Burke and Ernzerhof (GGA-PBE) was used for the treatment of the exchange and correlation contributions.[74,75] Additional corrections for van-der-Waals forces were included using the DFT-D3 method with Becke-Johnson dumping function.[76,77] The Brillouin zone was sampled on a Γ-centered k-point grid (α-$MgSrP_3N_5O_2$: 5×5×3 β-$MgSrP_3N_5O_2$: 4×2×6). The energy convergence criterium was set to 10^{-6} eV and the residual atomic forces were relaxed until the convergence criterion of $2 \cdot 10^{-2}$ eV/Å was reached. The energy versus volume data was computed by scaling the cell parameters from 95 to 105% (fixed *a*:*b*:*c* ratio). The enthalpy as a function of the pressure was obtained by fitting the energy versus volume data to the Universal Equation of State.[46]

2.5 Acknowledgements

The authors gratefully acknowledge the computational and data resources provided by the Leibniz Supercomputing Centre (www.lrz.de). We also thank Dr. Lisa Gamperl and Amalina Buda for carrying out SEM-EDX measurements and Christian Minke for NMR measurements. Furthermore, we thank Kristian Witthaut (all at Department of Chemistry at LMU Munich) for inspiring discussions.

2.6 References

[1] S. Wendl, M. Mallmann, P. Strobel, P. J. Schmidt, W. Schnick, *Eur. J. Inorg. Chem.* **2020**, 841.

[2] A. Marchuk, P. Schultz, C. Hoch, O. Oeckler, W. Schnick, *Inorg. Chem*. **2016**, *55*, 974.

[3] S. J. Sedlmaier, J. Schmedt auf der Günne, W. Schnick, *Dalton Trans.* **2009**, 4081.

[4] Y. Q. Li, A. C. A. Delsing, G. De With, H. T. Hintzen, *Chem. Mater*. **2005**, *17*, 3242.

[5] F. Wang, W. Wang, L. Zhang, J. Zheng, Y. Jin, J. Zhang, *RSC Adv.* **2017**, *7*, 27422.

[6] M. Bykov, E. Bykova, V. Dyadkin, D. Baumann, W. Schnick, L. Dubrovinsky, N. Dubrovinskaia, *Acta Crystallogr.* **2015**, *E71*, 1325.

[7] D. Baumann, S. J. Sedlmaier, W. Schnick, *Angew. Chem. Int. Ed.* **2012**, *51*, 4707; *Angew. Chem.* **2012**, *124*, 4785.

[8] H. Huppertz, O. Oeckler, A. Lieb, R. Glaum, D. Johrendt, M. Tegel, R. Kaindl, W. Schnick, *Chem. Eur. J.* **2012**, *18*, 10857.

[9] S. J. Sedlmaier, E. Mugnaioli, O. Oeckler, U. Kolb, W. Schnick, *Chem. Eur. J.* **2011**, *17*, 11258.

[10] H. Daicho, Y. Shinomiya, A. Nakano, H. Sawa, S. Matsuishi, H. Hosono, *Chem. Commun.* **2018**, *54*, 884.

[11] S. Horstmann, E. Irran, W. Schnick, *Angew. Chem. Int. Ed. Engl.* **1997**, *36*, 1873; Angew. Chem. **1997**, *109*, 1938.

[12] M. Nentwig, S.D. Kloß, L. Neudert, L. Eisenburger, W. Schnick, O. Oeckler, *Chem. Eur. J.* **2019**, *25*, 14382.

[13] D. Günther, L. Eisenburger, W. Schnick, O. Oeckler, *Z. Anorg. Allg. Chem.* **2022,** 648**,** e202200280 DOI:10.1002/zaac.202200280.

[14] F. J. Pucher, W. Schnick, *Z. Anorg. Allg. Chem.* **2014**, *640*, 2708.

[15] F. Karau, W. Schnick, *Z. Anorg. Allg. Chem.* **2006**, *632*, 231.

[16] L. Eisenburger, V. Weippert, C. Paulmann, D. Johrendt, O. Oeckler, W. Schnick, *Angew. Chem. Int. Ed.* **2022**, *61*, e202202014; *Angew. Chem.* **2022**, *134*, e202202014.

[17] L. Eisenburger, V. Weippert, O. Oeckler, W. Schnick, *Chem. Eur. J.* **2021**, *27*, 14184.

[18] S.D. Kloß, N. Weidmann, R. Niklaus, W. Schnick, *Inorg. Chem.* **2016**, *55*, 9400.

[19] R. Marchand, A. Jayaweera, P. Verdier, J. Lang, *C. R. Acad. Sci., Ser. C*, **1976**, *283*, 675.

[20] S. J. Sedlmaier, D. Weber, W. Schnick, *Z. Kristallogr. - NCS* **2012**, *227*, 1.

[21] B. E. Warren, *Z. Kristallogr. – Cryst. Mater.* **1930**, *74*, 131.

[22] J. M. S. Skakle, R. Herd, *Powder Diffr.* **1999**, *14*, 195.

[23] V. V. Brazhkin, Y. Katayama, A. G. Lyapin, H. Saitoh, *Phys. Rev. B* **2014**, *89*, 104203.

[24] S. Correll, N. Stock, O. Oeckler, J. Senker, T. Nilges, W. Schnick, *Z. Anorg. Allg. Chem.* **2004**, *630*, 2205.

[25] S. Schneider, L. G. Balzat, B. V. Lotsch, W. Schnick, *Chem. Eur. J.* **2023**, *29*, e202202984.

[26] E.-M. Bertschler, R. Niklaus, W. Schnick, *Chem. Eur. J.* **2018**, *24*, 736.

[27] E.-M. Bertschler, R. Niklaus, W. Schnick, *Chem. Eur. J.* **2017**, *23*, 9592.

[28] S. M. Clarke, K. M. Powderly, J. P. S. Walsh, T. Yu, Y. Wang, Y. Meng, S. D. Jacobsen, D. E. Freedman, *Chem. Mater*. **2019**, *31*, 955.

[29] F. Liebau, *Structural Chemistry of Silicates: Structure, Bonding, and Classification*, Springer, Heidelberg, **1985**, 62.

[30] K. Momma, F. Izumi, *J. Appl. Crystallogr.* **2011**, *44*, 1272.

[31] L. Pauling, *J. Am. Chem. Soc*. **1929**, *51*, 1010.

[32] P. E. D. Morgan, *J. Mater. Sci.* **1986**, 4305.

[33] A. Fuertes, *Inorg. Chem*. **2006**, *45*, 9640.

[34] R. Hoppe, *Z. Naturforsch. A* **1995**, *6*, 555.

[35] R. Hoppe, S. Voigt, H. Glaum, J. Kissel, H. P. Müller, K. Bernet, *J. less-common met*. **1989**, *156*, 105.

[36] I. D. Brown, D. Altermatt, *Acta Crystallogr. B* **1985**, *41*, 244.

[37] N. E- Brese, M. O'Keeffe, *Acta Crystallogr. B* **1991**, *47*, 192.

[38] A. Altomare, C. Cuocci, C. Giacovazzo, A. Moliterni, R. Rizzi, N. Corriero, A. Falcicchio, *J. Appl. Crystallogr*. **2013**, *46*, 1231.

[39] M. O`Keeffe, M. A. Peskov, S. J. Ramsden, O. M. Yaghi, *Acc. Chem. Res*. **2008**, *41*, 1782.

[40] V. A. Blatov, A. P. Shevchenko, D. M. Proserpio, *Cryst. Growth Des.* **2014**, *14*, 3576.

[41] S. D. Kloß, N. Weidmann, R. Niklaus, W. Schnick, *Inorg. Chem.* **2016**, *55*, 9400.

[42] J.-M. Du, H.-Y. Zeng, L.-J. Song, Z.-C. Dong, H.-W. Ma, G.-C. Guo, J.-S. Huan, *Chinese J. Struct. Chem.* **2003**, *22*, 33.

[43] R. D. Shannon, *Acta Crystallogr. Sect. A* **1976**, *32*, 751.

[44] A. Marchuk, P. Schultz, C. Hoch, O. Oeckler, W. Schnick, *Inorg. Chem.* **2016**, *55*, 974.

[45] A. Neuhaus, *Chimia* **1964**, 18, 93.

[46] P. Vinet, J. H. Rose, J. Ferrante, J. R. Smith, *J. Phys.: Condens. Matter* **1989**, *1*, 1941.

[47] R. López, R. Gómez, *J Sol-Gel Sci Technol* **2012**, 61, 1.

[48] J. Tauc, R. Grigorovici, A. Vancu, *Phys. Status Solidi B* **1966**, *15*, 627.

[49] M.-H. Fang, C. O. M. Mariano, P.-Y. Chen, S.-F. Hu, R-S. Liu, *Chem. Mater.* **2020**, *32*, 1748.

[50] J. A. Kechele, O. Oeckler, F. Stadler, W. Schnick, *Solid State Sci.* **2009**, *11*, 537.

[51] O. Oeckler, F. Stadler, T. Rosenthal, W. Schnick, *Solid State Sci.* **2007**, *9*, 205.

[52] M. Seibald, T. Rosenthal, O. Oeckler, W. Schnick, *Crit. Rev. Solid State Mater. Sci.* **2014**, *39*, 215.

[53] X. Zhang, M.-H. Fang, Y.-T. Tsai, A. Lazarowska, S. Mahlik, T. Lesniewski, M. Grinberg, W. K. Pang, F. Pan, C. Liang, W. Zhou, J. Wang, J.-F. Lee, B.-M. Cheng, T.-L. Hung, Y.-Y. Chen, R.-S. Liu, *Chem. Mater.* **2017**, *29*, 6781.

[54] A. Kitai, *Materials for Solid State Lighting and Displays*, John Wiley and Sons, West Sussex, **2017**.

[55] R.-J. Xie, Y. Q. Li, N. Hirosaki, H. Yamamoto, *Nitride Phosphors and Solid-State Lighting*, Taylor & Francis, Boca Raton, **2011**.

[56] L. Eisenburger, O. Oeckler, W. Schnick, *Chem. Eur. J.* **2021**, *27*, 4461.

[57] R. S. Hafei, D. Maganas, P. Strobel, P. J. Schmidt, W. Schnick, F. Neese, *J. Am. Chem. Soc.* **2022**, *144*, 8038.

[58] P. Strobel, T. de Boer, V. Weiler, P. J. Schmidt, A. Moewes, W. Schnick, *Chem. Mater.* **2018**, *30*, 3122.

[59] High Color-Rendering, Full-Visible-Spectrum LEDs by Soraa. *LED professional Review* **2016**.

[60] A. Stock, H.Grüneberg, *Ber. Dtsch. Chem. Ges.* **1907**, *40*, 2573.

[61] K. J. Kingma, R.G. Pacalo, P. F. McMillan, *Eur. J. Solid State Inorg. Chem*. **1997**, *24*, 679.

[62] R. Suhrmann, K. Clusius, *Z. Anorg. Allg. Chem.* **1926**, *152*, 52.

[63] F. W. Karau, *Dissertation*, Ludwig-Maximilians-Universität München (Germany) **2007**.

[64] D. Walker, M. A.Carpenter, C. M. Hitch, *Am. Mineral.* **1990**, *75*, 1020.

[65] D. Walker, *Am. Mineral.* **1991**, *76*, 1092.

[66] D. C. Rubie, *Phase Transitions* **1999**, *68*,431.

[67] H. Huppertz, *Z. Kristallogr. - Cryst. Mater*. **2004**, *219*, 330.

[68] N. Kawai, S. Endo, *Rev. Sci. Instrum.* **1970**, *41*, 1178.

[69] Bruker AXS, Inc., *SADABS*, Madison, Wisconsin, USA, **2001**.

[70] G. M. Sheldrick, *Acta Crystallogr. Sect. C* **2015**, *71*, 3.

[71] A. A. Coelho, *TOPAS-Academic*, Version 6, Coelho Software, Brisbane (Australia), **2016.**

[72] Kresse, G.; Furthmüller, *J. Comput. Mater. Sci.* **1996**, *6*, 15.

[73] P. E. Blöchl, Phys. Rev. B: Condens. *Matter Mater. Phys.* **1994**, *50*, 17953.

[74] J. P. Perdew, K. Burke, M. Ernzerhof, *Phys. Rev. Lett.* **1996**, *77*, 3865.

[75] J. P. Perdew, J. P.; K. Burke, M. Ernzerhof, *Phys. Rev. Lett*. **1997**, *78*, 1396.

[76] S. Grimme, J. Antony, S. Ehrlich, H. Krieg, *J. Chem. Phys.* **2010**, *132*, 154104

[77] S. Grimme, S. Ehrlich, L. Goerigk, *J. Comput. Chem.* **2011**, *32*, 1456.

3 Tunable Narrow-Band Cyan-Emission of Eu^{2+}-doped Nitridomagnesophosphates $Ba_{3-x}Sr_x[Mg_2P_{10}N_{20}]:Eu^{2+}$ (x = 0–3)

Published in: *Angew. Chem.* **2024,** *136*, e202403648;

Angew. Chem. Int. Ed. **2024,** *63*, e202403648

Authors: Reinhard M. Pritzl, Monika M. Pointner, Kristian Witthaut, Philipp Strobel, Peter J. Schmidt, and Wolfgang Schnick

DOI: https://doi.org/10.1002/ange.202403648

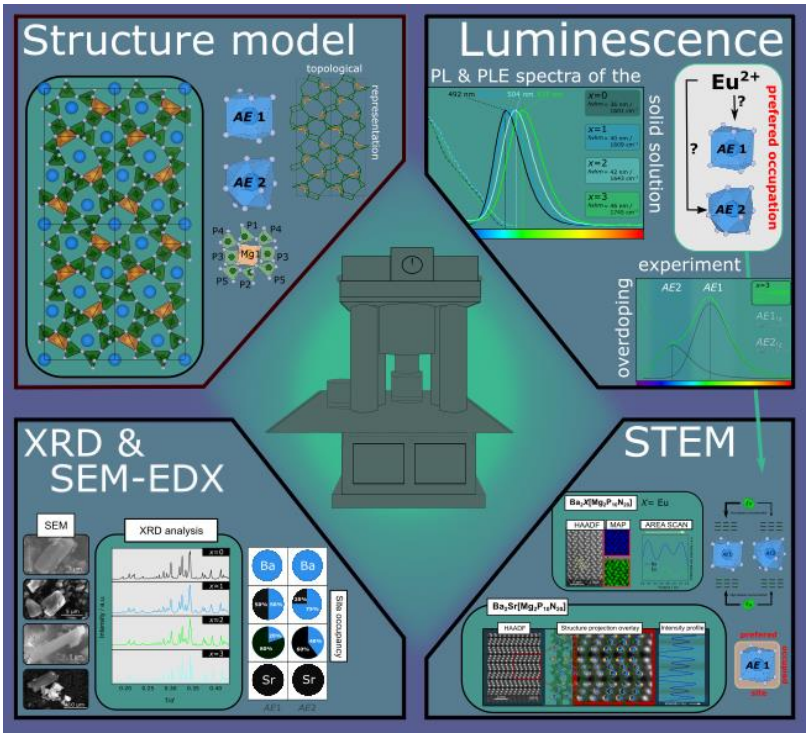

Abstract. Tetrahedron-based nitrides offer a wide range of properties and applications. Highly condensed nitridophosphates are examples of nitrides that exhibit fascinating luminescence properties when doped with Eu^{2+}, making them appealing for industrial applications. Here, we present the first nitridomagnesophosphate solid solution series $Ba_{3-x}Sr_x[Mg_2P_{10}N_{20}]:Eu^{2+}$ (x = 0–3), synthesized by a high-pressure high-temperature approach using the multianvil technique (3 GPa, 1400 °C). Starting from the binary nitrides P_3N_5 and Mg_3N_2 and the respective alkaline earth azides, we incorporate Mg into the P/N framework to increase the degree of condensation κ to 0.6, the highest observed value for alkaline earth nitridophosphates. The crystal structure was elucidated by single-crystal X-ray diffraction, powder X-ray diffraction, energy-

dispersive X-ray spectroscopy (EDX), and solid-state NMR. DFT calculations were performed on the title compounds and other related highly condensed nitridophosphates to investigate the influence of Mg in the P/N network. Eu^{2+}-doped samples of the solid solution series show a tunable narrow-band emission from cyan to green (492–515 nm), which is attributed to the preferred doping of a single crystallographic site. Experimental confirmation of this assumption was provided by overdoping experiments and STEM-HAADF studies on the series as well on the stoichiometric compound $Ba_2Eu[Mg_2P_{10}N_{20}]$ with additional atomic resolution energy-dispersive X-ray spectroscopy (EDX) mapping.

3.1 Introduction

In recent years, nitridophosphates have received considerable attention in the development of new phosphors for modern solid-state lighting (*SSL*), since materials doped with Eu^{2+} are capable of emitting in the full visible spectral range, making them suitable for use in phosphor-converted light-emitting diodes (pcLEDs).[1–4] For potential applications, these materials require not only excellent luminescence properties alongside a rigid host lattice, but also chemical and thermal stability.[5] The latter are often correlated by the degree of condensation κ, which indicates the ratio of tetrahedral centers (also called network forming cations, *NFC*) to coordinated N atoms ($\kappa = n(NFC):n(N)$).[6] The upper limit of κ is determined by electrostatics and is for ternary nitridophosphates κ = 3/5 which corresponds to the degree of condensation of the binary nitride P_3N_5. This limit can be raised by introducing additional chemical elements with lower oxidation states than P^{+V} as *NFC*s.[7] The observation of narrow-band ($AEP_2N_4:Eu^{2+}$ (*AE* =Ca, Sr)) and ultra-narrow-band emission ($AEP_8N_{14}:Eu^{2+}$ (*AE* = Ca, Sr, Ba) in alkaline earth nitridophosphates highlights the significance of highly condensed anionic networks for tailored optical responses.[8,9] However, the introduction of further *NFC*s not only influences the degree of condensation but also opens opportunities for creating novel host structures and coordination environments for the activator sites, to enable unique luminescence properties for suitable activator ions such as Eu^{2+}.[10,11] The observed luminescence in Eu^{2+}-doped phosphors results from transitions between the excited state $4f^6(^7F)5d^1$ and the ground state $4f^7(^8S_{7/2})$ of the activator ion, where the energy of the lowest excited state of Eu^{2+} ions in a host lattice is highly affected by the local environment due to the nephelauxetic effect and crystal field splitting.[12–14] Based on this, our study aims to contribute to the growing compositional and structural diversity of tetrahedron-based nitridophosphate phosphors. Specifically, we present the investigation of the solid solution series

$Ba_{3-x}Sr_x[Mg_2P_{10}N_{20}]:Eu^{2+}$ (x = 0–3), introducing a new class of alkaline earth metal magnesonitridophosphates as promising host lattices of Type IV phosphors, according the classification of Sohn *et al.*[15] The first part of our study focuses on the synthesis, structure elucidation and characterization of this new structure type. The following section concentrates on deciphering the intricate relationship between the structure of these materials and their luminescent properties. This includes a detailed investigation of the luminescence behavior as well as an in depth evaluation and experimental localization of Eu^{2+} doping through advanced STEM-HAADF studies.

3.2 Results and Discussion

3.2.1 Synthesis and Structure Elucidation

The solid solution $Ba_{3-x}Sr_x[Mg_2P_{10}N_{20}]:Eu^{2+}$ (x = 0–3) was synthesized from stoichiometric amounts of the binary nitrides P_3N_5 and Mg_3N_2 and the respective metal azides, as well as EuN as dopant, using a Walker-type multianvil press (3 GPa, 1400°C) according to Equation (3.1):

$$10\ P_3N_5 + 2\ Mg_3N_2 + 9\ M(N_3)_2 \rightarrow 3\ M_3[Mg_2P_{10}N_{20}]:Eu^{2+} + 24\ N_2 \qquad (3.1)$$

The title compounds were obtained as air- and moisture-stable, crystalline products. The synthesis of the stoichiometric representatives $AE_3[Mg_2P_{10}N_{20}]$ (AE = Sr, Ba) yielded single crystals which could be used for single crystal structure analysis (scXRD). Based on these, the crystal structures of $AE_3[Mg_2P_{10}N_{20}]$ with AE = Ba, Sr were solved and refined from single-crystal X-ray diffraction data in the monoclinic space group $P2_1/c$ (no. 14).[16] The crystallographic data are summarized in Table S3.1, while Wyckoff positions, atomic coordinates, anisotropic displace parameters, as well as interatomic distances and angles are given in Tables S3.2–3.7. Low cost crystallographic calculations (CHARDI, BVS and MAPLE; Tables S3.8–3.12) as well as ^{31}P NMR spectroscopy experiments support the structure solution (Figure S3.1).

3.2.2 Structure Description

Since magnesium participates in the tetrahedral anionic framework as a network-forming cation (*NFC*), $AE_3[Mg_2P_{10}N_{20}]$ exhibits the hitherto highest degree of condensation in multinary nitridophosphates, with $\kappa = n(NFC):n(N)) = 0.6$ ($\kappa_{max,\ obs} = 0.57$ in HP_4N_7, MP_4N_7 (M = Li, Na, K,

Rb, Cs), AEP_8N_{14} (*AE* = Mg, Ca, Sr, Ba).[9,17–20] The anionic 3D framework of the crystal structure is based of all-side vertex-sharing Q^4-type $MgN^{[3]}_4$, $PN^{[2]}_3N^{[3]}$ and $PN^{[2]}_2N^{[3]}_2$ tetrahedra (superscripted coordination numbers in square brackets, Figure 3.1a). Focusing only on the P/N framework, two striking structural motifs become apparent. Namely, branched *zweier* double chains and layers of condensed *dreier* ring chains on the other, according to Liebau's silicate nomenclature (Figure 3.1d).[21] These motifs are connected by common vertices, forming smaller and larger channels along [100], in which only the M^{2+} cations are localized in the smaller ones and both Mg^{2+} and M^{2+} ions in the larger ones (Figure 3.1b). The Mg^{2+} ions are distorted tetrahedrally coordinated by nitrogen and connected to PN_4 tetrahedra on all sides. This creates highly condensed regions in which each N of the MgN_4 tetrahedra is triply-bound ($N^{[3]}$), restricting the size of the larger channels. The cross-linking with the resulting *sechser* ring channels is illustrated in the topological representation in Figure 3.1b. In addition, this is underlined by the comparison of the point symbols (with and without Mg as *NFC*) determined by the TOPOS software (Supporting Information).[22]

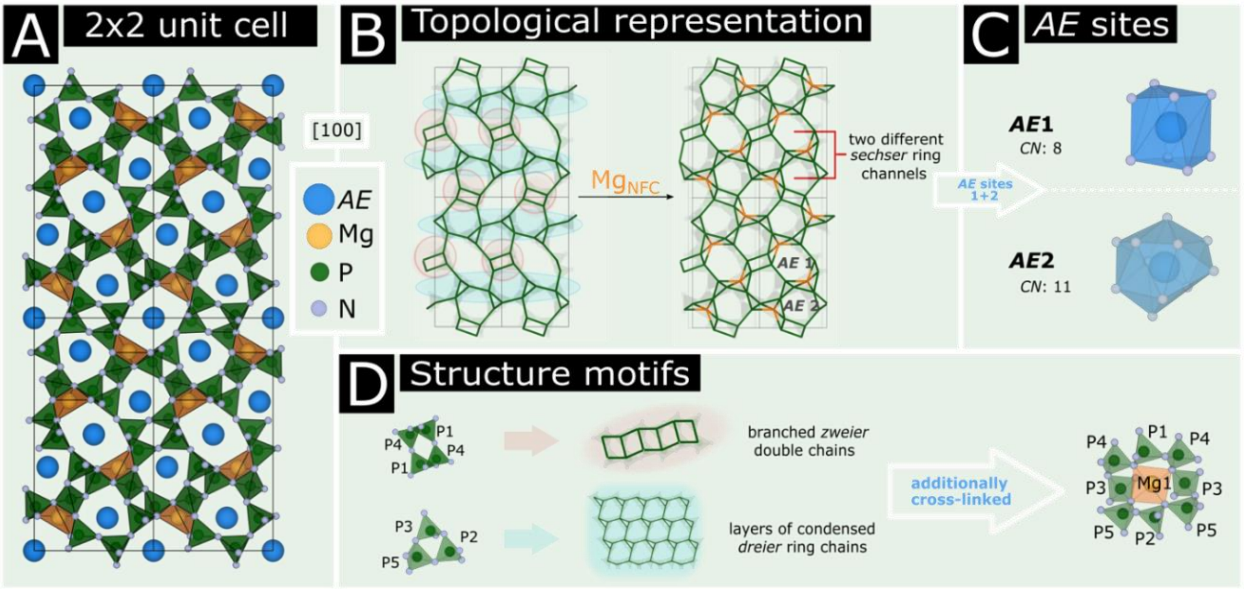

Figure 3.1. Structure of $AE_3[Mg_2P_{10}N_{20}]:Eu^{2+}$: a) Representation of 2x2 supercell projection along [100], *AE*=Ba/Sr in blue, Mg and MgN_4 tetrahedra in orange, P and PN_4 tetrahedra in green, N in gray ; b) Topological representation of the anionic P/N framework (left side) and with Mg as *NFC* (right side), each connection line exemplifies a P–N–P (green) or Mg–N–P (half orange/half green) bond, structural motifs are highlighted ; c) Coordination of the *AE*=Ba/Sr site ; d) Structure motifs of $AE_3[Mg_2P_{10}N_{20}]:Eu^{2+}$.

To the best of our knowledge, $M_3[Mg_2P_{10}N_{20}]$ represents an unprecedented structure type, as both point symbols have not been described in literature before. As already mentioned, the AE^{2+} sites

are located in different channels, which leads to two non-equivalent cation sites, shown in Figure 3.1c. The first site *AE*1 (Ba1/Sr1) is coordinated by eight N atoms (*CN* = 8), in the form of a slightly distorted cuboid according to Bauer's distortion index.[23] The second site *AE*2 (Ba2/Sr2) is irregularly coordinated by 11 N atoms (*CN* = 11), with relatively large interatomic distances Sr/Ba–N (2.650–3.321 Å), compared to site *AE*1 with Sr/Ba–N (2.631–3.014 Å). An illustration of the coordination polyhedral of both sites is provided in Figure 3.1c. To gain more detailed structural insight of the solid solution series, Rietveld refinements were performed additionally on

$Ba_{3-x}Sr_x[Mg_2P_{10}N_{20}]$ (x = 1, 2).For this purpose, the structural model of $Ba_3[Mg_2P_{10}N_{20}]$ for $Ba_2Sr[Mg_2P_{10}N_{20}]$ and $Sr_3[Mg_2P_{10}N_{20}]$ for $BaSr_2[Mg_2P_{10}N_{20}]$ was used as a starting point. During refinement, the lattice parameters, fractional atomic coordinates as well as site occupancy of the heavy cations were refined. All refinements indicate either phase-pure synthesis of the title compounds or the presence of only very small amounts of unidentified by-products (marked by asterisks). A graphical illustration of the refinements is given in Figures S3.2–S3.5; additional supporting information can be found in Tables S3.13–3.17. The series shows an increase in the lattice parameters *a*, *b*, *c* and *V*, which is due to the larger ionic radius of Ba^{2+} (Ba^{2+}>Sr^{2+}).[24] Figure 3.2 shows that with increasing Sr content a mixed Ba/Sr occupation of both sites occurs, but *AE*1 is distinctly favored by Sr. SEM-EDX measurements (Tables S3.18–S3.20) confirm the Ba/Sr contents obtained by Rietveld refinement. In general, only the cation values and atomic ratios (Ba/Sr/Mg/P) were examined in detail, as the anion values were slightly affected by surface-bound oxygen or surface hydrolysis. The measured cation values and determined atomic ratios align within typical accuracy limits with the expected values. Since Eu could not be detected by EDX due to the low doping level (~1 mol% with respect to *AE*), Eu was neglected in all refinements.

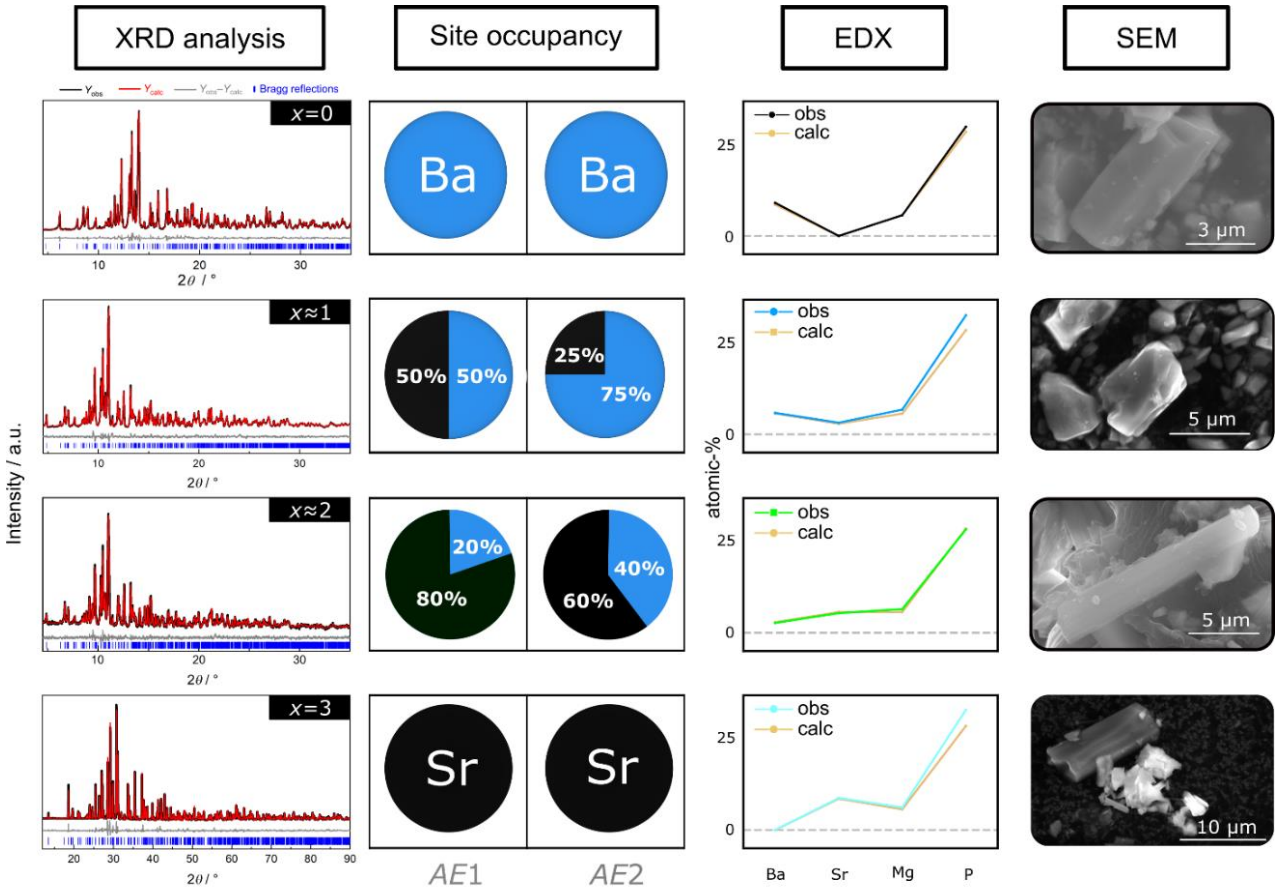

Figure 3.2. Rietveld refinements (selected ranges) of the solid solutions series $Ba_{3-x}Sr_x[Mg_2P_{10}N_{20}]:Eu^{2+}$ with corresponding site occupation of the alkaline earth metal sites, EDX values and SEM images.

3.2.3 DFT Calculations

Highly condensed alkaline earth metal nitridophosphates have been discussed in literature as potential phosphors for LED applications. Experimental photoluminescence (PL) data are available for these compounds, but no other fundamental parameters such as the band gap (E_g), the Debye temperature (Θ_D), the bulk modulus (K), the shear modulus (G) or the Poisson's ratio.[8,9] In order to roughly classify the title compounds in this context, periodic density functional theory (DFT) calculations (PBE and LMBJ level) were carried out.[25,26] For this purpose, the previously mentioned parameters were calculated for the stoichiometric representatives of the solid solution $Ba_{3-x}Sr_x[Mg_2P_{10}N_{20}]$ (x = 0, 3), AEP_2N_4 (AE = Ca, Sr, Ba) and AEP_8N_{14} (AE = Ca, Sr, Ba) (Table 3.1). The band gaps of the terminal representatives $Ba_3[Mg_2P_{10}N_{20}]$ and $Sr_3[Mg_2P_{10}N_{20}]$ were determined to be 3.8 and 4.2 eV, respectively. These are comparable to the other highly condensed nitridophosphates and are generally in the expected

range of other known nitride representatives (e.g. $M[Mg_2Al_2N_4]$ (M = Ca, Sr, Ba).[27] The calculated bandgaps of $Sr_3[Mg_2P_{10}N_{20}]$ makes it a potentially suitable host material for doping, because wide band gaps ≥4 eV are required for pcLED applications. However, these are approximate values that must subsequently be verified by experiments of undoped samples. The few highly condensed nitridophosphate-based phosphors ($\kappa \geq ½$) exhibit good luminescence properties with respect to the emission maxima λ_{max} and the full width at half maximum (*fwhm*). Yet, no empirical values regarding their efficiency (quantum yields Φ) are available. Without experimental data, the structural rigidity, which depends on the degree of crosslinking, can be used as an indicator for their efficiency. It is difficult to determine the rigidity of condensed structure in the solid state just by structural comparisons. An indication regarding vibrational rigidity is given by the Debye temperature Θ_D, which can be experimentally determined, either from low-temperature heat capacity measurements or from atomic displacement parameter determination from scattering studies, typically neutron scattering. However, calculated Debye temperatures can also be used as a guidance, those can be extracted from ab initio density functional theory calculations using the quasi-harmonic Debye model.[6, 28–30] The calculations are based on the bulk modulus and Poisson ratio, requiring these parameters to be calculated as well (Table S3.22).

Table 3.1. Overview of band gaps and Debye temperatures of highly condensed nitridophosphates, calculated by DFT methods.

Compound	Band gap LMBJ / PBE [eV]	Debye Temperature [K]
CaP_2N_4	4.34 / 4.34	615.0
SrP_2N_4	4.36 / 4.36	621.0
BaP_2N_4	3.92 / 3.92	552.3
CaP_8N_{14}	4.05 / 4.05	822.3
SrP_8N_{14}	4.12 / 4.12	779.6
BaP_8N_{14}	4.10 / 4.10	721.9
$Sr_3[Mg_2P_{10}N_{20}]$	4.23 / 4.22	653.5
$Ba_3[Mg_2P_{10}N_{20}]$	3.85 / 3.85	640.8

Within a substance class, larger Θ_D indicate more strongly cross-linked and therefore more rigid lattices. The performed calculations show that with a constant P/N ratio, the insertion of tetrahedrally coordinated Mg can be regarded as a *NFC*, based on the significantly increases of Θ_D, being overall slightly higher than for AEP_2N_4 (*AE* = Ca, Sr, Ba). It should be mentioned that the incorporation of MgN_4 tetrahedra does not contribute significantly to the rigidity of the network presumably due to the more ionic character compared to the PN_4 tetrahedra. Nevertheless, since different structure types are compared within a small data set considering the low number of known representatives, the result should be discussed with some caution.

3.2.4 Luminescence

The room temperature photoluminescence (*PL*) and photoluminescence excitation spectra (*PLE*) were measured on individual particles to investigate the basic luminescence properties of Eu^{2+}-doped samples of the solid solution series (nominal Eu content 1 mol%). The corresponding spectra are depicted in Fig. 3.3.

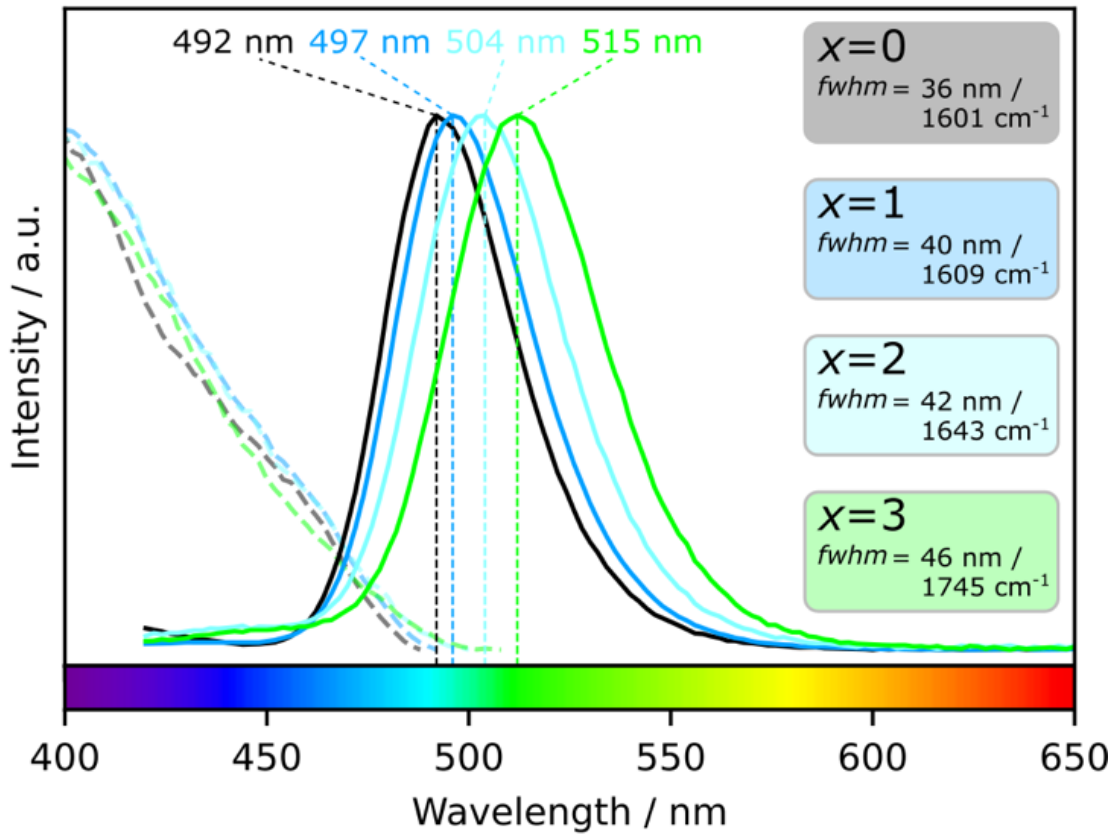

Figure 3.3. Room temperature *PLE* & *PL* spectra of the solid solutions series $Ba_{3-x}Sr_x[Mg_2P_{10}N_{20}]:Eu^{2+}$ upon excitation at 400 nm.

Upon irradiation by UV to blue light (λ_{exc} = 400 nm), all samples of $Ba_{3-x}Sr_x[Mg_2P_{10}N_{20}]:Eu^{2+}$ (x = 0, 1, 2, 3) show strong cyan emission, each with a single narrow-band emission profile (x = 0: λ_{max} = 492 nm, *fwhm* = 36 nm/1601 cm^{-1}; x = 1: λ_{max} = 497 nm, *fwhm* = 40 nm/ 1609 cm^{-1}; x = 2: λ_{max} =504 nm, *fwhm* = 42 nm/1643 cm^{-1}; x = 3: λ_{max} = 515 nm, *fwhm* = 46 nm/1745 cm^{-1}). The observed narrow-band emissions are a consequence of the highly condensed crystal structure (κ = 3/5) caused by the additional *NFC* (Mg) incorporation into the nitridophosphate framework, as well as the strong covalent bonding character of the resulting *NFC*–N bonds (Mg/P–N).[31] The consequently very rigid host lattice in combination with long activator-ligand contact lengths restricts the local structure relaxation of Eu^{2+} in its excited state and eventually leads to small Stokes shift, narrow-band emission.[32–34] The observed emission red-shift with increasing Sr content can be explained by the reduction of the lattice parameters due to the smaller ionic radius of Sr^{2+} compared to Ba^{2+} while maintaining the same coordination sphere for the dopand. As a result, the average interatomic distances *AE*–N decreases compared to x = 0, leading to stronger relaxation of Eu^{2+} in its excited state, a larger Stokes shift and thus to broader and red-shifted emission bands as often observed for isotypic series of compounds with different-sized substitutional host cations.[35] This observation is valid for both non-equivalent crystallographic *AE* sites, namely *AE*1 and *AE*2, where Eu^{2+} ions may be located. However, since the emissions are very narrow-band, allowing the assumption that they are likely due to the occupancy of only one independent *AE* site. This is supported by the fact that the two coordination spheres are clearly different from each other (*CN*, average bond length, *V*). To distinguish which of the two *AE* sites are preferred by Eu^{2+} and where the observed narrow emission bands in the solid solution originate from, we conducted a deliberate overdoping experiment at point $Ba_{3-x}Sr_x[Mg_2P_{10}N_{20}]:Eu^{2+}$ (x = 3; nominal Eu content 6 mol%). The reason for selecting the terminal point of the solid solution series is that it contains the maximum Sr content on both crystallographic *AE* sites. Eu^{2+} and Sr^{2+} have comparable ionic radii ($r_{CN=8}(Eu^{2+})$ = 1.25 Å, $r_{CN=8}(Sr^{2+})$ =1.26 Å).[24] Therefore, in the case of overdoping, it is plausible that the second *AE* site will also be occupied by Eu^{2+}.[36] The *PLE* and *PL* spectra (excitation at 400 nm) with corresponding fit are shown in Fig. 3.4. Several effects can be observed here: Primarily, a clear broadening of the emission profile, mainly caused by an additional shoulder in the blue region, which can be fitted as a single emission band (high energy band). Limiting the observed emission to the occupation of the two cation sites by Eu^{2+} and not from a possible occupation of interstitial sites, we can conclude that this emission band originates from the *AE*2 site. As mentioned in the structural description, *AE*2 has a higher *CN* and therefore a longer average interatomic distance compared to *AE*1. An in average longer interatomic distance weakens the influence of the nearest

nitrogen ions on the Eu^{2+} ions due to the nephelauxetic effect and crystal field splitting, resulting in a blue shift. The significantly lower intensity of the high-energy band compared to the cyan band may be due to reabsorption effects or energy transfer, because the emission band of Eu2 (*AE*2 site) overlaps with the excitation band of Eu1 (*AE*1 site).

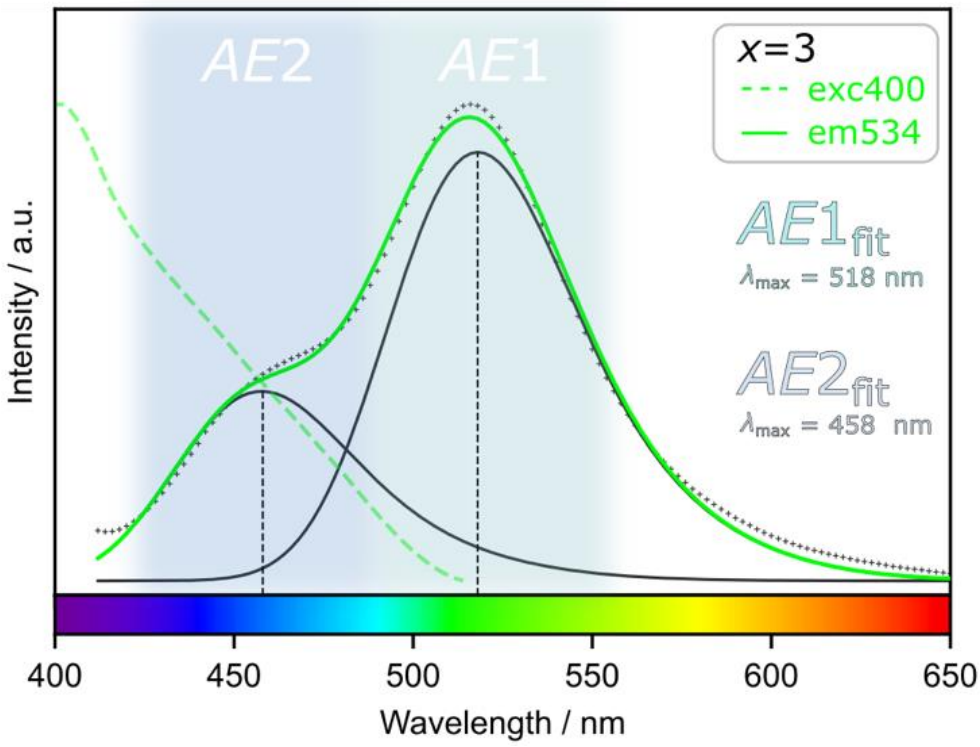

Figure 3.4. Room temperature *PLE* & *PL* spectra of the overdoping experiment of $Sr_3[Mg_2P_{10}N_{20}]:Eu^{2+}$ upon excitation at 400 nm.

In general, the observed luminescence properties of the solid solution series $Ba_{3-x}Sr_x[Mg_2P_{10}N_{20}]:Eu^{2+}$ (x = 0–3) can be compared with other narrow-band nitride-based phosphors, such as $BaSi_2O_2N_2:Eu^{2+}$ (Ba222, λ_{max} = 494 nm, *fwhm* ≈ 35 nm), $Sr[Be_6ON_4]:Eu^{2+}$ (λ_{max} = 495 nm, *fwhm* ≈ 35 nm) or β-$MgSrP_3N_5O_2$ (λ_{max} = 502 nm, *fwhm* ≈ 42 nm), which have been discussed in the literature as promising candidates for closing the so-called cyan gap in white light-emitting diodes (pc-wLEDs).[10,32,37] In addition to an optimum emission position, a very small Stokes shift, high thermal stability and high conversion efficiency are also necessary for optimum excitation with blue light. However, we so far only investigated the internal quantum efficiency (*IQE*) and general thermal properties (temperature-dependent *PL* spectra and high-temperature resistance (HTXRD)) of the terminal representative only for x = 0 (1 mol% Eu^{2+} concentration referred to Ba) in bulk. This is due to the complexity of synthesizing the solid solution series and the low yield resulting from the necessary HP/HT conditions (multianvil

technique synthesis). Measurements (excitation at 440 nm) on the as-synthesized powder samples reveal that $Ba_3[Mg_2P_{10}N_{20}]:Eu^{2+}$ achieves an impressive *IQE* of 74%, which can be further improved upon synthesis optimization. For the investigation of the thermal behavior of $Ba_3[Mg_2P_{10}N_{20}]:Eu^{2+}$ temperature dependent luminescence spectra were captured (Figure 3.5). The sample shows band narrowing with decreasing temperature and no appreciable shift in λ_{max}. It also shows moderate thermal quenching (*TQ*) with a relative emission intensity of 83% at 300 K (with respect to 6 K). For temperature dependent *PL* spectra up to 520 K see Figures S3.6 & S3.7. Furthermore, thermal stability up to 1073 K can be observed, with a low anisotropic thermal expansion of ($a \approx 0.5\%$, $b \approx 0.2\%$, $c \approx 0.2\%$; Figures S3.8 & S3.9), which makes it suitable for potential pc-LED applications.

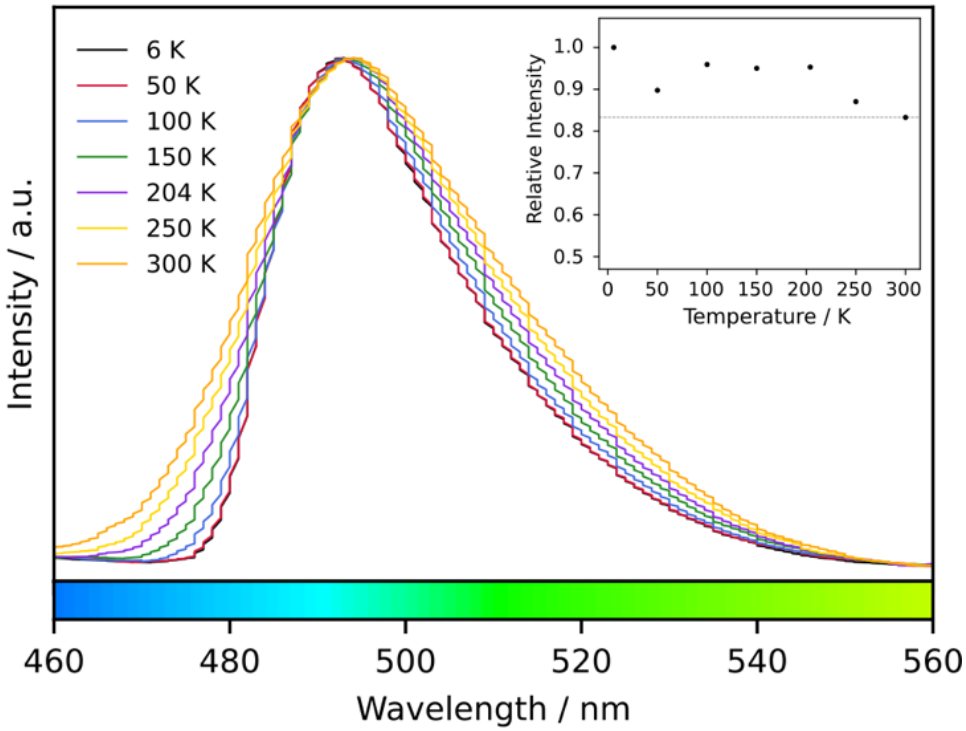

Figure 3.5. Normalized temperature dependent *PL* spectra of $Ba_3[Mg_2P_{10}N_{20}]:Eu^{2+}$ with 1 mol% Eu^{2+}. Inset: Relative integrated emission intensities for determination of the *TQ* behavior.

3.2.5 STEM Analysis

In order to verify the preferential occupation of Sr on the *AE*1 site consistent with the Rietveld refinement, additional atomic resolution scanning transmission electron microscopy high-annular dark-field analysis (STEM-HAADF) with a Z contrast proportional to Z^2 ($Z_{Sr} = 38$, $Z_{Ba} = 56$, $Z_{Eu} = 63$) was performed.[38] For this purpose, the solid solution with $x = 1$ was selected, as the electron density difference of the Ba/Sr occupation ratio of *AE*1

(50% Sr : 50% Ba) and *AE*2 (25% Sr : 75% Ba) is more pronounced and should therefore result in a stronger contrast in the HAADF images. Single crystals oriented along the crystallographic axis [100], [010] or [001] allow independent analysis of the individual *AE*-Wyckoff sites, which can be seen in Figure 3.6 as bright triples of alternating sequence. The atomic arrangement of these triplets is *AE*2–*AE*1–*AE*2. An averaged integration over these triplet shows a decreased intensity of the *AE*1 site caused by the lower electron density of the higher Sr content compared to *AE*2.

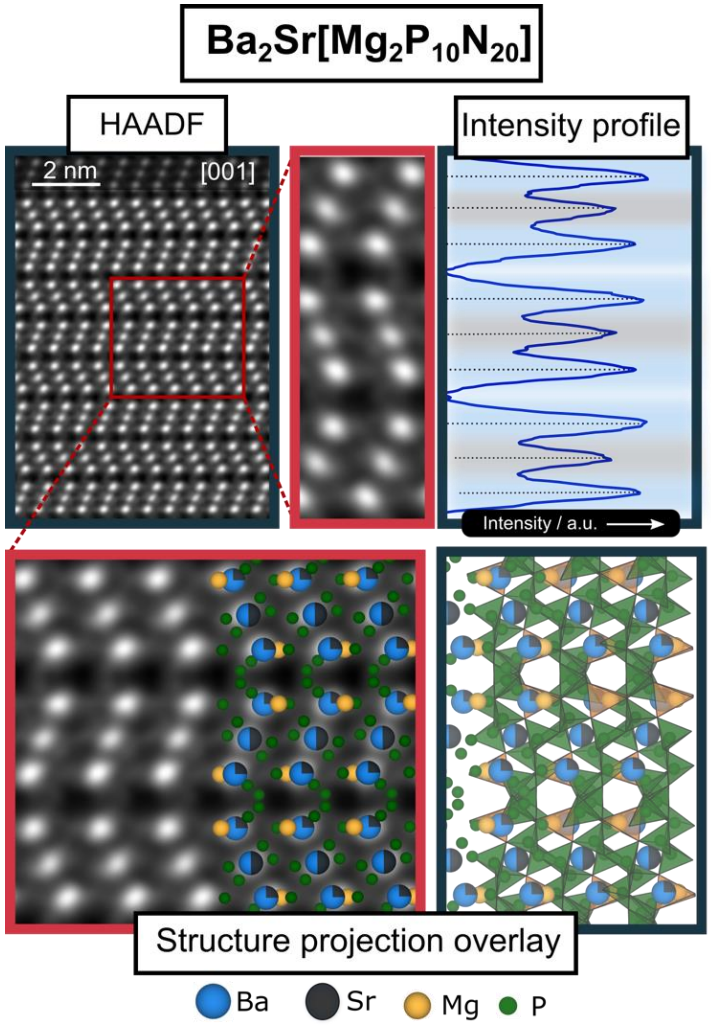

Figure 3.6. STEM high-angle annular dark-field (HAADF) images with structure overlay of $Ba_2Sr[Mg_2P_{10}N_{20}]$ (bottom right side). An integrated intensity profil of the area scan shows differences in the mixed occupation (top right side).

To confirm the assumption made in the luminescence section that Eu^{2+} favors the *AE*1 site due to the similar ionic radii of Eu^{2+} to Sr^{2+}, an atomic resolution STEM-EDX map of the Eu-rich sample $Ba_2Eu[Mg_2P_{10}N_{20}]$ (high Eu content and high electron density for *Z*-contrast) was acquired.

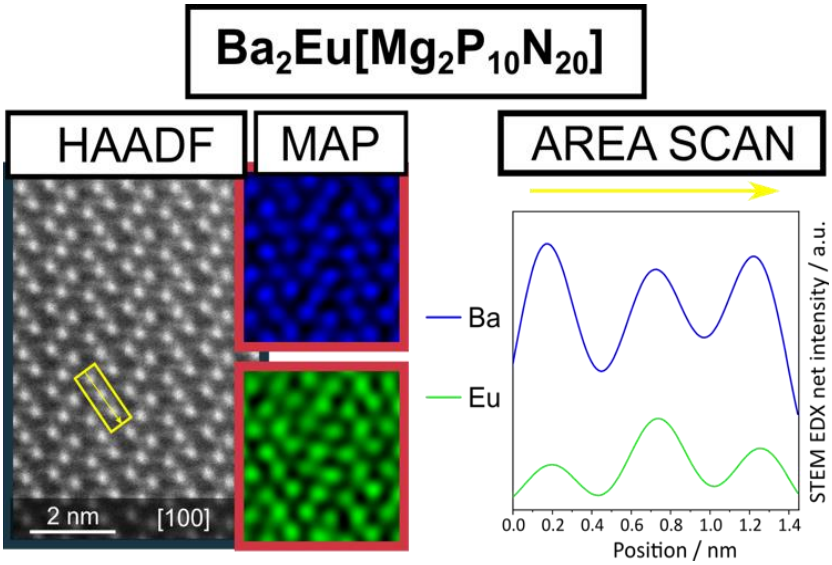

Figure 3.7. STEM-HAADF images (left) with atomic resolution EDX map (middle) and area scan with integrated intensities of the marked triplet (right).

By integrating the EDX signal over *AE*2–*AE*1–*AE*2 triplets, we obtained the average atomic composition of the sites. The analysis shows that the *AE*2 sites have a higher Ba occupation and a lower Eu occupation as expected, while the *AE*1 sites have a higher Eu occupation and a lower Ba occupation (see Figure 3.7). The results of the STEM-HAADF study are consistent with the observations and conclusions of the luminescence analysis and confirm that the observed narrow band emissions of the solid solution series are due to the preferred doping of the *AE*1 site (Figure 3.8).

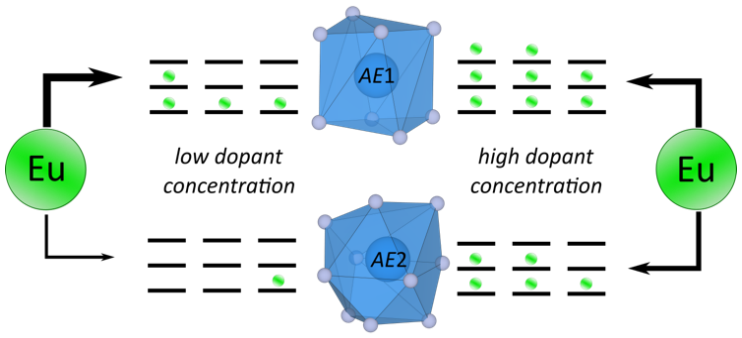

Figure 3.8. *AE* site dependent preferred occupation with low and high Eu^{2+} concentration. Low dopant concentration leads to favored occupation of the *AE*1 site, whereas high dopant concentration fills both sites *AE*1 and *AE*2.

3.3 Conclusion

In this contribution, we report on the crystal structure and luminescence properties of the solid solution series $Ba_{3-x}Sr_x[Mg_2P_{10}N_{20}]:Eu^{2+}$ (x = 0–3), the first representative of alkaline earth metal nitridomagnesophosphates. The crystal structure refined from single-crystal X-ray diffraction data are supported by powder X-ray diffraction data, EDX spectroscopy, solid-state NMR experiments as well as low-cost crystallographic calculations (MAPLE, BVS and CHARDI). The crystal structure is composed of a highly condensed 3D nitridophosphate-based framework, which is additionally reinforced by distorted MgN_4 tetrahedra. The band gaps of the two terminal representatives were calculated using DFT methods (x = 0: 3.85 eV; x = 3: 4.23 eV). In addition, the Debye temperatures were calculated in order to obtain an impression of the rigidity of the structures shown. For comparison these calculations were also performed for the highly condensed nitridophosphates AEP_2N_4 (*AE* = Ca, Sr, Ba) and AEP_8N_{14} (*AE* = Ca, Sr, Ba). The Eu^{2+} doped title compounds show intense narrow-band emission (x = 0: λ_{max} = 492 nm, *fwhm* = 36 nm/1601 cm^{-1}; x = 1: λ_{max} = 497 nm, *fwhm* = 40 nm/ 1609 cm^{-1}; x = 2: λ_{max} = 504 nm, *fwhm* = 42 nm/1643 cm^{-1}; x = 3: λ_{max} = 515 nm, *fwhm* = 46 nm/ 1745 cm^{-1}) in the cyan spectral range, when excited with blue to UV light. The observed narrow-band emission could be attributed to the occupation of one of the two *AE* sites by the dopant from an overdoping experiment, which could be confirmed by electron microscopy studies with atomic resolution. As a consequence of the complex synthesis (multianvil technique, HP/HT synthesis), only the terminal representative with x = 0 was additionally investigated with regard to internal quantum efficiency (*IQE* = 74%) and thermal quenching behavior (*TQ*) from 6 K to 300 K (*TQ* = 84%). $Ba_{3-x}Sr_x[Mg_2P_{10}N_{20}]:Eu^{2+}$ (x = 0–3) is a promising candidate for next-generation pc-wLEDs as the Ba/Sr ratio allows for specific control of the spectral range between 490–520 nm, closing the so-called cyan gap (480–520 nm) that often occurs in this type of phosphor-converted LEDs. Future work should focus on determining the luminescence behavior of other points in this solid solution and optimizing the luminescence properties for potential applications.

3.4 Experimental Part

3.4.1 Preparation of Starting Materials

Synthesis of P_3N_5: Semicrystalline phosphorus(V) nitride was prepared through ammonolysis reaction of P_4S_{10} (approx. 7.0 g, Sigma-Aldrich 99.99%) with ammonia (Air Liquide, 5.0) at 850 °C in a fused silica boat.[35] According to Stock and Grüneberg, the silica boat was first loaded

with P_4S_{10} in an Ar counterflow and the apparatus was saturated with NH_3 for 4 h before heating to 850 °C, holding this temperature for 4 h and finally cooling to room temperature. The product was obtained as an orange powder and identified by PXRD, FTIR and CHNS analysis.

Synthesis of $AE(N_3)_2$ (*AE* = Ba,Sr): The alkaline earth metal azides $AE(N_3)_2$ (*AE*=Ba,Sr) were synthesis through an ion exchange reaction of aqueous HN_3 with the respective carbonates according to Suhrmann *et al.*.[36] HN_3 was formed by passing aqueous NaN_3 (Acros Organics, 99%, extra pure) through a cation exchanger and carefully dropped into an aqueous suspension of the carbonates. After the reaction has ended, respectively impurities were filtered off and the solvent was removed by rotation evaporation. The products were obtained as colorless needles, which were identified by PXRD and FTIR analysis.

Caution: HN_3 is explosive in dry form and highly poisonous. Special care is mandatory!

3.4.2 Preparation of Title Compounds

Synthesis of $Ba_{3-x}Sr_x[Mg_2P_{10}N_{20}]:Eu^{2+}$ (*x* = 0–3): The title compounds were synthesized under high-pressure high-temperature conditions (*T* = 1400°C, *p* = 3 GPa) using a 1000t hydraulic press (Voggenreiter, Germany) with a modified Walker-type module. Details to the synthesis setup and of the handling of the Walker-type multianvil press described in literature.[37] All following synthesis steps were performed in an argon-filled glovebox (Unilab, MBraun, Garching, O_2 < 1 ppm, H_2O <1 ppm). Stoichiometric amounts of the starting materials $AE(N_3)_2$, Mg_3N_2 and P_3N_5 as well as EuN as dopant were mixed in an agate mortar, transferred into a h-BN crucible (HeBoSint S100, Henze, Kempten, Germany) and sealed with a h-BN cap. After placing in an prepared octahedron ($MgO:Cr_2O_3$ (5%), edge length 18 mm, Ceramic Substrates & Components, Isle of Wight, UK), the setup was compressed to 3 GPa and heated up to 1400 °C within 15 min. The temperature was hold for 120 min before cooling to room temperature within 180 min and slowly decompressing the system.

3.4.3 Single-Crystal X-ray Diffraction (SCXRD)

To determine the structure using SC-XRD, we collected combined φ- and ω-scans of a $AE_3[Mg_2P_{10}N_{20}]$ (*AE* = Sr, Ba) single crystals on a Bruker D8 Venture TXS diffractometer with Mo-K_α radiation (λ = 0.71073 A), rotating anode, and multilayer monochromator. The data were indexed, integrated, and absorption-corrected using the multi-scan method. The space group was determined using the APEX3 software package.[38-40] The structure was solved using direct methods by SHELXT and refined by full-matrix least square methods using SHELXL.[41,42] The results were visualized using VESTA software.[43]

3.4.4 Powder X-ray Diffraction (PXRD) and Rietveld Refinement

For XRD measurements, the ground products were pre-filled and sealed in glass capillaries (0.3 mm, Hilgenberg GmbH). Measurements were performed on a Stoe STADI P diffractometer with Cu-$K_{\alpha1}$ (λ = 1.5406 Å) radiation or Ag-$K_{\alpha1}$ (λ = 0.5594 Å) radiation, Ge(111) monochromator and Mythen1K detector in modified Debye-Scherrer geometry. Subsequently, each data set was Rietveld refined using the software TOPAS.[44,45]

3.4.5 Temperature Dependent Powder X-ray Diffraction (HT-PXRD)

Temperature-dependent powder X-ray diffraction patterns were measured using a STOE Stadi P diffractometer (STOE & Cie GmbH, Darmstadt) with Mo-$K_{\alpha1}$ radiation (λ = 0.71073 Å), a Ge(111) monochromator, and an IP-PSD detector. The pre-ground sample was sealed in a silica glass capillary (Hilgenberg, Malsfeld) with an outer diameter of 0.3 mm. The sample was heated from 50 to 950 °C in 50 °C increments and subsequently cooled down to ambient temperature in 50 °C increments. At every dwell step, diffraction patterns were measured within 1 h at a constant temperature.

3.4.6 Scanning Electron Microscopy (SEM) and Energy-Dispersive X-ray (EDX) Spectroscopy

Energy dispersive X-ray (EDX) measurements were performed to investigate the chemical composition and morphology of the samples, using a Dualbeam Helios Nanolab G3 UC (FEI, Hillsboro, Oregon, USA) with a X–Max80 SDD detector (Oxford Instruments, Abingdon, UK). For prevention of possible electrostatic charging during the measurements, the samples were carbon pre-coated using a high-vacuum sputter coater (CCU-010, Safematic GmbH, Zizers, Switzerland).

3.4.7 Transmission Electron Microscopy (TEM)

The samples were ground using absolute ethanol, and a resulting suspension drop was deposited onto a TEM grid coated with a lacey carbon film (Plano GmbH, Wetzlar, Germany). The grid was placed on a double-tilt low background holder and introduced into a Cs DCOR probe-corrected Titan Themis 300 TEM (FEI, USA). The TEM is equipped with a X-FEG source, a post-column filter (Enfinium ER-799), a US1000XP/FT camera system (Gatan, Germany), and a windowless, 4-quadrant Super-X EDX detector (FEI, USA). TEM images were captured using a 4k × 4k FEI Ceta CMOS camera. The microscope operated at a 300 kV accelerating voltage with a semiconvergence angle of 16.6 mrad, 50 µm aperture, and HAADF detector inner half angle of 33 mrad for a 245 mm camera length. Digital Micrograph was used for Fourier filtering of STEM images. The software Velox was used to obtain STEM images and atomic-resolution EDX maps.[46–49]

3.4.8 Solid-State Magic Angle Spinning (MAS) NMR Spectroscopy

^{31}P NMR spectra were collected with a DSX AVANCE spectrometer (Bruker) with a magnetic field of 11.7 T. The samples were filled into a 2.5 mm rotor, which was mounted on a commercial MAS probe (Bruker). The rotation frequency of the samples in the experiments was 20 kHz. The obtained data were analyzed using device-specific software.

3.4.9 Charge Distribution (CHARDI) and Bond-Valence-Sum (BVS) Calculations

CHARDI values were performed using VESTA. Bond-valence-sum calculations were done with the EXPO2014 software.[50–52]

3.4.10 Density Functional Theory Calculations

Periodic density functional theory calculations as implemented in the Vienne ab initio simulation package (VASP) was used to perform first principle electronic structure calculations.[53–55] VASP separates Core and valence electrons using projector-augmented waves (PAW).[56, 57] For all optimizations the exchange and correlation energy is calculated using the generalized gradient approximation (GGA), as described by Perdew, Burke and Ernzerhof (PBE).[58] The optimizations were performed via RMM-DIIS and an energy cutoff of 520 eV.[59] An additional dispersion correction term was calculated within the DFT-D3 method with Becke-Johnson damping function

to properly consider vdW interactions like London dispersion forces.[60] For a deeper insight into the electronic structure all band gaps were calculated both within PBE and local modified Becke-Johnson (LMBJ) approximation.[61, 62] Non-spherical contributions to the gradient of the density in the PAW spheres where included when using LMBJ. Elastic tensors were calculated by performing finite distortions and deriving the elastic constants from the strain-stress relationship. The bulk modulus, Poisson ratio and Debye temperature were calculated using the Voigt-Reuss-Hill approximations.[63–65] The Brillouin zones were sampled on appropriate Γ- centered *k*-point grids (0.2/Å) ensuring well-converged structures and the interpolation of the *k* space was done via the tetrahedron method with Blöchl corrections. The energy convergence criterion was set to 10^{-7} eV and the residual atomic forces were relaxed until a convergence criterion of 10^{-3} eV/Å.

3.4.11 Luminescence Measurements

To investigate the luminescence properties, individual particles of the title compounds were separated and measured using a HORIBA Fluoromax4 spectrofluorimeter system connected via optical fibers to an Olympus BX51 microscope for data acquisition. Low temperature measurements of $Ba_3[Mg_2P_{10}N_{20}]:Eu^{2+}$ were performed from 300 to 6 K on a thick-bed powder layer using a fiber-coupled spectroscopy system containing a thermally stabilized LED light source and a fiber optic spectrometer from Ocean Optics (HR2000+ES) in an evacuated cooling chamber. The samples were cooled via a liquid He compressor system (Advance Research System Inc., ARS4HW). Temperature-depended measurements were performed on an a very thin powder layer sandwiched between an alumina substrate and a cover glass, heated on a Linkam THMS600 stage and the emission under 415 nm excitation was measured with a calibrated Ocean Insight HR2000Plus ES spectrometer controlled by the measurement software SweepMe! (Axel Fischer and Felix Kaschura, SweepMe! - A multi-tool measurement software (sweep-me.net)).

Internal and external quantum efficiency were measured on a custom-built tool comprising an integrating sphere and a CAS spectrometer (Instrument Systems) used for phosphor production quality control. The setup is calibrated weekly with standard phosphors emitting in the green to red spectral range. The absolute quantum efficiency of a garnet phosphor calibration standard (Philips U728) has been certified from the Physikalisch-Technische Bundesanstalt (PTB) Braunschweig, Germany.

3.5 Acknowledgements

We are very grateful to Dr. Marwin Dialer for stimulating discussions and graphical support. Additionally, we thank Christian Minke for NMR measurements and Amalina T. Buda for performing the SEM-EDX measurements and although for her insightful discussions (all at the Department of Chemistry of LMU Munich).

3.6 References

[1] S. Wendl, M. Mallmann, P. Strobel, P. J. Schmidt, W. Schnick, *Eur. J. Inorg. Chem.* **2020**, *10*, 841.

[2] A. Marchuk, S. Wendl, N. Imamovic, F. Tambornino, D. Wiechert, P. J. Schmidt, W. Schnick, *Chem. Mater*. **2015**, *27*, 6432.

[3] S. Wendl, S. Mardazad, P. Strobel, P.J. Schmidt, W. Schnick, *Angew. Chem. Int. Ed.* **2020**, *59*, 18240.

[4] S. Wendl, M. Zipkat, P. Strobel, P.J. Schmidt, W. Schnick, *Angew. Chem. Int. Ed.* **2021**, *60*, 4470.

[5] P. Pust, P. J. Schmidt, W. Schnick, Nat. Mater. 2015, 14,454–458.

[6] K. A. Denault, J. Brgoch, S. D. Kloß, M. W. Gaultois, J. Siewenie, K. Page R. Seshadri, *ACS Appl. Mater. Interfaces* **2015**, 7 7264.

[7] S.D. Kloß, W. Schnick, *Angew. Chem. Int. Ed.* **2019**, *58*, 7933.

[8] F.J. Pucher, A. Marchuk, P.J. Schmidt, D. Wiechert, W. Schnick, *Chem. Eur. J.* **2015**, *21*, 6443.

[9] S. Wendl, L. Eisenburger, P. Strobel, D. Günther, J.P. Wright, P.J. Schmidt, O. Oeckler, W. Schnick, *Chem. Eur. J.* **2020**, *26*, 7292.

[10] R.M. Pritzl, N. Prinz, P. Strobel, P.J. Schmidt, D. Johrendt, W. Schnick, *Chem. Eur. J.* **2023**, *29*, e202301218.

[11] M. Dialer, M.M. Pointner, S.L. Wandelt, P. Strobel, P.J. Schmidt, L. Bayarjargal, B. Winkler, W. Schnick, *Adv. Optical Mater.* **2023**, 2302668.

[12] R.-J. Xie, N. Hirosaki, T. Suehiro, F.-F. Xu, M. Mitomo, *Chem. Mater.* ***2006****, 18,* 5578.

[13] P. Dorenbos, *J. Lumin.* **2003**, *104*, 239.

[14] T.M. Tolhurst, P. Strobel, P. J. Schmidt, P. W. Schnick, A. Moewes, *Chem. Mater.* **2017**, *29,* 7976.

[15] W.B. Park, S.P. Singh, K.-S. Sohn, *J. Am. Chem. Soc.* **2014**, *136*. 2363.

[16] Deposition Numbers 2332859 (for $Ba_3[Mg_2P_{10}N_{20}]$), 2332860 (for $Sr_3[Mg_2P_{10}N_{20}]$), contain the supplementary crystallographic data for this paper. These data are provided free of charge by the joint Cambridge Crystallographic Data Centre and Fachinformationszentrum Karlsruhe Access Structures service.

[17] S. Wendl, L. Seidl, P. Schüler, W. Schnick, *Angew. Chem. Int. Ed.* **2020**, *59*, 23579.

[18] S. Schneider, S. Klenk, S.D. Kloß, W. Schnick, *Chem. Eur. J.* **2024**, *30*, e202303251.

[19] D. Baumann, W. Schnick, *Inorg. Chem.* **2014**, *53*, 7977.

[20] K. Landskron, E. Irran, W. Schnick, *Chem. Eur. J*. **1999**, *5*, 2548.

[21] The terms *zweier, dreier, vierer* etc. has been established by Liebau and is derived from the German word of the numerals *eins* (1), *zwei* (2), *drei* (3), *vier* (4), etc. by adding the suffix "*er*", describing the repeating structural units of tetrahedra. F. Liebau, Structural Chemistry of Silicates: Structure, Bonding, and Classification, Springer, Heidelberg, **1985**.

[22] V. A. Blatov, A. P. Shevchenko, D. M. Proserpio, *Cryst. Growth Des.* **2014**, *14*, 3576.

[23] W. Baur, *Acta Crystallogr. B.* **1974,** *30*, 1195

[24] R. D. Shannon, *Acta Crystallogr. Sect. A* **1976**, 32, 751.

[25] P. Hohenberg, W. Kohn, *Phys. Rev.* **1965**, *136*, 864.

[26] W. Kohn, L. J. Sham, *Phys. Rev.* **1965**, *140(4A)*, 1133.

[27] P. Pust, F. Hintze, C. Hecht, V. Weiler, A. Locher, D. Zitnanska, S. Harm, D. Wiechert, P.J. Schmidt, W. Schnick, *Chem. Mater.* **2014**, *26*, 6113.

[28] K.A. Denault, J. Brgoch, M.W. Gaultois, A.A. Mikhailovsky, R. Petry, H. Winkler, S.P. DenBaars, R. Seshadri, *Chem. Mater.* **2014**, *26*, 2275.

[29] J.D. Furman, B.C. Melot, S.J. Teat, A.A. Mikhailovsky, A.K. Cheetham, *Phys. Chem. Chem. Phys.* **2011**, *13*, 7622.

[30] Y. Zhuo, A.M. Tehrani, A.O. Oliynyk, A.C. Duke, J. Brgoch, *Nat. Commun.* **2018**, *9*, 4377.

[31] G. Blasse, A. Bril, *Philips Tech. Rev.* **1970**, *31*, 314.

[32] A. Kechele, O. Oeckler, F. Stadler, W. Schnick, *Solid State Sci.***2009**,*11*, 537.

[33] O. Oeckler, F. Stadler, T. Rosenthal, W. Schnick, *Solid State Sci*. **2007**, *9*,205.

[34] M. Seibald, T. Rosenthal, O. Oeckler, W. Schnick, *Crit. Rev. Solid State Mater. Sci*. **2014**, *39*, 21.

[35] A. Meijerink, G. Blasse, *J. Lumin.* **1989**, *43*, 283.

[36] M.-H. Fang, C. O. M. Mariano, P.-Y. Chen, S.-F. Hu, R.-S. Liu, *Chem. Mater.* **2020**, *32*, 1748.

[37] P. Strobel. T. de Boer, V. Weiler, P.J. Schmidt, A. Moewes, W. Schnick, *Chem. Mater.* **2018**, 30, 3122.

[38] S. Pennycook, *Annu. Rev. Mater. Sci.* **1992**, *22*, 171.

[39] A. Stock, H. Grüneberg, *Ber. Dtsch. Chem. Ges.* **1907**, *40*, 2573.

[40] R. Suhrmann, K. Clusius, *Z. Anorg. Allg. Chem.* **1926**, *152*, 52.

[41] H. Huppertz, *Z. Kristallogr. Cryst. Mater.* **2004**, *219*, 330−338.

[42] SAINT, Data Integration Software, Madison, Wisconsin (USA), **1997**.

[43] Bruker-AXS, APEX3, Vers. 2016.5-0, Karlsruhe (Germany), **2016**.

[44] Bruker-AXS, XPREP Reciprocal Space Exploration, Vers. 6.12, Karlsruhe (Germany), **2001**.

[45] G. M. Sheldrick, *Acta Crystallogr. Sect. C*, **2015**, *71*, 3.

[46] G. M. Sheldrick, SHELXS-97 Program of the Solution of Crystal Structure, University of Göttingen, Göttingen (Germany), **1997**.

[47] K. Momma, F. Izumi, *J. Appl. Crystallogr.* **2011**, *44*, 1272.

[48] A. A. Coelho, TOPAS-Academic v4.1, Brisbane (Australia), **2007**.

[49] H. M. Rietveld, *J. Appl. Crystallogr.* **1969**, *2*, 65.

[50] I. Gatan, DigitalMicrograph, Version 3.6.5, Pleasanton, California (USA), **1999**.

[51] J. L. Lábár, *Ultramicroscopy* **2005**, *103*, 237.

[52] J. P. Stadelmann, *jEMS software package*, Version 3.60907U2011, Saas-Fee (Switzerland), **2011**.

[53] Thermo Fisher Scientific, *Velox*, Waltham, Massachusetts (USA), **2021**.

[54] A. Altomare, C. Cuocci, C. Giacovazzo, A. Moliterni, R. Rizzi, N. Corriero, A. Falcicchio, *J. Appl. Crystallogr*. **2013**, *46*, 1231.

[55] N. E. Brese, M. O'Keeffe, *Acta Crystallogr. Sect. B.* **1991**, *47*, 192.

[56] D. Brown, D. Altermatt, *Acta Crystallogr. Sect. B.* **1985**, *41*, 244.

[57] G. Kresse, J. Hafner, *Phys. Rev. B.* **1993**, *47*, 558.

[58] G. Kresse, J. Furthmüller, *Comput. Mat. Sci.* **1996**, *6*, 15.

[59] G. Kresse, J. Furthmüller, *Phys. Rev. B.* **1996**, *54*, 169.

[60] G. Kresse, D. Joubert, *Phys. Rev. B.* **1991**, *59*, 1758.

[61] P. E. Blöchl, *Phys. Rev. B*. **1994**, *50*, 17953.

[62] J.P. Perdew, K. Burke, M. Ernzerhof, *Phys. Rev. Lett.* **1996**, *77*, 3865.

[63] P. Pulay, Chem. *Phys. Lett.* **1991,** *73*, 393.

[64] S. Grimme, S. Ehrlich, L. Goerigk, *J. Comput. Chem.* **2011**, *32*, 1456.

[65] T. Rauch, M. A. L. Marques, S. Botti, *Phys. Rev. B.* **2020**, *101*, 245163.

[66] H.J. Monkhorst, J.D. Pack, *Phys. Rev. B.* **1976**, *13*, 5188.

[67] W. Voigt, *Lehrbuch der Kristallphysik*, Teubner, Leipzig (Germany), **1928**.

[68] A. Reuss, *Z. Angew. Math. Mech.* **1929**, *9*, 49.

[69] R. Hill, *P. Phys. Soc. A*, **1952**, *65*, 349.

4 $ZnH_2P_4N_8$: Case Study on Topochemical Imidonitridophosphate High-Pressure Synthesis

Published in: *Chem. Eur. J.* **2024**, *30*, e202402741.

Authors: Reinhard M. Pritzl, J. Steinadler, Amalina T. Buda, Sebastian Wendl, and Wolfgang Schnick

DOI: https://doi.org/10.1002/chem.202402741

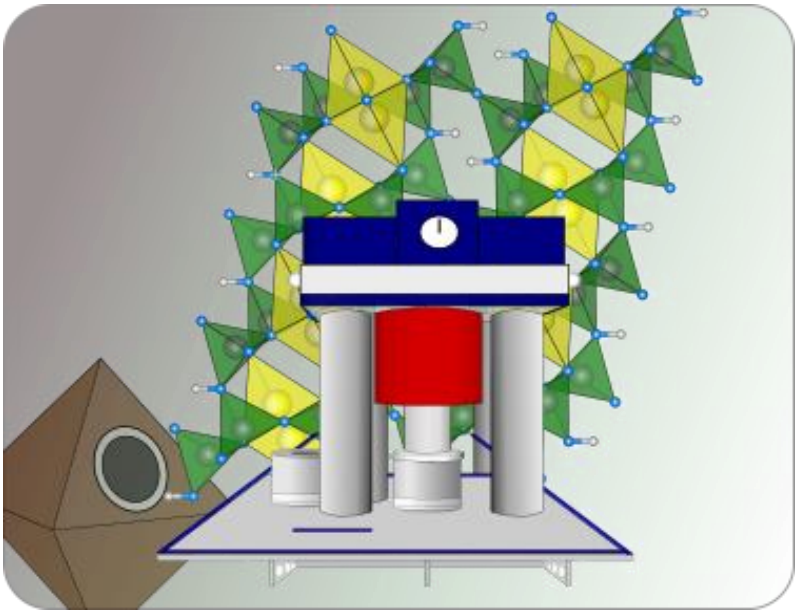

Abstract: Nitridophosphates are subject of current research, as they have a broad spectrum of properties and potential applications, such as ion conductors or luminescent materials. Yet, the subclass of imidonitridophosphates has been studied less extensively. The primary reason is that the controlled N–H functionalization of nitridophosphates is not straight forward, making targeted synthesis more challenging. Inspired by the high-pressure (HP) post-synthetic modification of nitridophosphates, we present the topochemical HP deprotonation of phosphorus nitride imides using the high-pressure polymorph β-HPN_2 as an example. Additional incorporation of Zn^{2+} results in the first quaternary transition metal imidonitridophosphate $ZnH_2P_4N_8$. The crystal structure was elucidated by single-crystal X-ray diffraction (SCXRD), energy-dispersive X-ray spectroscopy (EDX), powder X-ray diffraction (PXRD) and solid-state magic angle spinning nuclear magnetic resonance spectroscopy (MAS NMR). In addition, the presence of H as part of an imide group was confirmed by IR spectroscopy. The potential of this defunctionalization

approach for controlling the N–H content is demonstrated by the preparation of partially deprotonated intermediates $Zn_xH_{4-2x}P_4N_8$ ($x \approx 0.5,\ 0.85$). This topochemical high-pressure reaction represents a promising way to prepare, control and manipulate new imide-based materials without altering their overall anionic framework.

4.1 Introduction

Silicate analogous materials have become increasingly important in materials chemistry. Nitride compounds, along with oxides and oxonitrides, are already used in high-performance materials for applications such as high-temperature, thermal and ion conduction, and semiconductor materials.[1–5] The classes of tetrahedron-based structures also include the (imido)-nitridophosphates. Their structural similarities to silicates are frequently discussed due to the isoelectronic element combinations of Si/O and P/N.[5] The ternary HPN_2 illustrates the similarities to silicates directly. As a consequence of the isoelectronicity to SiO_2, this nitride imide crystallizes in two modifications, structurally related to high and low cristobalite.[6,7] In contrast to ternary P/N/H compounds, quaternary ones have been sparsely studied. The major reason for this is the low thermal stability of the nitride precursors required for synthesis. P_3N_5 is one of the most common starting materials for the preparation of (imido)nitridophosphates. It has a decomposition temperature of 850 °C, α-HPN_2 even only 570 °C.[7,8] According to *Le Chatelier*, this restriction can be circumvented by application of elevated pressure. For example the lowly condensed representatives $Na_{10}[P_4(NH)_6N_4](NH_2)_6(NH_3)_{0.5}$ and $Rb_8[P_4N_6(NH)_4](NH_2)_2$ were synthesized by Jacobs et al. under ammonothermal conditions in autoclaves.[9,10] The synthesis of highly condensed networks, such as the imidonitridophosphate $BaP_6N_{10}NH$, requires not only high pressure but also high temperatures to facilitate bond cleavage and reformation.[11] Targeting nitridophosphates a number of synthesis routes under medium-/high-pressure have been established in recent years.[5]

However, these are only restrictedly transferable to imidonitridophosphates. For example, the mineralizer-assisted route can be used for certain imidonitridophosphates, as illustrated by SrP_3N_5NH. The latter was synthesized under high-pressure and high-temperature (HP/HT) conditions using stoichiometric amounts of $Sr(N_3)_2$, P_3N_5, and NH_4Cl.[12] However, the consistent incorporation of N–H groups into the target compound is not observed, as shown by the synthesis of many pure nitridophosphates crystallized by the addition of ammonium halides.[13–16] More efficient could be the direct addition of phosphorus nitride imides (e.g. amorphous or crystalline α-HPN_2) to the reaction mixture, as exemplified in the syntheses of $MH_4P_6N_{12}$ (M = Mg, Ca).[17]

Here, the tendency is evident that providing pre-organized anionic $[PN_3(NH)]^{6-}$ motifs leads to their integration in the desired product. The aforementioned methods are employed to attain a specific molecular formula with a desired degree of condensation, with the stoichiometry selected accordingly. However, the directed influence on structural details is typically limited. Nevertheless, this control is essential for the development of new compounds with desired properties, as it ensures that the outcome is not left to chance. In contrast to the direct synthesis routes mentioned above, post-synthetic modification is a way of preserving the anionic main motif to a certain extent. Wendl *et al*. showed that highly condensed 3D frameworks in particular allow for topotactic control over the cation environments.[18] Starting from a nitridophosphate-based precursor, ion exchange or metathesis reaction has been carried out using metal halides. In this process, cations with larger ionic radii are typically replaced by smaller ones under high/medium pressure conditions. More stable by-products drive this process. This reaction strategy uses the stronger interaction between smaller cations and the anionic backbone, resulting in their incorporation into a more energetically favorable product. That such exchanges are not limited to this reaction direction is shown by the deprotonation of the nitride imide sodalite $Zn_5H_4[P_{12}N_{24}]Cl_2$ with $ZnCl_2$ resulting in $Zn_7[P_{12}N_{24}]Cl_2$.[19,20] Transferred to the high-pressure conditions required for the stabilization of many imidonitridophosphates, this reaction provides a possibility for selective deprotonation of existing H/P/N compounds. Due to the 3D structure with channels in which amide groups are localized, the ternary high-pressure polymorph β-HPN_2 was considered as a model compound for this purpose. In this contribution, we report on the synthesis of the first quaternary transition metal imidonitridophosphate, namely $ZnH_2P_4N_8$, by controlled de-functionalization of a phosphorus nitride imide high-pressure polymorph, retaining its anionic backbone. The structure was elucidated by single-crystal X-ray diffraction data (SCXRD), and confirmed using MAS NMR, EDX, FTIR and powder X-ray diffraction data (PXRD). Furthermore, a series of partially deprotonated representatives with the general stoichiometric formula $Zn_xH_{4-2x}P_4N_8$ ($x \approx 0, 0.5, 0.85, 1$) were prepared and analyzed by PXRD, MAS NMR and EDX spectroscopy. Additionally, a direct synthesis approach of the stoichiometric $ZnH_2P_4N_8$ is presented.

4.2 Results and Discussion

4.2.1 Synthesis

$Zn_xH_{4-2x}P_4N_8$ ($x \approx 0.5, 0.85, 1$) was synthesized according to two different routes (Equation (4.1) and (4.2)) after empirical optimization.

Both, topochemical deprotonation and nitride/azide reaction lead to the stoichiometric imidonitridophosphate $ZnH_2P_4N_8$. According to Equation (4.1) an excess (10 mol-%) of the respective halide stoichiometry is necessary to prepare also partially de-functionalized representatives.

Topochemical deprotonation approach starting from ternary β-HPN_2:

$$x\ ZnCl_2 + 4\ \beta\text{-}HPN_2 \rightarrow Zn_xH_{4-2x}P_4N_8 + 2x\ HCl \quad (4.1)$$

Nitride/azide approach:

$$2\ Zn_3N_2 + 8\ P_3N_5 + 3\ NH_4N_3 \rightarrow 6\ ZnH_2P_4N_8 + 4\ N_2 \quad (4.2)$$

The generated HCl favors the formation and growth of single crystals of $ZnH_2P_4N_8$ with a length of up to 20 µm (Figure 4.1). However, according to Equations (4.1) and (4.2) different amounts of the title compound were obtained together with $Zn_8P_{12}N_{24}O_2$, β-HP_4N_7 and unknown side phases. Due to the better crystal quality after synthesis according to Equation (4.2), single-crystals of this approach were used for structure analysis of $ZnH_2P_4N_8$. Detailed information on both high-pressure approaches can be found in the Experimental Section. Since the title compound is stable to moisture and air, potentially occurring water-soluble by-products such as the starting material $ZnCl_2$, were removed by washing with de-ionized water. $Zn_xH_{4-2x}P_4N_8$ ($x \approx 0.5, 0.85, 1$) were isolated as dark grayish crystalline solids. The respective elemental compositions were analyzed via Rietveld refinements on PXRD data (with free refinement of the Zn occupations and subsequent fixation within the errors) and EDX spectroscopy on individual crystals (Tables S4.1–4.4, Figure S4.1). As the latter method is very surface-sensitive, the low oxygen contents detected can be attributed to surface hydrolysis caused by the washing step. However, the results obtained are within the usual error range of the analysis method. Synthesis experiments based on Equation (4.1) but using the low-pressure polymorph α-HPN_2 instead of β-HPN_2 resulted in an unidentifiable product with a high amorphous content.

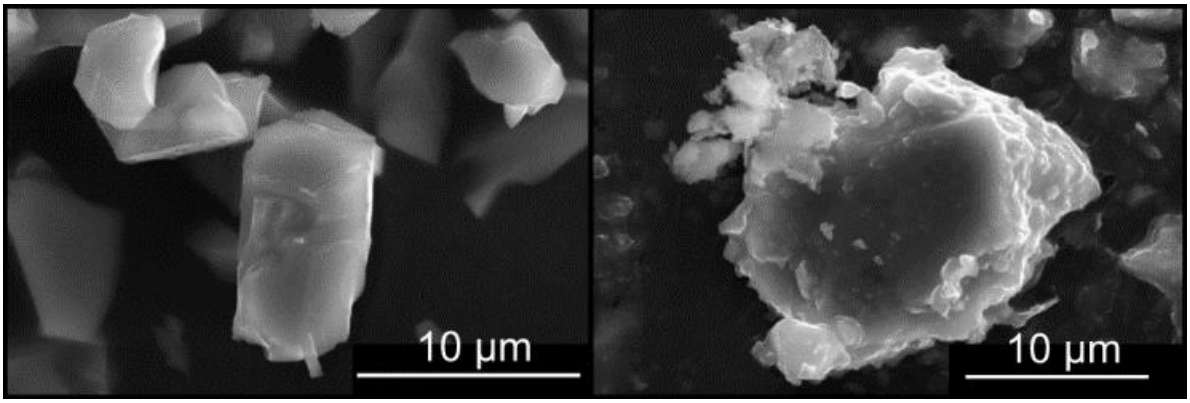

Figure 4.1. SEM images of $ZnH_2P_4N_8$ crystals with a maximum diameter of ca. 10–20 µm; left: obtained from nitride/azide direct synthesis, right: obtained from topochemical deprotonation reaction.

4.2.2 Structure Elucidation

Structure elucidation was performed by single-crystal X-ray diffraction (SCXRD). Deposition Numbers (2300728 and 2379986) contain the supplementary crystallographic data for this paper. These data are provided free of charge by the joint Cambridge Crystallographic Data Centre and Fachinformationszentrum Karlsruhe Access Structures service (http://www.ccdc.cam.ac.uk/structures). $ZnH_2P_4N_8$ was solved and refined in the monoclinic space group *P*2/*c* (no.13) with $Z = 2$, with a unit cell dimension $a = 7.9230(4)$, $b = 4.8990(2)$, $c = 7.9708(3)$ Å, and $\beta = 107.725$ °, comparable to the initial ternary imide β-HPN_2 ($a = 7.89365(5)$, $b = 4.81867(2)$, $c = 8.11718(4)$ Å, $\beta = 108.0548$°).[6] Refined crystallographic data are given in Table 1, more detailed information on the single-crystal refinement is provided in the Supporting Information (Table S4.5–4.8). During structure refinement, valence electrons of N–H bonds could be determined from difference Fourier maps. The corresponding interatomic N–H distance was restrained for common distances in imidonitridophosphates (0.90(2) Å) and the H atoms were refined isotropically, while all non-hydrogen atoms were refined anisotropically without any further restraints.[12,17] The single-crystal structure of $ZnH_2P_4N_8$ was confirmed by Rietveld refinement of a representative powder X-ray diffraction pattern (Figure 4.2). The chemical composition was verified by energy-dispersive X-ray spectroscopy (EDX) on individual crystals. No other elements than Zn, P, N and O were detected, having an atomic ratio of Zn : P : N ≈ 1 : 4 : 9. The nitrogen content is slightly lower than the expected value, but can be explained by shadowing due to the unfavorable orientation of the crystals to the EDX detector during the analysis.[21]

Table 4.1. Crystallographic data from single-crystal refinement of $ZnH_2P_4N_8$.

Formula	**$ZnH_2P_4N_8$**
Crystal system	monoclinic
Space group	*P2/c* (No.13)
Lattice parameters [Å, °]	a = 7.9230(4)
	b = 4.8990(2)
	c = 7.9708(3)
	β = 107.725(2)
Cell volume [Å^3]	294.70(2)
Formula units [cell]	2
Density [g cm^{-3}]	3.419
μ [mm^{-1}]	5.197
Diffractometer	Bruker D8 Venture
Radiation	Mo-K$_\alpha$ (λ = 0.71073 Å)
Temperature [K]	299(2)
F(000)	296
Θ range [°]	4.16 – 32.02
Total no. of reflections	4131
Independent reflections (>2σ)	850
Refined parameters	69
Restraints	1
R_{int} ; R_σ	0.0296; 0.0327
R1 (all data); R1 (F^2>2σ(F^2))	0.0400; 0.0307
wR2 (all data); wR2 (F^2>2σ(F^2))	0.0784; 0.0750
Goodness of fit	1.064
$\Delta\rho_{max}$; $\Delta\rho_{min}$ [e Å^{-3}]	0.615; –0.575

[a] Estimated standard deviations are given in parentheses.

In contrast to Zn, lighter elements such as N are affected more strongly, therefore their content is often underestimated. However, the average atomic ratio of Zn : P agrees with the values corresponding to the empirical sum formula. The results of the performed CHNS analysis are consistent with the expected nitrogen content (Table S4.9). However, the hydrogen content is also elevated and significantly higher than the theoretical values. This can be attributed to the already

mentioned surface hydrolysis, as well as small amounts of the sodalite-type $Zn_{7-x}H_{2x}[P_{12}N_{24}]Cl_2$ which is homeotypic with $Zn_8P_{12}N_{24}O_2$.[19,22] FTIR spectra of the sample (Figure S4.2) show an N–H band in the range 2700–3400 cm^{-1} and confirm imide in the sample. Additional absorption bands in the fingerprint region are due to P–N–P framework vibration modes. The analysis of the phase width of partially defunctionalized representatives of the series $Zn_xH_{4-2x}P_4N_8$ ($x \approx 0.5$, 0.85, 1) was carried out analogously by performing PXRD, EDX and MAS NMR. Rietveld refinements on PXRD data were based on the structural model obtained from SCXRD data as described above (see Supporting Information).

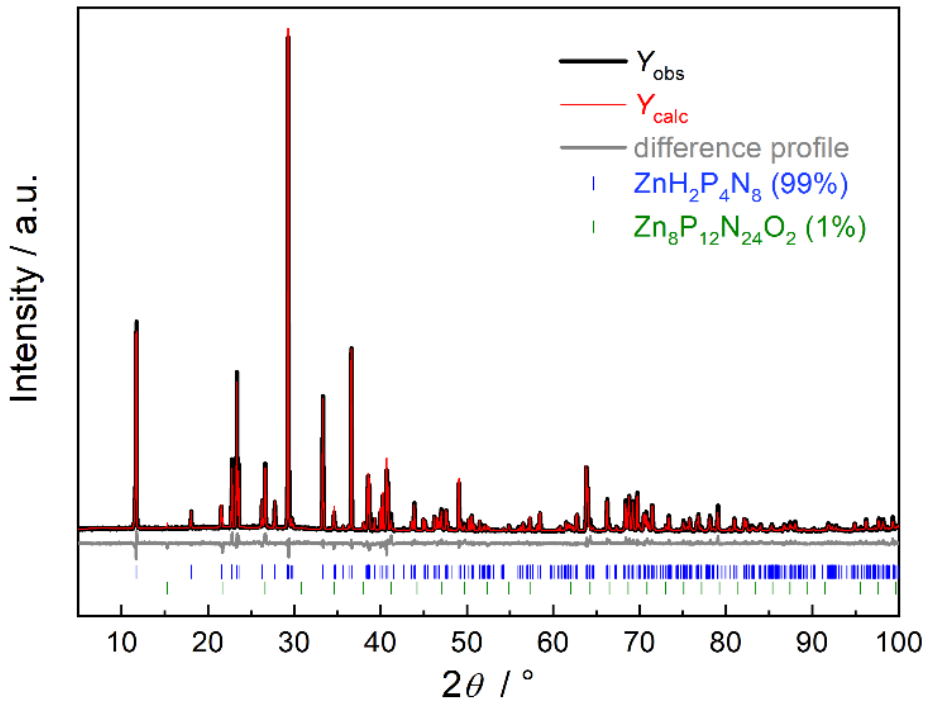

Figure 4.2. Rietveld refinement of $ZnH_2P_4N_8$; observed (black) and simulated (red) powder X-ray diffraction pattern with difference profile (gray). Vertical bars indicate the positions of the Bragg reflections of the desired product (blue) and oxonitridic by-product (green).

4.2.3 Structure Description

As expected for a product obtained by a topochemical reaction, $ZnH_2P_4N_8$ shows the same network topology of the anionic P/N framework as the precursor β-HPN_2, which crystallizes in a distorted *α*-crystobalite type variant. It can be classified as a highly condensed transition metal imidonitridophosphate with a degree of condensation of $\kappa = n(P) : n(N) = ½$, consisting of a three-dimensional network of all-side vertex-sharing PN_4 tetrahedra. According to the silicate nomenclature of Liebau the PN_4 tetrahedra form three different *sechser*-ring types, which assume a distorted armchair conformation.[23] Two of these *sechser*-ring types can be seen along [010]

(see Figure 4.3). A stacking sequence A B A is created by alternating between larger and smaller channels. The larger channels contain zinc atoms, while the smaller channels contain only hydrogen atoms, which are covalently bound to one quarter of the N atoms.

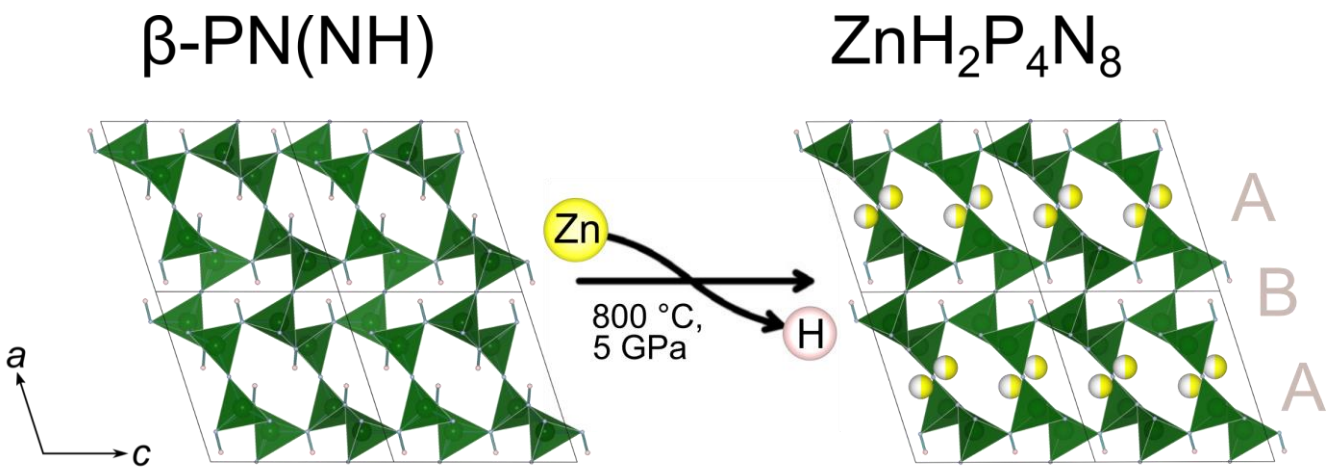

Figure 4.3. Schematic reaction for β-HPN_2 with $ZnCl_2$. Zn atoms in yellow, protons in rose, PN_4 tetrahedra in green.

In the larger channels, zinc occupies a split position (half occupation of Wyckoff position 4*g*) without any indication of zinc alignment (see figure 4.4). The pore size of the smaller channels of β-HPN_2 is apparently insufficient for Zn^{2+} incorporation, which supports the assumption that the P/N framework is maintained during the reaction.

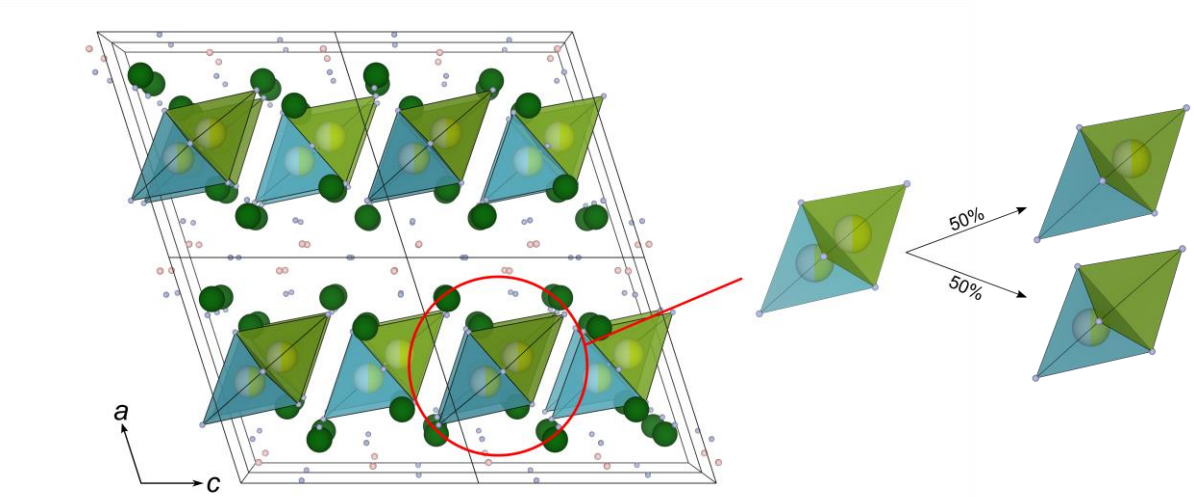

Figure 4.4. Crystal structure of $ZnH_2P_4N_8$ along [010]. The half occupation of Wyckoff sides 4*g* by zinc was highlighted, resulting in a tetrahedral coordination of zinc by nitrogen.

The zinc ions show a tetrahedral coordination by nitrogen with Zn–N bond lengths in a range of 1.961(3)–2.158(2) Å, which is in good agreement with the sum of the corresponding ionic radii reported by Shannon (ionic radii Zn^{2+} = 0.6 Å, N^{3-} = 1.46 Å).[24] Furthermore, these interatomic distances are comparable to those of related compounds such as Zn_2PN_3 or $Zn_6[P_{12}N_{24}]$.[21,25] The P–N bond lengths of $ZnH_2P_4N_8$ are between 1.608(3) Å and 1.667(2) Å and are in good agreement with the bond lengths of other known nitridophosphates.[26–28] The observed PN_4 tetrahedra are distorted, as evidenced by the N–P–N bond angles (104.22(11)–117.88(12)°) which diverge from the regular tetrahedral angle 109.5°. Furthermore, the P–N–P bond angles show values between 125.8(2)° and 141.03(12)°. These are plausible for the existing *sechser*-ring types and show comparable angles to those of the host structure β-HPN_2 (P–N–P bonding angles: 126.0(2)–147.85(4) °).[6] More detailed information on interatomic distances and angles is given in Tables S4.7 and S4.8.

4.2.4 Solid-State NMR Studies

In order to confirm the obtained structure model from X-ray diffraction data the prepared samples were investigated by solid-state NMR spectroscopy. NMR spectroscopy is a highly effective technique for investigating the local structure of selected nuclei within a given compound.[29,30] The focus within these investigations was on the H atoms, as their scattering factor in X-ray diffraction experiments is low. During the Rietveld refinements (Table S4.10, Figure S4.3), the H content was just deduced from the degree of occupation of Zn^{2+} with respect to charge neutrality (premise of the topochemical reaction when starting from β-HPN_2). For this purpose, ^{1}H, ^{31}P and $^{31}P\{^{1}H\}$ cross-polarization experiments were performed on the title compound $ZnH_2P_4N_8$ first. For interpretation of the obtained spectra, as well as to gain structural insights from topochemical HP partially de-protonated intermediates, these experiments were also performed on $Zn_xH_{4-2x}P_4N_8$ ($x \approx 0$, 0.5, 0.85). All respective spectra are shown in Figure S4.4–4.7 in the Supporting Information.

As the unit cell of $ZnH_2P_4N_8$ features one crystallographic H site (Wyck. 4*g*, Table S4.5), only one resonance line is expected in the ^{1}H MAS spectrum. The spectrum shows one main signal at 5.9 ppm (Figure 4.5), which can be assigned to $ZnH_2P_4N_8$, and a small narrow signal at 1.2 ppm resulting from surface hydrolysis, which is in line with the EDX results (spinning side bands are marked with asterisks).[6]

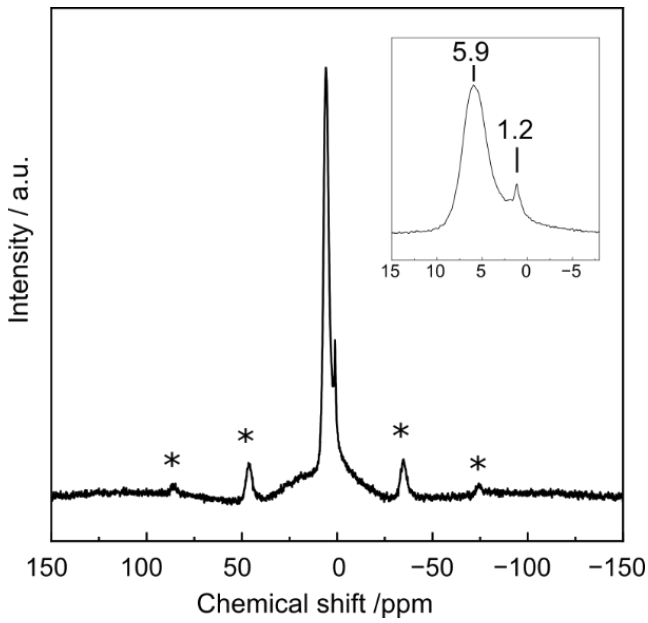

Figure 4.5. The ^{1}H MAS spectrum shows one signal at 5.9 ppm, corresponding to one crystallographic H position in the structure model of $ZnH_2P_4N_8$; weak signal at 1.2 ppm can be attributed to small amounts of hydrolysis product; observed sidebands are marked with asterisks.

Figure 4.6a shows the ^{31}P spectrum (black), which reveals four signals with a chemical shift of δ = 6.4, −4.7, −10.3, and −22.1 ppm. The signal at δ = 6.4 ppm can be assigned to the minor side phase of $Zn_8P_{12}N_{24}O_2$, observed in the PXRD as well, which is in line with the absence of this signal in the $^{31}P\{^{1}H\}$ cross-polarization experiment (Figure 4.6a, gray). The three major signals at δ = −4.7, −10.3, and −22.1 ppm are preserved in the cross-polarization spectrum and can be assigned to the title compound.

Upon closer examination of the three signals, it becomes evident that the signals are not perfectly symmetric but exhibit additional intensity besides their maxima. Especially the one at −22.1 ppm shows a significant shoulder on the left. For this reason, a deconvolution of these ^{31}P signals was initially carried out with four Voigt functions. Nevertheless, the signal shoulders and areas of low intensity could only be satisfactorily fitted with a minimum of four additional Voigt functions (total = eight Voigt functions, Figure 4.6b). The four major signals (green) are superimposed on four minor signals (blue). The integral ratio of the four major signals is about 1.3 : 1.1 : 1 : 1.9 (A : B : C : D). However, the structure model obtained from X-ray diffraction data shows only two crystallographic P sites with equal site multiplicity (Wyck. 4*g*), which does not seem to be consistent with the observed signals. Nevertheless, the structural model obtained from the X-ray diffraction data represents an average over long distances, rather than over specific areas.

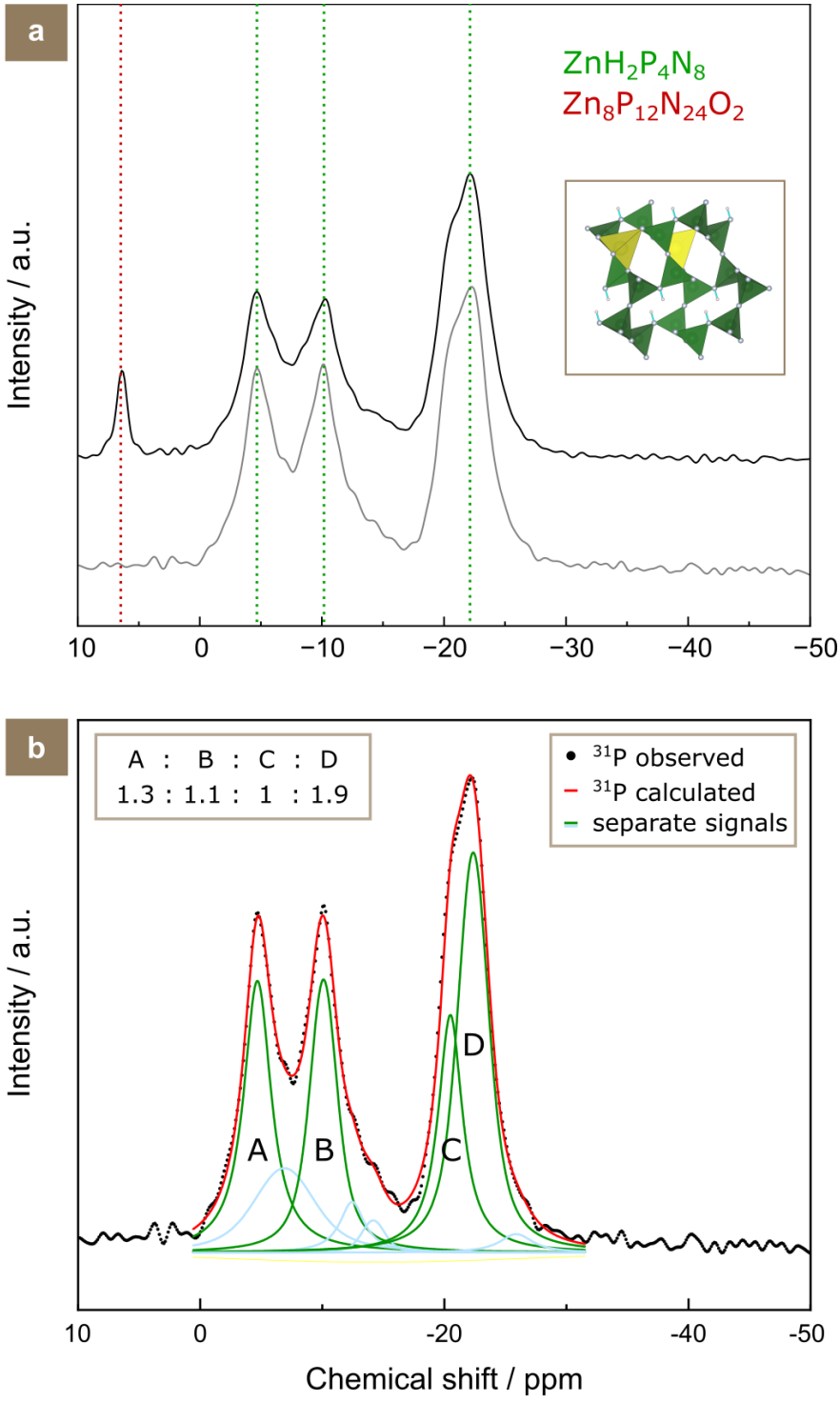

Figure 4.6. a) The ^{31}P spectrum (black) shows three major signals at −4.7, −10.3, and −22.1 ppm, which can be assigned to $ZnH_2P_4N_8$ (they are preserved in the $^{31}P\{^1H\}$ cross-polarization spectrum (gray)). The fourth signal at 6.4 ppm can be assigned to $Zn_8P_{12}N_{24}O_2$. The section box shows a possible local arrangement of the partial real structure in $ZnH_2P_4N_8$, ZnN_4 tetrahedra in yellow, PN_4 tetrahedra in green, N–H functionality in blue. b) The $^{31}P\{^1H\}$ cross-polarization NMR spectrum of $ZnH_2P_4N_8$ (gray); Deconvolution by eight Voigt functions indicates a lower local symmetry, since significantly more than two signals expected for two P sites with equal multiplicity in the structure model (obtained by SCXRD) are observed.

In contrast, the local surroundings of the investigated nuclei are the cause of the respective resonance positions in the NMR spectra. The observed discrepancy can be attributed to the split positions of the Zn^{2+} ions, which in the real structure lead to numerous local environments for the ^{31}P atoms. These environments are differentially shielded / unshielded by proximity to the zinc (high electron density) or to the imide groups (lower electron density). This indicates that the SCXRD structure model assumes a higher symmetry than is actually present locally.

Returning to the observed signals in Figure 4.6, a possible explanation for the integral ratios of the major signals is that a symmetry reduction to *Pc* (no. 7) has occurred locally, comparable to the mineral γ-eucryptite ($LiAlSiO_4$).[31,32] This would result in four independent crystallographic P sites with the same site multiplicity (Wyck. 2*a*) and two independent Zn sites with a site occupancy of ½ (Figure 4.6a, section box; Table S4.11). Regardless the occupation Zn1 = 1 and Zn2 = 0 or *vice versa*, the resulting Zn–P distances can be divided into three categories: short (occure.: 1×; Zn–P: 2.88 Å), medium (occur.: 1×; Zn–P: 3.03 Å), and long (occur.: 2×; Zn–P: 3.06–3.07 Å). These findings align with the observed integrals of approx. 1 : 1 : 2 (signals A : B : D). However, it is not possible to ascertain unequivocally which of the two occupation variants is present in the title compound. In order to gain a more comprehensive understanding of the data, it is necessary to include the $^{31}P\{^1H\}$ cross-polarization spectra from β-HPN_2 and $Zn_xH_{4-2x}P_4N_8$ ($x \approx$ 0.5, 0.85). This will allow us to interpret the signals more accurately. Figure 4.7 illustrates the strong dependence of the local environment on the Zn content, which is highlighted by color and small arrows. The lowest Zn content ($x \approx 0.5$) indicates the presence of numerous potential local variants, with a tendency towards a real symmetry in space group *Pc* for the title compound $ZnH_2P_4N_8$. The shoulder of the main signal (Figure 4.6, signal C, integral = 1) still indicates regions in $ZnH_2P_4N_8$ that correspond to those of β-HPN_2 and in which almost no Zn has been incorporated (compare Figure 4.7, spectra $x = 0$ with $x \approx 0.5$ and $x = 1$), which is in line with the Zn split positions. This observation is also consistent with assumption of a topochemical reaction according Equation (4.1), from which we can now even deduce a possible topotactic reaction-mechanism with complete preservation of the β-HPN_2 framework during the reaction. However, this conclusion should be confirmed by *in situ* experiments.

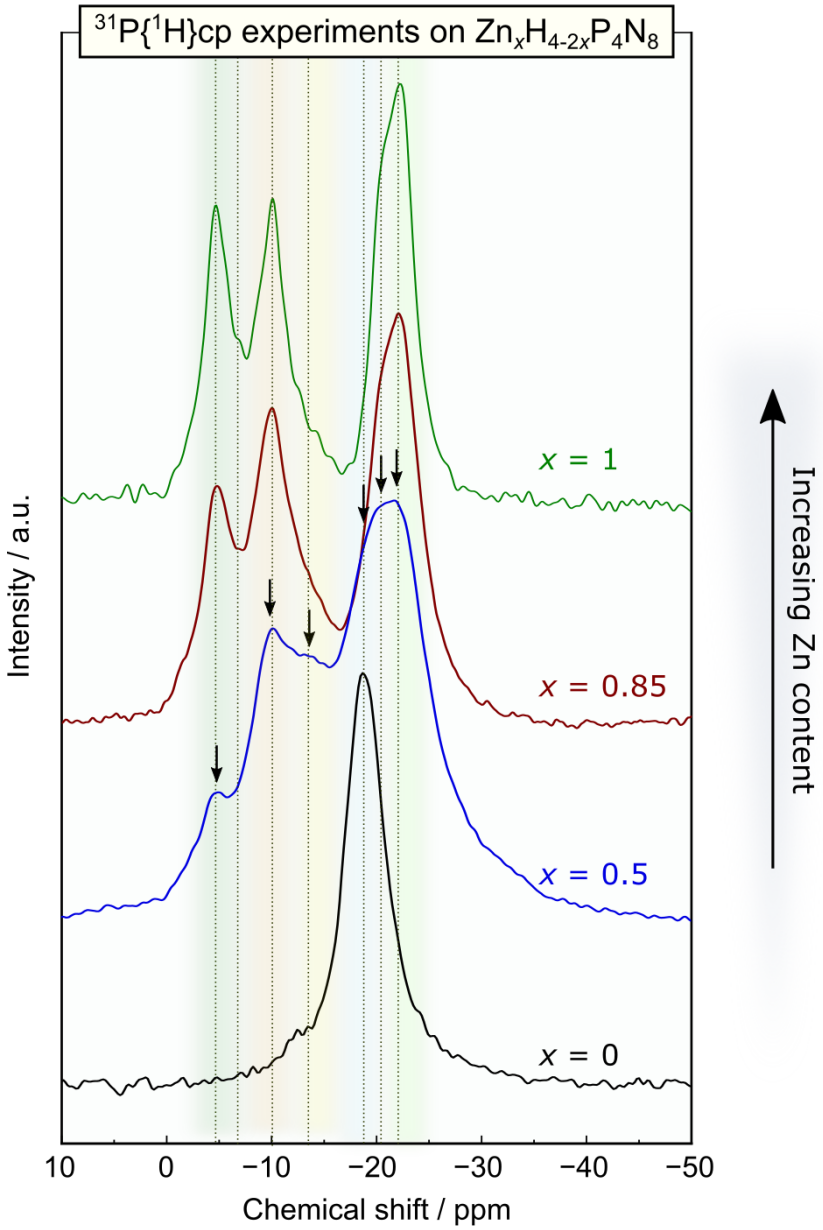

Figure 4.7. $^{31}P\{^1H\}$ cross-polarization experiments of $Zn_xH_{4-2x}P_4N_8$ ($x \approx$ 0, 0.5, 0.85, 1). Signal ranges that can be identified in the individual experiments are highlighted in color.

4.3 Conclusion

In this contribution, we present the synthesis and structural elucidation of the quaternary imidonitridophosphate $ZnH_2P_4N_8$ via high-pressure/high-temperature syntheses. The crystal structure refined from single-crystal X-ray diffraction data (SCXRD) is supported by powder X-ray diffraction data (PXRD), energy-dispersive X-ray spectroscopy (EDX) and solid-state NMR experiments. Two reaction approaches are presented, with the main focus on the novel synthetic route of (partial) high-pressure defunctionalization of a pre-synthesized phosphorus nitride imide. By partial defunctionalization and incorporation of Zn^{2+} ions into the PN-framework, this

synthetic approach is a promising extension to the known synthesis routes of (imido)nitridophosphates, preserving the anionic P/N-structure and gaining enhanced structural control during synthesis. Solid-state MAS NMR experiments on different stoichiometric compositions of $Zn_xH_{4-2x}P_4N_8$ provide insight into the real structure of $ZnH_2P_4N_8$ (local environment) and allow conclusions to be drawn about the reaction mechanism of a topochemical reaction. The crystal structure of $ZnH_2P_4N_8$ can be described as P/N based cation filling variant of distorted low-cristobalite. Zn^{2+} is located in the larger channels, while hydrogen is covalently bound to N in the smaller ones. Further studies could investigate the complete deprotonation of β-HPN_2 using smaller cations like lithium. A comparative analysis on the topologically similar alumosilicate *γ*-eucryptite (a polymorph of $LiAlSiO_4$, with filled quartz structure) demonstrates that lithium can occupy both larger and smaller channels in this related substance class.[32] In summary, this route extends the synthetic possibilities for the synthesis of (imido)nitridophosphates and shows great potential for synthetic control with respect to classical direct syntheses. Furthermore, it seems to be a suitable method for the preparation of transition metal (imido)nitridophosphates, since the competitive reaction for the formation of quite stable phosphides is prevented by the choice of relatively moderate high pressure/high temperature conditions. Future research should concentrate on the expansion of this synthetic route to encompass other phosphorus nitride imide polymorphs, such as β-HP_4N_7 as well as the incorporation of additional cations to provide a more comprehensive assessment of the synthetic potential of this route. Furthermore, these initial conclusions regarding the reaction mechanism should be subjected to further investigation through *in situ* experiments.[33]

4.4 Experimental Part

4.4.1 Preparation of Starting Materials

Synthesis of P_3N_5: P_3N_5 was synthesized according to *Stock* et al. by an ammonolysis reaction of P_4S_{10} (Sigma Aldrich, 99%) at 850 °C for 4 h (heating rate: 5 °C·min^{-1}).[34] For this purpose, the silica reaction tube was heated out in advance and then saturated with NH_3 for 4 h. After cooling down to room temperature (5 °C·min^{-1}), the received orange product is used without further processing. Phase purity was confirmed by PXRD, Elemental analysis (CHNS) and FTIR measurements.

Synthesis of NH_4N_3: NH_4N_3 was synthesized according to Frierson *et al.* by sublimation of NaN_3 (Acros Organics, 99%) and NH_4NO_3 (Grüssing, 99%).[35] The starting materials were ground and transferred to a Schlenk tube. The lower part of the Schlenk tube was placed into a glass oven and its valve was opened before starting the heating step at 200 °C for 12 h (heating rate: 5 °C·min^{-1}). The product was obtained as colorless crystals in the top of the Schlenk tube. Phase purity was confirmed by PXRD and FTIR measurements.

4.4.2 Preparation of $ZnH_2P_4N_8$

The title compound was prepared by high-pressure/high-temperature synthesis according two distinct approaches (1) and (2). According (1) different equivalents of pre-synthesized β–HPN_2 and $ZnCl_2$ (10% excess, Merck, > 97.0%) were used. According equation (2) stoichiometric amounts of Zn_3N_2 (AlfaAesar, 99.99%), P_3N_5 and NH_4N_3 were ground together under inert gas conditions. The reaction conditions of 800 °C and 5 GPa were achieved by combining a hydraulic 1000t press (Voggenreiter, Mainleus, Germany) with the multianvil technique using a modified Walker module. The starting materials were mixed in an argon-filled glove box (<1 ppm O_2, < 0.1 ppm H_2O; Unilab, MBraun, Garching) and placed in an h-BN crucible of size 18/11 (cavity diameter = 1.6 mm, cavity depth = 2.3 mm; HeBoSint® S100, Henze, Kempten, Germany). The crucible was sealed with a cap of h-BN, inserted into two 18/11-assembly sized graphite furnaces and centered using MgO spacers. For thermal insulation this construct was transferred into a zirconia sleeve; electrical contact was achieved by two Mo discs. The as-prepared assembly was placed into a center drilled octahedron consisting of Cr_2O_3 (6%) substituted MgO (Ceramic Substrates & Components, Isle of Wight, U.K.). Eight tungsten carbide (substituted with 7% Co) cubes (Hawedia, Marklkofen, Germany) with truncated edges (edge length = 11 mm) were used as anvils. Initially the sample was pressed to 5 GPa within 200 min before being heated to the target temperature of 800 °C (heating rate: 100 °C·min^{-1}). After 15 min dwell time the sample was cooled down to ambient temperature within 15 min. The assembly was decompressed within 600 min and the obtained product was recovered from the crucible and washed with deionized water for purification. Schematic drawings of the octahedral pressure cell and the Walker-type module are illustrated in Figure S4.8. Additional information regarding high-pressure/high-temperature synthesis can be found in literature.[36]

4.4.3 Single-Crystal X-ray Diffraction (SCXRD)

For single-crystal XRD measurements $ZnH_2P_4N_8$ single crystals were isolated by a MicroMount™ (Bruker). The single-crystal X-ray diffraction data were collected on a Bruker D8 Venture TXS diffractometer (rotating anode, Mo-K_α radiation, λ = 0.71073 Å, multilayer monochromator). Indexing and integration as well as determination of the space group was performed by the APEX3 software package.[37–39] The crystal structure was solved using the SHELXS-97 algorithm and refined by full matrix least-squares methods using WinGX.[40,41]

4.4.4 Powder X-ray Diffraction (PXRD)

The ground product was placed and sealed in a glass capillary (d = 0.3 mm, Hilgenberg GmbH) for PXRD measurement. The measurement was performed using a Stoe STADI P diffractometer with Mo-$K_{\alpha1}$ (λ = 0.71073 A) radiation, Ge(111) monochromator and Mythen 1K detector in modified Debye-Scherrer geometry. Rietveld refinement of the measured data was performed using TOPAS software.[42]

4.4.5 Scanning Electron Microscopy

SEM imaging and EDX measurements were made by a Dualbeam Helios Nanolab G3 UC (FEI, Hillsboro) equipped with a X-Max 80 SDD detector (Oxford Instruments, Abingdon). For this purpose single crystallites were fixed on an adhesive carbon pad and coated by a high-vacuum sputter coater (BAL-TEC MED 020, Bal Tec A) to ensure electrical conductivity.

4.4.6 Fourier Transform Infrared Spectroscopy

The FTIR spectrum was collected on a Spectrum BX II spectrometer with DuraSampler ATR-device (Perkin Elmer) at ambient conditions.

4.4.7 Solid-state Magic Angle Spinning (MAS) NMR Spectroscopy

^{31}P, ^{1}H, and $^{31}P\{^{1}H\}$ cross-polarization NMR experiments were performed with a AVANCE DSX 500 MHz NMR spectrometer (Bruker) with a magnetic field of 11.7 T. The samples were filled

and compacted into a 2.5 mm rotor, which was mounted on a commercial MAS probe (Bruker). The sample rotation frequency was about 20 kHz. The obtained data were analysed using ORIGIN Pro 2022b. All spectra were indirectly referenced to ^{1}H in 100% TMS at –0.1240 ppm.

4.5 Acknowledgements

We thank Christian Minke for MAS NMR measurements and especially Dr. Thomas Bräuniger for expert help in interpreting the spectra (both at the Department of Chemistry of LMU Munich).

4.6 References

[1] H. Kiyono, T. Nukui, T. Akashi, S. Shimada, *Trans. Mater. Res. Soc. Jpn.* **2008**, *33*, 953.

[2] F.L. Riley, *J. Am. Ceram. Soc.* **2000**, *83*, 245.

[3] S.F. Palguev, R.P. Lesunova, L.S: Karenina, *Solid State Ionics*, **1986**, *20*, 255.

[4] A. Zakutayev, *J. Mater. Chem. A* **2016**, *4*, 6742.

[5] S.D. Kloß, W. Schnick, *Angew. Chem. Int. Ed.* **2019**, *58*, 7933.

[6] A. Marchuk, F.J. Pucher, F.W. Karau, W. Schnick, *Angew. Chem. Int. Ed.* **2014**, *53*, 2469.

[7] W. Schnick, J. Lücke, *Z. Anorg. Allg. Chem.* **1992**, *610*, 121.

[8] S. Horstmann, E. Irran, W. Schnick, *Angew. Chem. Int. Ed. Engl.* **1997**, *36*, 1873.

[9] H. Jacobs, S. Pollok, F. Golinski, *Z. Anorg. Allg. Chem.* **1994**, *620*, 1213.

[10] F. Golinski, H. Jacobs, *Z. Anorg. Allg. Chem.* **1995**, *621*, 29.

[11] S. Wendl, L. Eisenburger, M. Zipkat, D. Günther, J.P. Wright, P.J. Schmidt, O. Oeckler, W. Schnick, *Chem. Eur. J.* **2020**, *26*, 5010.

[12] S. Vogel, W. Schnick, *Chem. Eur. J.* **2018**, *24*, 14275.

[13] F.J. Pucher, W. Schnick, *Z. Anorg. Allg. Chem.* **2014**, *640*, 2708.

[14] F.J. Pucher, A. Marchuk, P.J. Schmidt, D. Wiechert, W. Schnick, *Chem. Eur. J.* **2015**, *21*, 6443.

[15] L. Eisenburger, V. Weippert, C. Paulmann, D. Johrendt, O. Oeckler, W. Schnick, *Angew. Chem. Int. Ed.* **2022**, *61*, e202202014.

[16] L. Eisenburger, V. Weippert, O. Oeckler, W. Schnick, *Chem. Eur. J.* **2021**, *27*, 14184.

[17] A. Marchuk, V.R. Celinski, J. Schmedt auf der Günne, W. Schnick, *Chem. Eur. J.* **2015**, *21*, 5836.

[18] S. Wendl, L. Seidl, P. Schüler, W. Schnick, *Angew. Chem. Int. Ed.* **2020**, *59*, 23579.

[19] W. Schnick, J. Lücke, *Z. Anorg. Allg. Chem.* **1994**, *620*, 2014.

[20] W. Schnick, J. Lücke, *Angew. Chem. Int. Ed. Engl.* **1992**, *31*, 213.

[21] L. Gamperl, P. Strobel, P.J. Schmidt, W. Schnick, *Chem. Eur. J.* **2022**, *28*, e202200760.

[22] F. Karau, O. Oeckler, F. Schäfers, R. Niewa, W. Schnick, *Z. Anorg. Allg. Chem.* **2007**, *633*, 1333.

[23] The terms *vierer*, *fünfer*, *sechser* etc. were introduced by Liebau and are derived from the German word of the digits *vier* (4), *fünf* (5), *sechs* (6), etc. by adding the suffix "*er*", describing the repeating structural units of tetrahedra. F. Liebau, Structural Chemistry of Silicates: Structure, Bonding, and Classification, Springer, Heidelberg (Germany), **1985**.

[24] R.D. Shannon, *Acta Crystallogr. Sect. A* **1976**, *32*, 751.

[25] S.J. Sedlmaier, M. Eberspächer, W. Schnick, *Z. Anorg. Allg. Chem.* **2011**, *637*, 362.

[26] R.M. Pritzl, M.M. Pointner, K. Witthaut, P. Strobel, P.J. Schmidt, W. Schnick, *Angew. Chem. Int. Ed.* **2024**, *63*, e202403648.

[27] M.M. Pointner, R.M. Pritzl, J.M. Albrecht, L. Blahusch, J.P. Wright, E. L. Bright, C. Giacobbe, O. Oeckler, W. Schnick, *Chem. Eur. J.* **2024**, *30*, e202400766.

[28] M. Dialer, M.M. Pointner, S.L. Wandelt, P. Strobel, P.J. Schmidt, L. Bayarjargal, B. Winkler, W. Schnick, *Adv. Optical Mater.* **2024**, *12*, 2302668.

[29] T. Polenova, R. Gupta, A. Goldbourt, *Anal. Chem*. **2015**, *87*, 5458.

[30] B. Reif, S. E. Ashbrook, L. Emsley, *Nat. Rev. Methods Primers*, **2021**, *1*, 2.

[31] P. Norby, *Zeolites*, **1990**, *10*, 193.

[32] A. Gordeeva, I. Z. Jenei, K. Spektor, O. Y. Vekilova, U. Häussermann, *Z. Naturforsch. B* **2021**, *76*, 599.

[33] S.J. Ambach, R.M. Pritzl, S. Bhat, R. Farla, W. Schnick, *Inorg. Chem.* **2024**, *63*, 3535.

[34] A. Stock, H. Grüneberg, *Ber. Dtsch. Chem. Ges.* **1907**, *40*, 2573.

[35] W.J. Frierson, *Inorg. Synth.* **1946**, *8*, 136.

[36] H. Huppertz, *Z. Kristallogr*. **2004**, *219*, 330.

[37] Bruker-AXS, *APEX3*, Vers. 2016.5-0, Karlsruhe (Germany), **2016.**

[38] Bruker-AXS, *XPREP Reciprocal Space Exploration*, Vers. 6.12, Karlsruhe (Germany), **2001**.

[39] SAINT, *Data Integration Software*, Madison, Wisconsin (USA), **1997**.

[40] G.M. Sheldrick, *Acta Crystallogr. Sect. C*, **2015**, *71*, 3.

[41] G.M. Sheldrick, *SHELXS-97 Program of the Solution of Crystal Structure*, University of Göttingen, Göttingen (Germany), **1997**.

[42] A.A. Coelho, *TOPAS-Academic v4.1*, Brisbane (Australia), **2007**.

5 $CaLi_2PN_3$ – A Quaternary Chain-Type Nitridophosphate by Medium-Pressure Synthesis

Published in: *Chem. Eur. J.* **2024**, *30*, e202402521.

Authors: Reinhard M. Pritzl, Nadine Fahle, Kristian Witthaut, Sebastian Wendl, and Wolfgang Schnick

DOI: https://doi.org/10.1002/chem.202402521

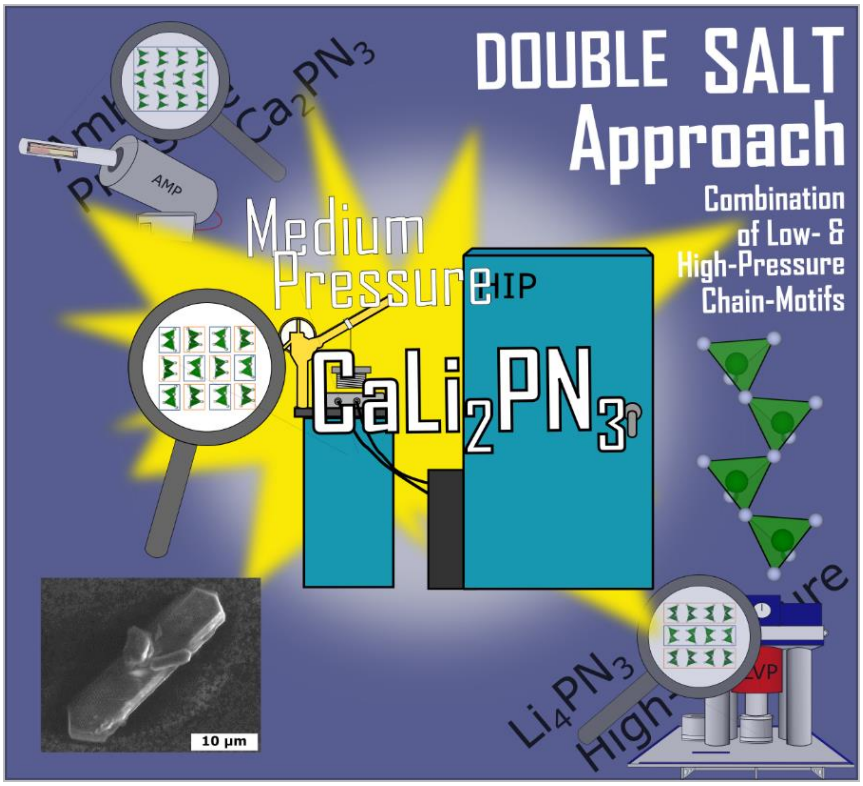

Abstract. Nitridophosphates are in the focus of current research interest due to their structural versatility and properties, such as ion conductivity, ultra-incompressibility and luminescent properties when doped with suitable activator ions. Multinary representatives often require thorough investigation due to the competition with the thermodynamically more stable binary and ternary compounds. Another point of concern is the synthetic control of structural details, which is usually limited by conventional bottom-up syntheses. In this study, we report on the synthesis and characterization of the quaternary nitridophosphate $CaLi_2PN_3$. Various synthesis protocols were used for the preparation of $CaLi_2PN_3$, including the novel nitridophosphate double salt

approach. The crystal structure was solved and refined from single-crystal X-ray diffraction data and confirmed by Rietveld refinement, solid-state NMR spectroscopy, EDX measurements and low-cost crystallographic calculations. The experimental results were corroborated by DFT calculations, which revealed the electronic band structure. Formation energy calculations allowed conclusions to be drawn about the stability in comparison to the initial ternary nitridophosphates. The synthesis of $CaLi_2PN_3$ exemplifies the enormous potential of medium-pressure syntheses in the field of nitridophosphate research. Furthermore, the presented new synthesis route allows a certain degree of structural control, which is a promising addition to previous synthesis strategies in nitridophosphate chemistry.

5.1 Introduction

Nitridophosphates exhibit a multifaceted structural diversity with structural motifs similar to those of oxosilicates. In recent years, a large number of representatives has been prepared using various synthetic approaches. These range from (pressure) ampoules, hot isostatic press (HIP) to multianvil press (LVP) or diamond anvil cell synthesis.[1–6] In this context a number of synthetic strategies and synthesis protocols has been developed. For instance, the nitride/azide routes, metathesis reactions, and the Li_3N self-flux have been established.[7] Nonetheless, the influence of these bottom-up synthesis methods on the structural details is limited. The degree of condensation κ (i.e. ratio of tetrahedra centers (P) and ligands (N)) can be influenced by selecting the stoichiometry of the reactants, which is oriented on the desired molecular formula.[8,9] However, the post-synthetic modification developed by Wendl *et al*. allows for a certain extent of synthetic control.[10] In contrast to the classic bottom-up approaches, a top-down approach was developed. Ion exchange reactions were conducted by reacting pre-synthesized alkaline earth metal nitridophosphates with other metal halides under elevated pressure. In addition to topotactic ion exchange, atomic rearrangements were also observed, which resulted in the formation of different P/N substructures or structure types in general. A comparison of all previously mentioned routes reveals that elevated pressure is beneficial for synthesis. The challenge of nitridophosphate synthesis is primarily due to the limited thermal stability of nitride precursors, such as P_3N_5, and the desired products.[11] Thermal decomposition is usually prevented by increasing the synthesis pressure (*SP*). A more detailed examination of the literature reveals a trend indicating less harsh reaction conditions in terms of *SP* are required for lowly-condensed nitridophosphates ($\kappa < ½$) than for highly condensed representatives ($\kappa \geq ½$).[9,12–14] For example MP_2N_4 (*M* = Ge, Be, Cd, Mn, Ca, Sr, Ba) and MP_8N_{14} (*M* = Fe, Co, Ni, Mg, Ca, Sr, Ba) have only

been prepared in the GPa regime, while Li_7PN_4, $Li_{12}P_3N_9$, Mg_2PN_3, Ca_2PN_3 and $Sr_3P_3N_7$ are attainable using pressure ampoules or ammonothermal reaction conditions.[10,12,14–22] All of the latter representatives have isolated anionic structural motifs in common, namely infinite vertex-sharing chains of PN_4 tetrahedra. A comparison of this chain motifs reveals that the simplest case observed in nitridophosphates is unbranched *zweier*-single chains (based on Liebau's nomenclature for silicates).[23] These have so far been observed in the absence of additional network-forming cations *NFC* (*NFC* = additional, tetrahedrally coordinated cations) in Ca_2PN_3 (ambient conditions, ampoules), Li_4PN_3 (high-pressure conditions, LVP), and have recently been reported in $GePN_3$ (ultra-high-pressure conditions, diamond anvil cell (DAC)).[6,12,14] This observation was our starting point to search for novel quaternary chain-type nitridophosphates. A synthesis under medium-pressure conditions where both lithium and calcium are present as counter cations appears to offer a promising starting point for further research. In this contribution, we report on synthesis and structural investigation of $CaLi_2PN_3$, the first quaternary alkaline / alkaline earth metal nitridophosphate. Two distinct synthesis approaches are presented: A well-established bottom-up approach, which involves the use of azide/nitride precursors and a novel, exploratory top-down double salt approach using nitridophosphate-based chain-type precursors, with the objective of retaining the anionic structural motifs. We have succeeded in growing single crystals suitable for structure determination using single-crystal X-ray diffraction data and provide a comprehensive structural analysis by combining PXRD, SEM-EDX, MAS NMR and low-cost crystallographic calculations (*LCC*). Formation energy calculations and the calculation of the band structures complement the characterization.

5.2 Results and Discussion

5.2.1 Synthesis

$CaLi_2PN_3$ was obtained by solid-state medium-pressure reactions at 900 °C and 200 MPa under N_2 atmosphere (Experimental Section). Two different synthesis strategies were identified as optimal after empirical optimization (A and B):

A) Bottom-up synthesis using the nitride/azide route:

$$6\ Ca(N_3)_2 + 4\ Li_3N + 6\ P_{red} \rightarrow 6\ CaLi_2PN_3 + 11\ N_2 \quad (5.1)$$

$$2\ Ca_3N_2 + 12\ LiN_3 + 6\ P_{red} \rightarrow 6\ CaLi_2PN_3 + 11\ N_2 \quad (5.2)$$

B) Top-down double salt synthesis using pre-synthesized chain-type nitridophosphates:

$$Ca_2PN_3 + Li_4PN_3 \rightarrow 2\ CaLi_2PN_3 \quad (5.3)$$

According to Equations (5.1–5.3), different amounts of $CaLi_2PN_3$ were obtained together with varying amounts of Ca_2PN_3, $Li_{10}P_4N_{10}$ and CaO. The results of the corresponding Rietveld refinements can be found in Figures S5.1&5.2 and Table S5.1. The highest phase portions were obtained by Equation (5.1), however, unassignable reflections observed in the powder diffraction of the bottom-up syntheses indicate the presence of unknown minor side phase(s). The elucidation of this is subject of future research. According to Equations (5.1) and (5.2), the use of metal azides is necessary for bottom-up synthesis, as no $CaLi_2PN_3$ was formed using only nitrides as starting materials (P_{red} / P_3N_5, Li_3N, Ca_3N_2).

The best results for the synthesis were obtained at temperatures of 880–900 °C, which seems to be a compromise for the synthesis temperatures of many lithium nitridophosphates (α-/β-$Li_{10}P_4N_{10}$ (*T*: 630–720 °C), $LiPN_2$ (*T*: 800 °C), $Li_{12}P_3N_9$ (*T*: 790 °C) or the high-pressure polymorph Li_4PN_3 (*T*: 820 °C) and Ca_2PN_3 (*T*: 1200 °C).[2,12,14,24–26]

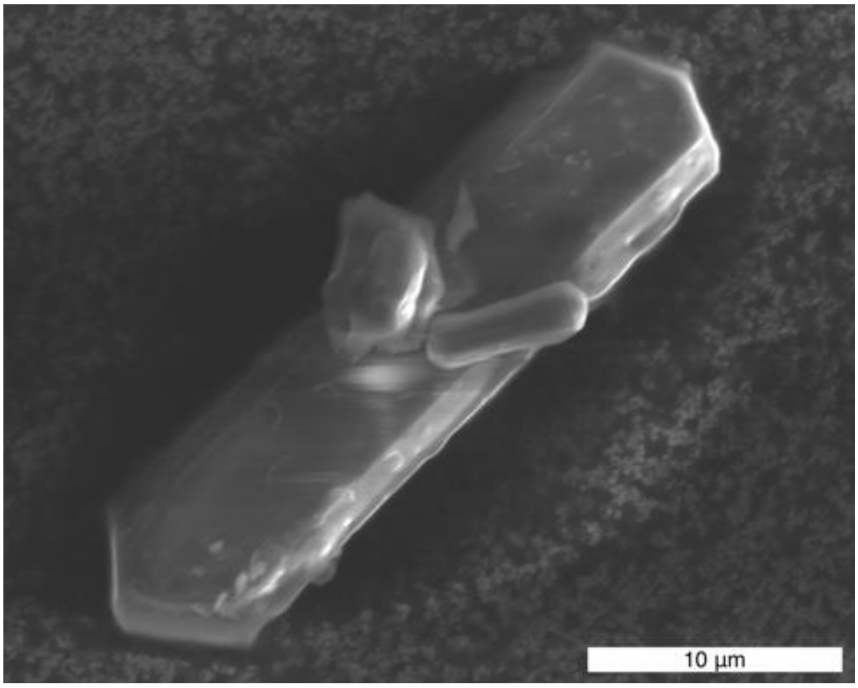

Figure 5.1. SEM image of an isolated single-crystal of $CaLi_2PN_3$.

The title compound was isolated as colorless crystals (up to 30 µm in length, Figure 5.1) that are sensitive to air or moisture. In order to select suitable crystals for single-crystal structure analysis (SCXRD) and to distinguish them from the minor side phases (detected by PXRD), their photoluminescence properties were exploited by doping with Eu^{2+}. Crystals of the side phase

Ca_2PN_3:Eu^{2+} show a deep red emission with $\lambda_{em\,,\,max}$ = 650 nm upon irradiation with UV to blue light.[2] For this purpose, small amounts of $EuCl_2$ (~1mol% with respect to Ca^{2+} according Equation (2)) were added during synthesis. At room temperature, $CaLi_2PN_3$ does not exhibit any discernable luminescent properties when irradiated with UV to blue light.

5.2.2 Structure Elucidation

The crystal structure of $CaLi_2PN_3$ was solved and refined from single-crystal X-ray diffraction data. $CaLi_2PN_3$ crystallizes in monoclinic space group *C*2/*c* (no. 15) with eight formula units per unit cell and lattice parameters *a* =11.3397(4), *b* = 11.5881(4), *c* = 4.9408(2) Å, *β* = 113.966(1)° (Table 5.1, Experimental Section).[27] All atomic positions were determined during the structure solution process and the displacement parameters are refined anisotropically (Wyckoff positions, atomic coordinates, anisotropic displacement parameters, interatomic distances and angles are given in Tables S5.2–5.5). Solid-state ^{31}P MAS spectroscopy experiments support the proposed structure model with phosphorus on one independent crystallographic site (Wyckoff 8*f*). The observed chemical shift *δ* = 15.1 ppm (*fwhm* = 4.2 ppm, Figures S5.3–5.5) is in a typical range for lithium (oxo)nitridophosphates and also partially observed in alkaline earth metal nitridophosphates.[24,28–30] The consistency observed in both distinctive compound classes can serve as a benchmark for future mixed alkali/alkaline earth nitridophosphates. ^{6}Li & ^{7}Li MAS spectra confirm the presence of lithium in the prepared samples (Figures S5.6&5.7). However, due to the small chemical shift differences of the $^{6/7}$Li MAS NMR signals, no clear differentiation from the signals of the Li containing side phases is possible. In order to prove the absence of imide functionality (N–H) in the title compound ^{31}P{^{1}H} NMR experiments were performed (Figures S5.8&5.9). The observed signals do not correspond to any of the positions of the signals in the direct ^{31}P spectra, which suggests there is no hydrogen present in $CaLi_2PN_3$. Nevertheless, the observed signals indicate that the minor unknown side phases contain imide/amide groups.

To confirm the elemental composition, SEM-EDX investigations were carried out on selected crystallites. Only the atomic cation ratios were considered, as the tendency for hydrolysis falsifies both the anion and total atomic values.

The measured values are consistent with the theoretical values and are within the typical error range of this method, thereby corroborating the elemental composition (Table S5.6). The electrostatic plausibility of the crystal structure was analyzed by various low-cost crystallographic calculations, including bond-valence sums (BVS) and charge distribution (CHARDI) calculations (Tables S5.7&5.8).[31–33] These confirm the consistency of the structure model.

Table 5.1. Crystal data for $CaLi_2PN_3$; estimated standard deviations are given in parentheses.

Formula	**$CaLi_2PN_3$**
Crystal system	monoclinic
Molecular weight / g·mol^{-1}	253.92
Space group	*C*2/*c* (no. 15)
Lattice parameters / Å,°	*a* = 11.3397(4)
	b = 11.5881(4)
	c = 4.9408(2)
	β = 113.966(1)
Cell volume / Å^3	593.28(4)
Formula units per cell	8
Calculated density / g·cm^{-1}	2.843
μ / mm^{-1}	2.378
T_{min} / T_{max}	0.958 / 1.000
Radiation	Mo-K$_\alpha$ (λ = 0.71073 Å)
Temperature / K	293(2)
F(000)	496
θ range / °	3.516 < θ < 28.694
Total no. of reflections	5109
Independent reflections (>2σ)	764 (734)
Refined parameters	65
R_{int}; R_σ	0.0252; 0.0164
*R*1 (all data); *R*1 (F^2>2σ(F^2))	0.0175; 0.0165
*wR*2 (all data); w*R*2 (F^2>2σ(F^2))	0.0421; 0.0417
Goodness of fit	1.121
$\Delta\rho_{max}$; $\Delta\rho_{min}$ / e·Å^{-3}	0.362; −0.314

5.2.3 Structure Description

As expected for κ =1/3 $CaLi_2PN_3$ consists of infinite *zweier*-single-chains of vertex-sharing PN_4-tetrahedra, running along *c*, with $^1_\infty[PN_2N_{2/2}]^{4-}$ according to Niggli.[34] Simplified, the structure can be described as a cationic filling variant of the recently reported nitridophosphate $Ge^{IV}PN_3$,

which crystallizes in the $CoGeO_3$ structure type, synthesized under high-pressure conditions (approx. 44 GPa).[6,35] A structural overview is shown in Figure 5.2.

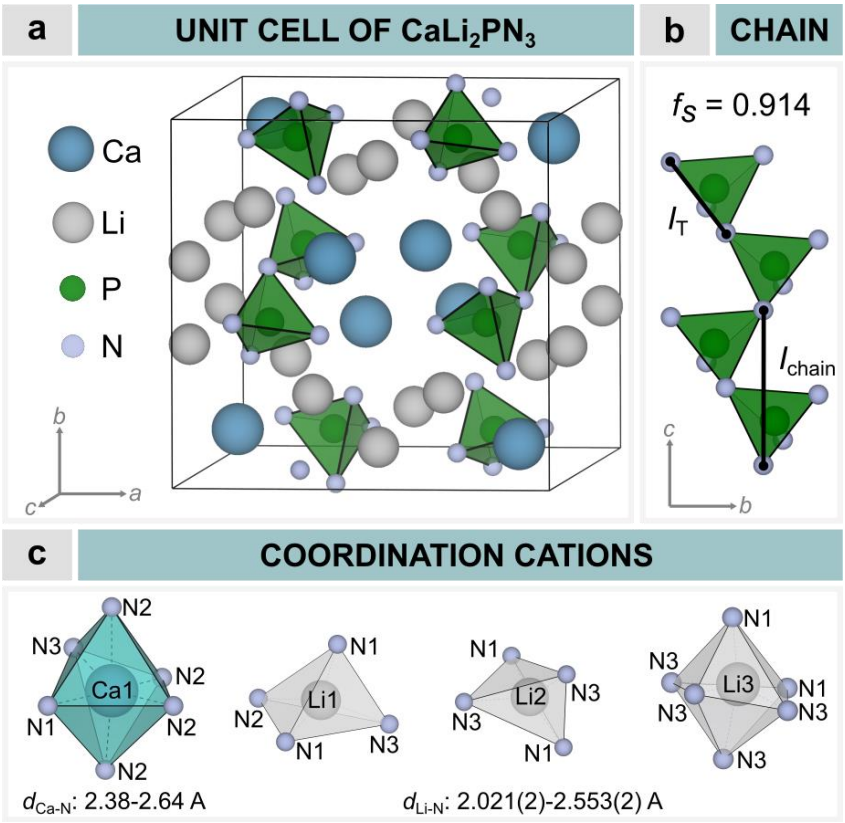

Figure 5.2. Structure model of $CaLi_2PN_3$; a) unit cell with PN_4 tetrahedra-motif in green, Ca atoms in blue, Li atoms in gray, N atoms in light-blue; b) PN_4-tetrahedra chain with stretch. factor (and respective parameters); c) coordination spheres of Ca (cyan) and Li (gray) atoms in $CaLi_2PN_3$.

Given that $CaLi_2PN_3$ is formally composed of the chain-type nitridophosphates Ca_2PN_3 (synthesized at ambient pressure conditions) and Li_4PN_3 (synthesized at high-pressure conditions), it is advisable to undertake a comparison with the other two compounds (Figure 5.3). However, it should be noted that these three compounds do not share the same reference coordinate system with regard to the direction of the anionic chains. In order to facilitate a more accurate comparison, a new coordinate system is introduced, whereby the *x axis* points in the direction of the individual *zweier*-chains, the *y* axis in the direction of the alignment of the unbridged terminal $N^{[1]}$ and the *z axis* in the direction of the layer sequence. All three compounds comprise a single P site, which has the consequence that the resulting chains within a distinct compound can be converted into each other solely by means of symmetry operations (for the sake of clarity, only inversion centers are illustrated in Figure 5.3, the chain arrangement section). This approach facilitates a straightforward comparison of the chains in terms of their arrangement,

alignment (inclination) and elongation. To gain a more comprehensive understanding, it is essential to initially examine the elongation of the PN_4-tetrahedra chains. This can be quantified by the stretching factor $f_s = I_{chain}/(I_T \times P)$, which was originally introduced by Liebau for the classification of chain silicates.[23] The definition of I_{chain} and I_T is provided in Figure 5.2b. The periodicity $P = 2$, as expected for *zweier* single-chains, leads to maximally stretched (= relaxed) chains with $f_s = 1$ for Ca_2PN_3, to less stretched chains with $f_s = 0.923$ for Li_4PN_3 and to the most compressed chains within this series of compounds with $f_s = 0.914$ for $CaLi_2PN_3$ (Figure 5.2b).[12, 14] Less stretched PN_4-tetrahedra *zweier*-chains have been reported for Mg_2PN_3 and Zn_2PN_3.[12,36] Examination of the P–N distances($d_{P–N}$ = 1.61–1.72 Å) shows that these are within the typical range for nitridophosphates.[37–39] As expected, the distances to the terminal N[1] (1.6084(12) Å and 1.6268(13) Å) are significantly shorter than to the bridging N[2] (1.7147(14) Å and 1.7269(12) Å). This compression is reflected in the P–N–P angles of the respective chains, with $CaLi_2PN_3$ having the most acute angle with P–N–P = 123.44(8)°. The compression also allows the chains to be distinguished in terms of their inclination along the *x*-axis. To better illustrate this, the color code gray and white was chosen in Figure 5.3 to achieve maximum contrast.

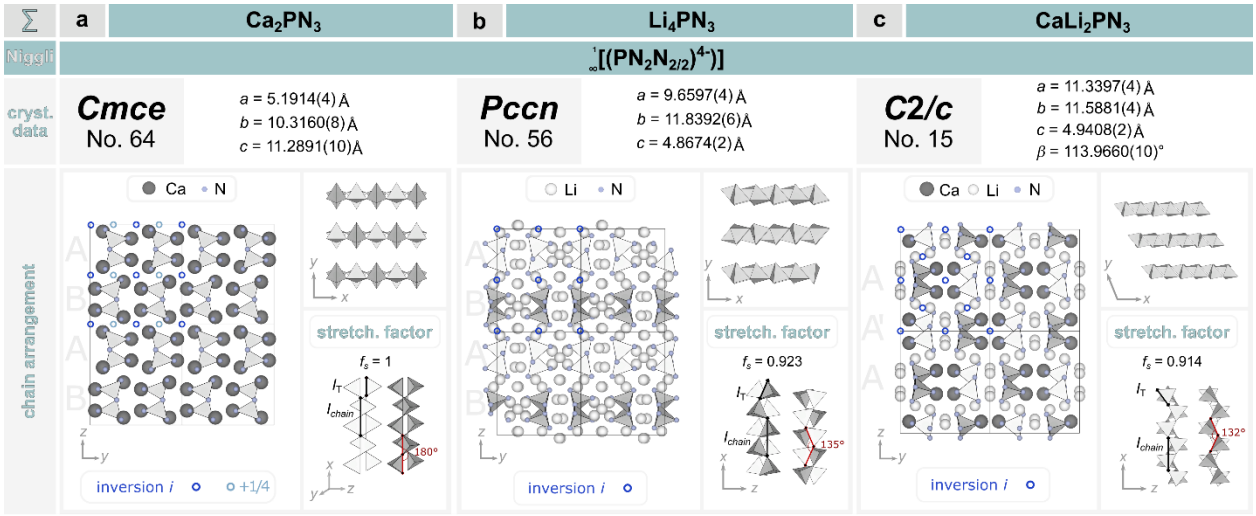

Figure 5.3. Structural Comparison of the chain-type nitridophosphates Ca_2PN_3 (a), Li_4PN_3 (b) and $CaLi_2PN_3$ (c) in terms of their chain arrangement and stretching factor. PN_4-tetrahedra chains in gray; saw-tooth arrangement into the plane (bright) and out of the plane (dark).

The chains can be classified into two groups: those whose sawtooth arrangement points into the plane (Figure 5.3, dark chains) and those whose arrangement leads out of the plane (Figure 5.3, bright chains). It is not possible to classify the chains of Ca_2PN_3 in this context due to the maximum elongation. Furthermore, a classification can be made with regard to the orientation of the terminal $N^{[1]}$ atoms. This results in different arrangement patterns, which can be classified into layer sequences along *z*: Ca_2PN_3: A-B-A; Li_4PN_3: A-B-A and $CaLi_2PN_3$: A-A'-A. In the case of $CaLi_2PN_3$ the following layer can be formed by translation of ½ in *y* direction. When all the above classification criteria are combined, a kind of checkerboard pattern emerges in the case of $CaLi_2PN_3$, which is absent in either of the other two compounds. This arrangement and alignment of the chains result in $CaLi_2PN_3$ exhibiting areas dominated by unbridged $N^{[1]}$ and areas dominated by bridged $N^{[2]}$ comparable to Li_4PN_3. The divalent Ca^{2+} ions are localized in the former and are coordinated in a distorted octahedral fashion by six nitrogen atoms (*CN* = 6, $d_{Ca–N}$ = 2.3468(12)–2.6367(11) Å; Figure 5.2c). The interatomic distances are slightly shorter compared to the distances described in the literature for Ca_2PN_3 ($d_{Ca–N}$ = 2.4331(13)–3.0074(11) Å), but on average these correspond to the sum of the respective Shannon radii.[12,40] However, to enable a more accurate comparison of the coordination polyhedral, minimum bounding ellipsoid analysis (MBE) was performed for both Ca_2PN_3 and $CaLi_2PN_3$.[41] The basis of MBE, the ellipsoidal approximation, enables the comparison of the distortion of different polyhedra, especially irregular ones based on the bonding distances. Consequently, the Ca^{2+} coordination polyhedra in Ca_2PN_3 can be described as distorted pentagonal bipyramids (*CN* = 7) and as distorted square pyramids (*CN* = 5). Therefore, the CaN_6 octahedra in $CaLi_2PN_3$ represent an average in *CN* of the two polyhedra of Ca_2PN_3 and are significantly less distorted (Figures S5.10&5.11, Tables S5.9&5.10). In combination with the reduced Ca^{2+} polyhedron volume, this could be a plausible explanation for the absence of luminescence behavior, as previously outlined in the synthesis section. The given possible dopant position is very small and therefore unfavorable for an occupation by Eu^{2+} ions.[42] The Ca^{2+} octahedra are connected to each other by common vertices and edges and share also edges and vertices with PN_4-tetrahedra. Three PN_4 tetrahedra-chains are connected to each other by one Ca^{2+} octahedron. A partial topological representation (Figure S5.12) also allows the arrangement of Ca^{2+} between the PN_4 tetrahedra-chains to be described as sawtooth-like (the shortest Ca–Ca distances ($d_{Ca–Ca}$ = 3.2291(5) Å) are connected as a blue line). Li^+ ions are coordinated by nitrogen with *CN* = 4 (Li1 and Li2) and 6 (Li3), as determined by MBE.[41] The resulting polyhedra share common corners and/or edges, resulting also in a sawtooth-like arrangement (Figure S5.13).

5.2.4 Density Functional Theory Calculations (DFT)

Given the unavailability of a phase-pure synthesis of the title compound and the consequent limitation of the experimental analysis, we have decided to conduct periodic DFT calculations.[43–45] The calculated band structures (Figure 5.4) and densities of states (DOS, Figure S5.14)) indicate that $CaLi_2PN_3$ is an electronically wide band gap semiconductor. The theoretical indirect band gap is estimated to be 3.35 eV, which is comparable to that of ZnO (direct band gap: 3.37 eV) and GaN (direct band gap: 3.40 eV).[46,47] The indirect transition between valence band (between V and Γ point) and the conduction band minimum (at V point) is shown (green arrow). Near the Fermi level (shifted to 0 eV), the contributions primarily originate from 2p states of N.

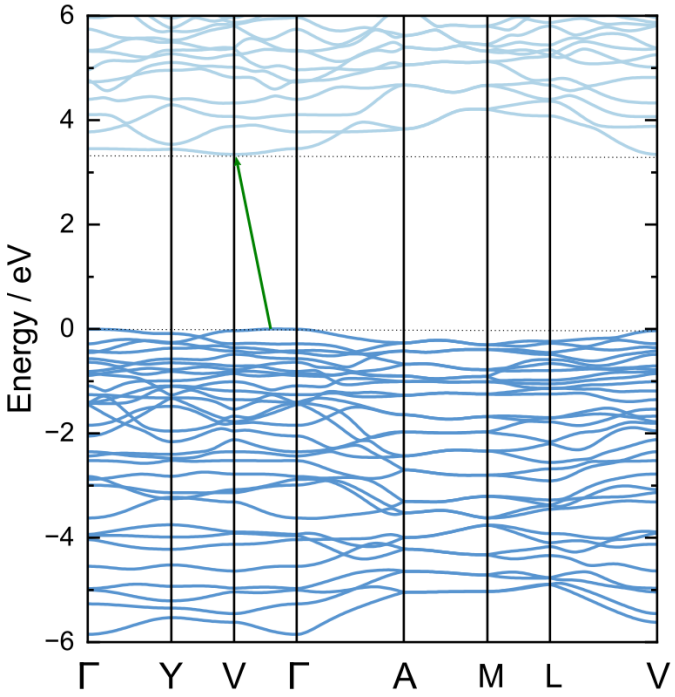

Figure 5.4. Calculated band structure of $CaLi_2PN_3$. Green arrow indicates the indirect transition (indirect band gap).

On the other hand, the total DOS in the conduction band is almost exclusively dominated by the contribution of Ca (3d), whereas the contributions of P and N are negligible.

In addition to the electronic properties, the stability of $CaLi_2PN_3$ was investigated by calculating the formation energy E_{form} from the total energies E_{tot} of the constituent compounds Li_4PN_3 and Ca_2PN_3 according to equation (5.4):

$$\Delta_f E = E_{tot}(CaLi_2PN_3) - E_{tot}(Li_4PN_3) - E_{tot}(Ca_2PN_3) \quad (5.4)$$

These calculations show that the formation of $CaLi_2PN_3$ results in an energy gain relative to the two starting nitridophosphates. This is evident by the formation energy per formula unit

$\Delta_f E$ = 13.75 eV (Table S5.11). A potential explanation for the notable enhancement in stability relative to the compounds Li_4PN_3 and Ca_2PN_3 is the less distorted Ca^{2+} coordination environment accompanied by the previously described significantly shorter bond distances, as well as the less distorted Li positions, analyzed by MBE.

5.3 Conclusion

In this contribution, we report on the successful preparation of the first quaternary lithium alkaline metal earth nitridophosphate, $CaLi_2PN_3$, via MP/HT synthesis. The azide route established for nitridophosphate synthesis and a for nitridophosphate synthesis novel double salt approach were employed to prepare the title compound with different phase content. Single-crystals suitable for structure elucidation allowed the crystal structure to be determined from single-crystal X-ray diffraction data. The elemental ratio determined by EDX analysis on selected crystallites is consistent with the proposed structure model. Solid-state MAS NMR analysis and low-cost crystallographic calculations support the obtained results. The crystal structure can be described as a novel cation-filling variant of $GePN_3$, which crystallizes in the $CoGeO_3$ structure type. In terms of structural chemistry, it can be regarded as a combination of the low-pressure compound Ca_2PN_3 and the high-pressure compound Li_4PN_3. This is experimentally supported by the aforementioned double salt synthesis. The experimental results were corroborated by quantum chemical calculations, which also revealed the electronic structure (indirect band gap ~3.35 eV). Furthermore, calculations were conducted to determine the formation energies of the title compound and the two separate nitridophosphates. These calculations support the plausibility of the proposed structural model and contribute to the understanding of the formation during synthesis. In summary, we were able to synthesize and structurally elucidate a novel quaternary nitridophosphate by comparing structural motifs and combine them in a novel compound by medium-pressure synthesis. The presented synthesis strategy offers considerable potential for further exploration of low-condensed nitridophosphates through the controlled combination and stabilization of pre-synthesized structural motifs (e.g. non-condensed $[PN_3]^{4-}$, $[PN_4]^{7-}$ or $[P_3N_9]^{12-}$ anions) under medium pressure conditions.

5.4 Experimental Part

5.4.1 Preparation of Starting Materials

Synthesis of $Ca(N_3)_2$: $Ca(N_3)_2$ was synthesized by an ion exchange reaction of $CaCO_3$ (Sigma Aldrich, 99.995%) with aqueous HN_3 according to Suhrmann et al.[48] The aqueous HN_3 was formed by passing an aqueous solution of NaN_3 (Acros Organics, 99%, extra pure) through a cation exchanger (Amberlyst 15). The solution was carefully dropped into an aqueous suspension of $CaCO_3$ until the eluate exhibited pH = 7. Residues of the carbonate was filtered and the solvent removed *in vacuo*. $Ca(N_3)_2$ was obtained as colorless crystals, which were investigated for phase-purity by powder X-ray diffraction.

Caution: HN_3 required special care when handling. Special care must also be taken with diluted solutions, as these are extremely explosive and produce vapors that are toxic if inhaled.

Synthesis of P_3N_5: Semi-crystalline P_3N_5 was prepared through ammonolysis reaction of P_4S_{10} (Sigma Aldrich, 99.99%) with pre-dried NH_3 (Air Liquide, 5.0) according Stock and Grüneberg.[49] For this purpose, a quartz boat was placed in a tube furnace and dried at 1000 °C under reduced pressure of 10^{-3} mbar. After a cooling down step, the quartz boat was loaded with approx. 7 g P_4S_{10} and the apparatus was saturated with NH_3 for 1 h and subsequently heated up to 850 °C with 10 K/min. The obtained P_3N_5 was analysed by PXRD and CHNS analysis.

Synthesis of $LiPN_2$: $LiPN_2$ was prepared according to a new synthesis protocol under medium-pressure/high-temperature conditions in a hot isostatic press (HIP, AlP6-30H, American Isostatic Presses, Inc., Columbus Ohio, USA). For this purpose, Li_3N (Rockwood Lithium, 94%) and P_{red} (Chempur, ≥ 99.999%) in a molar ratio 2 : 6 were ground together in Ar-filled glovebox (MBraun, < 1 ppm H_2O, < 1 ppm O_2). The reactants were filled in a tungsten crucible, closed by a lid and placed in the security crucible made of corundum. This assembly was closed with another lid and transferred into the pressure module of the HIP. The pressure was constantly increased up to 82 MPa. Subsequently the reaction temperature was increased up to 1200 °C, ending with the reaction pressure of 200 MPa. After maintaining these conditions for 10 h, the sample was allowed to cool down to 20 °C and the pressure was released. The product was obtained as colourless sinter cake. After washing with water and ethanol the product was analysed by PXRD.

Synthesis of Li_4PN_3: Li_4PN_3 was prepared using high-pressure/high-temperature conditions using a modified Walker-type multianvil press (Voggenreiter, Mainleus, Germany). For this purpose a new synthesis protocol using Li_3N (Rockwood Lithium, 94%), $LiPN_2$ and P_3N_5 in a molar ratio of 5.25 : 1 : 1 was developed. The reaction was carried out at a reaction pressure of 8 GPa and a reaction temperature of 1000 °C for 60 min. More details on multianvil synthesis can be found in the literature.[50] The obtained Li_4PN_3 was handled under inert-gas conditions and analysed by PXRD.

Synthesis of Ca_2PN_3: Ca_2PN_3 was prepared using medium-pressure/high-temperature conditions in a hot isostatic press (HIP, AlP6-30H, American Isostatic Presses, Inc., Columbus Ohio, USA). For this purpose, Ca_3N_2 (ABCR, 99%) and P_{red} (Chempur, ≥ 99.999%) in a molar ratio of 2 : 3 were reacted under a nitrogen atmosphere at 1200 °C and 150 MPa according to *Wendl* et al.[2] Ca_2PN_3 was obtained as colorless/light beige sinter cake, handled under inert-gas conditions and analysed by PXRD.

5.4.2 Preparation of $CaLi_2PN_3$

The title product was prepared under medium-pressure/high-temperature conditions in a hot isostatic press (HIP, AlP6-30H, American Isostatic Presses, Inc., Columbus Ohio, USA). For this purpose, the starting materials (in a molar ratio according Equations 1–3) were ground together in an Ar-filled glovebox (MBraun, < 1 ppm H_2O, < 1 ppm O_2). The reactants were filled in a tungsten crucible, closed by a lid and placed in the security crucible made of corundum. This assembly was closed with another lid and transferred into the pressure model of the HIP. The pressure was constantly increased up to 70 MPa. Subsequently the reaction temperature was increased up to 900 °C, ending with the reaction pressure of 200 MPa. After maintaining these conditions for 10 h, the sample was allowed to cool down to 20 °C and the pressure was released. The product was obtained as colourless crystals, which are sensitive against moisture and air.

5.4.3 Single-Crystal X-ray Diffraction (SCXRD)

SCXRD data were collected using combined φ- and ω-scans on a single-crystal of $CaLi_2PN_3$ on a D8 Venture TXS diffractometer (Bruker) with Mo-K_α radiation (λ = 0.71073 A). The data were indexed, integrated, and absorption-corrected using the multi-scan method. The space group was determined using the APEX3 software package.[51–53] The structure was solved using direct methods (SHELXT) and refined by full-matrix least square methods (SHELXL). [54,55] The results were visualized using VESTA software.[56]

5.4.4 Powder X-ray Diffraction (PXRD) and Rietveld Refinement

PXRD measurements were performed on pre-grounded samples of the bulk materials. These were pre-filled, compacted and sealed in glass capillaries (0.3 mm, Hilgenberg GmbH) under Ar atmosphere (Ar-filled glovebox; Unilab, MBraun, Garching, O_2 < 1 ppm, H_2O <1 ppm). Measurements were performed on a Stoe STADI P diffractometer with Cu-$K_{\alpha1}$ (λ = 1.5406 Å) radiation with Ge(111) monochromator and Mythen 1K detector in modified Debye-Scherrer geometry. Subsequently, each data set was used for Rietveld refinement using the software TOPAS.[57]

5.4.5 Scanning Electron Microscopy (SEM) with Energy-Dispersive X-ray Spectroscopy (EDX)

The morphology and chemical composition of the title compound were investigated using a Helios Nanolab G3 UC (FEI, Hillsboro) dual-beam scanning electron microscope with an X-Max 80 SDD EDX detector (Oxford Instruments, Abingdon). For this purpose, the analysis samples were fixed on pre-dried carbon adhesive pads and carbon coated.

5.4.6 Solid-State Magic Angle Spinning (MAS) NMR Spectrosopy

^{31}P, ^{1}H, $^{31}P\{^{1}H\}$, ^{6}Li and ^{7}Li NMR spectra were collected with a DSX AVANCE spectrometer (Bruker) with a magnetic field of 11.7 T. The samples were filled and compacted into a 2.5 mm rotor, which was mounted on a commercial MAS probe (Bruker). The sample was rotated at a rotation frequency of 20 kHz. The obtained data were analysed using ORIGIN Pro 2022b.

5.4.7 Quantum-Chemical Calculations (DFT)

Periodic density-functional theory (DFT) calculations were performed using the Vienna *ab initio* simulation package (VASP).[43-45] In VASP the core and valence electrons are separated using projector-augmented waves (PAW).[58,59] The exchange and correlation energy is calculated using the generalized gradient approximation (GGA), as described by Perdew, Burke and Ernzerhof (PBE).[60] For the structure optimization (RMM-DIIS), the Brillouin zone was sampled on Γ-centered *k*-point grids (4x4x7 for $Ca_2Li_4P_2N_6$, 7x7x3 for Ca_2PN_3 and 3x3x6 for Li_4PN_3) and the interpolation of the *k* space was done via tetrahedron method with Blöchl corrections. [61] Full ionic degrees of freedom, i.e. atomic positions, cell shape and cell volume were used. Both Hellmann-Feynmann forces and stress tensors were calculated. The energy convergence criterion was set to 10^{-6} eV and the residual atomic forces were relaxed until the convergence criterion of 10^{-5} eV/Å was reached. Successive static calculations were performed with a convergence criterion of 10^{-8} eV and a plane wave energy cutoff of 500 eV. The band structure was calculated for the Bloch vector k along the lines Γ (0,0,0) to Y (-0.5,0.5,0) to V (0,0.5,0) to Γ (0,0,0) to A (0,0,0.5) to M (-0.5,0.5,0.5) to L (0,0.5,0.5) and back to V (0,0.5,0). The energy zero is taken at the Fermi level.

5.5 Acknowledgements

The authors thank Dr. Lisa Gamperl and Amalina T. Buda for carrying out SEM-EDX measurements and Christian Minke for NMR measurements (all at Department of Chemistry at LMU Munich).

5.6 References

[1] S.J. Sedlmaier, E. Mugnaioli, O. Oeckler, U. Kolb, W. Schnick, *Chem. Eur. J.* **2011**, *17*, 11258.

[2] S. Wendl, S. Mardazad, P. Strobel, P.J. Schmidt, W. Schnick, *Angew. Chem. Int. Ed.* **2020**, *59*, 18240.

[3] M.-H. Fang, H.-P. Hsueh, T. Vasudevan, W.-T. Huang, Z. Bao, N. Majewska, S. Mahlik, H.-S. Sheuc, R.-S. Liu, *J. Mater. Chem. C*, **2021**, *9*, 8158.

[4] R.M. Pritzl, M.M. Pointner, K. Witthaut, P. Strobel, P.J. Schmidt, W. Schnick, *Angew. Chem. Int. Ed.* **2024**, *63*, e202403648.

[5] S.J. Ambach, M. Pointner, S. Falkai, C. Paulmann, O. Oeckler, W. Schnick, *Angew. Chem. Int. Ed.* **2023**, *62*, e202303580.

[6] S.J. Ambach, G. Krach, E. Bykova, K. Witthaut, N. Giordano, M. Bykov, W. Schnick, *Inorg. Chem.* **2024**, *63*, 8502.

[7] S.D. Kloß, W. Schnick, *Angew. Chem. Int. Ed.* **2019**, *58*, 7933.

[8] G. Krach, J. Steinadler, K. Witthaut, W. Schnick, *Angew. Chem. Int. Ed.* **2024**, e202404953.

[9] R.M. Pritzl, K. Witthaut, M. Dialer, A.T. Buda, V. Milman, L. Bayarjargal, B. Winkler, W. Schnick, *Angew. Chem. Int. Ed.* **2024**, e202405849.

[10] S. Wendl, L. Seidl, P. Schüler, W. Schnick, *Angew. Chem. Int. Ed.* **2020**, *59*, 23579.

[11] S. Horstmann, E. Irran, W. Schnick, *Z. Anorg. Allg. Chem.* **1998**, *624*, 620.

[12] V. Schultz-Coulon, W. Schnick, *Z. Anorg. Allg. Chem.* **1997**, *623*, 69.

[13] M. Mallmann, C. Maak, R. Niklaus, W. Schnick, *Chem. Eur. J.* **2018**, *24*, 13963.

[14] E.-M. Bertschler, R. Niklaus, W. Schnick, *Chem. Eur. J.* **2017**, *23*, 9592.

[15] M. Mallmann, S. Wendl, P. Strobel, P.J. Schmidt, W. Schnick, *Chem. Eur. J.* **2020**, *26*, 6257.

[16] S.J. Ambach, C. Somers, T. de Boer, L. Eisenburger, A. Moewes, W. Schnick, *Angew. Chem. Int. Ed.* **2023**, *62*, e202215393.

[17] F.J. Pucher, S.R. Römer, F.W. Karau, W. Schnick, *Chem. Eur. J.* **2010**, *16*, 7208.

[18] F.J. Pucher, F.W. Karau, J. Schmedt auf der Günne, W. Schnick, *Eur. J. Inorg. Chem.* **2016**, 1497.

[19] F.J. Pucher, A. Marchuk, P.J. Schmidt, D. Wiechert, W. Schnick, *Chem. Eur. J.* **2015**, *21*, 6443.

[20] S.D. Kloß, O. Janka, T. Block, R. Pöttgen, R. Glaum, W. Schnick, *Angew. Chem. Int. Ed.* **2019**, *58*, 4685.

[21] S. Wendl, L. Eisenburger, P. Strobel, D. Günther, J.P. Wright, P.J. Schmidt, O. Oeckler, W. Schnick, *Chem. Eur. J.* **2020**, *26*, 7292.

[22] W. Schnick, J. Luecke, *J. Solid State Chem.* **1990**, *87*, 101.

[23] The term *zweier* has been established by Liebau deriving from the German word of the numeral two (zwei (2)) by adding the suffix "er", describing the repeating structural units of tetrahedra. F. Liebau, Structural Chemistry of Silicates: Structure, Bonding, and Classification, Springer, Heidelberg, **1985**, p. 58.

[24] E.-M. Bertschler, C. Dietrich, T. Leichtweiß, J. Janek, W. Schnick, *Chem. Eur. J.* **2018**, *24*, 196.

[25] W. Schnick, U. Berger, *Angew. Chem. Int. Engl*. **1991**, *30*, 830.

[26] W. Schnick, J. Lücke, *Z. Anorg. Allg. Chem.* **1990**, *588*, 19.

[27] Deposition Number 2365190 (for $CaLi_2PN_3$]) contain the supplementary crystallographic data for this paper. These data are provided free of charge by the joint Cambridge Crystallographic Data Centre and Fachinformationszentrum Karlsruhe Access Structures service.

[28] S. Schneider, S. Kreiner, L.G. Balzat, B.V. Lotsch, W. Schnick, *Chem. Eur. J.* **2023**, *29*, e202301986.

[29] E.-M. Bertschler, R. Niklaus, W. Schnick, *Chem. Eur. J.* **2018**, *24*, 736.

[30] R.M. Pritzl, N. Prinz, P. Strobel, P.J. Schmidt, D. Johrendt, W. Schnick, *Chem. Eur. J.* **2023**, *29*, e202301218.

[31] I.D. Brown, *Chem. Rev.* **2009**, *109*, 6858.

[32] A. Altomare, C. Cuocci, C. Giacovazzo, A. Moliterni, R. Rizzi, N. Corriero, A. Falcicchio, *J. Appl. Crystallogr.* **2013**, *46*, 1231.

[33] M. Nespolo, B. Guillot, *J. Appl. Crystallogr.* **2016**, *49*, 317.

[34] J. Lima-de-Faria, E. Hellner, F. Liebau, E. Makovicky, E. Parthe, *Acta Crystallogr.* **1990**, *A46*, 1.

[35] D.R. Peacor, *Z. Kristallogr. Cryst. Mater.* **1968**, *126*, 299.

[36] S.J. Sedlmaier, M. Eberspächer, W. Schnick, *Z. Anorg. Allg. Chem.* **2011**, *637*, 362.

[37] S. Vogel, A.T. Buda, W. Schnick, *Angew. Chem. Int. Ed.* **2018**, *57*, 13202.

[38] S.D. Kloß, W. Schnick, *Inorg. Chem.* **2018**, *57*, 4189.

[39] E.-M. Bertschler, C. Dietrich, J. Janek, W. Schnick, *Chem. Eur. J.* **2017**, *23*, 2185.

[40] R. D. Shannon, *Acta Crystallogr. Sect. A*, **1976**, *32*, 751.

[41] J. Cumby, J. P. Attfield, *Nat. Commun.* **2017**, *8*, 14235.

[42] M.-H. Fang, C. O. M. Mariano, P.-Y. Chen, S.-F. Hu, R.-S. Liu, *Chem. Mater*. **2020**, *32*, 1748.

[43] G. Kresse, J. Furthmüller, *Comput. Mat. Sci.* **1996**, *6*, 15.

[44] G. Kresse, J. Furthmuller, *Phys. Rev. B*, **1996**, *54*, 11169.

[45] G. Kresse, J. Hafner, *Phys. Rev. B*, **1993**, *47*, 558.

[46] K. Osamura, K. Nakajima, Y. Murakami, P. H. Shingu, A. Ohtsuki, *Solid State Commun.* **1972**, *11*, 617.

[47] S.T. Tan, B.J. Chen, X.W. Sun, W.J. Fan, H.S. Kwok, X.H. Zhang, S.J. Chua, *J. Appl. Phys.* **2005**, *98*, 013505.

[48] R. Suhrmann, K. Clusius, *Z. Anorg. Allg. Chem.* **1926**, *152*, 52.

[49] A. Stock, H. Grüneberg, *Ber. Dtsch. Chem. Ges.* **1907**, *40*, 2573.

[50] H. Huppertz, *Z. Kristallogr. Cryst. Mater.* **2004**, *219*, 330.

[51] Bruker-AXS, APEX3, Vers. 2016.5-0, Karlsruhe (Germany), **2016**.

[52] Bruker-AXS, XPREP Reciprocal Space Exploration, Vers. 6.12, Karlsruhe (Germany), **2001**.

[53] SAINT, Data Integration Software, Madison, Wisconsin (USA), **1997**.

[54] G. M. Sheldrick, *Acta Crystallogr. Sect. C*, **2015**, *71*, 3.

[55] G. M. Sheldrick, SHELXS-97 Program of the Solution of Crystal Structure, University of Göttingen, Göttingen, **1997**.

[56] K. Momma, F. Izumi, *J. Appl. Crystallogr*. **2011**, *44*, 1272.

[57] A. A. Coelho, TOPAS-Academic v4.1, Brisbane, **2007**.

[58] P. E. Blochl, *Phys. Rev. B*, **1994**, *50*, 17953.

[59] G. Kresse, D. Joubert, *Phys. Rev. B*, **1999**, *59*, 1758.

[60] J. P. Perdew, K. Burke, M. Ernzerhof, *Phys. Rev. Lett.* **1996**, *77*, 3865.

[61] P. Pulay, *Chem. Phys. Lett.* **1980**, *73*, 393.

6 Adamantane-Type Nitridophosphate Phosphors $AE_xLi_{10-2x}P_4N_{10}:Eu^{2+}$ via Medium-Pressure Ion-Exchange Reactions

Submitted to: *Angew. Chem. Int. Ed.* **2024***; Angew. Chem.* **2024**.

Authors: Reinhard M. Pritzl, Amalina T. Buda, K. Witthaut, Peter J. Schmidt and Wolfgang Schnick

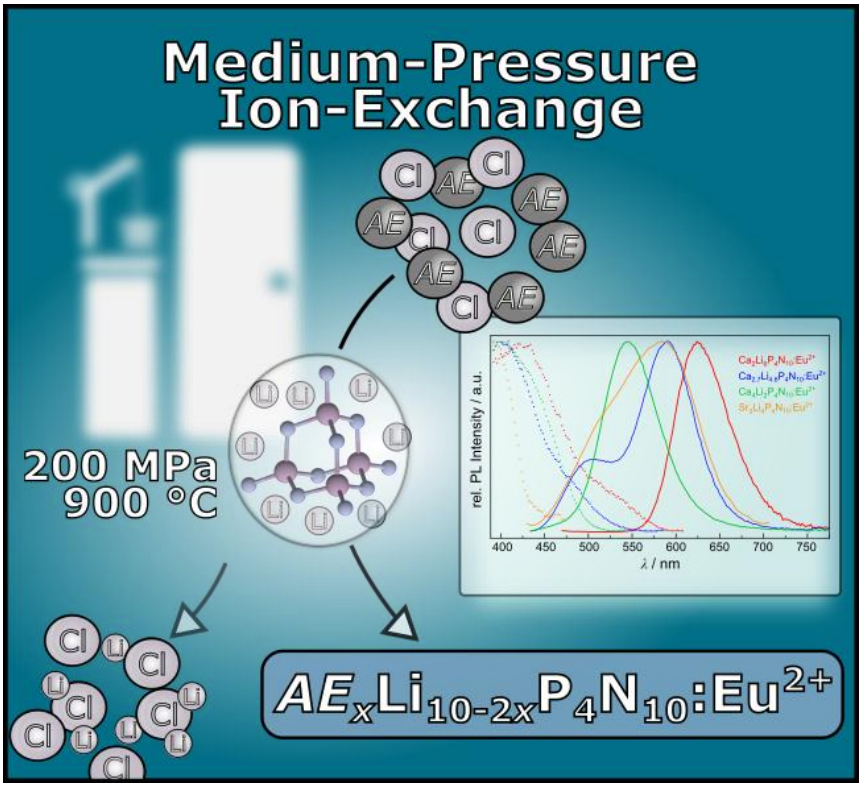

Abstract. Nitridophosphates have emerged as promising host compounds in the field of solid-state lighting. Their industrial relevance has increased significantly, mainly due to recent advances in synthetic approaches under medium-pressure (MP) conditions, including ammonothermal synthesis and hot isostatic pressing (HIP). In this study, we report on the synthesis and characterization of the quaternary representatives $Ca_xLi_{10-2x}P_4N_{10}$ (x = 2, 2.7, 4) and $Sr_3Li_4P_4N_{10}$, prepared via a simplified ion exchange reaction under MP conditions, starting from the nitridophosphate-based lithium ion conductor $Li_{10}P_4N_{10}$. The synthesis route allowed for the

preservation of the anionic $[P_4N_{10}]^{10-}$ structural motif of the starting material, while simultaneously introducing potential doping sites for Eu^{2+} by incorporating divalent alkaline earth cations (Ca^{2+}/Sr^{2+}). Upon excitation of Eu^{2+} doped samples with blue light, strong luminescence due to parity-allowed $4f^6(^7F)5d^1 \rightarrow 4f^7(^8S_{7/2})$ transition can be observed in the red ($Ca_2Li_6P_4N_{10}:Eu^{2+}$: λ_{max} = 626 nm), yellow/orange ($Ca_{2.7}Li_{4.6}P_4N_{10}:Eu^{2+}$: λ_{max1} = 506 nm, λ_{max2} = 592 nm and $Sr_3Li_4P_4N_{10}:Eu^{2+}$: λ_{max} = 596 nm) and green ($Ca_4Li_2P_4N_{10}:Eu^{2+}$: λ_{max} = 546 nm) spectral regions of the visible light. The compounds presented, together with the simplified synthetic approach, demonstrate the significant potential of ion exchange on Li ion conductors for the development of novel nitridophosphates in the future.

6.1 Introduction

Phosphor-converted light-emitting diodes (pc-LEDs) have revolutionized the global lighting market with increased longevity, color rendering and enormous energy savings. In order to improve the quality of pc-LEDs in a variety of applications, the quest is to either modify existing solid-state lighting (*SSL*) phosphor systems or identify and develop novel host materials.[1-3] In the past few years, nitridophosphates have received considerable attention in this context. In addition to the great potential for the discovery of unprecedented structures and associated host lattices, they often exhibit a number of beneficial properties.[4-6] These include high thermal and chemical stability, as well as promising optical properties like large band gaps, often observed in many Eu^{2+} doped representatives.[7-11] Nevertheless, nitridophosphate synthesis has always been challenging. The most commonly used nitridic starting material P_3N_5 thermally decomposes above 850 °C at ambient pressure.[12] An established synthesis strategy is to apply high-pressures (multianvil or diamond anvil technique) during reaction, to prevent decomposition and elimination of molecular N_2.[13,14] In recent years, both previously known and completely novel nitridophosphate compounds have been successfully synthesized under medium-pressure (MP) conditions. This has demonstrated that the pressure range typically applied under HP/HT conditions may often exceed the actual synthesis pressure required for nitridophosphate synthesis. Especially lowly condensed P/N representatives ($\kappa < ½$; degree of condensation κ = atomic ratio of tetrahedra centers to tetrahedra vertices) seem to be synthesizable under these reaction conditions. This can be achieved through either direct synthesis or ion exchange reactions on pre-synthesized P/N precursors.[15,16] Examples of this include the syntheses of $Ba_3[PN_3]O$ with isolated $[PN_3]^{4-}$ anions, and the *catena*-type nitridophosphates Ca_2PN_3, $CaLi_2PN_3$ and Mg_2PN_3.

These were successfully synthesized by bottom-up (direct synthesis), top-down (double salt synthesis), or ion exchange reactions in a hot isostatic press (HIP; $p_{max} \leq 200$ MPa).[6,9,16-18] An alternative synthesis method that provides sufficient pressure for stabilization is the ammonothermal approach ($p_{max} \leq 200$ MPa).[19,20] This method has been employed to prepare Ba_2PO_3N ($\kappa = 1/4$) and $Sr_3P_3N_7$ ($\kappa = 1/3$), as well as (oxo)nitridophosphates with non-condensed P/N substructures.[21,22] A review of the literature indicates that numerous other lowly condensed nitridophosphates have been successfully synthesized via this method.[23] In particular, representatives with adamantane-like T2 supertetrahedra substructures ($[P_4N_{10}]$) have been observed increasingly. In addition to the ternary nitridophosphates α-/β-$Li_{10}P_4N_{10}$, imidonitridophosphates with this subunit are particularly accessible through this method.[23-25] Following the recent discovery of $Ba_4P_4N_8(NH_2):Eu^{2+}$, an imidonitridophosphate with T2 supertetrahedra building blocks with promising luminescent properties, the focus was placed on the discovery and characterization of additional novel nitridophosphates built up of this structural unit.[26,27] To achieve enhanced luminescence properties, particularly with respect to reducing the thermal quenching behavior, it is beneficial to develop host structures that exhibit minimal or no N–H functionality.[28] A promising synthesis strategy is to begin with pre-synthesized, imide-free adamantane-type nitridophosphates and to preserve their structural motif under hydrogen-free synthesis conditions.[16,18] In this study, both are subjected by ion exchange reaction of the Li^+ ionic conductor $Li_{10}P_4N_{10}$ under medium pressure (MP) conditions using a hot isostatic press (HIP), thereby creating suitable activator sites (luminescence centers). We report on the simplified synthesis approach of the quaternary nitridophosphates $Ca_xLi_{10-2x}P_4N_{10}:Eu^{2+}$ (x = 2, 2.7, 4) and $Sr_3Li_4P_4N_{10}:Eu^{2+}$. Their crystal structures were elucidated by X-ray diffraction data and corroborated by solid-state MAS NMR experiments, SEM-EDX analyses on individual particles and ICP-OES measurements on the bulk materials. The optical properties were investigated using diffuse reflectance spectroscopy on non-doped samples. The identified optical band gaps were compared with the theoretical band gaps calculated using density-functional theory (DFT) calculations. This study also explored the luminescence behavior of Eu^{2+}-doped samples of all title compounds under UV to blue light excitation. Given the promising luminescence characteristics for potential applications, $Ca_2Li_6P_4N_{10}:Eu^{2+}$ was subjected to a more detailed examination. In summary, this work proposes an effective strategy for the synthesis of novel nitridophosphate phosphors by ion-exchange reaction on pre-synthesized nitridophosphate Li ion-conductors. This approach enables large-scale production in the medium-pressure regime and offers insights into their further development. Furthermore, a Eu^{2+} doped example from the

compound series was applied in pc-LEDs to demonstrate that highly efficient phosphors are a viable outcome of this promising strategy.

6.2 Results and Discussion

6.2.1 Synthesis

The title compounds $AE_xLi_{10-2x}P_4N_{10}:Eu^{2+}$ (x (Ca) = 2, 2.7, 4; x (Sr) = 3), have been initially observed in heterogeneous products obtained by an ion-exchange reaction of the Li^+ ion conductor $Li_{10}P_4N_{10}$ with $CaCl_2$ (respectively $SrCl_2$), together with small amounts of $EuCl_2$. The pre-mortared reactant mixture was hot isostatically pressed at 200 MPa and 900 °C for 10 h. More detailed information on the MP synthesis is given in the Supporting Information.

$$x\,AECl_2 + Li_{10}P_4N_{10} \rightarrow AE_xLi_{10-2x}P_4N_{10} + 2x\,LiCl \qquad (6.1)$$

(*AE* = Ca, Sr; x(Ca) = 2, 2.7, 4; x(Sr) = 3)

Bulk samples of all title compounds were obtained after synthesis optimization (defined stoichiometric weight x according to Equation 6.1) based on the results of X-ray diffraction data (SCXRD/PXRD) and elemental analysis (energy dispersive X-ray spectroscopy (SEM-EDX) and inductively coupled plasma (ICP-OES).[29] For purification, the colorless sinter-cakes were washed with dry ethanol to remove the formed LiCl by-product and potentially unknown minor side phases. The obtained products hydrolyze within few hours on exposure to moisture and ambient air atmosphere. For investigations of the luminescence behavior, the title compounds were prepared with a nominal Eu^{2+} concentration of approx. 1 mol% with respect to the *AE* concentration.

6.2.2 Structure Elucidation

The crystal structures of $Ca_xLi_{10-2x}P_4N_{10}:Eu^{2+}$ (x = 2, 2.7, 4) and $Sr_3Li_4P_4N_{10}:Eu^{2+}$ were determined by single-crystal X-ray diffraction, applying direct methods and confirmed by Rietveld refinements on powder diffraction data. While $Ca_2Li_6P_4N_{10}$ crystallizes in tetragonal space group $I\bar{4}2d$ (no. 122) with a = 9.8906(2), c = 9.5917(2) Å and Z = 4, $Ca_4Li_2P_4N_{10}$ crystallizes in *Pnma* (no. 62) with a = 8.4439(4), b = 10.5549(6) and c = 10.4130(7) Å and Z = 4.

$Ca_{2.7}Li_{4.6}P_4N_{10}$ (a = 7.6074(3), b = 8.0676(3) , c = 8.4435(3) Å and α = 101.582(1), β = 93.937(2), γ = 113.888(2)° and Z = 2) and $Sr_3Li_4P_4N_{10}$ (a = 7.6338(5), b = 7.8369(6) and c = 8.5239(6) Å and α = 106.076(3), β = 92.775(3), and γ = 94.078(3)° and Z = 2) crystallizes both in triclinic space group $P\overline{1}$ (no. 2). All *AE*, P and N positions were determined during structure solution, Li positions were localized during structure refinement from difference Fourier maps. Further crystallographic data (Wyckoff positions, atomic positions, isotropic and anisotropic displacement parameters as well as interatomic distances and angles) are given in Tables S6.1–6.15 (Supporting Information).[30] Nevertheless, Rietveld refinements based on powder X-ray data corroborate the structure models obtained from single-crystal data in bulk (Figure 6.1, Tables S6.16–6.20). To further confirm the crystal structure models, ^{31}P, ^{7}Li and ^{1}H solid-state MAS NMR spectroscopy experiments were performed (see Supporting Information, Figure S6.1). The ^{1}H NMR experiments indicate the presence of small amounts of hydrogen in all samples. However, the signal strength and width do not allow any conclusions to be drawn about hydrogen (or only negligible amounts) in the title compounds and are consistent with the surface hydrolysis mentioned above. The findings of the FTIR investigations are in alignment with the aforementioned results. (Figure S6.2). The ^{31}P spectra show in each case one main signal (in the case of $Ca_{2.7}Li_{4.6}P_4N_{10}$ two maxima can be suspected), with chemical shifts of δ_{iso} = 6.1–10.7 ppm. In comparison to the starting compound α-$Li_{10}P_4N_{10}$ (δ_{iso} = 12.7 ppm), the chemical shifts are observed to be upfield shifted.[15] As expected for the one crystallographic P site in $Ca_2Li_6P_4N_{10}$ (highest crystal symmetry) the signal width (*fwhm* = 1.8 ppm) is narrower than for the other compounds. Conversely, the very broad ^{31}P signals (*fwhm* = 16.3, 19.8 and 28.3 ppm) in the spectra of the compounds with x = 2.7, 3 and 4, indicates the superposition of several P signals, which is in accordance with several P sites in the structure models obtained from SCXRD data. Furthermore, this could indicate that the Li atoms in the second coordination sphere do not necessarily require 100% occupation. This would result in a notable enlargement of the potential local environments of the P atoms, consequently leading to a broadening of the ^{31}P MAS signal.[31] However, due to the small chemical shift differences, the ^{7}Li NMR studies carried out do not allow any structural conclusions to be drawn and can only be used as evidence for Li within the compounds (Figure S6.1). In order to determine the elemental composition of the title compounds, energy-dispersive X-ray spectroscopy (EDX) measurements were performed on selected crystallites. In all measurements, only Ca or Sr, P, N and O were detected. The relative atomic ratios of the heavy elements (*AE*/P) correlate with the expected ratios obtained from the crystal structure models (Figure S6.3, Tables S6.21–S6.24). However, the element Li could not be reliably detected or quantified by EDX measurements. The detected oxygen can be attributed to

surface hydrolysis, resulting from the mandatory washing step with dry ethanol and the contact with air during preparation for the SEM measurements. The Li contents were determined using inductively coupled plasma spectroscopy (ICP-OES). The measured relative *AE* : Li : P ratios are in good agreement with the expected values. However, discrepancies in the absolute contents were observed, likely due to the susceptibility of the samples to hydrolysis (Table S6.25).

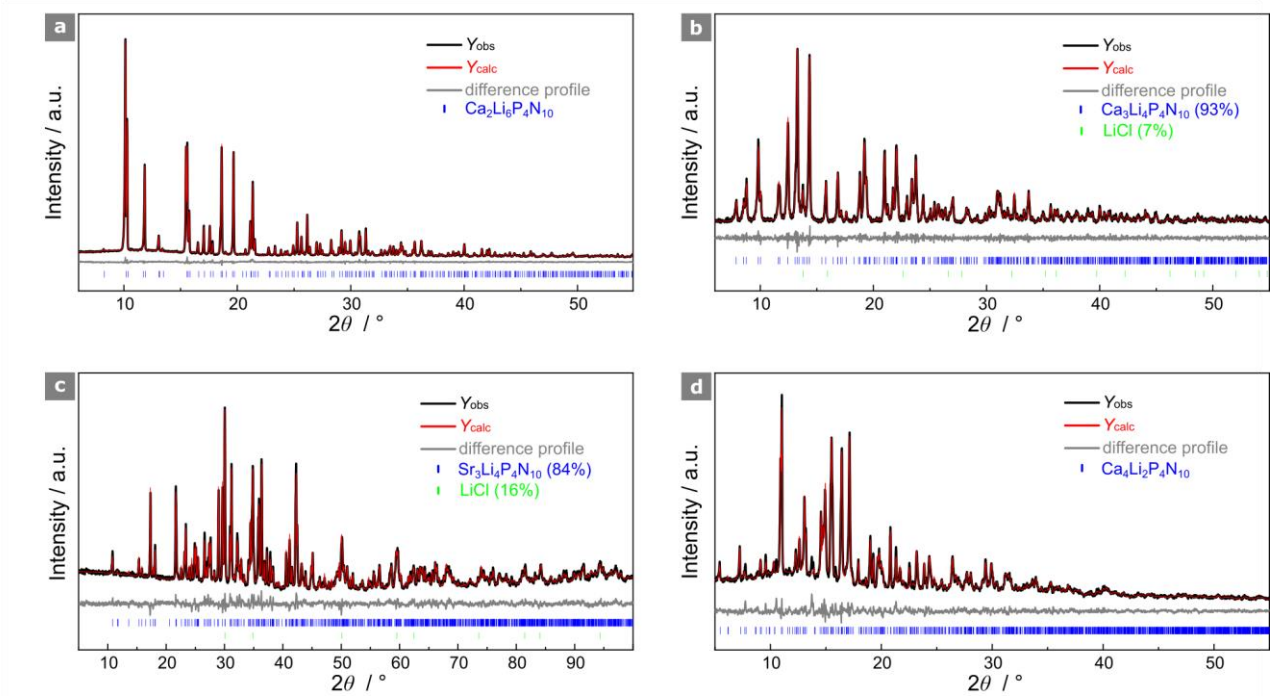

Figure 6.1. Rietveld refinements of a) $Ca_2Li_6P_4N_{10}$, b) $Ca_{2.7}Li_{4.6}P_4N_{10}$, c) $Ca_4Li_2P_4N_{10}$, and d) $Sr_3Li_4P_4N_{10}$. Observed (black line, and calculated X-ray diffraction patter (red line) with the difference curve (gray line). Vertical bars indicate the positions of the Bragg reflections of the corresponding title compound (blue) and LiCl (green). In c) $Ca_4Li_2P_4N_{10}$ a small amount of an unknown minor phase is present, as indicated in the difference plot.

6.2.3. Crystal Structure Description

As anticipated for the presented ion-exchange reactions, all title compounds are built up of isolated adamantane-type T2 super-tetrahedra anions $[P_4N_{10}]^{10-}$, which serve as the fundamental building units *FBU*s (Figure 6.2a, left). These units exhibit a degree of condensation of $\kappa = n(P)/\ n(N) = 0.4$, as expected. Principally, the arrangement of the T2 supertetrahedra is similar to the situation in α-$Li_{10}P_4N_{10}$, where two different orientations A and B occur. Orientations A and B face each other with their triangular surfaces and are rotated by ~60° (Figure 6.2a, right).[32] They differ slightly in terms of offset and the distance between the T2 units, which is due to the diversified content of the cations with different formal charges (AE^{2+}/Li^+; Figure 6.2b). To

simplify the representation of the packing of the T2 supertetrahedra, these are formed by linking only the terminal N's of the $[P_4N_{10}]^{10-}$ anions. The greatest difference in the T2 arrangement of the title compounds can be observed in the comparison between the compounds with highest and lowest Ca content ($Ca_4Li_2P_4N_{10}$ and $Ca_2Li_6P_4N_{10}$). For purposes of clarity, additional directions for the respective title compounds are provided in the Supplementary Information (Figure S4). The observed P–N distances are comparable to those of other adamantane-type nitridophosphates (α-/β-$Li_{10}P_4N_{10}$ and $Ba_4P_4N_8(NH)_2$) as well as other less condensed lithium and alkaline earth nitridophosphates (e.g. $Li_{12}P_3N_9$, $Li_{18}P_6N_{18}$, $Sr_3P_3N_7$, and $CaLi_2PN_3$), with the distances to the terminal N atoms generally shorter than those to the bridging N atoms.[15,18,22,26,32-34]

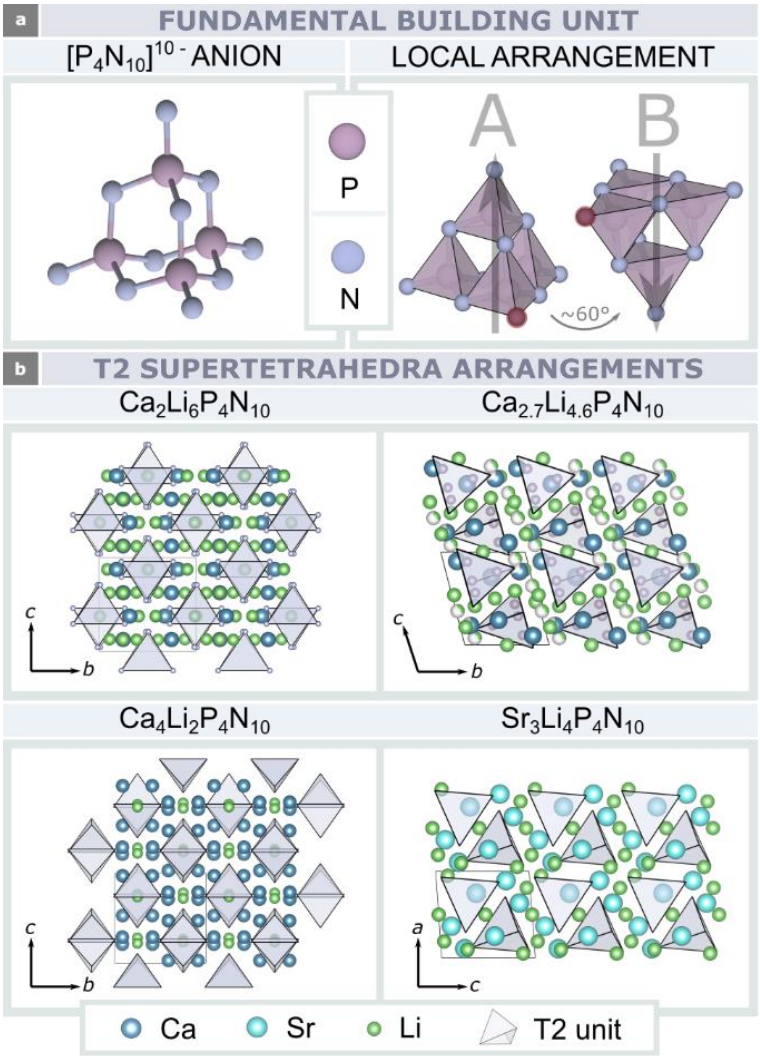

Figure 6.2. a) Adamantane-like $[P_4N_{10}]^{10-}$ fundamental building unit (*FBU*); left: ball-and-stick representation of the *FBU* (P atoms: purple, N atoms: gray); right: local arrangement of the *FBU* with PN_4 tetrahedra (purple) in two different orientations (A and B); one N atom has been colored red for reasons of clarity. b) Representation of supercells ($Ca_2Li_6P_4N_{10}$: 2×2, $Ca_{2.7}Li_{4.6}P_4N_{10}$: 3×2, $Ca_4Li_2P_4N_{10}$: 2×2, $Sr_3Li_4P_4N_{10}$: 3×2).

The T2 supertetrahedra are encased in a matrix of *AE* and Li ions, which are exclusively coordinated by N atoms. Figure 6.2b illustrates the localization of cations between the T2 supertetrahedra and the resulting alteration in the arrangement of the *FBU*s, with elementary cells depicted for reference. For this purpose, viewing directions were chosen, in which the T2 supertetrahedra are periodically arranged with regard to their inclination and orientation. The resulting *AE* coordination spheres can be described as distorted polyhedra with coordination numbers *CN* = 6–9. The *AE*–N distances of all compounds are approximately the sums of the respective Shannon radii (ionic radii Ca^{2+} = 1.06–1.18 Å; Sr^{2+} = 1.21–1.36 Å; N^{3-} = 1.46 Å).[35] These distances are comparable to those of other nitridophosphate compounds (Ca_2PN_3 : $d_{Ca–N}$ = 2.52–2.66 Å, CaP_2N_4 : $d_{Ca–N}$ = 2.51–2.73 Å, CaP_8N_{14} : $d_{Ca–N}$ = 2.53–2.56 Å, $Sr_3P_3N_7$: $d_{Sr–N}$ = 2.77–2.89 Å).[22,36,37] All specific *AE*–N distances can be found in the Supporting Information (Tables S6.8–6.11). Since the different coordination spheres of the *AE* ions are necessary to understand the observed luminescence, these are presented and discussed in more detail in this section. The Li atoms form partially distorted polyhedra with *CN* = 3–6, exhibiting interatomic Li–N distances ($d_{Li–N}$ = 1.94–2.59 Å) which are approximately the sum of the ionic radii according to Shannon.[35] Larger distances correspond to higher *CN* (ionic radii Li^+ = 0.59–0.92 Å, N^{3-} = 1.46 Å).

6.2.4. Density Functional Theory Calculations (DFT) and UV/Vis Reflectance Spectroscopy for Band Gap Estimation

The electronic structures of the title compounds were investigated by quantum chemical calculations at the DFT-PBE0 level. As illustrated in Figure S6.5, the electronic band structures reveal band gaps for all the title compounds, with only minor energy differences between direct and indirect transitions for the compounds with *AE* = Ca, while $Sr_3Li_4P_4N_{10}$ shows an indirect transition. The band gap energies amount to 4.1 eV ($Ca_2Li_6P_4N_{10}$), 4.2 eV ($Ca_{2.7}Li_{4.6}P_4N_{10}$), 4.0 eV ($Ca_4Li_2P_4N_{10}$) and 4.0 eV ($Sr_3Li_4P_4N_{10}$), which agrees with the transparent and colorless bulk samples and are in the order of magnitude of established nitride phosphors such as $Sr[LiAl_3N_4]$ (SLA: 4.14 eV).[38] Nevertheless quantum chemical calculations tend to underestimate band gaps. Therefore, the optical band gaps were determined by diffuse reflectance UV/Vis measurements on non-doped samples of all title compounds. For this purpose, the measured reflectance spectra *R* were transformed into pseudo-absorption spectra using the Kubelka-Munk function $F(R) = (1-R)^2/2R$. By plotting $h\nu$ versus $(F(R)h\nu)^{1/n}$ (Tauc plot), the optical band gaps can be determined by a linear regression fit (tangent) on the inflection points.[39]

The estimated optical bandgaps can be determined at the intersection of the tangent with the *x*-axis. For all calculations, the Kubelka-Munk exponent $n = ½$ was selected, indicating direct allowed transitions (even in the case of $Sr_3Li_4P_4N_{10}$, as otherwise inconsistent results are obtained).[40] Nevertheless, this is in line with the small energetic differences between direct and indirect transitions from the theoretical calculations. All Tauc plots with respective tangents are illustrated in Figure 6.3a. The optical band gap for $Ca_2Li_6P_4N_{10}$ amounts to 5.4 eV, 5.6 eV for $Ca_{2.7}Li_{4.6}P_4N_{10}$, 5.3 eV for $Ca_4Li_2P_4N_{10}$, and 4.6 eV for $Sr_3Li_4P_4N_{10}$. In the case of $Ca_4Li_2P_4N_{10}$ a second plateau at 4.5–5.2 eV is observable, which we attribute to the present minor side phases, since the phase-pure preparation of a non-doped sample was not possible in this case. Nevertheless, the relative differences between the calculated and optical band gaps of all Ca compounds show good agreement, reinforcing this assumption. Moreover, the determined band gaps (both electronic and optical) are well-suited for doping, as they fulfill the required criteria for the use in pc-LED applications, specifically band gaps ≥ 4 eV.[41]

6.2.5. Luminescence Properties

To investigate the luminescence properties of Eu^{2+}-doped samples (nominal Eu^{2+} concentration of ~1 mol% with respect to AE^{2+} content) room temperature photoluminescence (*PL*) and photoluminescence excitation spectra (*PLE*) were recorded for individual particles of $Ca_2Li_6P_4N_{10}:Eu^{2+}$, $Ca_{2.7}Li_{4.6}P_4N_{10}:Eu^{2+}$, $Sr_3Li_4P_4N_{10}:Eu^{2+}$ and $Ca_4Li_2P_4N_{10}:Eu^{2+}$. The corresponding spectra are depicted in Figure 6.3b. Upon excitation with UV to blue light, all samples show strong emission in the red ($Ca_2Li_6P_4N_{10}:Eu^{2+}$: λ_{max} = 626 nm, *fwhm* = 73 nm / 1854 cm^{-1}), orange ($Sr_3Li_4P_4N_{10}:Eu^{2+}$: λ_{max} = 596 nm, *fwhm* = 122 nm / 3812 cm^{-1}), yellow ($Ca_{2.7}Li_{4.6}P_4N_{10}:Eu^{2+}$: $\lambda_{max,1}$ = 508 nm, $fwhm_1$ = 82 nm / 3146 cm^{-1}, $\lambda_{max,2}$ = 592 nm, $fwhm_2$ = 68 nm / 1922 cm^{-1}) or green ($Ca_4Li_2P_4N_{10}:Eu^{2+}$: λ_{max} = 546 nm, *fwhm* = 74 nm / 2466 cm^{-1}) spectral region. Based on the ionic radii and charge, it can be assumed that Eu^{2+} generally prefers to occupy the AE^{2+} positions. This preference arises because the Li^+ and P^{5+} sites are not suitable due to their much smaller ion sizes (ionic radii Li^+: 59–92 pm, P^{5+}: 17 pm, Ca^{2+}: 100–134 pm, Sr^{2+}: 118–144 pm, Eu^{2+}: 117–135 pm).[35] Typically for Eu^{2+}, the luminescence behavior is strongly dependent on the Eu–ligand distances and consequently the *AE*–N distances in the presented host compounds. Given the similarity of the ionic radius of Sr^{2+} and Eu^{2+} a clearer relationship can be established in terms of site occupancy, thereby enabling an in-depth investigation of the emission profile of $Sr_3Li_4P_4N_{10}:Eu^{2+}$. The observed broad emission in the orange spectral region (λ_{max} = 596 nm, *fwhm* = 122 nm / 3812 cm^{-1}) can be attributed to the

presence of three potential activator sites (Sr1–3), as evidenced by the crystal structure (Table S6.6).

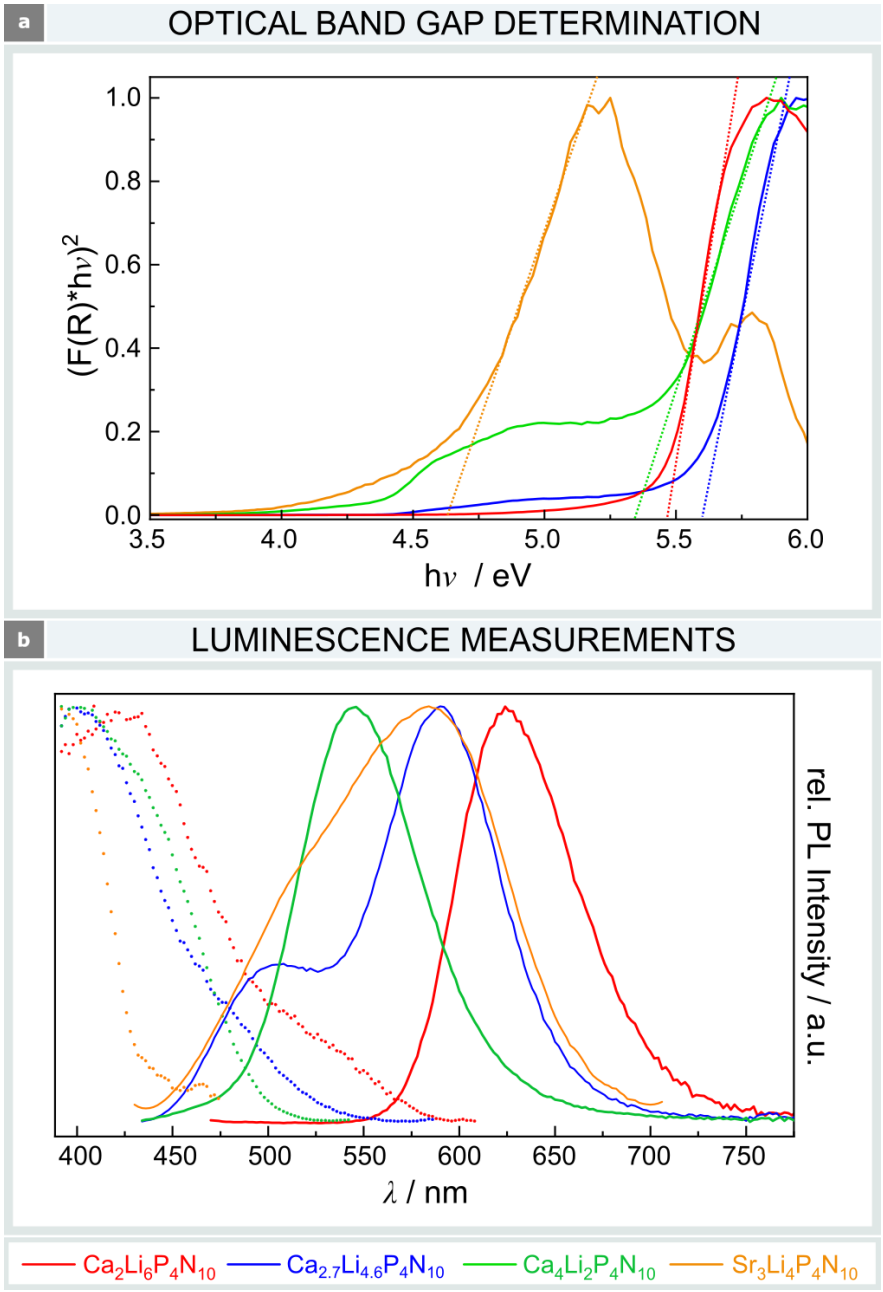

Figure 6.3. a) Optical band gap determination on undoped samples of all title compounds; b) *PL* and *PLE* spectra of Eu^{2+} doped (~1mol% Eu^{2+} concentration with respect to the AE^{2+} content); color code: $Ca_2Li_6P_4N_{10}$: red, $Ca_{2.7}Li_{4.6}P_4N_{10}$:blue, $Ca_4Li_2P_4N_{10}$: green, $Sr_3Li_4P_4N_{10}$: orange.

Since all sites show comparable effective coordination numbers CN_{eff} (Sr1 = 6.7, Sr2 = 6.6 & Sr3 = 5.9), with similar average interatomic distances ($d_{\varnothing Sr-N}$= 2.85, 2.86 and 2.93 Å) and polyhedra volumes (V: ~43–46 $Å^3$), no preferred site occupation is to be

expected, leading to the observed asymmetric, broad emission profile (Figure 6.4a). The composed emission spectrum could not be satisfactorily fitted by site-associated Pekarian curve functions, supporting this observation. In the case of the other compounds with *AE* = Ca, the interpretation is less clear and requires a more detailed analysis for each case. In general, a discernible trend towards an emission red-shift is evident as the Ca content is decreased. Under the assumption of similar Stokes shifts, the observed emission red-shift can be attributed to both, the nephelauxetic effect and ligand field splitting. The nephelauxetic effect and the ligand field splitting are strongly associated. Therefore a more precise interpretation is not possible within the scope of this work without supplementary calculations of the ligand field splitting of the irregular activator site environments.[42] However, if the ligand field splitting is neglected and only the nephelauxetic effect is used as an explanation, it is in line with the observed first sphere coordination numbers *CN* ($Ca_2Li_6P_4N_{10}:Eu^{2+}$: 1×(6+2); $Ca_{2.7}Li_{4.6}P_4N_{10}:Eu^{2+}$: 2×(5+2) & 1×6; $Ca_4Li_2P_4N_{10}:Eu^{2+}$: 2×6) of the potential activator sites. The greater number of ligands in the first coordination sphere of Eu^{2+} comparable contact lengths results in an enhanced nephelauxetic effect, which in turn reduces the 4*f*–5*d* transition energies. This results to the observed red-shift of both, absorption and emission bands. To enable a clearer description and classification in the following sections, we propose the introduction of two categories for the AEN_x polyhedra, which are independent of their distortion. The classification of *AE*N*x* polyhedra is dependent on two primary factors: the mean bond distances and the polyhedron volumes. AEN_x polyhedra exhibiting long mean bond distances (≥ 2.76 Å) and large polyhedron volumes (≥ 38 $Å^3$) are categorized in category I. Conversely, AEN_x polyhedra with shorter mean distances and smaller polyhedron volumes are categorized in category II. With a Eu^{2+} occupancy of Cat. I sites compared to Cat. II sites, higher energy bands (blue shift) should be emitted due to the reduced influence of the ligands on the activator ion.[43] This allows us to interpret the observed spectra more accurately. In the crystal structure of $Ca_4Li_2P_4N_{10}:Eu^{2+}$ there are two Ca sites with the same site symmetry (both Wyck 8*d*). Cat. I, with a polyhedral volume of V = 38.4 $Å^3$, an average AE–N distance of $d_{ØAE-N}$ = 2.76 Å, and an effective coordination number (CN_{eff}) of 5.4. Ca2 in Cat. II, with a smaller coordination polyhedron (V = 30.7 $Å^3$, $d_{ØAE-N}$ = 2.68 Å, and CN_{eff} = 4.7). If both sites are occupied by Eu^{2+}, the significant differences in parameters suggest either the appearance of two distinct emission bands or a broad emission resulting from the overlap of both bands. The *PL* spectrum of $Ca_4Li_2P_4N_{10}:Eu^{2+}$ exhibits one symmetric emission band with *fwhm* = 74 nm / 2466 cm^{-1}, which indicates that one of the two site categories is preferably occupied by Eu^{2+} (Figure 6.4b). A review of the literature indicates that Eu^{2+} exhibits an occupation preference for polyhedra with a volume of less than ~35 $Å^3$.[7,43] Polyhedra with a

volume of approx. 40 Å^3 or greater are not or are only minimally occupied. In the presented cases, this would imply a preferred occupation of the *AE* sites of category II, namely Ca2. Smaller fractions of shorter wavelength emission energy originating from the Ca1 site may be transferred efficiently to the Ca2 site by energy transfer or re-absorption effects. Nonetheless, the experimental confirmation of this assumption must be elucidated in subsequent work.

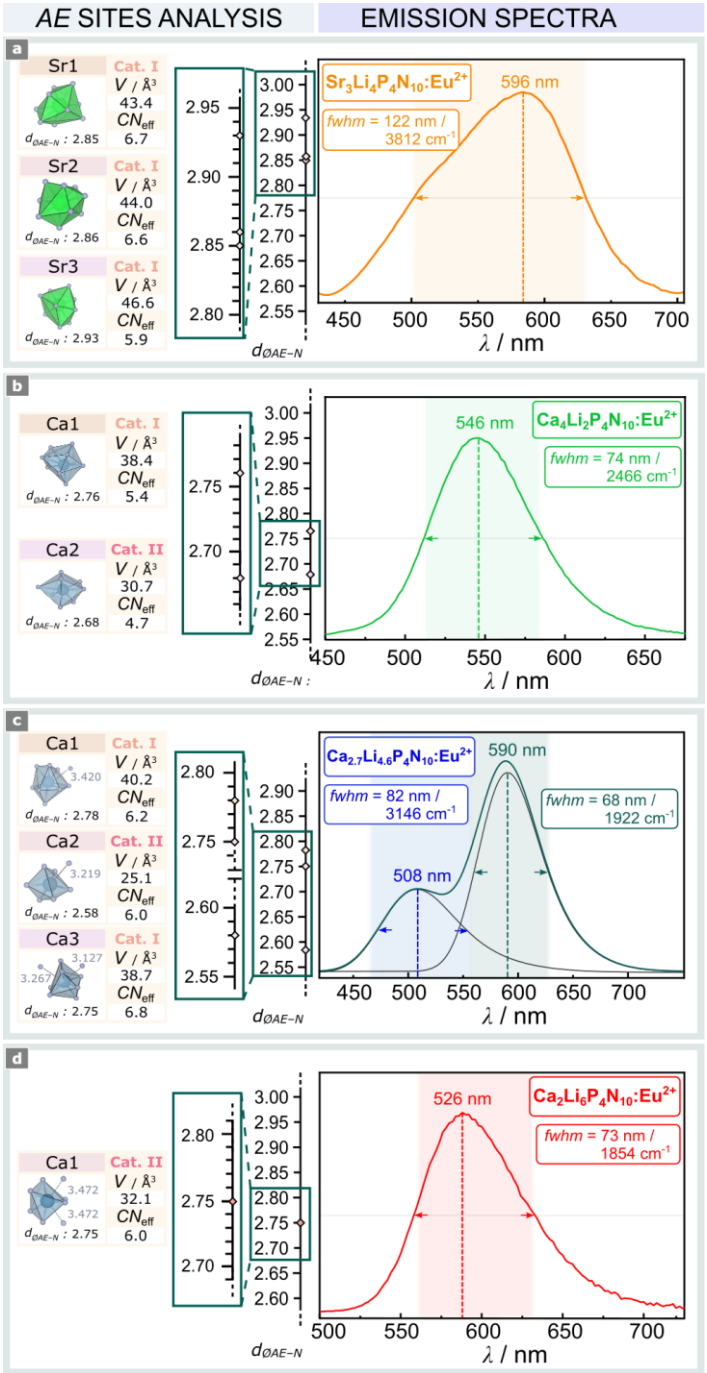

Figure 6.4. *PL* spectra of the title compounds with respective *AE* (*AE* = Ca, Sr) coordination spheres. The polyhedra were classified in two categories (Cat. I & Cat. II) on the basis of their resulting associated volumes and average bond lengths. a) $Sr_3Li_4P_4N_{10}:Eu^{2+}$, b) $Ca_4Li_4P_4N_{10}:Eu^{2+}$, c) $Ca_{2.7}Li_{4.6}P_4N_{10}$, and d) $Ca_2Li_6P_4N_{10}:Eu^{2+}$.

$Ca_{2.7}Li_{4.6}P_4N_{10}:Eu^{2+}$ features three Ca sites, which can also classified in these categories (2 × Cat. I, 1 × Cat. II). Both Ca sites (Ca1&3) of Cat. I exhibit a *CN* = 5+2 (CN_{eff}: 6.2/6.8) with average interatomic distances $d_{\varnothing Ca–N}$ ~2.8 Å and polyhedron volumina of V~39–40 Å^3. In contrast, Ca2 has a shorter average interatomic distance $d_{\varnothing Ca2–N}$ ~2.6 Å and polyhedron volume V~25 Å^3. This is consistent with the two superimposed emission bands visible in the deconvolution of the fitted emission profile (λ_1 = 506 nm, λ_2 = 592 nm) with significantly different Stokes shifts (Figure 6.4c).[44] The clearly lower intensity of the high-energy band may be due to less preferred occupation of the Cat. I sites (Ca1&3), reabsorption effects or energy transfer, attributable to the overlap of the excitation band of Eu2 (Ca2 site) with the emission band of Eu1/3 (Ca1/3). Therefore, it is not necessarily possible to draw conclusions about a preferred occupation of the sites in $Ca_{2.7}Li_{4.6}P_4N_{10}:Eu^{2+}$. In the case of $Ca_2Li_6P_4N_{10}:Eu^{2+}$ (in the following abbreviated as CLPN), the interpretation of the relatively narrow emission band with λ_{max} = 626 nm (*fwhm* = 73 nm / 1854 cm^{-1}, color coordinates (*CIE*) *x* = 0.6515, *y* = 0.3482) is considerably more straightforward. The crystal structure contains one single crystallographic Ca site (with high site symmetry Wyck. 8*d*, compared to the *AE* sites of the other title compounds), which indicates that this position is the only viable doping site for Eu^{2+}. The coordination of Ca can be described as distorted octahedra (CN_{eff}: 6.0; $d_{\varnothing Ca–N}$ = 2.50 Å, $V \approx 18$ Å^3), but in the second sphere are two further N atoms with $d_{Ca–N}$ = 3.4720(10) Å, which makes a 6+2 description ($d_{\varnothing Ca–N}$ = 2.75 Å; $V \sim 32$ Å^3) a more suitable description. Both, the average interatomic distance $d_{\varnothing Ca\text{-}N}$= 2.75 Å and CN_{eff} are comparable to those observed in $Ca_{2.7}Li_{4.6}P_4N_{10}:Eu^{2+}$. It is assumed that the observed red-shift is therefore originating from a larger ligand field splitting. The excitation spectrum reaches its maximum at approx. 430 nm, which is within the typical wavelength range of commercial blue emitting (In,Ga)N-LEDs. Given this suitable absorption range, a further assessment of the phosphor properties by means of standard pc-LED device manufacturing processes is straightforward. To test the application potential of CLPN for high color rendering quality white pc-LEDs a comparison with industry standard red emitting nitride phosphors has been performed. Figure 6.5a shows a comparison of the luminescence behavior of CLPN with respect to two commercially established red-emitting nitride phosphors CASN ($CaAlSiN_3:Eu^{2+}$) and SCASN ($(Sr/Ca)AlSiN_3:Eu^{2+}$).[45,46] In addition to a slightly blue-shifted emission maxima at 626 nm (*CASN*: λ_{max}: ~630 nm, = 86 nm / 2166 cm^{-1}; S*CASN*: λ_{max}: ~628 nm, *fwhm* = 76 nm / 1897 cm^{-1}) CLPN exhibit a narrower emission band (*fwhm* = 73 nm / 1854 cm^{-1}). This narrower emission band is attributed to one distinct emission center and lead to a reduction of the spillover in the deep red (>650 nm).[46]

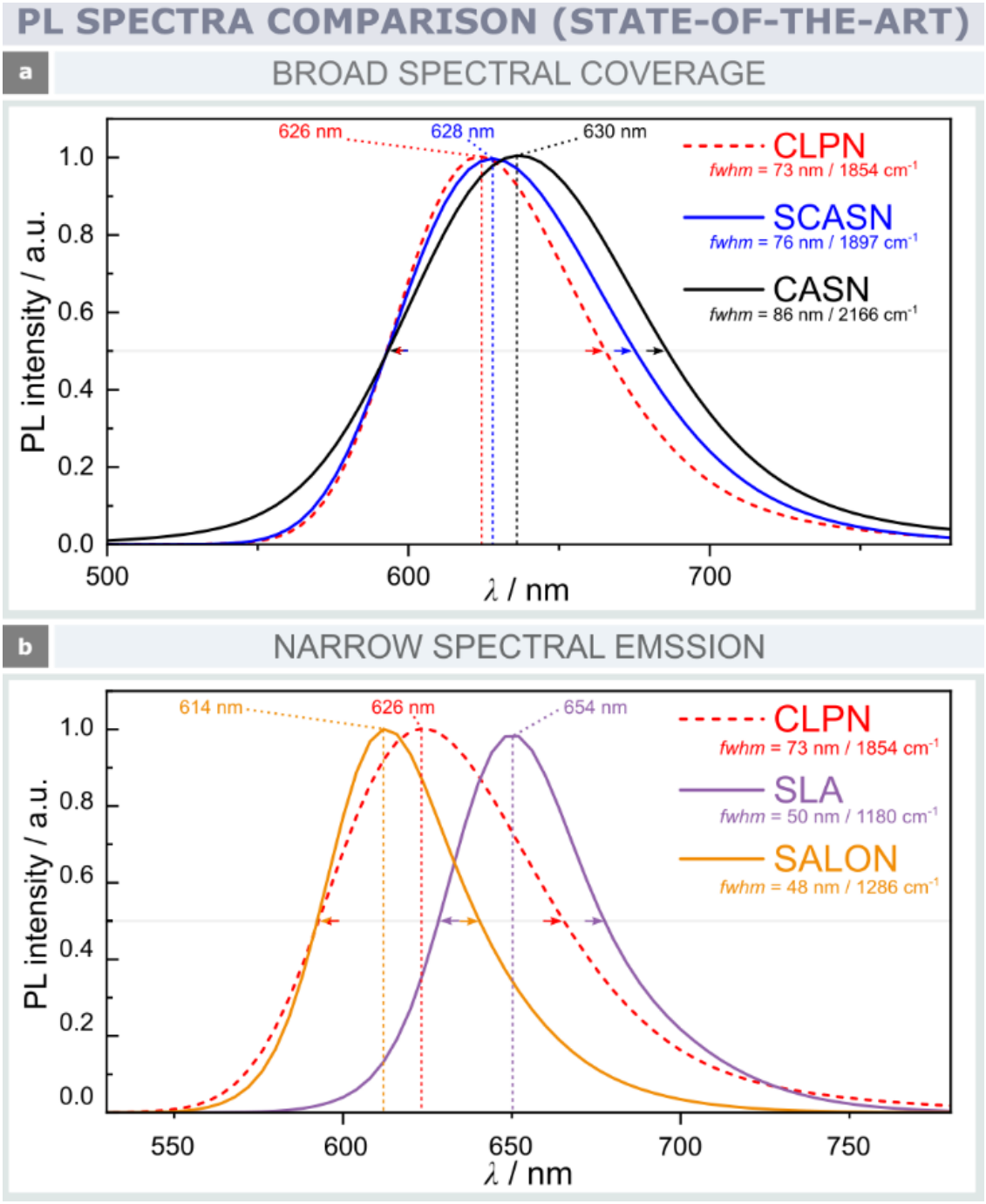

Figure 6.5. a) Comparison of normalized emission spectra of CLPN (red dotted curve) with respect to commercially established red emitting nitride phosphors CASN (black) and SCASN (blue); b) comparison of normalized emission spectra of CLPN (red dotted curve) with the state-of-the-art red emitting phosphors SLA (purple) and SLAO (orange).

A further comparison of the normalized emission spectra of CLPN with two state of the art narrow-band red-emitting phosphors, namely $Sr[LiAl_3N_4]:Eu^{2+}$ (SLA) and $Sr[Li_2Al_2O_2N_2]:Eu^{2+}$ (SALON), is shown in Figure 6.5b.[47,48] A significant quality criterion for white pc-LEDs is high color quality, which is determined by a number of factors. Established parameters are the color

rendering index (*CRI*) and specifically for high-*CRI* applications the additional *R9* index.[49] This separate index provides information about the rendering of red colored objects. Furthermore, for energy efficient illumination a high luminous efficacy of radiation (*LER* ≈ total lumens per spectral power) is indispensable. For this purpose, white spectra were synthesized from emission data of InGaN LEDs (blue emission) and emissions and absorption parameters (derived from single phosphor particle measurements) of a commercial $Y_3(Al,Ga)_5O_{12}:Ce^{3+}$ garnet phosphor (green emission), CLPN, SCASN and CASN phosphors (red emission). The iterative modeling approach takes phosphor-phosphor interactions into account and allows data normalization to identical pc-LED color points. Figure S6.6 shows the spectral power distribution (*SPD*; energy distribution over the spectrum (= power per unit area per unit wavelength) of the white emitting pc-LED comprising CLPN with a correlated color temperature (*CCT*) of 2700 K (*CIE* $x = 0.458$, $y = 0.410$) in comparison device modeling of pc-LEDs with the same configuration but with SCASN and CASN as red emitting phosphors. Here, the aforementioned reduction of the SPD in the deep red range (> 650 nm) can be observed. The pc-LED comprising CLPN shows an increase in light quality, measured by the average color rendering index $R_a8 = 94.3$ and $R9 = 54.5$ and an increased luminous efficacy (*LER* = 309 Lm/W_{opt}). The comparison with commercial SCASN and CASN is illustrated in Figure S6.7. To estimate the luminescent behavior of CLPN at typical LED operating temperatures, luminescence spectra at various temperatures were collected. As given in Figure 6.6 temperature-dependent *PL* spectra show band-narrowing with decreased temperature (*fwhm*@6K = 49 nm / 1246 cm^{-1}) and no significant shift in the emission maxima at cryogenic temperatures. The sharp zero phonon line (*ZPL*) at ~600 nm and higher transitions noticeable as shoulders for the 6 K spectrum indicate a high structural ordering. The relative photoluminescence intensity (in comparison to the emission intensity at 6 K) at 300 K is noteworthy, reaching 92%. However, at 423 K (possible operation temperature of pc-LED devices) the relative photoluminescence intensity is approx. 78%, indicating moderate thermal quenching behavior.[3] The entire temperature-dependent measurement (relative intensities up to 450 K) can be seen in the inset in Figure 6.6. Quantum efficiency measurements revealed an internal quantum efficiency (*IQE*; the ratio of emitted to absorbed photons) of approximately 48% and an external quantum efficiency (*EQE*; the ratio of emitted to total photons) of around 40% for excitation at 440 nm. These values were determined for the as-synthesized samples and can be further enhanced through optimization of a number of factors such as stoichiometry, sample purity, particle size and morphology, and e.g. the activator doping level.

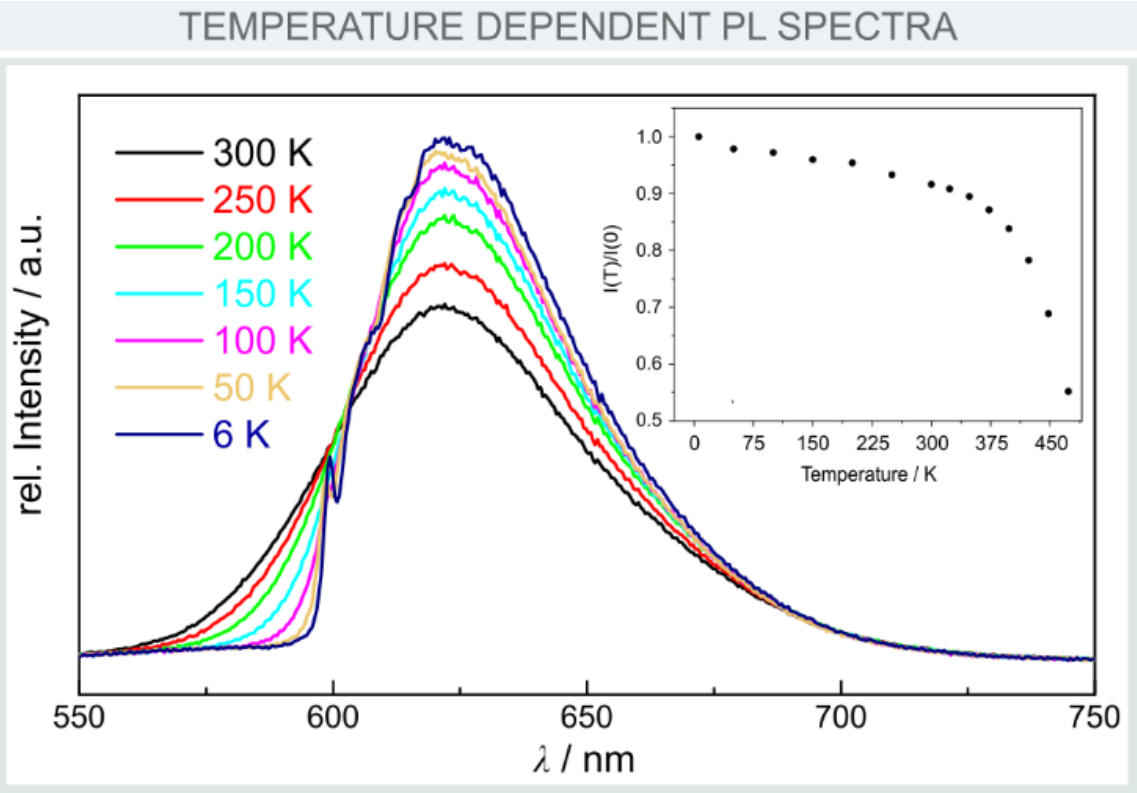

Figure 6.6. Temperature dependent *PL* spectra of CLPN with 1 mol% Eu^{2+}. A sharp zero phonon line (*ZPL*) is resolved at ~600 nm for the 6 K spectrum. Inset: Relative integrated emission intensities for determination the *TQ* behaviour.

6.3. Conclusion

Here, we present the first quaternary adamantane-type nitridophosphates $AE_xLi_{10-x}P_4N_{10}$ (*AE* = Ca (*x* = 2, 2.7, 4), Sr (*x* = 3)), synthesized under medium-pressure conditions, using a hot isostatic press (HIP). A straightforward ion-exchange reaction, starting from pre-synthesized adamantane-type lithium-ion conductor $Li_{10}P_4N_{10}$ and the corresponding alkaline earth halides, results in the formation of crystalline bulk samples of the title compounds, which enables structure elucidation by single-crystal and powder X-ray diffraction data. The presented simple approach preserved the anionic structural motif of the used precursor and resulted in the formation of completely new crystal structures with potential *AE* sites for the incorporation of activator ions (= luminescence centers), namely Eu^{2+}. Elemental analysis and solid-state NMR measurements corroborate the assumed structure models. DFT calculations reveal non-conducting materials properties with electronic band gaps ~4 eV. Moreover, the optical band gaps have been estimated through diffuse reflectance spectroscopy on undoped samples, followed by Tauc-method analysis. Eu^{2+} doped

samples of $AE_xLi_{10-2x}P_4N_{10}$ show red (*AE* = Ca, $x = 2$), orange (*AE* = Sr, $x = 3$), yellow (*AE* = Ca, $x = 2.7$) and green (*AE* = Ca, $x = 4$) luminescence, when excited with UV to blue light. The observed luminescence properties were attributed to the respective activator sites, and the potential preferential doping of these sites was discussed. The luminescence behavior of $Ca_2Li_6P_4N_{10}:Eu^{2+}$ (λ_{max} = 626 nm, *fwhm* = 73 nm / 1854 cm^{-1}) is investigated in more detail (*IQE*, *QE*, thermal quenching behavior, color point, white pc-LED simulation) due to the high potential for an industrial application. All used starting materials are either commercially available or easy to prepare and can therefore be implemented on a large scale. The medium-pressure ion-exchange reaction of $Li_{10}P_4N_{10}$ presented here could facilitate the exploration of novel, highly efficient nitridophosphate-based phosphor materials. Further research on this could focus on the use of alternative halide equivalents. In addition, studies on compounds containing Ba^{2+}, along with Ca^{2+} and Sr^{2+} ions as (co-)luminescence centers, have shown promising results but remain the focus of ongoing research. The presented simplified synthesis of quaternary nitridophosphates by ion-exchange reaction of nitridophosphate Li-ion conductors can be possibly extended in the future to other representatives, such as $Li_{12}P_3N_9$ or $Li_{18}P_6N_{16}$, with the aim of achieving degrees of condensation and structural motifs for alkaline earth nitridophosphates that were previously not feasible.

6.4 Experimental Part

6.4.1 Medium-Pressure/High-Temperature Synthesis

The starting material $Li_{10}P_4N_{10}$ was prepared using the synthesis-protocol described below, starting from stoichiometric amounts (molar ratio: 10 : 12) of Li_3N (Rockwood Lithium, 94%) and P_{red} (Chempur, ≥99.999%). The title compounds were prepared from the as-synthesized $Li_{10}P_4N_{10}$ and stoichiometric amounts of $EACl_2$ (*AE* = Ca, Sr) according to the reaction equation (1) given in the main text.

Synthesis protocol: Medium-pressure synthesis were performed under N_2 atmosphere (99.9%) in a hot isostatic press (HIP, AIP6-30H, American Isostatic Presses, Inc., Columbus, Ohio, USA). The starting materials were ground together in an agate mortar, pre-pressed to a synthesis pill and transferred into a tungsten crucible. The reaction crucible was placed in a security crucible made of corundum, which was closed with a lid. This assembly was transferred into the pressure module of the HIP. The atmosphere in the vessel was flushed for three times with argon. After the

flushing-steps, the pre-operating-pressure was build up (70 MPa, Maximator, DLE-5-30-2). Subsequently, the reaction temperature was increased up to 880°C (900°C for the title compounds), ending with a reaction pressure of 200 MPa. After maintaining these conditions for 50 h (10 h for the title compounds), the sample was allowed to cool down and the pressure was released (ambient pressure and temperature conditions). The products were obtained as colorless sinter cakes and further analyzed.

6.4.2 Single-Crystal X-ray Diffraction (SCXRD)

For crystal harvesting, selected crystals of the title compounds were isolated on MicroMounts (MiTeGen) under inert gas conditions and sealed with a protective cap. Single crystal X-ray diffraction data were collected on a Bruker D8 Venture diffractometer (radiation type: Mo-K_αBruker, USA). Integration and multi-scan absorption correction were performed using APEX3.[50-52] The crystal structures were solved by direct methods using SHELXT and refined against F^2 by full-matrix least-squares method using SHELXL.[53,54] The individual chosen spaces groups were checked by PLATON.[55,56] All *AE* (*AE* = Ca, Sr), P and N atom positions were determined during structure solution; Li atom positions were localized during structure refinement from difference Fourier maps. In the case of $Ca_4Li_2P_4N_{10}$ the obtained structure model was further refined using powder X-ray diffraction data (Rietveld method; more information in the Powder X-ray diffraction section) due to insufficient data quality.

6.4.3 Powder X-ray Diffraction (PXRD) and Rietveld Refinement

To check the phase content (respectively phase purity) the samples were sealed under inert gas conditions in a glass capillary (Hilgenberg, Ø = 0.3 mm). Powder X-ray diffraction experiments were performed on a STOE StadiP diffractometer (Stoe & Cie, Germany). The measurement set up was in parafocusing Debye-Scherrer geometry with Ge(111) single-crystal monochromator (radiation type: Cu-$K_{\alpha1}$ or Mo-$K_{\alpha1}$) and Mythen 1K detector. Rietveld refinements (on basis of the single crystal structure models) were performed on the collected powder X-ray diffraction data using the TOPAS Academic 6.[57] The peak profiles were described with the fundamental parameter approach. Potential preferred orientation of the crystallites were accounted by a harmonic function of 4th order. The background was modeled by a shifted Chebyshev polynomial.[58,59]

6.4.4 Scanning Electron Microscopy (SEM) and Energy-Dispersive X-ray (EDX) Spectroscopy

Analysis of the morphology and chemical composition (*AE*, P, N, (O)) of the title compounds was conducted using a dual-beam Helios Nanolab G3 UC (FEI, Hillsboro) scanning electron microscope (SEM) equipped with an X-Max 80 SDD EDX detector (Oxford Instruments, Abingdon). For this purpose, crystals from the analysis samples were mounted on pre-dried (*in vacuo*) carbon adhesive pads and carbon-coated to improve conductivity and minimize charge buildup.

6.4.5 Inductively Coupled Plasma with Optical Emission Spectroscopy (ICP OES)

ICP-OES experiments were performed on a Varian Vista RL (40 MHz RF generator) and VistaChip CCD detector.

6.4.6 Solid-state Magic Angle Spinning (MAS) NMR Spectroscopy

^{7}Li, ^{31}P, and ^{1}H NMR experiments were performed on a AVANCE DSX 500 MHz NMR spectrometer (Bruker) with a magnetic field of 11.7 T. The sample were filled and compacted under inert gas conditions into a 2.5 mm rotor, which was mounted on a commercial MAS probe (Bruker). The sample was rotated at a rotation frequency of 20 kHz. The obtained data were analyzed using ORIGIN Pro 2022b. All spectra were indirectly referenced to ^{1}H in 100% TMS at –0.1240 ppm.

6.4.7 UV/Vis Spectroscopy

Diffuse reflectance UV/Vis spectra of undoped samples were recorded on a Jasco V-650 UV/Vis spectrometer (Jasco, Germany). All spectra were analyzed in a range from 240–800 nm with a step size of 1 nm.

6.4.8 Quantum Chemical Calculations (DFT)

Periodic density-functional theory (DFT) calculations were performed using the Vienna ab initio simulation package (VASP).[60-62] The core and valence electrons are separated using projector-augmented waves (PAW).[63,64] To calculate the exchange and correlation energy generalized gradient approximation (GGA) according to Perdew, Burke and Ernerhof (PBE), were used.[65] For the structure optimization (RMM-DIIS), the Brillouin zone sampling was performed on a Γ-centered k-mesh of 5×5×5 for $Ca_2Li_6P_4N_{10}$, 7×7×7 for $Ca_{2.7}Li_{4.6}P_4N_{10}$, 7×6×6 for $Ca_4Li_2P_4N_{10}$, and 7×7×7 for $Sr_3Li_4P_4N_{10}$.[66] Due to the observed partial occupancy of two Li sites and one Ca site in the crystal structure of $Ca_{2.7}Li_{4,6}P_4N_{10}$ we constructed a charge neutral model "$Ca_3Li_4P_4N_{10}$" with full occupancy of the Ca site and no occupancy of the partially occupied Li sites. All residual atomic forces are relaxed to 10^{-5} eV/Å and the electronic convergence criterion was set to 10^{-7} eV with an energy cutoff of 520 eV for all calculations. Force and stress tensors are calculated in all cases. For both structural and electronic relaxation, a vdW dispersion energy correction was included by the DFT-D3(BJ) method with the Becke-Johnson damping function and non-spherical contributions to the gradient.[67,68] Using the meta-GGA functional local modified Becke-Johnson (LMBJ) a more detailed analysis of the band gap has been obtained.[69,70] Band structure calculations were performed on generated *k*-paths (SUMO) with eigenvalues obtained from static pre-calculations.[71]

6.4.9 Luminescence Measurements

Eu^{2+} doped samples (1 mol% Eu^{2+} relative to the AE^{2+} content) were analyzed using a HORIBA Fluoromax 4 system connected via optical fibers to an Olympus BX51 optical microscope for data acquisition. For this purpose, single particles were mounted on adhesive pads and room temperature *PL* and *PLE* spectra were recorded in a range from 400–800 nm with a 2 nm step size. Low temperature measurements were performed from 300–6 K on a thick-bed powder layer using a fiber-coupled spectroscopy system containing a thermally stabilized LED light source and a fiber optic spectrometer from Ocean Optics (HR2000+ES) in an evacuated cooling chamber. The controlled cooling was achieved through a liquid He compressor (Advance Research System Inc., ARS4HW). For temperature-dependent measurements thin layers of the samples were sandwiched between an alumina substrate and a cover glass. The samples were heated on a Linkam THMS600 stage and the PL spectra were measured with an Ocean Insight HR2000Plus ES spectrometer and a 415 nm emitting LED light source coupled with a reflectance fiber optic.

Internal (*IQE*) and external (*EQE*) quantum efficiency measurements were performed on a custom-built tool comprising an integrating sphere and a CAS spectrometer (Instrument Systems) used for phosphor production quality control. This setup is verified and calibrated weekly with standard phosphors emitting in the green–red spectral range.

6.4.10 Color Rendering Indices (CRI) Ra8 and R9

The CRI is a dimensionless index which is a measure of a light source's ability to accurately rendering the colors of objects in comparison to a reference light source, such as natural sunlight or an incandescent lamp. The CRI scale ranges from 0 (no color reproducibility) to 100 (perfect color reproducibility; naturally and realistically rendering). Ra8 represents the average CRI value based on the first eight test colors (TCS 01-TCS 08), which are standardized to include a range of 'muted' colors, such as pastel tones and various shades of grey. R9 specifically assesses the light source's ability to accurately reproduce saturated red tones (includes the additional test colors TCS 09–TCS 15).

6.5 Acknowledgements

We would like to thank Christian Minke for NMR measurements and Alice Dias for ICP-OES investigations, as well as Dr. Marwin Dialer for general support (all at the Department of Chemistry at LMU Munich).

6.6 References

[1] E.F. Schubert, J.-K. Kim, *Science* **2005**, *308*, 1274.

[2] J.H. Oh, S. J. Yang, Y.R. Do, *Light: Sci. Appl.* **2014**, *3*, e14.

[3] S. Hariyani, M. Sójka, A. Setlur, J. Brgoch, *Nat. Rev. Mater.* **2023**, *8*, 759.

[4] S.J. Ambach, A. Koldemir, K. Witthaut, S. Kreiner, T. Bräuniger, R. Pöttgen, W. Schnick, *Chem. Eur. J.* **2024**, *30*, e202401428.

[5] S.J. Ambach, M. Pointner, S. Falkai, C. Paulmann, O. Oeckler, W. Schnick, *Angew. Chem. Int. Ed.* **2023**, *62*, e202303580.

[6] R.M. Pritzl, K. Witthaut, M. Dialer, A.T. Buda, V. Milman, L. Bayarjargal, B. Winkler, W. Schnick, *Angew. Chem. Int. Ed.* **2024**, *63*, e202405849.

[7] R.M. Pritzl, M.M. Pointner, K. Witthaut, P. Strobel, P.J. Schmidt, W. Schnick, *Angew. Chem. Int. Ed.* **2024**, *63*, e202403648.

[8] S. Wendl, L. Eisenburger, P. Strobel, D. Günther, J.P. Wright, P.J. Schmidt, O. Oeckler, W. Schnick, *Chem. Eur. J.* **2020**, *26*, 7292.

[9] M.-H. Fang, H.-P. Hsueh, T. Vasudevan, W.-T. Huang, Z. Bao, N. Majewska, S. Mahlik, H.-S. Sheuc, R.-S. Liu, J. *Mater. Chem. C* **2021**, *9*, 8158.

[10] S. Wendl, S. Mardazad, P. Strobel, P.J. Schmidt, W. Schnick, *Angew. Chem. Int. Ed.* **2020**, *59*, 18240.

[11] G. Krach, J. Steinadler, K. Witthaut, W. Schnick, *Angew. Chem. Int. Ed.* **2024**, *63*, e202404953.

[12] S. Horstmann, E. Irran, W. Schnick, *Z. Anorg. Allg. Chem.* **1998**, *624*, 620.

[13] S.D. Kloß, W. Schnick, *Angew. Chem. Int. Ed.* **2019**, *58*, 7933.

[14] S. Vogel, M. Bykov, E. Bykova, S. Wendl, S.D. Kloß, A. Pakhomova, N. Dubrovinskaia, L. Dubrovinsky, W. Schnick, *Angew. Chem. Int. Ed.* **2020**, *59*, 2730

[15] E.-M. Bertschler, C. Dietrich, T. Leichtweiß, J. Janek, W. Schnick, *Chem. Eur. J.* **2018**, *24*, 196.

[16] S. Wendl, L. Seidl, P. Schüler, W. Schnick, *Angew. Chem. Int. Ed.* **2020**, *59*, 23579.

[17] L. Zhao, S. Wang, G. Wang, L. Cai, L. Sun, J. Qiu, *ACS Nano* **2024**, *18*, 11804.

[18] R.M. Pritzl, N. Fahle, K. Witthaut, S. Wendl, W. Schnick, *Chem. Eur. J.* **2024**, *30*, e202402521.

[19] J. Häusler, W. Schnick, *Chem. Eur. J.* **2018**, *24*, 11864.

[20] M. Zajac, R. Kucharski, K. Grabianska, A. Gwardys-Bak, A. Puchalski, D. Wasik, E. Litwin-Staszewska, R. Piotrzkowski, J. Z Domagala, M. Bockowski, *Prog. Cryst. Growth Charact. Mater.* ***2018***, *64*, 63.

[21] S. Wendl, M. Mallmann, P. Strobel, P.J. Schmidt, W. Schnick, *Eur. J. Inorg. Chem.* **2020**, *2020*, 841.

[22] M. Mallmann, S. Wendl, P. Strobel, P.J. Schmidt, W. Schnick, *Chem. Eur. J.* **2020**, *26*, 6257.

[23] M. Mallmann, S. Wendl, W. Schnick, *Chem. Eur. J.* **2020**, *26*, 2067.

[24] F. Golinski, H. Jacobs, *Z. Anorg. Allg. Chem*. **1995**, *621*, 29.

[25] H. Jacobs, S. Pollok, F. Golinski, *Z. Anorg. Allg. Chem*. **1994**, *620*, 1213.

[26] F.M. Engelsberger, R.M. Pritzl, J. Steinadler, K. Witthaut, T. Bräuniger, P.J. Schmidt, W. Schnick, *Chem. Eur. J.* **2024**, *accepted*, DOI: 10.1002/chem.202402743.

[27] W.B. Park, S.P. Singh, K.-S. Sohn, *J. Am. Chem. Soc*. **2014**, *136*, 2363.

[28] W. DeW. Horrocks, D. R. Sudnick, *J. Am. Chem. Soc*. **1979**, *101*, 334.

[29] N. Hirosaki, T. Takeda, S. Funahashi, R.-J. Xie, *Chem. Mater*. **2014**, *26*, 4280.

[30] Deposition Numbers 2390824 (for $Ca_2Li_6P_4N_{10}$), 2390554 (for $Ca_{2.7}Li_{4.6}P_4N_{10}$), 2390555 (for $Ca_4Li_2P_4N_{10}$) and 2390556 (for $Sr_3Li_4P_4N_{10}$) contain the supplementary crystallographic data for this paper. These data are provided free of charge by the joint Cambridge Crystallographic Data Centre and Fachinformationszentrum Karlsruhe.

[31] M. Dialer, K. Witthaut, T. Bräuniger, P.J. Schmidt, W. Schnick, *Angew. Chem. Int. Ed.* **2024**, *63*, e202401419.

[32] W. Schnick, U. Berger, *Angew. Chem. Int. Engl*. **1991**, *30*, 830.

[33] E.-M. Bertschler, R. Niklaus, W. Schnick, *Chem. Eur. J.* **2017**, *23*, 9592.

[34] E.-M. Bertschler, C. Dietrich, J. Janek, W. Schnick, *Chem. Eur. J.* **2017**, *23*, 2185.

[35] R. D. Shannon, *Acta Crystallogr. Sect. A* **1976**, *32*, 751.

[36] V. Schultz-Coulon, W. Schnick, *Z. Anorg. Allg. Chem.* **1997**, *623*, 69.

[37] F.J. Pucher, A. Marchuk, P.J. Schmidt, D. Wiechert, W. Schnick, *Chem. Eur. J.* **2015**, *21*, 6443.

[38] T.M. Tolhurst, T.D. Boyko, P. Pust, N.W. Johnson, W. Schnick, A. Moewes, *Adv. Optical Mater.* **2015**, *3*, 546.

[39] J. Tauc, R. Grigorovici, A. Vancu, *Phys. Status Solidi B* **1966**, *15*, 627.

[40] R. López, R. Gómez, J. Sol-Gel, *Sci. Technol.* **2012**, *61*, 1.

[41] L. Gamperl, G. Krach, P.J. Schmidt, W. Schnick, *Eur. J. Inorg. Chem.* **2019**, *2019*, 4985.

[42] R. S. Hafei, D. Maganas, P. Strobel, P. J. Schmidt, W. Schnick, F. Neese, *J. Am. Chem. Soc.* **2022**, *144*, 8038.

[43] M.-H. Fang, C.O.M. Mariano, P.-Y. Chen, S.-F. Hu, R.-S. Liu, *Chem. Mater.* **2020**, *32*, 1748.

[44] M. de Jong, L. Seijo, A. Meijerink, F.T. Rabouw, *Phys. Chem. Chem. Phys.* **2015**, *17*, 16959.

[45] H. S. Kim, K.-I. Machida, T. Horikawa, H. Hanzawa, *J. Alloys Compd.* **2015**, *633*, 97.

[46] H. Watanabe, N. Kijima, *J. Alloys Compd.* **2009**, *475*, 434.

[47] P. Pust, V. Weiler, C. Hecht, A. Tücks, A.S. Wochnik, A.-K. Henß, D. Wiechert, C. Scheu, P.J. Schmidt, W. Schnick, *Nat. Mater.* **2014**, *13*, 891.

[48] G.J. Hoerder, M. Seibald, D. Baumann, T. Schröder, S. Peschke, P.C. Schmid, T. Tyborski, P. Pust, I. Stoll, M. Bergler, C. Patzig, S. Reißaus, M. Krause, L. Berthold, T. Höche, D. Johrendt, H. Huppertz, *Nat. Commun.* **2019**, *10*, 1824.

[49] M.R. Krames, O.B. Shchekin, R. Mueller-Mach, G.O. Mueller. L. Zhou, G. Harbers, M.G. Craford, *J. Disp. Tech.* **2007**, *3*, 160.

[50] Bruker-AXS, APEX3, Vers. 2016.5-0, Karlsruhe (Germany), 2016.

[51] Bruker-AXS, XPREP Reciprocal Space Exploration, Vers. 6.12, Karlsruhe (Germany), 2001.

[52] SAINT, *Data Integration Software*, Madison, Wisconsin (USA) **1997**.

[53] G.M. Sheldrick, *Acta Crystallogr. Sect. C* **2015**, *71*, 3.

[54] G.M. Sheldrick, *SHELXS-97 Program of the Solution of Crystal Structure*, University of Göttingen, Göttingen (Germany) **1997**.

[55] A.L. Spek, *J. Appl. Crystallogr.* **2003**, *36*, 7.

[56] A.L. Spek, *Acta Crystallogr. Sect. D* **2009**, *65*, 148.

[57] A.A. Coelho, *TOPAS-Academic v4.1*, Brisbane (Australia), **2007**.

[58] R.W. Cheary, A.A. Coelho, J.P. Cline, *J. Res. Natl. Inst. Stand. Technol*. **2004**, *109*, 1.

[59] R.W. Cheary, A.A. Coelho, *J. Appl. Crystallogr.* **1992**, *25*, 109.

[60] G. Kresse, J. Furthmüller, *Comput. Mat. Sci*. **1996**, *6*, 15.

[61] G. Kresse, J. Furthmuller, *Phys. Rev. B* **1996**, *54*, 11169.

[62] G. Kresse, J. Hafner, *Phys. Rev. B* **1993**, *47*, 558.

[63] P.E. Blochl, *Phys. Rev. B* **1994**, *50*, 17953.

[64] G. Kresse, D. Joubert, *Phys. Rev. B* **1999**, *59*, 1758.

[65] J.P. Perdew, K. Burke, M. Ernzerhof, *Phys. Rev. Lett.* **1996**, *77*, 3865.

[66] P. Pulay, *Chem. Phys. Lett.* **1980**, *73*, 393.

[67] S. Grimme, J. Antony, S. Ehrlich, S. Krieg, *J. Chem. Phys.* **2010**, *132*, 154104.

[68] S. Grimme, S. Ehrlich, and L. Goerigk, *J. Comput. Chem.* **2011**, *32*, 1456.

[69] T. Rauch, M. A. L. Marques, and S. Botti, *Phys. Rev. B* **2020**, *101*, 245163.

[70] H.J. Monkhorst, J.D. Pack, *Phys. Rev. B* **1976**, *13*, 5188.

[71] A.M. Ganose, A.J. Jackson, D.O. Scanlon, *J. Open Source Softw.* **2018**, *3*, 717.

7 Trigonal Planar $[PN_3]^{4-}$ Anion in the Nitridophosphate Oxide $Ba_3[PN_3]O$

Published in: *Angew. Chem.* **2024**, *136*, e202405849;

Angew. Chem. Int. Ed. **2024**, *63*, e202405849.

Authors: Reinhard M. Pritzl, Kristian Witthaut, Marwin Dialer, Amalina T. Buda, Victor Milman, Lkhamsuren Bayarjargal, Björn Winkler, and Wolfgang Schnick

DOI: https://doi.org/10.1002/anie.202405849

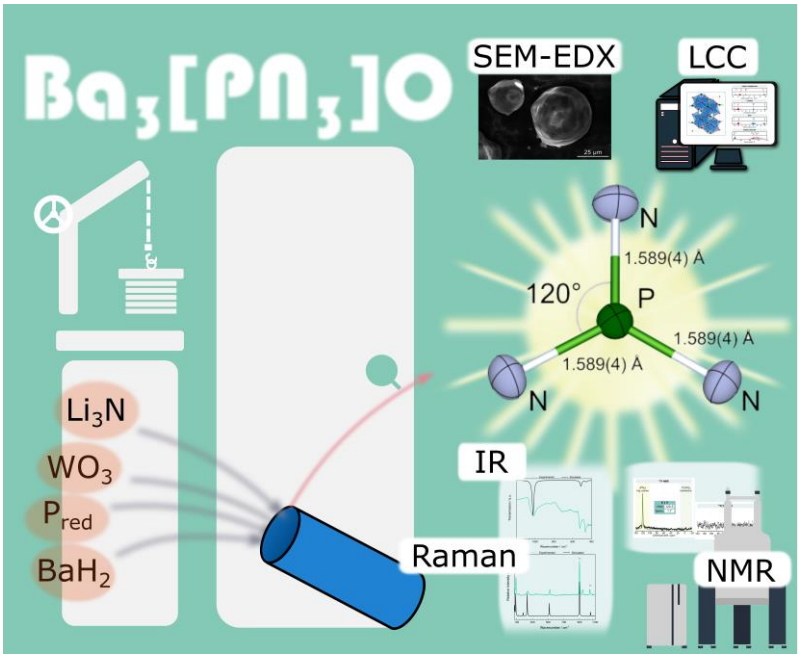

Abstract: Nitridophosphates, with their primary structural motif of isolated or condensed PN_4 tetrahedra, meet many requirements for high performance materials. Their properties are associated with their structural diversity, which is mainly limited by this specific building block. Herein, we present the alkaline earth metal nitridophosphate oxide $Ba_3[PN_3]O$ featuring a trigonal planar $[PN_3]^{4-}$ anion. $Ba_3[PN_3]O$ was obtained using a hot isostatic press by medium-pressure high-temperature synthesis (MP/HT) at 200 MPa and 880 °C. The crystal structure was solved and refined from single-crystal X-ray diffraction data in space group $R\bar{3}c$ (no.167) and confirmed by SEM-EDX, magic angle spinning (MAS) NMR, vibrational spectroscopy (Raman, IR) and low-cost crystallographic calculations (*LCC*). MP/HT synthesis reveals great potential by extending the structural chemistry of P to include trigonal planar $[PN_3]^{4-}$ motifs.

7.1 Introduction

Phosphorus nitrides and nitridophosphates are of fundamental interest in the field of materials science, especially in solid-state chemistry. Their wide range of applications results from their fascinating materials properties, which can be attributed to their great structural versatility. They are currently used as high-performance materials, such as ionic conductors, flame retardants, ultra-hard materials, or luminescent materials in pcLEDs.[1–4] Nitridophosphates are structurally related to oxosilicates, which represent the most abundant class of minerals in nature. Both nitridophosphates and oxosilicates contain tetrahedra as the predominant structural motif. This similarity can be rationalized as the combination P/N and Si/O are isolobal.[5] Similar to the (oxo)silicates, phosphorus also shows coordinations numbers *CN* = 5 (trigonal bipyramids and square pyramids) and *CN* = 6 (octahedra) under increased pressure in addition to the *CN* = 4 for tetrahedra already mentioned.[6–10] Since nitridophosphates can achieve a higher degree of condensation κ (= atomic ratio of network-forming cation (*NFC*) to coordinating atoms) than (oxo)silicates, which results from the ability of the $N^{[3]}$ atoms to be threefold coordinated, they should be able to achieve a higher structural diversity in theory.[11,12]

Nevertheless, if we compare the nitridophosphates with other nitrides with more covalent sub-structures, it is noticeable that in addition to the structural motif of tetrahedra, a threefold coordination of the *NFC* by N can be observed. For instance, nitridoberyllates have condensed structures that consist of trigonal planar units as the central structural motif.[13,14] Nitridoborates show additionally isolated anions containing trigonal planar coordinated $B^{[3]}$. So far, $[B_2N_4]^{8-}$, cyclic $[B_3N_6]^{9-}$ or even completely non-condensed $[BN_3]^{6-}$ anions have been described in the literature.[15–17] Recent reports detail the stabilization of a novel trigonal planar guanidinate (i. e. nitridocarbonate) anion, namely $[CN_3]^{5-}$, under high-pressure.[18,19]

To return to P^{+V}, there are molecular chemical approaches that build on the work of Niecke et al. from the 1970s and have experienced a renaissance in recent years. Large steric residues enabled the stabilization of P^{+V} in threefold coordination by N in both neutral and charged species.[20–23] However, a trigonal $[PN_3]^{4-}$ anion, the fundamental motif of this coordination unit, could never be realized so far. Regarding nitridophosphates there are several reasons, mainly of methodological nature. The preparation of crystalline nitridophosphates frequently requires temperatures above the decomposition temperature of their nitride precursors.[6,24] According to *Le Chatelier*, the application of pressure prevents the irreversible elimination of molecular N_2. The P/N building blocks, which usually occur as PN_4 tetrahedra in the starting materials, are stabilized by the application of high pressure or their *CN* is even increased.[7,8,11]

In this context, we report on the serendipitous discovery of $Ba_3[PN_3]O$, consisting of unprecedented isolated trigonal planar $[PN_3]^{4-}$ anions, obtained during the exploration of nitridophosphates using red phosphorus (P_{red}) as a non-preorganized starting material in the medium pressure (MP) regime.[4]

7.2 Results and Discussion

7.2.1 Synthesis and Structure Elucidation

$Ba_3[PN_3]O$ was prepared in a solid-solid/solid-liquid medium-pressure high-temperature (MP/HT) reaction at 880 °C and 200 MPa under nitrogen atmosphere in a hot isostatic press using BaH_2, P_{red}, Li_3N and WO_3 in a molar ratio of 9:3:6:1 as starting materials. The incorporation of oxygen into $Ba_3[PN_3]O$ seems to be of essential importance. No oxygen-free, exclusively nitridic variant with isolated triangular PN_3 motifs was obtained under the synthesis conditions used here, such as the hypothetical $Ba_9[PN_3]_3N_2$. In particular, WO_3 seems to be necessary as an oxidizing agent because experiments with other oxygen sources such as BaO, Li_2O and c-PON did not lead to the target compound.

More detailed information of the MP/HT synthesis of $Ba_3[PN_3]O$ is provided in the Supporting Information. $Ba_3[PN_3]O$ was obtained as orange, rounded block like crystals, which are highly sensitive to moisture and air, as expected for a lowly condensed nitridophosphate (κ = 1/3, Figure S7.1).[25] The structure was solved and refined from single-crystal X-ray diffraction data (scXRD, $R\bar{3}c$ (no. 167), a = 7.8315(3), c = 16.9865(5) Å, Z = 6, $R1$ = 0.0168; Tables S7.1–7.5) and confirmed by Rietveld refinement on a representative powder X-ray diffraction pattern (Figure S7.2, Table S7.6&7.7).[26] The unknown minority phase is attributed to the addition of WO_3 since no W is present in the crystal structure of the title compound. Figure 7.1 shows the crystal structure of $Ba_3[PN_3]O$, with the coordination environment of Ba (blue) and P (green). $Ba_3[PN_3]O$ crystallizes isotypically to Ba_3NiO_4 and $Ba_9Ge_3N_{10}$, which present trigonal planar $[NiO_3]^{6-}$ and $[GeN_3]^{5-}$ anions as structural motifs, respectively.[27,28] $Ba_3[PN_3]O$ exhibits $[PN_3]^{4-}$ anions which are isoelectronic to the carbonate anion $[CO_3]^{2-}$.[29] Because of this unusual coordination environment of P, we will discuss the process of structure determination and examine the crystal structure in more detail. The aim is not only to reliably elucidate the crystal structure, but also to determine benchmark values for common analytical methods for this unprecedented structural motif and to prove the consistency through all methods available. During the refinement process of the single-crystal X-ray diffraction data, the quality of the data allowed for an unambiguous assignment of all element types, especially O and N.

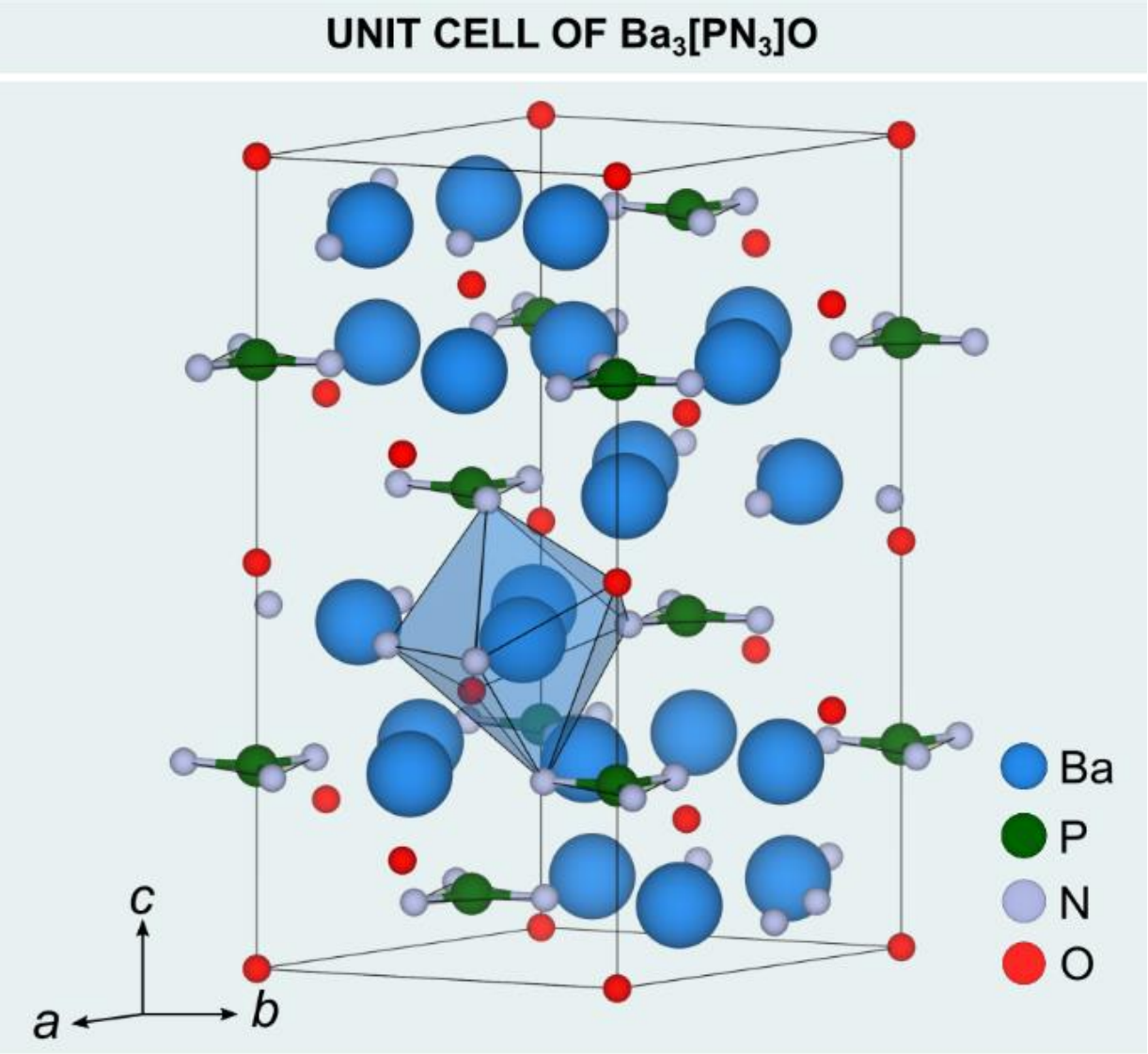

Figure 7.1. The crystal structure of $Ba_3[PN_3]O$, built up of trigonal planar $[PN_3]^{4-}$ anions (green) and $[BaN_5O_2]$ polyhedra (blue; for illustration purposes only one polyhedron has been drawn); atom color coding: Ba = blue, P = green, N = gray, O = red.

Unambiguous here means that the refinement led to significantly worse *R*-values or even became unstable for other ordering and compositional variants. However, since both N and O cannot usually be reliably distinguished by X-ray diffraction data due to their similar atomic form factors, the general structural model with the empirical formula $Ba_3[P(N,O)_3](N,O)$ was initially considered.[30] To verify the elemental composition and confirm P in the compound and its unique coordination environment, we analyzed selected crystals using SEM-EDX. Only the elements Ba, P, N and O were detected, whereby the relative atomic ratios of the heavy elements (Ba : P ~ 3 : 1) correlate well with the expected ratio obtained from the single-crystal structure model. However,

the anion values fluctuate significantly, which may be caused by the tendency for surface hydrolysis (Table S7.8).

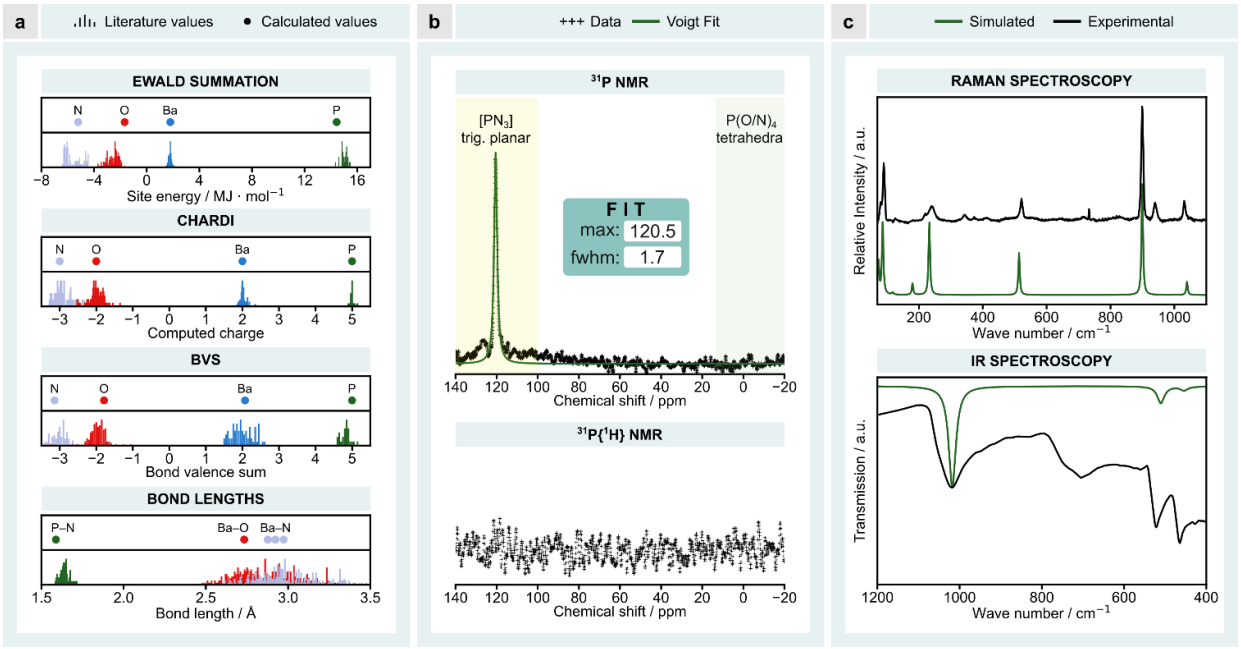

Figure 7.2. Analytical overview; a) Graphical representation of low-cost crystallographic calculations (*LCC*), calculated values in the top row of each method, reference data from literature on the bottom rows. b) top: ^{31}P NMR spectrum (black) of $Ba_3[PN_3]O$ showing one narrow signal at 120.5 ppm (highlighted in yellow), which can be assigned to the single crystallographic P site in the crystal structure, expected area of $P(O/N)_4$ tetrahedra highlighted in green; bottom: ^{31}P-{^{1}H} cross polarization NMR spectrum of of $Ba_3[PN_3]O$ showing no signal (exclusion of H in crystal structure). c) Experimental (black) and calculated (obtained with DFT-PBE0 method, green) FTIR (top) and Raman (bottom) spectrum of $Ba_3[PN_3]O$.

Using these results and the information of the scXRD structure model (two anion sites: 18*e* & 6*b*), only two charge-balanced compounds can be derived: $Ba_3[P^{+V}N_3]O$ or $Ba_3[P^{+III}O_3]N$. According to the valence shell electron pair repulsion theory (VSEPR), a trigonal planar $[P(O/N)_3]^{x-}$ anion should only occur with P^{+V} and not with P^{+III}.[31] In the case of nonbonding lone pair electrons, as necessary for P^{+III}, a trigonal pyramidal anion geometry like in P_4O_6 would rather be expected.[32] To substantiate this assumption, the formal charges were investigated through low-cost crystallographic calculations (*LCC*) and compared with literature known compounds (Figure 7.2a, Table S7.9–7.14). The results of the Ewald summation, CHARDI and BVS agree very well with the expected values from the literature, and further support the initial $Ba_3[P^{+V}N_3]O$ structural model. From a structural chemistry point of view, Ba^{2+} is sevenfold coordinated (distorted pentagonal bipyramidal coordination by 2×O and 5×N) by the anions, with $d_{Ba–N}$ = 2.8765(3)–2.9728(8) Å and $d_{Ba–O}$= 2.73298(9) Å (Figure 7.3a). These distances are in the

typical range for (oxo)nitridophosphates and correspond approximately to the sum of the Shannon radii, which additionally supports the selected assignment of the anion sites.[33–36] The triangular anion $[PN_3]^{4-}$ shows equidistant P–N distances with $d_{P–N}$= 1.589(4) Å and N–P–N angles of 120° (Figure 7.3b). These relatively short P–N distances for nitridophosphates, especially compared to higher *CN*, and regular bond angles of 120° for a trigonal planar anion allow conclusions to be drawn about the bonding situation. A comparison with the trigonal-planar ($P^{+V}N_3$) motifs in molecular crystals known from the literature is also useful.[20–23]

These molecular subunits show significant differences in their respective P–N bond lengths. In our case, the observed $d_{P–N}$ values lie in between the shorter and longer distances of e.g. [bis-(trimethylsilyl)amino]bis(trimethylsilylimino)phosphorene ($d_{P–N}$ = 1.513(3) and 1.638(4) Å).[21] From this observation, a multiple-bonding character for the P–N bonds can be deduced. The three resonance structures show that two electrons are distributed over four atoms by π-interaction and explain the shortened bond lengths on average (Figure 7.3c).

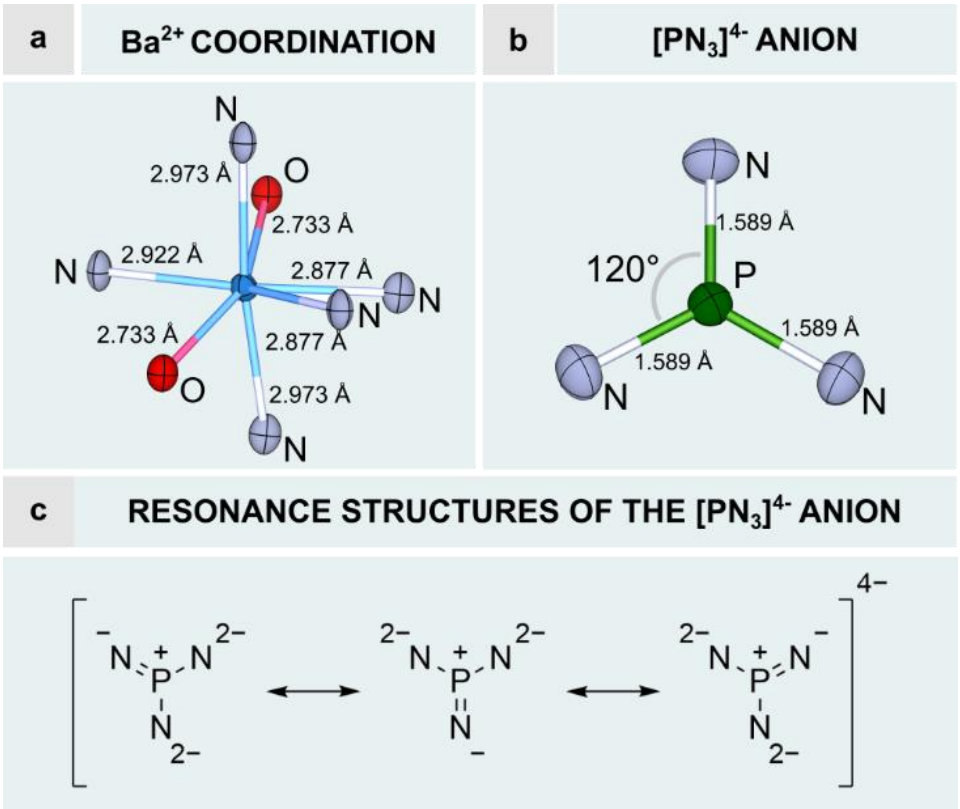

Figure 7.3. Coordination environment of Ba (a) and P (b) in $Ba_3[PN_3]O$ with corresponding interatomic distances; atom color coding: Ba = blue, P = green, N = gray, O = red. c) Resonance structures of the $[PN_3]^{4-}$ subunit.

The reverse view on the environment of the O^{2-} anions shows an octahedral coordination by Ba^{2+} ions (Figure S7.3). The central positon of O^{2-} in the Ba octahedra helps to buffer the charge of the

large Ba^{2+} cations, which seems to be necessary to stabilize the $[PN_3]^{4-}$ anion and prevent electrostatic repulsion. This concept has been previously discussed in the literature for $Ho_3[PN_4]O$, which contains isolated $[PN_4]^{7-}$ anions.[37] Taking these structural results into account, the question as to whether the anion positions could be partially occupied by O/N remains. To answer this, we performed ^{31}P MAS NMR spectroscopy on a representative powder sample. This has been established as a powerful technique for studying the local environment, i.e. bond distances, *CN*, disorder and mixed-occupancy.[38–40]

7.2.2 MAS NMR

The ^{31}P MAS NMR spectrum (Figure 7.2b, top) shows one narrow signal at 120.5 ppm, which agrees well with the one crystallographic highly symmetric P site in $Ba_3[PN_3]O$. The halfwidth of the signal (*fwhm* = 1.7 ppm) shows no sign of a mixed-occupancy of the ligands, as this would result in a significant broadening of the signal. Further, the chemical shift is clearly distinct from the typically observed signals of tetrahedrally coordinated P sites of alkaline earth metal (oxo)nitridophosphates (from 10 to –25 ppm).[34, 41–43] Similar to the ^{11}B-NMR of *h*- and *c*-BN, where the isotropic chemical shift of boron in trigonal and tetrahedral environments differs by about 20 ppm, a comparable trend with a significantly larger shift was observed in the ^{31}P-NMR spectrum.[44]

Since we used BaH_2 as starting material and due to the isolobal relationship between O and NH^{2-}, the next important step is to exclude the incorporation of H in our compound. For this purpose, we performed additional ^{1}H and $^{31}P\{^{1}H\}$ MAS-NMR measurements. The absence of ^{31}P signals in the ^{31}P-$\{^{1}H\}$ cross polarization NMR spectrum (Figure 7.2b, bottom) proves that there is no hydrogen in the immediate environment of phosphorus in $Ba_3[PN_3]O$ and therefore not present in the crystal structure. However, several signals in the ^{1}H NMR spectrum (0–5 ppm) show that side phases contain hydrogen, albeit with negligible signal intensity (Figure S7.4).

7.2.3 Vibrational Spectroscopy

To validate the proposed structure model and further investigate the new $[PN_3]^{4-}$ anion, we conducted vibrational spectroscopic studies. We measured IR and Raman spectra of the title compound and compared them to the respective theoretical spectra obtained through quantum chemical calculations using the DFT-PBE0 method. The IR measurements were performed on the bulk, while the Raman measurements were performed on a coarse-grained sample. For

classification, the symmetries of the lattice vibrations in the long wave-length limit of $Ba_3[PN_3]O$ can be described by the irreducible representation:

$$\Gamma_{irreducible} = 2\,A_{1g} + 3\,A_{1u} + 5\,A_{2g} + 6\,A_{2u} + 9\,E_u + 7\,E_g,$$

Where the $2\,A_{1g} + 7\,E_g$ are Raman active, the modes with $5\,A_{2u} + 8\,E_u$ symmetry are IR active and the three acoustic modes have $A_{2u} + E_u$ symmetry.

The Raman spectrum shows the intense symmetric stretching vibrations (ν_1) at 900 cm^{-1}, the less intense antisymmetric stretching vibrations (ν_2) at 1032 cm^{-1} and the asymmetric deformation (ν_4) at 522 cm^{-1} of the $[PN_3]^{4-}$ anion as calculated (Figure 7.2c, top). The further observed signals at 522, 242, 220, 90, and 80 cm^{-1} are attributed to lattice vibrations. Raman bands at 942, 721 and in the range of 430–311 cm^{-1} cannot be assigned and presumably originate from the unknown minority phases mentioned above. The FTIR spectrum shows the expected strong antisymmetric stretching vibrations (ν_2) of the $[PN_3]^{4-}$ anion at 1022 cm^{-1} and 512 cm^{-1}, as well as the out-of-plane bending mode (δ) at 455 cm^{-1} (Figure 7.2c, bottom). Additional weak absorption between 3500–3100 cm^{-1} (Figure S7.5) may be attributable to possible minor NH_x contaminations in the sample, which is in agreement with the result of the ^1H NMR study. The broad absorption band in the range of 780–650 cm^{-1} results from the unknown side phase.

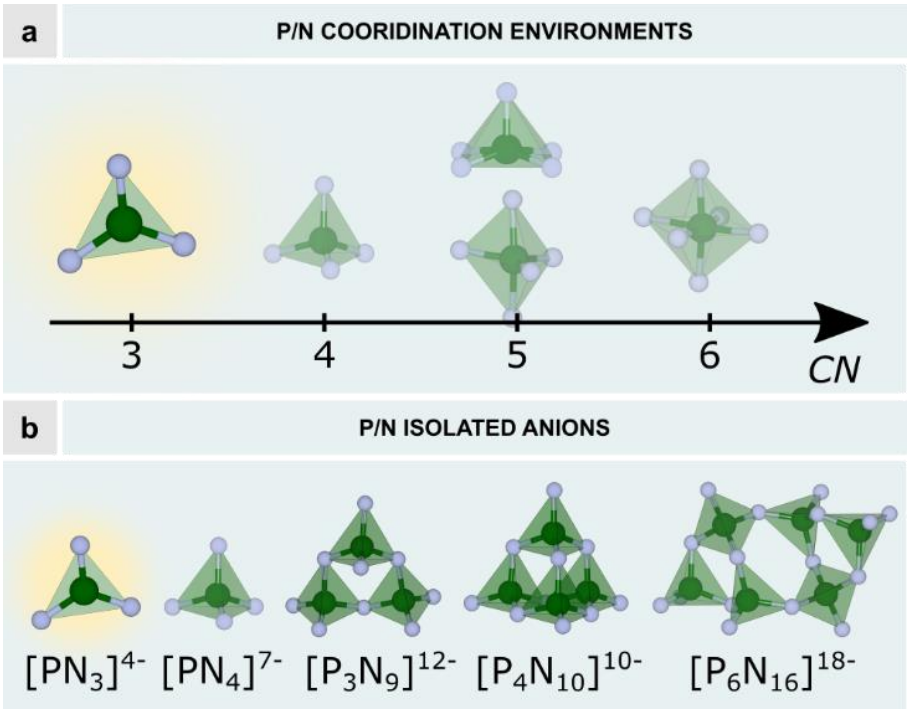

Figure 7.4. a) Coordination environments of P^{+V} in nitrides, b) isolated P^{+V}/N anions; yellow highlighted is the novel trigonal planar $[PN_3]^{4-}$ anion.[1,7,8,45–49]

Finally, to provide a broader structural context for the new anion $[PN_3]^{4-}$, Figure 7.4a shows all coordination environments of P^{+V} in phosphorus nitrides/nitridophosphates observed to date, and Figure 7.4b shows a classification to the isolated anionic motifs of these substance classes.[1,7,8,45-49]

7.3 Conclusion

In summary, this contribution reports on $Ba_3[PN_3]O$, a new barium nitridophosphate oxide, containing trigonal planar $[PN_3]^{4-}$ anions observed for the very first time. The crystal structure was elucidated by scXRD data and confirmed by Rietveld refinement based on PXRD data. While a trigonal nitridic environment has already been reported for $[BeN_3]$, $[BN_3]$ and $[CN_3]$ for the second period and for $[XN_3]$ (X = Mn, Fe, Co, Ge] for the fourth period, we were able to close this gap with $[PN_3]$ and detect the first representative of the third period.[18,19,28,50–54] This makes P the most versatile network-forming cation of the main group nitrides and oxonitrides in terms of its coordination environment, as it can assume coordination numbers of three to six. Low-cost crystallographic calculations, i.e. CHARDI, BVS, Ewald summation and interatomic distances, as well as MAS NMR and vibrational spectroscopy support the structural analysis beyond doubt and provide first reference values for this structural motif. The discovery of $Ba_3[PN_3]O$ by medium pressure synthesis represents a significant expansion of the structural chemistry of phosphorus and is a promising first step towards the development of completely new covalent anionic P/N motifs such as in nitridoborates. Future work will investigate the use of this anion as a central and simplest building block for the preparation of novel (oxo)nitridophosphates, e.g. ortho-$[PN_3O]^{6-}$ anions, and in particular as a promising starting material for molecular chemistry.

7.4 Experimental Part

7.4.1 Starting Materials

All starting materials were used as purchased (manufacturer and purities in parentheses)

Li_3N (Rockwood Lithium, 94%)

P_{red} (Chempur, ≥ 99.999%)

BaH_2 (Materion, 99.9%)

WO_3 (fisher scientific, 99+%)

7.4.2 Medium-Pressure High-Temperature Synthesis

$Ba_3[PN_3]O$ was synthesized in a medium-pressure, high-temperature reaction from Li_3N, P_{red}, BaH_2 and WO_3. The starting materials (in a molar ratio 6:3:9:1) were ground together in an argon-filled glovebox (MBraun, < 1 ppm H_2O, < 1 ppm O_2) and filled into a Ta crucible. This crucible was closed with a Ta lid and placed in the second security crucible made of corundum. This assembly was closed with a corundum lid and transferred into the pressure module of a hot isostatic press (HIP, AIP6-30H, American Isostatic Presses, Inc., Columbus, Ohio, USA). More details on the HIP synthesis can be found in the literature.[4] The assembly was constantly increased to 70 MPa. Subsequently, the sample was heated to 880 °C within 172 min, ending up with the reaction pressure of 200 MPa. After the reaction time of 10 h (at constant 200 MPa), the sample was allowed to cool down to 20 °C and the pressure was released. The product was obtained as an orange sinter cake, which is sensitive against moisture and air.

7.4.3 Single-Crystal X-ray Diffraction (SCXRD)

For structure determination by SCXRD, a combination of φ- and ω-scans of a $Ba_3[PN_3]O$ single crystal were collected on a Bruker D8 Venture TXS diffractometer with Mo-K_α radiation (λ = 0.71073 Å), rotating anode and multilayer monochromator. Received data were indexed, integrated, absorption corrected (multi-scan-method) and the space group was determined using the APEX3 software package.[55–57] The structure was solved using the SHELXT algorithm, refined against F^2 by the SHELXL implement of WinGX, with the least-squares method.[58,59] The results were visualized using the VESTA software.[60]

7.4.4 Powder X-ray Diffraction (PXRD) and Rietveld refinement

PXRD data were collected on a STOE Stadi P diffractometer (STOE & Cie GmbH, Darmstadt) in modified Debye-Scherrer geometry with Ag-Kα_1 radiation, λ = 0.5594 Å a MYTHEN 1K strip detector and a Ge(111) monochromator. For measurement, the samples were ground with amorphous boron (for dilution) and sealed in a glass capillary (0.4 mm outer diameter, Hilgenberg, Malsfeld) and centered in the beam on a rotating goniometer head. Verification of $Ba_3[PN_3]O$ as main constituent of synthesized samples, the collected data were refined using the Rietveld method with the TOPAS Academic software.[61,62]

7.4.5 Scanning Electron Microscopy (SEM) and Energy-Dispersive X-ray (EDX) Spectroscopy

For SEM imaging and chemical analysis by EDX measurements, the sample was prepared on a pre-dried self-adhesive carbon foil. The analysis was done by a Dualbeam Helios Nanolab G3 UC (FEI, Hilsboro) with an X-Max 80 SDD detector (Oxford Instruments, Abingdon). Data and images were recorded with an acceleration voltage of 25 kV and processed with the Aztec software.

7.4.6 Solid-State MAS NMR Spectroscopy

Solid-state MAS NMR spectra were recorded on an Avance III 500 spectrometer (Bruker, Karlsruhe) with 11.7 T magnet (500.25 MHz ^{1}H frequency) and double resonance MAS probe. The pre-ground sample was filled into a ZrO_2 rotor with an outer diameter of 2.5 mm. The NMR spectra were collected at 20 kHz spinning frequency.

7.4.7 Fourier-Transform Infrared Spectroscopy (FTIR)

The infrared spectra of $Ba_3[PN_3]O$ were measured by a Bruker Alpha II FTIR spectrometer with a diamond attenuated total reflectance (ATR) unit, in an Ar-filled glovebox.

7.4.8 Raman Spectroscopy

Raman measurements were carried out with a custom set-up in Frankfurt described in detail elsewhere.[63] We used an OXXIUS S.A. Laser-Boxx LMX532 laser (λ = 532 nm) and a spectrograph (Princeton Instruments ACTON SpectraPro 2300i) equipped with a Pixis256E CCD camera. Measurements were performed in reflection geometry with the polarized laser light, where the sample was clamped between two glass slides in order to avoid any exposure to air.

7.4.9 Low-Cost Crystallographic Calculations

Bond-valence sum calculations were performed using the software EXPO2014.[64]
We determine the BVS parameters R_0 (P^{+V}–N^{-III}) = 1.777 for trigonal planar coordination.
Charge distribution calculations were performed using CHARDI2015 (Build 21).[65]
Site potentials were calculated with the EWALD Summation class of Pyton Materials Genomics (pymatgen).[66,67]

7.4.10 Density Functional Theory Calculations (DFT)

7.4.10.1 IR spectra

For this work first-principle electronic structure calculations were used to obtain vibrational frequencies comparable to the experimentally obtained spectrum. Periodic density functional theory (DFT) calculations were performed via the Vienna *ab initio* simulation package (VASP).[68–70] Projector augmented waves (PAW) were used and contributions of the exchange and correlation energy were treated in the generalized gradient approximation (GGA), as described by Perdew, Burke and Ernzerhof (PBE).[71–73] A dense *k*-point sampling with a 6x6x3 Gamma centered grid and a plane wave energy cutoff of 520 eV ensured a well-converged structure. Structure parameters were optimized via conjugate gradient algorithm with a convergence criterion of 10^{-5} eV/Å for interatomic forces and an electronic convergence criterion of 10^{-7} eV.[74] The vibrational frequencies were extracted from density-functional perturbation theory (DFPT) linear response calculations with the plotIR script shared by Dr. Karhánek.

7.4.10.2 Raman spectra

Atomistic model calculations were carried out within the framework of DFT and the pseudopotential method using the CASTEP simulation package.[75,76] Norm-conserving pseudopotentials were generated “on the fly” using the parameters provided with the CASTEP distribution. These pseudopotentials have been extensively tested for accuracy and transferability.[73] The pseudopotentials were employed in conjunction with plane waves up to a kinetic energy cutoff of 1020 eV. The calculations were carried out with the PBE exchange-correlation functional. Monkhorst-Pack grids were used for Brillouin zone integrations with a distance of < 0.026 $Å^{-1}$ between grid points.[77,78] Convergence criteria included an energy change of < 5×10^{-6} eV/atom, a maximal force of < 0.01 eV/Å, and a maximal deviation of the stress tensor < 0.02 GPa from the imposed stress tensor. Phonon frequencies were obtained from density functional perturbation theory (DFPT) calculations.[79] Raman intensities were computed using DFPT with the ‘2n+1’ theorem approach.[80] It should be stressed that all calculations were carried out in the athermal limit, i.e., the influence of temperature and zero-point motion were not taken into account. Full geometry optimizations reproduced the experimentally determined structure to within the accuracy expected from DFT-GGA-PBE calculations, i.e. lattice parameters of the DFT ground state structure (a = 7.9232 Å, c = 17.2037 Å) were larger by ~1.3% with respect to the experimental values due to the well established GGA-underbinding.

7.5 Acknowledgements

We thank Christian Minke for NMR measurements. We would also like to thank Prof. Dr. Konstantin Karaghiosoff for stimulating discussions on this topic (both at Department of Chemistry, LMU Munich). BW is grateful for support through the BIOVIA Science Ambassador program.

7.6 References

[1] E.-M. Bertschler, C. Dietrich, T. Leichtweiß, J. Janek, W. Schnick, *Chem. Eur. J.* **2018**, *24*, 196.

[2] M.S. Choudhary, J.K. Fink, K. Lederer, H.A. Krässig, *J. Appl. Polym. Sci*.**1987**, *34*, 863.

[3] S. Vogel, M. Bykov, E. Bykova, S. Wendl, S.D. Kloß, A. Pakhomova, N. Dubrovinskaia, L. Dubrovinsky, W. Schnick, *Angew. Chem. Int. Ed.* **2020**, *59*, 2730.

[4] S. Wendl, S. Mardazad, P. Strobel, P.J. Schmidt, W. Schnick, *Angew. Chem. Int. Ed.* **2020**, *59*, 18240.

[5] P. Hofmann, H. R. Schmidt, *Angew. Chem. Int. Ed.* **1986**, *25*, 837.

[6] K. Landskron, H. Huppertz, J. Senker, W. Schnick, *Angew. Chem. Int. Ed.* **2001**, *40*, 2643.

[7] D. Baumann, W. Schnick, *Angew. Chem. Int. Ed.* **2014**, *53*, 14490.

[8] S.J. Ambach, M. Pointner, S. Falkai, C. Paulmann, O. Oeckler, W. Schnick, *Angew. Chem. Int. Ed.* **2023**, *62*, e202303580.

[9] L. Gorelova, A. Pakhomova, G. Aprilis, Y. Yin, D. Laniel, B. Winkler, S. Krivovichev, I. Pekov, N. Dubrovinskaia, L. Dubrovinsky, *Inorg. Chem. Front.* **2022,** *9*, 1735.

[10] E. Bykova, M. Bykov, A. Černok, J. Tidholm, S.I. Simak, O. Hellman, M.P. Belov, I.A. Abrikosov, H.-P. Liermann, M. Hanfland, V.B. Prakapenka, C. Prescher, N. Dubrovinskaia, L. Dubrovinsky, *Nat. Commun.* **2018**, *9*, 4789.

[11] S. Horstmann, E. Irran, W. Schnick, *Angew. Chem. Int. Ed. Engl.* **1997**, *36*, 1873.

[12] S.D. Kloß, O. Janka, T. Block, R. Pöttgen, R. Glaum, W. Schnick, *Angew. Chem. Int. Ed.* **2019**, *58*, 4685.

[13] T. Giftthaler, P. Strobel, V. Weiler, A. Haffner, A. Neuer, J. Steinadler, T. Bräuniger, S.D. Kloß, S. Rudel, P.J. Schmidt, W. Schnick, *Adv. Optical Mater.* **2023**, 2302343.

[14] M. Somer, W. Carrillo-Cabrera, E.-M. Peters, K. Peters, H.G. von Schnering, *Z. Kristallogr. Cryst. Mater.* **1996**, *211*, 635.

[15] J. Gaudé, L. Haridon, J. Guyader, J. Lang, *J. Solid State Chem.* **1985**, *59*, 143.

[16] O. Reckeweg, H.-J. Meyer, *Z. Anorg. Allg. Chem.* **1999**, *625*, 866.

[17] O. Reckeweg, H.-J. Meyer, *Angew. Chem. Int. Ed*. **1999**, *38*, 1607.

[18] A. Aslandukov, P.L. Jurzick, M. Bykov, A. Aslandukova, A. Chanyshev, D. Laniel, Y. Yin, F.I. Akbar, S. Khandarkhaeva, T. Fedotenko, K. Glazyrin, S. Chariton, V. Prakapenka, F. Wilhelm, A. Rogalev, D. Comboni, M. Hanfland, N. Dubrovinskaia, L. Dubrovinsky, *Angew. Chem. Int. Ed*. **2023**, *62*, e202311516.

[19] L. Brüning, N. Jena, E. Bykova, P.L. Jurzick, N.T. Flosbach, M. Mezouar, M. Hanfland, N. Giordano, T. Fedotenko, B. Winkler, I.A. Abrikosov, M. Bykov, *Angew. Chem. Int. Ed*. **2023,** *62*, e202311519.

[20] E. Niecke, W. Flick, *Angew. Chem. Int. Ed*. **1974**, *13*, 134.

[21] S. Pohl, B. Krebs, *Chem. Ber.* **1977**, *110*, 3183.

[22] O. J. Scherer, N. Kuhn, *Chem. Ber.* **1974**, *107*, 2123.

[23] F. Dielmann, C. E. Moore, A.L. Rheingold, G. Bertrand, *J. Am. Chem. Soc.* **2013**, *135*, 14071.

[24] F. Karau, W. Schnick, *Z. Anorg. Allg. Chem.* **2006**, *632*, 231.

[25] S.D. Kloß, W. Schnick, *Angew. Chem. Int. Ed.* **2019**, *58*, 7933.

[26] Deposition number 2336088 ($Ba_3[PN_3]O$), contain the supplementary crystallographic data for this paper. These data are provided free of charge by the joint Cambridge Crystallographic Data Centre and Fachinformationszentrum Karlsruhe Access Structures service.

[27] J. Lander, *Acta Crystallogr*. **1951**, *4*, 148.

[28] D. G. Park, F. J. DiSalvo, *Bull. Korean Chem. Soc*, **2008**, *29*, 2413.

[29] H. Effenberger, K. Mereiter, J. Zemann, *Z. Kristallogr. Cryst. Mater.* **1981**, *156*, 233.

[30] P.J. Brown, A.G. Fox, E.N. Maslen, M.A. O'Keefe, B.T.M. Willis, in *International Tables for Crystallography Volume C: Mathematical, Physical and Chemical Tables* (Ed.: E. Prince), Springer Netherlands, Dordrecht, **2004**, p. 554.

[31] R. J. Gillespie, *J. Chem. Educ.* **1963**, *40*, 295.

[32] M. Jansen, M. Moebs, *Inorg. Chem.* **1984**, *23*, 4486.

[33] R.D. Shannon, *Acta Crystallogr. Sect. A*, **1976**, *32*, 751.

[34] R.M. Pritzl, N. Prinz, P. Strobel, P.J. Schmidt, D. Johrendt, W. Schnick, *Chem. Eur. J.* **2023**, *29*, e202301218.

[35] S.J. Sedlmaier, D. Weber, W. Schnick, *Z. Kristallogr. - NCS* **2012**, *227*, 1.

[36] S. Wendl, M. Mallmann, P. Strobel, P.J. Schmidt, W. Schnick, *Eur. J. Inorg. Chem.* **2020**, 841.

[37] S.D. Kloß, N. Weidmann, W. Schnick, *Eur. J. Inorg. Chem.* **2017**, 1930.

[38] T. Polenova, R. Gupta, A. Goldbourt, *Anal. Chem.* **2015**, *87*, 5458.

[39] B. Reif, S. E. Ashbrook, L. Emsley, *Nat. Rev. Methods Primers*, **2021**, *1*, 2.

[40] M. Dialer, K. Witthaut, T. Bräuniger, P.J. Schmidt, W. Schnick, *Angew. Chem. Int. Ed.* **2024**, *63*, e202401419.

[41] S. Wendl, W. Schnick, *Chem. Eur. J.* **2018**, *24*, 15889.

[42] S. Vogel, W. Schnick, *Chem. Eur. J.* **2018**, *24*, 14275.

[43] S.J. Sedlmaier, E. Mugnaioli, O. Oeckler, U. Kolb, W. Schnick, *Chem. Eur. J.* **2011**, *17*, 11258.

[44] T. Bräuniger, M. Jansen, *Z. Anorg. Allg. Chem.* **2013**, *639*, 857.

[45] D. Laniel, F. Trybel, A. Néri, Y. Yin, A. Aslandukov, T. Fedotenko, S. Khandarkhaeva, F. Tasnádi, S. Chariton, C. Giacobbe, E. Lawrence Bright, M. Hanfland, V. Prakapenka, W. Schnick, I.A. Abrikosov, L. Dubrovinsky, N. Dubrovinskaia, *Chem. Eur. J.* **2022**, *28*, e202201998.

[46] S. Vogel, M. Bykov, E. Bykova, S. Wendl, S.D. Kloß, A. Pakhomova, S. Chariton, E. Koemets, N. Dubrovinskaia, L. Dubrovinsky, W. Schnick, *Angew. Chem. Int. Ed.* **2019**, *58*, 9060.

[47] W. Schnick, J. Luecke, *J. Solid State Chem.* **1990**, *87*, 101.

[48] E.-M. Bertschler, R. Niklaus, W. Schnick, *Chem. Eur. J.* **2017**, *23*, 9592.

[49] E.-M. Bertschler, C. Dietrich, J. Janek, W. Schnick, *Chem. Eur. J.* **2017**, *23*, 2185.

[50] E. Elzer, P. Strobel, V. Weiler, P.J. Schmidt, W. Schnick, *Chem. Mater.* **2020**, *32*, 6611.

[51] M. Orth, R.-D. Hoffmann, R. Pöttgen, W. Schnick, *Chem. Eur. J.* **2001**, *7*, 2791.

[52] A. Tennstedt, C. Röhr, R. Kniep, *Z. Naturforsch. B,* **1993**, *48*, 794.

[53] S.D. Kloß, A. Haffner, P. Manuel, M. Goto, Y. Shimakawa, P.J. Attfield, *Nat. Commun.* **2021**, *12*, 571.

[54] T. Yamamoto, S. Kikkawa, F. Kanamaru, *J. Solid State Chem.* **1995**, *119*, 161.

[55] SAINT, *Data Integration Software*, Madison, Wisconsin (USA), **1997**.

[56] Bruker-AXS, *APEX3*, Vers. 2016.5-0, Karlsruhe (Germany), **2016**.

[57] Bruker-AXS, *XPREP Reciprocal Space Exploration*, Vers. 6.12, Karlsruhe (Germany), **2001**.

[58] G. M. Sheldrick, *Acta Crystallogr. Sect. C,* **2015**, *71*, 3.

[59] G. M. Sheldrick, *SHELXS-97 Program of the Solution of Crystal Structure*, University of Göttingen, Göttingen (Germany), **1997**.

[60] K. Momma, F. Izumi, *J. Appl. Crystallogr.* **2011**, *44*, 1272.

[61] A. A. Coelho, *TOPAS-Academic v4.1*, Brisbane (Australia), **2007**.

[62] H. M. Rietveld, *J. Appl. Crystallogr.* **1969**, *2*, 65.

[63] L. Bayarjargal, C.-J. Fruhner, N. Schrodt, B. Winkler, *Phys. Earth Planet. Inter.*, **2018**, *281*, 31.

[64] A. Altomare, C. Cuocci, C. Giacovazzo, A. Moliterni, R. Rizzi, N. Corriero, A. Falcicchio, *J. Appl. Crystallogr.* **2013,** *46*, 1231.

[65] M. Nespolo, *Acta Crystallogr. Sect. B,* **2016**, *72*, 51.

[66] A.Y. Toukmaji, J.A. Board, *Comput. Phys. Commun.* **1996**, *95*, 73.

[67] S. P. Ong, W.D. Richards, A. Jain, G. Hautier, M. Kocher, S. Cholia, D. Gunter, V.L. Chevrier, K.A. Persson, G. Ceder, *Comput. Mater. Sci.* **2013**, *68*, 314.

[68] G. Kresse, J. Hafner, *Phys. Rev. B*, **1993**, *47*, 558.

[69] G. Kresse, J. Furthmüller, *Comput. Mat. Sci*. **1996**, *6*, 15.

[70] G. Kresse, J. Furthmüller, *Phys. Rev. B*, **1996**, *54*, 169.

[71] G. Kresse, D. Joubert, *Phys. Rev. B*, **1999**, *59*, 1758.

[72] P. E. Blöchl, *Phys. Rev. B*, **1994**, *50*, 17953.

[73] J. P. Perdew, K. Burke, M. Ernzerhof, *Phys. Rev. Lett.* **1996**, *77*, 3865.

[74] W. H. Press, B. P. Flannery, S. A. Teukolsky, W. T. Vetterling, *Numerical Recipes* , Cambridge University Press, New York (USA), **1986**.

[75] P. Hohenberg, W. Kohn, *Phys. Rev. B*, **1964,** *136*, 864.

[76] S. J. Clark, M. D. Segall, C. J. Pickard, P. J. Hasnip, M. J. Probert, K. Refson, M. C. Payne, *Z. Kristallogr.* **2005**, *220*, 567.

[77] K. Lejaeghere, G. Bihlmayer, T. Björkman, P. Blaha, S. Blügel, V. Blum, D. Caliste, I. E. Castelli, S. J. Clark, A. Dal Corso, *Science*, **2016**, *351*, aad3000.

[78] H. J. Monkhorst, J. D. Pack, *Phys. Rev. B*, **1976**, *13*, 5188.

[79] K. Refson, P. R. Tulip, S. J. Clark, *Phys. Rev. B*, **2006**, *73*, 155114.

[80] K. Miwa, *Phys. Rev. B*, **2011**, *84*, 094304.

8 Summary

The research objective of this dissertation is divided into two main parts: Firstly, the explorative investigation and characterization of novel alkaline earth (oxo)nitridophosphates with the focus on their potential luminescent properties when doped with Eu^{2+}. Secondly, the development of new synthetic strategies to extend the established synthesis portfolio of nitridophosphate chemistry in general. Chapter 6 addresses both aspects in parallel.

In the first part, covered in Chapter 2 and 3, established high-pressure/high-temperature (HP/HT) synthesis methods were employed for the deliberate introduction of Mg^{2+} not only as counter cation (*CC*) but also as a network forming cation (*NFC*). Herein, high-pressure/high-temperature conditions are used to prevent the thermal decomposition of the targeted compounds, following *Le Chatelier`s* principle.

Chapters 4 to 7 focus on novel or further developing synthetic strategies for the preparation of imido-, oxo- and pure nitridophosphates or nitridophosphate oxides, aiming to expand the portfolio of synthesis routes for nitridophosphates. A significant amount of attention was dedicated to enhancing synthetic control over structural details, which is usually limited by conventional bottom-up syntheses. In this context, the successful deprotonation of phosphorus nitride imide polymorphs, while fully preserving the three-dimensional anionic framework, marked a significant enhancement (Chapter 4). Additionally, a double salt approach was employed for nitridophosphates for the first time, highlighting an innovative strategy (Chapter 5). Furthermore, the extension of the previously investigated ion exchange reaction to the precursors of nitridophosphate-based Li ion conductors represents a targeted continuation of this promising strategy (Chapter 6). It was also demonstrated that the fundamental building units (*FBU*s) for nitridophosphate-based materials can be broadened beyond the previously observed motifs (e.g. tetrahedra) through the careful selection of starting materials (Chapter 7). This finding emphasizes the potential for developing new structural motifs within this class of materials. More detailed information on the specific publications arising from this thesis is provided below in the individual chapter summaries.

8.1. From Framework to Layers Driven by Pressure – The Monophyllo-Oxonitridophosphate β-$MgSrP_3N_5O_2$ and Comparison to its α-Polymorph

Published in: R.M. Pritzl, N. Prinz, P. Strobel, P.J. Schmidt, D. Johrendt, W. Schnick, *Chem. Eur. J.* **2023**, *29*, e202301218.

Access via: 10.1002/chem.202301218

Reprinted at: Chapter 2, Supporting Information in Chapter 10.2

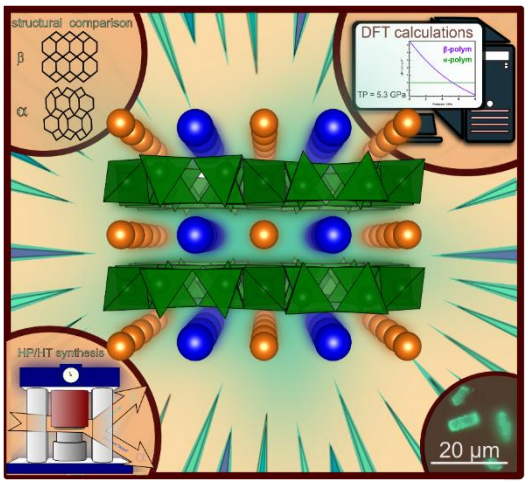

Oxonitridophosphates exhibit the potential for broad structural diversity and associated properties. The new high-pressure polymorph β-$MgSrP_3N_5O_2$:Eu^{2+}, an oxonitridophosphate with remarkable luminescent properties, was successfully synthesized using high-pressure, high-temperature methods (multianvil technique: 7 GPa, 1000 °C). Structural elucidation from single-crystal X-ray diffraction data revealed that β-$MgSrP_3N_5O_2$ crystallizes in the orthorhombic space group *Cmme* (no. 67), a = 8.8109(6), b = 12.8096(6), c = 4.9065(3) Å, Z = 4), exhibiting a layered structure isotypic to the mineral johachidolite. Further, a novel synthesis protocol for α-$MgSrP_3N_5O_2$ was developed. The elemental composition of the title compound was confirmed using EDX spectroscopy, while MAS NMR measurements validated the proposed structural model. Additionally, low-cost crystallographic calculations (CHARDI and MAPLE) further corroborate these findings. Density functional theory (DFT) calculations confirmed the energetic preference of the β-polymorph at elevated pressure, with a possible phase transition from α- to β-$MgSrP_3N_5O_2$ at approximately 5.3 GPa. The luminescence properties of Eu^{2+}-doped samples of both, α- and β-$MgSrP_3N_5O_2$ were systematically investigated, revealing blue emission for α-$MgSrP_3N_5O_2$ (λ_{max} = 438 nm) and cyan emission for β-$MgSrP_3N_5O_2$ (λ_{max} = 502 nm). This highlights β-$MgSrP_3N_5O_2$ as a promising material for filling the "cyan gap" (480–520 nm) in phosphor-converted white light-emitting diode (pc-wLEDs) applications.

8.2. Tunable Narrow-Band Cyan-Emission of Eu^{2+}-doped Nitridomagnesophosphates $Ba_{3-x}Sr_x[Mg_2P_{10}N_{20}]:Eu^{2+}$ (x = 0–3)

Published in: R.M. Pritzl, M.M. Pointner, K. Witthaut, P. Strobel, P.J. Schmidt, W. Schnick, *Angew. Chem. Int. Ed.* **2024,** *63*, e202403648; *Angew. Chem.* **2024**, *136*, e202403648.

Access via: 10.1002/ange.202403648

Reprinted at: Chapter 3, Supporting Information in Chapter 10.3

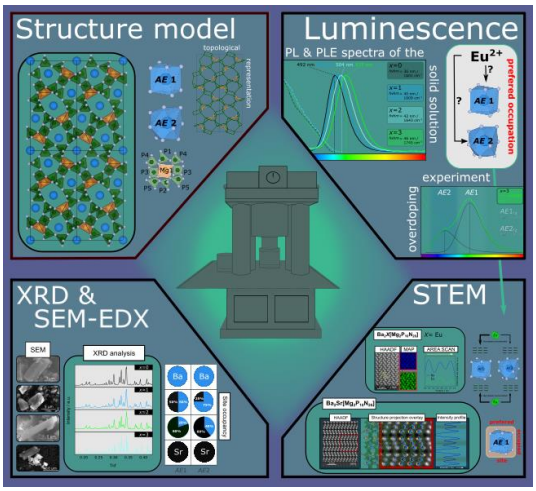

Tetrahedron-based nitrides exhibit diverse properties with significant industrial potential. Especially highly condensed nitridophosphates demonstrate remarkable properties like hardness or luminescence properties when doped with Eu^{2+}. The preparation of the first nitridomagnesophosphate solid solution series $Ba_{3-x}Sr_x[Mg_2P_{10}N_{20}] : Eu^{2+}$ (x=0–3), synthesized by a high-pressure/high-temperature approach using the multianvil technique (3 GPa, 1400 °C) is presented. Starting from the binary nitrides P_3N_5 and Mg_3N_2 and the respective alkaline earth azides, Mg was successfully incorporated into the P/N framework, resulting in an increased degree of condensation (κ = 0.6), the highest observed value for alkaline earth nitridophosphates. The crystal structures were determined by single-crystal and powder X-ray diffraction, supported by energy-dispersive X-ray spectroscopy (EDX) and solid-state NMR. Band gaps and Debye temperatures were calculated using DFT methods. Eu^{2+}-doped samples of the solid solution series show a tunable narrow-band emission from cyan to green (492–515 nm), which is attributed to the preferred doping of a single crystallographic site. This was experimentally confirmed by overdoping experiments and STEM-HAADF studies on the series as well on the stoichiometric compound $Ba_2Eu[Mg_2P_{10}N_{20}]$ with additional atomic resolution energy-dispersive X-ray spectroscopy (EDX) mapping.

8.3. $ZnH_2P_4N_8$: Case Study on Topochemical Imidonitridophosphate High-Pressure Synthesis

Published in: R.M. Pritzl, J. Steinadler, A.T. Buda, S. Wendl, W. Schnick, *Chem. Eur. J.* **2024**, e202402741.

Access via: 10.1002/chem.202402741

Reprinted at: Chapter 4, Supporting Information in Chapter 10.4

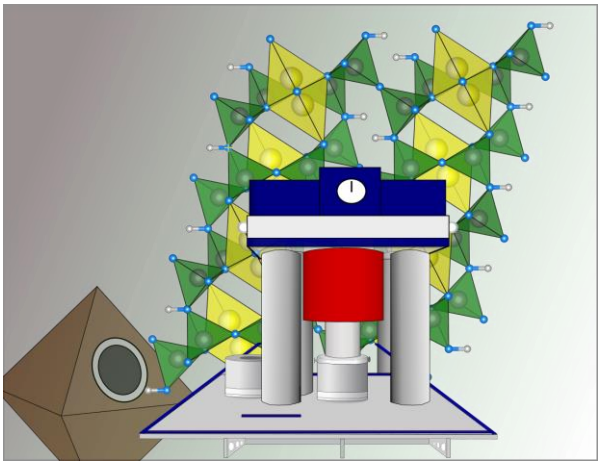

The preparation and structure elucidation of the first quaternary transition metal imidonitridophosphate $ZnH_2P_4N_8$ is presented. Employing the multianvil technique, the title compound was synthesized in high-pressure high-temperature reactions. Two different synthesis protocols are introduced: Direct synthesis from binary nitrides and ammonium azide, and a topochemical deprotonation of the high-pressure polymorph β-HPN_2 using $ZnCl_2$:

$$2\ Zn_3N_2 + 8\ P_3N_5 + 3\ NH_4N_3 \rightarrow 6\ ZnH_2P_4N_8 + 4\ N_2 \qquad (8.3.1)$$

$$x\ ZnCl_2 + 4\ \beta\text{-}HPN_2 \rightarrow Zn_xH_{4-2x}P_4N_8 + 2x\ HCl \qquad (8.3.2)$$

The crystal structure was elucidated by single-crystal X-ray diffraction (SCXRD), energy-dispersive X-ray spectroscopy (EDX), powder X-ray diffraction (PXRD), and solid-state NMR. In addition, the presence of H as part of an imide group was confirmed by FTIR spectroscopy. As expected for a product obtained by a topochemical reaction, the crystal structure of $ZnH_2P_4N_8$ shows the same network topology as the precursor β-HPN_2. The potential of this defunctionalization approach for controlling the N–H content is demonstrated by the preparation of partially deprotonated intermediates $Zn_xH_{4-2x}P_4N_8$ ($x \approx 0.5, 0.85$). NMR studies on the partially defunctionalized intermediates provided insights into the local structure and allows to propose a topotactic reaction mechanism.

8.4. $CaLi_2PN_3$ – A Quaternary Chain-Type Nitridophosphate by Medium-Pressure Synthesis

Published in: R.M. Pritzl, N. Fahle, K. Witthaut, S. Wendl, W. Schnick, *Chem. Eur. J.* **2024**, *30*, e202402521.

Access via: 10.1002/chem.202402521

Reprinted at: Chapter 5, Supporting Information in Chapter 10.5

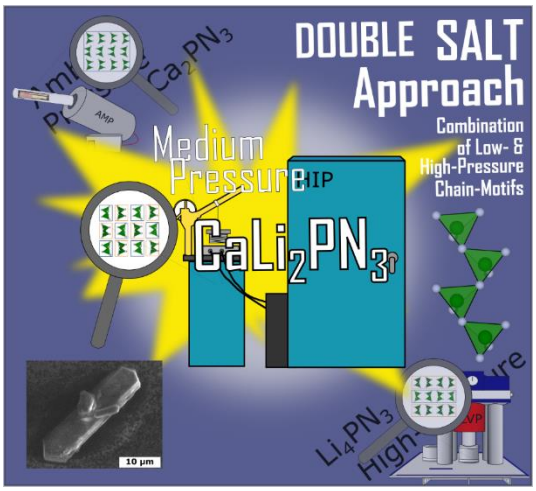

Multinary nitrides often necessitate thorough investigation due to the competition with the thermodynamically more stable binary and ternary compounds. Additionally, synthetic control of structural details is typically limited by conventional bottom-up synthesis methods. In this context, the successful synthesis of the first quaternary alkaline earth lithium nitridophosphate $CaLi_2PN_3$ under medium-pressure (MP) conditions is reported. Various synthesis protocols were used for the preparation of $CaLi_2PN_3$, including the novel nitridophosphate double salt approach.

$$Ca_2PN_3 + Li_4PN_3 \rightarrow 2\ CaLi_2PN_3 \qquad (8.4.1)$$

Single-crystal X-ray diffraction data allowed to solve the structure in the monoclinic space group *C*2/*c* (no. 15) with $a = 11.3397(4)$, $b = 11.5881(4)$, $c = 4.9408(2)$ Å and $\beta = 113.966(1)°$. The structure model was confirmed by Rietveld refinement, solid-state NMR spectroscopy, EDX measurements and low-cost crystallographic calculations. The crystal structure can be described as a novel cation-filling variant of $GePN_3$, which crystallizes in the $CoGeO_3$ structure type. DFT calculations reveal the electronic band structure (indirect band gap: ~3.35 eV) and formation energies calculations on $CaLi_2PN_3$ and the two separate nitridophosphates Li_4PN_3 and Ca_2PN_3 contribute to the understanding of the formation during synthesis.

8.5. Adamantane-Type Nitridophosphate Phosphors $AE_xLi_{10-2x}P_4N_{10}:Eu^{2+}$ via Medium-Pressure Ion-Exchange Reactions

Submitted to: R.M. Pritzl, A.T. Buda, K. Witthaut, P.J. Schmidt, W. Schnick, *Angew. Chem. Int. Ed.* **2024**, e202420565*; Angew. Chem.* **2024,** e202420565.

Access via: 10.1002/anie.202420565

Reprinted at: Chapter 6, Supporting Information in Chapter 10.6

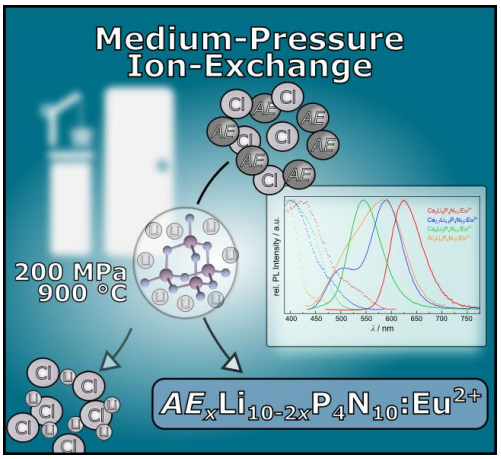

Nitridophosphates have gained attention as promising host materials for solid-state lighting, with their industrial significance growing due to advances in medium-pressure (MP) synthetic methods, such as ammonothermal synthesis and hot isostatic pressing (HIP). This study presents the synthesis and characterization of the quaternary compounds $Ca_xLi_{10-2x}P_4N_{10}$ (x = 2, 2.7, 4) and $Sr_3Li_4P_4N_{10}$, prepared via a simplified ion exchange reaction under MP conditions (Eq. 8.5). These compounds are derived from the nitridophosphate-based lithium ion conductor $Li_{10}P_4N_{10}$, preserving its $[P_4N_{10}]^{10-}$ structural motif while enabling the incorporation of divalent alkaline earth cations (Ca^{2+}/Sr^{2+}), offering potential doping sites for Eu^{2+}.

$$x\,AECl_2 + Li_{10}P_4N_{10} \rightarrow AE_xLi_{10-2x}P_4N_{10} + 2x\,LiCl \qquad (8.5)$$

(AE = Ca, Sr; x(Ca) = 2, 2.7, 4; x(Sr) = 3)

The crystal structures were determined through X-ray diffraction data and validated via solid-state MAS NMR, energy-dispersive X-ray spectroscopy (EDX) on single particles, and inductively coupled plasma (ICP) analysis of the bulk materials. Density functional theory (DFT) calculations and optical analyses of undoped samples, conducted via diffuse reflectance spectroscopy, reveal band gaps meeting the criteria for pc-LED applications (≥ 4 eV). Exploring the luminescence behavior of Eu^{2+}-doped samples reveals exciting luminescence and thermal behavior. Given the promising luminescence characteristics for potential applications, $Ca_2Li_6P_4N_{10}:Eu^{2+}$ was subjected to a more detailed examination with respect to state-of-the-art phosphors like CASN ($CaAlSiN_3:Eu^{2+}$), SCASN ($(Sr/Ca)AlSiN_3:Eu^{2+}$), as well as $Sr[LiAl_3N_4]:Eu^{2+}$ (SLA) and $Sr[Li_2Al_2O_2N_2]:Eu^{2+}$ (SALON).

8.6. Trigonal Planar $[PN_3]^{4-}$ Anion in the Nitridophosphate Oxide $Ba_3[PN_3]O$

Published in: R.M. Pritzl, K. Witthaut, M. Dialer, A.T. Buda, V. Milman, L. Bayarjargal, B. Winkler, W. Schnick., *Angew. Chem. Int. Ed.* **2024**, *63*, e202405849; *Angew. Chem.* **2024**, *136*, e202405849.

Access via: 10.1002/anie.202405849

Reprinted at: Chapter 7, Supporting Information in Chapter 10.7

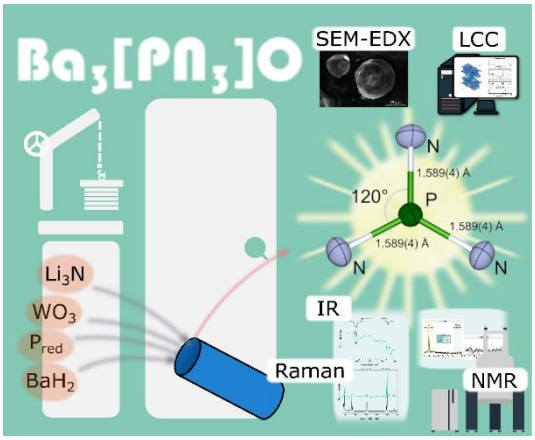

Nitridophosphates, characterized by their primary structural motif of isolated or condensed PN_4 tetrahedra, fulfill many requirements for high-performance materials. Their properties are closely linked to their structural diversity, which is primarily shaped by this specific building block. The first alkaline earth nitridophosphate oxide $Ba_3[PN_3]O$, featuring a trigonal planar $[PN_3]^{4-}$ anion, was successfully synthesized by medium-pressure/high-temperature synthesis (MP/HT) using a hot isostatic press, expanding the structural diversity tremendously. Its crystal structure was elucidated from single-crystal X-ray diffraction data ($R\bar{3}c$ (no. 167), a = 7.8315(3), c = 16.9865(5) Å, Z = 6) and confirmed by Rietveld refinement on a representative powder X-ray diffraction pattern. Various analytical methods, including EDX measurements, solid-state NMR and vibrational spectroscopy (Raman, IR), as well as low-cost crystallographic calculations (*LCC*), confirmed the structure model and provide benchmark values for these structural motif for the future. The title compound is discussed in the context of fundamental structural chemistry of inorganic phosphorus chemistry, as a trigonal-planar N-coordinated $[PN_3]^{4-}$ anion had been an unprecedented, but much sought-after structural motif, previously.

9 Discussion and Outlook

As outlined in Chapter 8, this dissertation focuses on fundamental research and the development of innovative synthetic strategies for the preparation of application-oriented nitridophosphate-based compounds. By employing medium- & high-pressure techniques, this work aims to uncover potential structure-property relationships and gain deeper insights into the characteristics of the synthesized compounds. Following the successful synthesis of novel compounds during this dissertation, the initial focus was on structure elucidation by XRD methods. This fundamental characterization was subsequently complemented by a multitude of analytical techniques and theoretical calculations, including NMR, IR and Raman spectroscopy, electron microscopy (SEM/STEM) as well as low-cost calculations such as MAPLE, CHARDI, BVS and MBE, along with DFT calculations. The addition of $EuCl_2$/EuN as a dopant often resulted in Eu^{2+} luminescence, which was not only used for identifying new compounds in phase mixtures ("means to an end") but also specifically applied and investigated once suitable host lattices were identified. Therefore, in this chapter, the findings are contextualized and discussed.

9.1 Progress in Synthetic Approaches

Nitridophosphates and their related representatives are presumably the most extensively studied nitride substance class. Over the past three decades, various synthesis pathways have been developed under elevated pressure (Figure 9.1).[1] Key synthetic approaches include:

A) Nitride route: The reaction of the binary nitride P_3N_5 and respective metal nitride is the most straightforward synthetic approach to nitridophosphates (leading to e.g. AE_2PN_3 (*AE* = Be, Mg, Ca, Zn). This strategy is limited by unavailability of some binary nitrides.[2-5]

B) Azide route: The reaction of alkaline earth metal azides ($AE(N_3)_2$) in combination with P_3N_5 resulted in some highly condensed representatives (e.g. AEP_2N_4 and AEP_8N_{14} (*AE* = Ca, Sr, Ba)).[6-8]

C) Mineralizer-assisted route: The strategic introduction of HCl or HF during the synthesis process, achieved through the deliberate addition of NH_4Cl, NH_4F, or the combined use of $(PNCl_2)_3$ and NH_4N_3, has proven effective in activating a range of refractory nitrides (e.g. h-BN, Si_3N_4, and TiN).[9-11]

D) Li_3N self-flux: An excess of Li_3N during synthesis, which can either be added directly as starting material or formed explicitly during synthesis (*in situ*), has successfully produced numerous Li/P/N compounds (e.g. $Li_{12}P_3N_9$).[12,13]

E) Metathesis route: The reaction of $LiPN_2$ with transition metal or rare-earth metal halides generates LiCl *in situ*, which not only acts as a flux but also serves as a driving force for the formation of various *TM/RE* nitridophosphate (e.g. $RE_2P_3N_7$ (*RE* = Pr, Sm, Eu, Ho, Yb)).[14]

F) Ion-exchange / Post-synthetic modification routes: The reaction of pre-synthesized alkaline earth nitridophosphates with halides of lighter alkaline earth homologues represents a specific form of metathesis. In this reaction, the preservation (in the case of ion-exchange) or rearrangement of condensed P/N motifs (post-synthetic modification) can occur arbitrarily (e.g. $CaH_4P_6N_{12}$).[4]

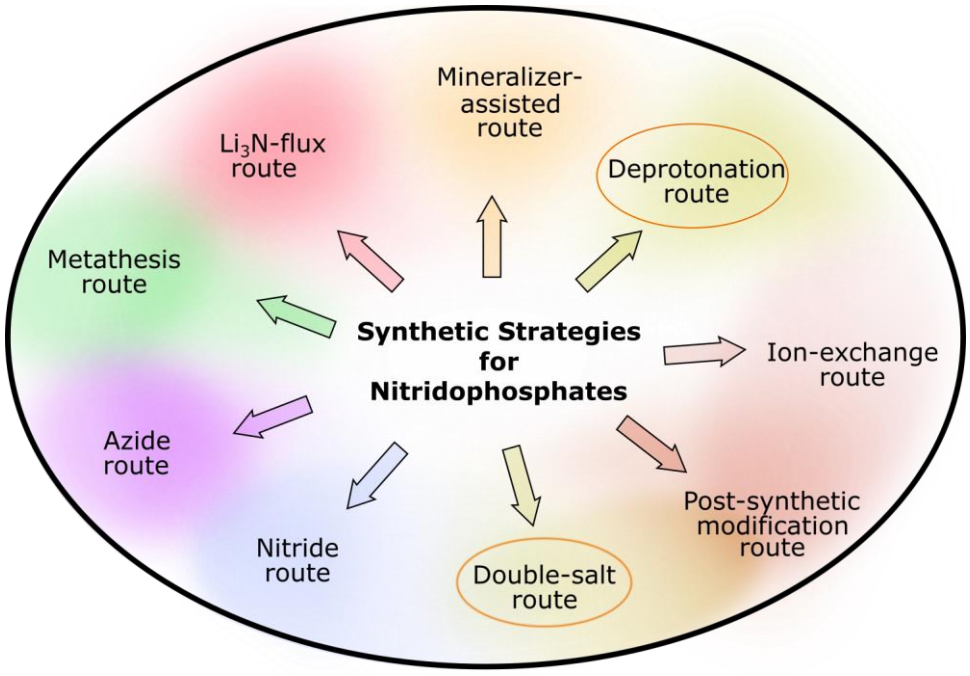

Figure 9.1. Overview of the synthetic routes established for nitridophosphate synthesis, as well as newly developed routes within this work (highlighted with an orange circle). The synthesis strategies of ion exchange reaction and post-synthetic modification (F) are listed separately despite the same process due to the resulting structural characteristics of the products.

The last method, in particular, offers a certain degree of control over the structural motifs in nitridophosphate synthesis (*top-down strategy*). Starting from this approach, the portfolio of

nitridophosphate synthesis was expanded during this thesis, with a particular emphasis on the preservation of the anionic P/N motifs.

The mineralizer-assisted route was extended to phosphorus nitride imides via high-pressure deprotonation of β-HPN_2, where the anionic 3D framework was fully preserved through a topochemical reaction. This approach can be seen as a combination of both the mineralizer-assisted and the ion exchange route. The release of HCl promotes crystal growth (a key advantage of the mineralizer-assisted route), while the cations of the pre-synthesized nitridophosphate-based compound are exchanged (2 $H^+ \rightarrow Zn^{2+}$). Notably, no P–N bond cleavage and reformation occurs, preserving the original P/N motif. This assumption still needs to be verified in future work. By varying the equivalents of metal halides ($ZnCl_2$), several intermediates ($Zn_xH_{4-2x}P_4N_8$, with $x \approx 0.5, 0.85, 1$) were successfully synthesized. In contrast to classical bottom-up reactions (A–E) and especially the overarching metathesis reaction, this method allows access not only to thermodynamically stable but also to metastable phases. This contrasts with the typical outcome of classical bottom-up approaches, where thermodynamically stable phases are normally obtained. Consequently, this route offers a significant advantage for the development of future compounds, particularly in terms of the targeted modification of properties. A continuation of this synthesis approach to the high-pressure polymorphs β-/γ-HP_4N_7 seems obvious, whereby an extension to ambient pressure reactions appears promising.[15,16]

The double salt synthesis, applied for the first time in nitridophosphate synthesis using the example of $CaLi_2PN_3$, can be regarded as a distinct and separate synthesis route. It combines the anionic structural motifs of nitridophosphates through a straightforward solid/solid reaction under elevated pressure. Since this approach uses pre-synthesized nitridophosphate precursors, it shares certain similarities with the post-synthetic-modification route. However, in contrast to that route, no cation exchange occurs. Instead, the cations and anionic chain motifs are combined in a novel compound. As a result, this synthetic strategy can be seen as an overlap of the post-synthetic-modification and the nitride route in the broadest sense. The success achieved in the double salt synthesis of *catena*-type nitridophosphates may be extended by the synthesis of a theoretical *catena*-type compound "$Ca_2Sr_3P_4N_{10}$". In this nitridophosphate, infinite *zweier* single chains of Ca_2PN_3 and infinite *dreier* double chains of $Sr_3P_3N_7$ could exist next to each other in a single compound.

And finally, the synthesis of $AE_xLi_{10-2x}P_4N_{10}$ (*AE* = Ca, x = 2, 2.7, 4; *AE* = Sr, x = 3) which might not be a development of a new synthesis protocol but rather the most obvious application of the ion exchange reaction route in the context of nitridophosphate chemistry. Here, the ion exchange

reaction was carried out on a nitridophosphate-based Li ion conductor, namely $Li_{10}P_4N_{10}$, with $AECl_2$ (*AE* = Ca, Sr). This reaction enabled the incorporation of pre-synthesized structural P/N motifs (adamantane-type $[P_4N_{10}]^{10-}$ anions) in the synthesis of alkaline earth nitridophosphates, which could not be achieved using the previously mentioned bottom-up strategies. Furthermore, the competition from thermodynamically more stable binary or ternary compounds that occurs by bottom-up approaches is elegantly circumvented. The LiCl formed during the reaction acts both as a flux and as a driving force for the formation of the desired products ($\Delta H^0(CaCl_2) < \Delta H^0(SrCl_2) < 2 \times \Delta H^0(LiCl)$).[17] The successful synthesis and characterization of four new compounds through this approach during the course of this work provides evidence that a transfer of this procedure to other nitridophosphate-based Li ion conductors is likely to yield a substantial number of new compounds in the future. Thus, it seems to be a matter of time before anionic motifs, such as the tricyclic $[P_6N_{16}]^{18-}$ anions, which have so far been considered unique to lithium nitridophosphates, are also observed in alkaline earth nitridophosphates. In addition, this route could lead to the incorporation of new structural motifs in alkaline earth nitride phosphates that were not observed at previous degrees of condensation. At a degree of condensation of $\kappa = 1/3$, for example, it is conceivable that the stabilization of $[P_3N_9]^{12-}$ anions (derived from $Li_{12}P_3N_9$) could be incorporated instead of the already observed infinite chains. Furthermore, at $\kappa = 4/7$, the formation of three-dimensional networks (starting from LiP_4N_7) instead of the known layered structures (e.g. SrP_8N_{14}) could be achieved (Figure 9.2).[8,18] The extensive variety of known lithium nitridophosphate-based compounds including (oxo)nitridophosphates (e.g. $Li_{8+x}P_3O_{10-x}N_{1+x}$ ($x = 1.4(5)$), $Li_{27-x}[P_4O_{7+x}N_{9-x}]O_3$ ($x \approx 1.9(3)$) and $Li_{5+x}P_2O_{6-x}N_{1+x}$ with $x \approx 0.9$) highlights the theoretical potential of this synthesis route alone, with just a few examples from our research group.[19-21]

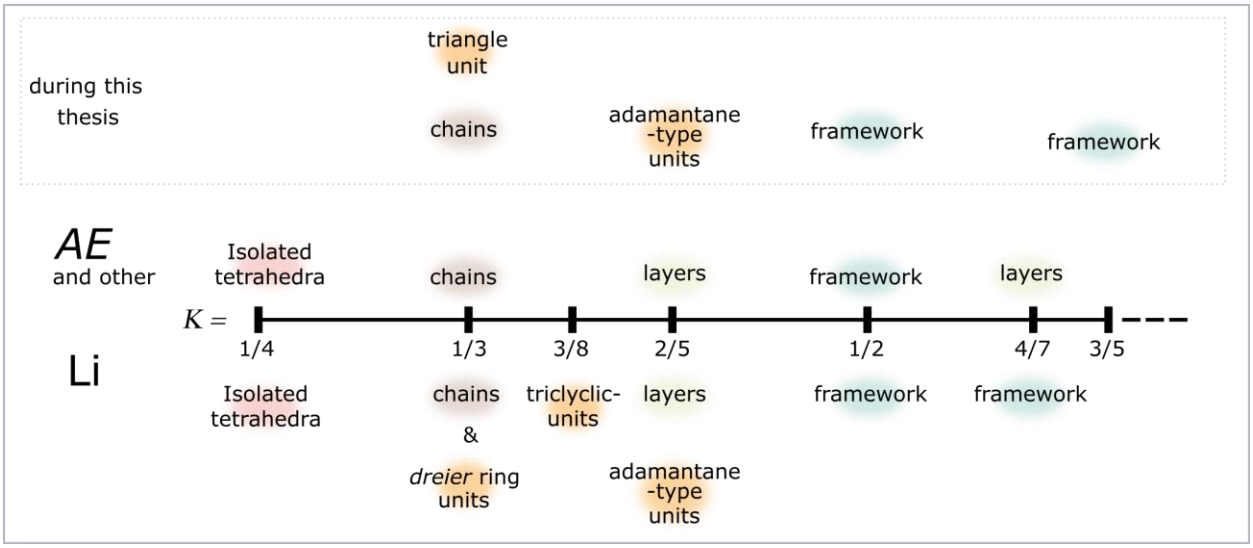

Figure 9.2. Frequently recurring degrees of condensation κ with their observed structural motifs for alkaline earth metal (*AE*) nitridophosphates (and other related representatives) and lithium nitridophosphates (Li). In addition, the P/N motifs for *AE* nitridophosphates with respective κ prepared within the scope of this thesis are listed.[5,6,8,13,18,22-25]

9.2 Structural Diversity of Nitridophosphate-based Compounds

Apart from the above mentioned investigation of novel synthetic approaches, this cumulative thesis deals with investigations on numerous novel nitridophosphates and related compounds: The oxonitridophosphate β-$MgSrP_3N_5O_2$, the nitridophosphate oxide $Ba_3[PN_3]O$, the imidonitridophosphate $Zn_xH_{4-2x}P_4N_8$ (x = 0.5, 0,85, 1) the nitridomagnesophosphates $Ba_{3-x}Sr_x[Mg_2P_{10}N_{20}]$ (x = 0–3), and the pure nitridophosphates $CaLi_2PN_3$ and $AE_xLi_{10-2x}P_4N_{10}$ (*AE* = Ca, x = 2, 2.7, 4; *AE* = Sr, x = 3). The discovered compounds exhibit not only structures that are isotypic to known compounds but also novel structure types, greatly expanding the structural diversity within the nitridophosphates-based materials and highlighting that their structural potential remains far from fully explored. Not only the substitution of alkaline earth metal ions but also transition metal ions (*TM*) or rare earth metal ions (*RE*) may be possible in this compounds. The high-pressure deprotonation route is particularly promising, as the synthesis temperature used for the preparation of transition metal imidonitridophosphate $ZnH_2P_4N_8$ (800 °C) is significantly lower than that of literature-reported *TM/RE* nitridophosphates (1200°C–1400°C). This strategy should reduce the potential for the formation of thermodynamically stable *TM/RE* phosphides and enable the formation of possible target phases.[26]

9.2.1 Mimicking of Minerals

Structural diversity is a key aspect in materials science. It is essential to deliberately alter new or known structures. Due to the isoelectronic relationship between the element combinations Si/O and P/N, it can be inferred that the newly synthesized nitridophosphates exhibit structural similarities to the class of oxosilicates. This is evident, on one hand, from the comparison of the parent compounds SiO_2, PON and HPN_2, along with their high-pressure modifications.[15,27-32] On the other hand, various mineral analogs of nitridophosphates also illustrate this similarity. Notable examples include the mica-like MP_6N_{11} (M = Al, In) and $AESi_3P_4N_{10}(NH)_2$ (AE = Mg, $Mg_{0.94}Ca_{0.06}$, Ca, Sr), as well as wurtzite-type M_2PN_3 (M = Be, Mg, Zn) or the frequently observed megacalsilite-type (a mineral of $KAlSiO_4$) within nitridophosphates with $\kappa = ½$ (e.g. AEP_2N_4, AE = Ca, Sr).[2,3,5,6,33-35] During this dissertation, the first johachidolite-type oxonitridophosphate β-$MgSrP_3N_5O_2$ was successfully synthesized using HP/HT techniques. It would be presumptuous to assert that the goal was specifically to create a nitridophosphate-based compound crystallizing in this structure type. Nonetheless, the discovery of this compound was facilitated by a cross-comparison of structures across different substance classes, depending on the degree of condensation (κ) as discussed in Chapter 2. The successful deduction of a layer-like nitridophosphate from this approach suggests that future synthesis strategies should adopt a reverse methodology: starting by examining the crystal structures of oxidic minerals with recurring structural types or motifs, and then specifically targeting the synthesis of nitridophosphates with the same degree of condensation κ.

9.2.2 Investigations on New Compound Classes

The discovery of silicon phosphorus nitride ($SiPN_3$) by Lücke *et al.* demonstrated that Si can be integrated into the tetrahedral centers of nitridophosphate networks, revealing the potential for creating mixed-element networks within these structures.[36] This development has paved the way for designing advanced materials with tailored properties by combining different elements within the same framework. Consequently, this initiated investigations into mixed nitridosilicatephosphates, starting with the work of Eisenburger *et al.* (e.g. $AESiP_3N_7$ with AE = Sr, Ba) and further systematic research in detail by Dialer *et al.* (e.g. $Sr_5Si_2P_6N_{16}$).[37,38] Apart from these findings, the incorporation of beryllium (Be), magnesium (Mg), and boron (B) as NFCs in phosphorus nitrides, namely in Be_2PN_3, BeP_2N_4, Mg_2PN_3 and BP_3N_6, indicates a growing interest in expanding the diversity of tetrahedral networks.[3,5,9,39] However, in the

substance class of nitridophosphates no other mixed tetrahedral networks than nitridosilicatephosphates (Si & P) had been explored prior to this work. The successful preparation of the solid-solution series $Ba_{3-x}Sr_x[Mg_2P_{10}N_{20}]$ (x = 0–3) has opened the class of nitridomagnesophosphates, by integrating magnesium (Mg) alongside phosphorus (P) in nitride tetrahedral networks. Given that Mg has already been successfully observed in in phosphorus nitrides in the case of the distorted wurtzite-like Mg_2PN_3, this suggests that the field is nearing the development of multinary nitridoberyllophosphates and nitridoborophosphates, if parallels can be drawn with the beryllium and boron phosphorus nitrides (e.g. Be_2PN_3, BP_3N_6) already mentioned.

9.2.3 Novel Structural Motifs

The discovery of $Ba_3[PN_3]O$, a compound featuring trigonal-planar $[PN_3]^{4-}$ anions indicates that there are still unexplored structural motifs that could stimulate future investigations. One promising research avenue could be the targeted examination of these anions' properties in different chemical environments, such as by incorporating them into other nitridophosphate frameworks or using them as structural building blocks in "hybrid materials". The double salt approach presented in this work could prove particularly useful for this task. Inspired by the nitridoborophosphate $Li_{47}B_3P_{14}N_{42}$, which contains three different nitridophosphate-based anions simultaneously ($[P_3N_9]^{12-}$, $[P_4N_{10}]^{10-}$ and $[B_3P_3N_{13}]^{15-}$), it now seems feasible to incorporate $[PN_3]^{4-}$ alongside other isolated anions.[40] Systematic research into such new structures could provide important insights into their stability, reactivity and potential applications. Based on $[B_3P_3N_{13}]^{15-}$, the development of purely P/N-based anions that combine the trigonal planar motif with PN_4 tetrahedra now also appears possible for the future. However, the greatest challenge moving forward will remain the stabilization of this structural motif in other compounds than $Ba_3[PN_3]O$.

9.2.4 Nitridophosphate-based Compounds as Luminescent Materials

Nitridophosphate-based compounds demonstrate considerable potential as luminescent materials when doped with Eu^{2+}. Prior to this work, several nitridophosphate-based phosphors had already been investigated, with observed emission colors across a broad spectral range. In the course of this thesis, ten additional representatives were successfully prepared, extending the coverage across the visible spectrum. Notably, both very narrow emission half-widths, particularly in the

cyan range (e.g. *fwhm* = 36 nm /1601 cm^{-1} in $Ba_3[Mg_2P_{10}N_{20}]:Eu^{2+}$), as well as very broad half-widths such as 122 nm/3812 cm^{-1} in $Sr_3Li_4P_4N_{10}:Eu^{2+}$ were observed (Figure 9.3).

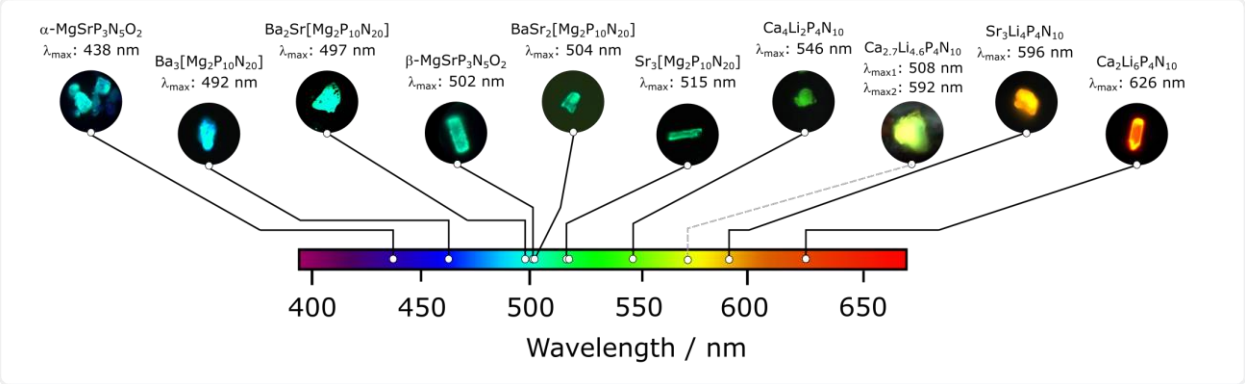

Figure 9.3. Illustration of the emission maxima (λ_{max}) positions of the discovered compounds in the visible spectral range.

Additionally, the primary focus was on the comprehensive investigation of the luminescence centers and their contribution to the observed emission profiles. Beyond theoretical considerations, factors such as the average *AE*–N distances, polyhedron volumes, coordination numbers (*CN*), and the symmetry of the activator site environment were taken into account. For example, these aspects could provide an explanation for the observed red-shift when comparing the emissions of the α- and β-$MgSrP_3N_5O_2:Eu^{2+}$ polymorphs.

In the solid solution series $Ba_{3-x}Sr_x[Mg_2P_{10}N_{20}]:Eu^{2+}$, where two crystallographically distinct *AE* sites (potential doping sites) are present, these considerations were experimentally investigated not only through overdoping experiments, but also via atomically resolved STEM-HAADF investigations, revealing that Eu^{2+} preferentially occupies only one of the available cation sites.[41] Along with β-$MgSrP_3N_5O_2$, these phosphors show the potential to close the cyan gap in pc-LEDs. Furthermore, a variation in the Ba/Sr ratio for $Ba_{3-x}Sr_x[Mg_2P_{10}N_{20}]:Eu^{2+}$ (x = 0–3) enables precise tuning of λ_{max} between 492 nm and 515 nm. Due to the high-pressure synthesis, however, it remains to be seen whether these results will have a direct impact on current applications in optoelectronics.

Moreover, some of the discovered phosphors exhibit luminescence characteristics that are comparable to, or even competitive with, established commercial phosphors such as $Ca_2Li_6P_4N_{10}:Eu^{2+}$ in comparison to $CaAlSiN_3:Eu^{2+}$ (CASN) and (Sr, Ca)$AlSiN_3:Eu^{2+}$ (SCASN).[42,43] These compounds, prepared via ion exchange starting from Li-ion conductors,

hold significant potential for optimization.[44-46] The resulting structures, and consequently their luminescence properties, can be progressively altered through the simultaneous use of different *AE* halides. In addition, subsequent modification (using the post-synthetic modification route), is possible, as initial promising approaches have shown. Following the successful demonstration of the proof-of-principle for nitride MgN_4/PN_4 tetrahedral systems in this work, and considering the significant potential of the *AE*-Li-P-N system for phosphor materials, the question arises whether these two substance classes can be used, particularly in the context of phosphor development, for mimicking host-structures of established phosphors. For example, established phosphors such as the aforementioned CASN or SLA ($Sr[LiAl_3N_4]:Eu^{2+}$) could be recreated by formal substitution of the tetrahedral centers on a nitridophosphate basis.[47] Therefore, compounds with theoretical sum formulas such as "$Ca[MgPN_3]:Eu^{2+}$" or "$Sr[LiMg_2PN_4]:Eu^{2+}$" can be named.

9.3. Concluding Remarks

Opening up innovative synthesis routes to multifaceted and previously unexplored materials naturally raises more questions than can be answered within the scope of this dissertation. However, raising questions is at the core of all scientific research, and, as noted in the introduction, it is also the driving force behind technological progress. The results presented here not only significantly expand the synthesis portfolio and structural diversity of nitridophosphates, but also lay the groundwork for future nitridophosphate-based applications, especially in the context of *SSL*. Although no compounds with new P/N(O) ratios were developed in this work, this shows that there is sufficient scope for future research on compounds with more frequently recurring degrees of condensation in the context of the cation ratio (*CR*) introduced in Chapter 2. All Eu^{2+}-doped compounds presented here show exceptional luminescence properties and offer enough room for optimization possibilities such as cation substitution or synthesis optimization.[45,46,48] In particular, the by now established ion exchange approach, which has been advanced in this work, provides the tool for this progress. We are only at the beginning of the systematic investigation and optimization of this class of materials with regard to its luminescence properties and time will tell whether and to what extent the presented results presented can be used as tools for this progress.

9.4. References

[1] S.D. Kloß, W. Schnick, *Angew. Chem. Int. Ed.* **2019**, *58*, 7933.

[2] S.J. Sedlmaier, M. Eberspächer, W. Schnick, *Z. Anorg. Allg. Chem.* **2011**, *637*, 362.

[3] G. Krach, J. Steinadler, K. Witthaut, W. Schnick, *Angew. Chem. Int. Ed.* **2024**, *63*, e202404953.

[4] S. Wendl, L. Seidl, P. Schüler, W. Schnick, *Angew. Chem. Int. Ed.* **2020**, *59*, 23579.

[5] V. Schultz-Coulon, W. Schnick, *Z. Anorg. Allg. Chem.* **1997**, *623*, 69.

[6] F.J. Pucher, A. Marchuk, P.J. Schmidt, D. Wiechert, W. Schnick, *Chem. Eur. J.* **2015**, *21*, 6443.

[7] S. Wendl, W. Schnick, *Chem. Eur. J.* **2018**, *24*, 15889.

[8] S. Wendl, L. Eisenburger, P. Strobel, D. Günther, J.P. Wright, P.J. Schmidt, O. Oeckler, W. Schnick, *Chem. Eur. J.* **2020**, *26*, 7292.

[9] S. Vogel, A.T. Buda, W. Schnick, *Angew. Chem. Int. Ed.* **2018**, *57*, 13202.

[10] A. Marchuk, L. Neudert, O. Oeckler, W. Schnick, *Eur. J. Inorg. Chem.* **2014**, 3427.

[11] L. Eisenburger, V. Weippert, C. Paulmann, D. Johrendt, O. Oeckler, W. Schnick, *Angew. Chem. Int. Ed.* **2022**, *61*, e202202014.

[12] E.-M. Bertschler, C. Dietrich, T. Leichtweiß, J. Janek, W. Schnick, *Chem. Eur. J.* **2018**, *24*, 196.

[13] E.-M. Bertschler, R. Niklaus, W. Schnick, *Chem. Eur. J.* **2017**, *23*, 9592.

[14] S.D. Kloß, N. Weidmann, R. Niklaus, W. Schnick, *Inorg. Chem.* **2016**, *55*, 9400.

[15] D. Baumann, W. Schnick, *Angew. Chem. Int. Ed.* **2014**, *53*, 14490.

[16] D. Baumann, W. Schnick, *Inorg. Chem.* **2014**, *53*, 7977.

[17] L.V. Gurvich, I.V. Veyts, C.B. Alcock in *Thermodynamic properties of individual substances*, Hemisphere Pub. Co., New York (USA), **1989**.

[18] S. Schneider, S. Klenk, S.D. Kloß, W. Schnick, *Chem. Eur. J.* **2024**, *30*, e202303251.

[19] S. Schneider, S. Kreiner, L.G. Balzat, B.V. Lotsch, W. Schnick, *Chem. Eur. J.* **2023**, *29*, e202301986.

[20] S. Schneider, E.-M. Wendinger, V. Baran, A.-K. Hatz, B.V. Lotsch, M. Nentwig, O. Oeckler, T. Bräuniger, W. Schnick, *Chem. Eur. J.* **2023**, *29*, e202300174.

[21] S. Schneider, L.G. Balzat, B.V. Lotsch, W. Schnick, *Chem. Eur. J.* **2023**, *29*, e202202984.

[22] E.-M. Bertschler, R. Niklaus, W. Schnick, *Chem. Eur. J.* **2018**, *24*, 736.

[23] S.D. Kloß, W. Schnick, *Inorg. Chem.* **2018**, *57*, 4189.

[24] W. Schnick, J. Luecke, *J. Solid State Chem.* **1990**, *87*, 101.

[25] W. Schnick, J. Lücke, *Z. Anorg. Allg. Chem.* **1990**, *588*, 19.

[26] S.D. Kloß, *Dissertation*, Ludwig-Maximilians-Universität München (Germany) **2018**.

[27] D. Baumann, S.J. Sedlmaier, W. Schnick, *Angew. Chem. Int. Ed*. **2012**, *51*, 4707.

[28] M. Bykov, E. Bykova, V. Dyadkin, D. Baumann, W. Schnick, L. Dubrovinsky, N. Dubrovinskaia, *Acta Crystallogr. Sect. E*, **2015**, *71*, 1325.

[29] A. Marchuk, F. J. Pucher, F. W. Karau, W. Schnick, *Angew. Chem. Int. Ed.* **2014**, *53*, 2469.

[30] W. Schnick, J. Lücke, *Z. Anorg. Allg. Chem.* **1992**, *610*, 121.

[31] K. Landskron, H. Huppertz, J. Senker, W. Schnick, *Angew. Chem. Int. Ed.* **2001**, *40*, 2643.

[32] E. Bykova, M. Bykov, A. Černok, J. Tidholm, S. I. Simak, O. Hellman, M.P. Belov, I.A. Abrikosov, H.-P. Liermann, M. Hanfland, V.B. Prakapenka, C. Prescher, N. Dubrovinskaia, L. Dubrovinsky, *Nat. Commun.* **2018**, *9*, 4789.

[33] S.J. Ambach, M. Pointner, S. Falkai, C. Paulmann, O. Oeckler, W. Schnick, *Angew. Chem. Int. Ed.* **2023**, *62*, e202303580.

[34] L. Eisenburger, P. Strobel, P.J. Schmidt, T. Bräuniger, J. Wright, E. Lawrence Bright, C. Giacobbe, O. Oeckler, W. Schnick, *Angew. Chem. Int. Ed.* **2022**, *61*, e202114902.

[35] F.J. Pucher, F.W. Karau, J. Schmedt auf der Günne, W. Schnick, *Eur. J. Inorg. Chem.* **2016**, 1497.

[36] H.-P. Baldus, W. Schnick, J. Lücke, U. Wannagat, G. Bogedain, *Chem. Mater.* **1993**, *5*, 845.

[37] L. Eisenburger, O. Oeckler, W. Schnick, *Chem. Eur. J.* **2021**, *27*, 4461.

[38] M. Dialer, M.M. Pointner, S.L. Wandelt, P. Strobel, P.J. Schmidt, L. Bayarjargal, B. Winkler, W. Schnick, *Adv. Optical Mater.* **2024**, *12*, 2302668.

[39] F.J. Pucher, S.R. Römer, F.W. Karau, W. Schnick, *Chem. Eur. J.* **2010**, *16*, 7208.

[40] E.-M. Bertschler, T. Bräuniger, C. Dietrich, J. Janek, W. Schnick, *Angew. Chem. Int. Ed.* **2017**, *56*, 4806.

[41] M.-H. Fang, C.O.M. Mariano, P.-Y. Chen, S.-F. Hu, R.-S. Liu, *Chem. Mater.* **2020**, *32*, 1748.

[42] K. Uheda, N. Hirosaki, H. Yamamoto, *Phys. Stat. Sol. Sect. A*, **2006**, *203*, 2712.

[43] H. Watanabe, N. Kijima, *J. Alloys Compd.* **2009**, *475*, 434.

[44] M.-H. Fang, Z. Bao, W.-T. Huang, R.-S. Liu, *Chem. Rev.* **2022**, *122*, 11474.

[45] G. Li, Y. Tiam, Y. Zhao, J. Lin, *Chem. Soc. Rev.* **2015**, *44*, 8688.

[46] Y. Wan, P. Dang, D. Liu, H. Lian, G. Li J. Lin, *Laser Photonics Rev.* **2024**, 2400651.

[47] P. Pust, V. Weiler, C. Hecht, A. Tücks, A.S. Wochnik, A.-K. Henß, D. Wiechert, C. Scheu, P.J. Schmidt, W. Schnick, *Nat. Mater.* **2014**, *13*, 891.

[48] L. Wang, R.-J. Xie, T. Suehiro, T. Takeda, N. Hirosaki, *Chem. Rev.* **2018**, *118*, 1951.

10 Appendix

10.1 List of Abbreviations

AE	**A**lkaline **E**arth
BVS	**B**ond **V**alence **S**ums
CASN	**C**a**A**l**S**i**N**$_3$:Eu^{2+}
CC	**C**ounter **C**ation
CCT	**C**orrelated **C**olor **T**emperature
CHARDI	**Cha**rge **Di**stribution in Solids
CIE	**C**ommission **I**nternationale d'**E**clairage
CLPN	**C**a$_2$**L**i$_6$**P**$_4$**N**$_{10}$:Eu^{2+}
CN	**C**oordination **N**umber
CR	**C**ation **R**atio
CRI	**C**olor **R**endering **I**ndex
DFT	**D**ensity **F**unctional **T**heory
DOS	**D**ensity **o**f **S**tates
EDX	**E**nergy **D**ispersive **X**-Ray Diffraction
EQE	**E**xternal **Q**uantum **E**fficiency
FBU	**F**undamental **B**uilding **U**nit
FTIR	**F**ourier-**T**ransform **I**nfra**r**ed
FWHM	**F**ull **W**idth at **H**alf **M**aximum
GGA	**G**eneralized **G**radient **A**pproximation
GOOF	**Go**odness **o**f **F**it
HAADF	**H**igh-**A**ngle **A**nnular **D**ark **F**ield
HP	**H**igh-**P**ressure
HT	**H**igh-**T**emperature
ICDD	**I**nternational **C**entre of **D**iffraction **D**ata
ICP-OES	**I**nductively **C**oupled **P**lasma **O**ptical **E**mission **S**pectroscopy
IR	**I**nfra**r**ed
IQE	**I**nternal **Q**uantum **E**fficiency

LCC	**L**ow-**C**ost **C**rystallographic **C**alculations
LED	**L**ight **E**mitting **D**iode
LER	**L**uminous **E**fficacy of **R**adiation
pc-LED	**P**hosphor **C**onverted **L**ight **E**mitting **D**iode
PL	**P**hoto**l**uminescence
PLE	**P**hoto**l**uminescence **E**xcitation
PXRD	**P**owder **X**-**R**ay **D**iffraction
RE	**R**are-**E**arth
SALON	**S**r[**L**i$_2$**A**l$_2$**O**$_2$**N**$_2$]:Eu^{2+}
SCASN	(**S**r,**C**a)**A**l**S**i**N**$_3$:Eu^{2+}
SCXRD	**S**ingle-**C**rystal **X**-**R**ay **D**iffraction
SEM	**S**canning **E**lectron **M**icroscopy
SLA	**S**r[**L**i**A**l$_3$N$_4$]:Eu^{2+}
SPD	**S**pectral **P**ower **D**istribution
SSL	**S**olid **S**tate **L**uminescence
STEM	**S**canning **T**ransmission **E**lectron **M**icroscopy
NFC	**N**etwork **F**orming **C**ation
NMR	**N**uclear **M**agnetic **R**esonance
MAPLE	**Ma**delung **P**art of the **L**attice **E**nergy
MAS	**M**agic-**A**ngle **S**pinning
MBE	**M**inimal **B**ounding **E**llipsoid
MP	**M**edium-**P**ressure
PAW	**P**rojector-**A**ugmented **W**aves
TM	**T**ransition **M**etal
VASP	**V**ienna **a**b **i**nitio **S**imulation **P**ackage
VSEPR	**V**alence **S**hell **E**lectron **P**air **R**epulsion Theory
UV	**U**ltra **V**iolet
QE	**Q**uantum **E**fficiency
ZPL	**Z**ero **P**honon **L**ine

10.2 Supporting Information for Chapter 2

Rietveld refinement α-$MgSrP_3N_5O_2$

Table S2.1. Data for the Rietveld refinement of a α-$MgSrP_3N_5O_2$ sample based on its single-crystal structure model (standard deviations in parentheses).

sum formula	α-$MgSrP_3N_5O_2$
formula weight / g·mol^{-1}	306.8786
crystal system	monoclinic
space group	$P2_1/c$ (no. 14)
lattice parameters / Å	a = 6.9464(13) b = 6.61609(12) c = 13.9558(3)
volume / Å^3	563.76(2)
Z	4
X-ray density / g·cm^{-3}	3.61561(13)
diffractometer	STOE Stadi P
radiation	Cu-$K\alpha_1$ (λ = 1.540596 Å)
monochromator	Ge(111)
detector	Mythen 1K
2Θ range / °	$5 \leq 2\Theta \leq 92.5$
data points	5840
number of reflections	494
refined parameters	95
background function	shifted Chebyshev, 10 polynomials
R values	R_p = 0.0811 R_{wp} = 0.1072 R_{exp} = 0.1055 R_{Bragg} = 0.0229
GooF (χ^2)	1.0165

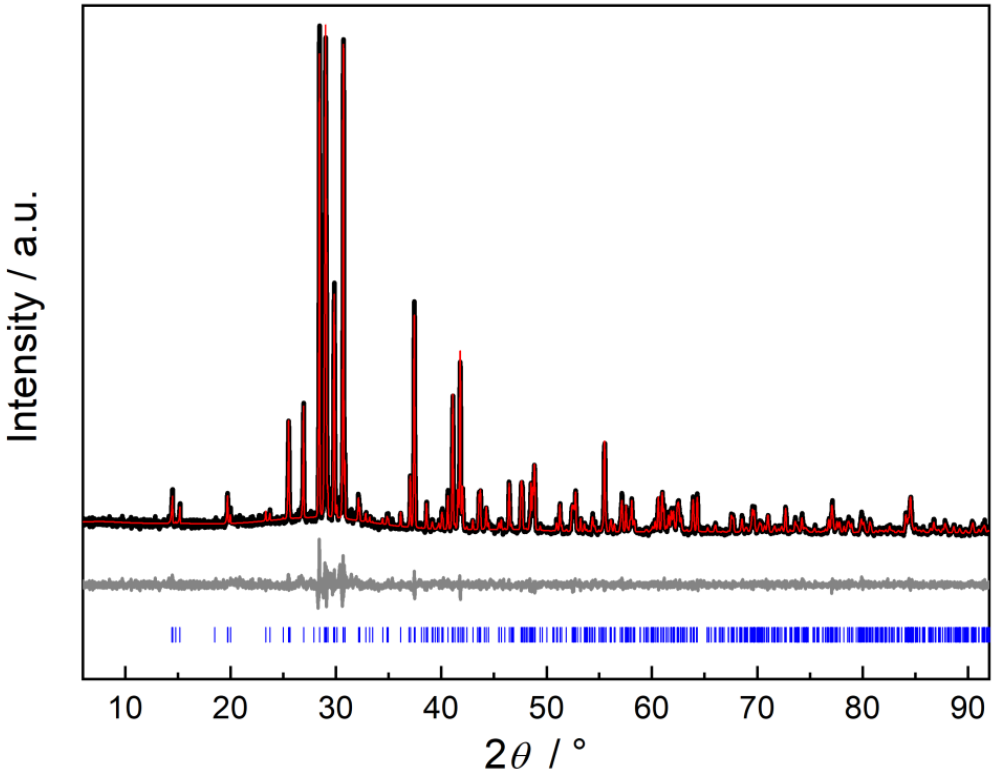

Figure S2.1. Rietveld refinements based on PXRD data collected from powder samples based on the structure model of α-$MgSrP_3N_5O_2$ data with observed (black) and calculated (red) powder X-ray diffraction patterns and the corresponding difference profiles (gray). Vertical blue bars indicate the position of the Bragg reflections of the respective compounds.

SEM-EDX analysis

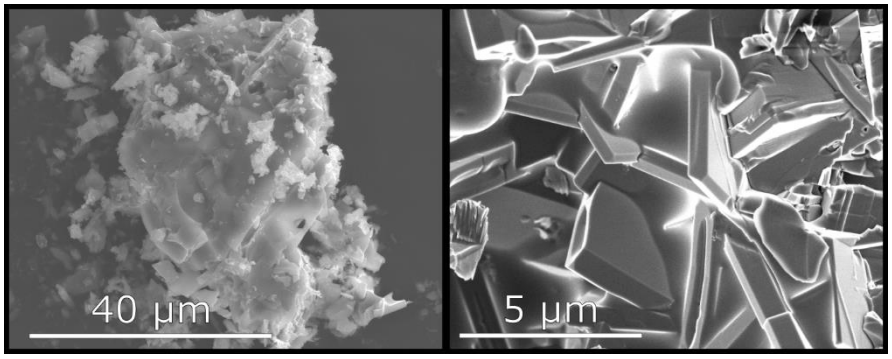

Figure S2.2. SEM image of the α- and β-$MgSrP_3N_5O_2$ single-crystal used for single-crystal X-ray diffraction (left side: α-type, right side: β-type).

Table S2.2: SEM EDX measurements of β-$MgSrP_3N_5O_2$.

β-$MgSrP_3N_5O_2$	**Mg**	**Sr**	**P**	**O**	**N**
measurement 1	7.9	7.6	22.8	21.3	40.4
measurement 2	7.3	7.5	22.0	23.0	40.3
measurement 3	7.8	7.7	23.4	20.1	41.0
measurement 4	7.4	6.6	21.3	20.5	44.1
measurement 5	7.2	6.7	21.2	20.8	43.8
measurement 6	8.5	7.4	23.7	18.4	42.0
Ø(SD)	**7.7(4)**	**7.3(4)**	**22.4(9)**	**21(1)**	**42(2)**
calculated	8.3	8.3	25	16.7	41.7

FTIR analysis

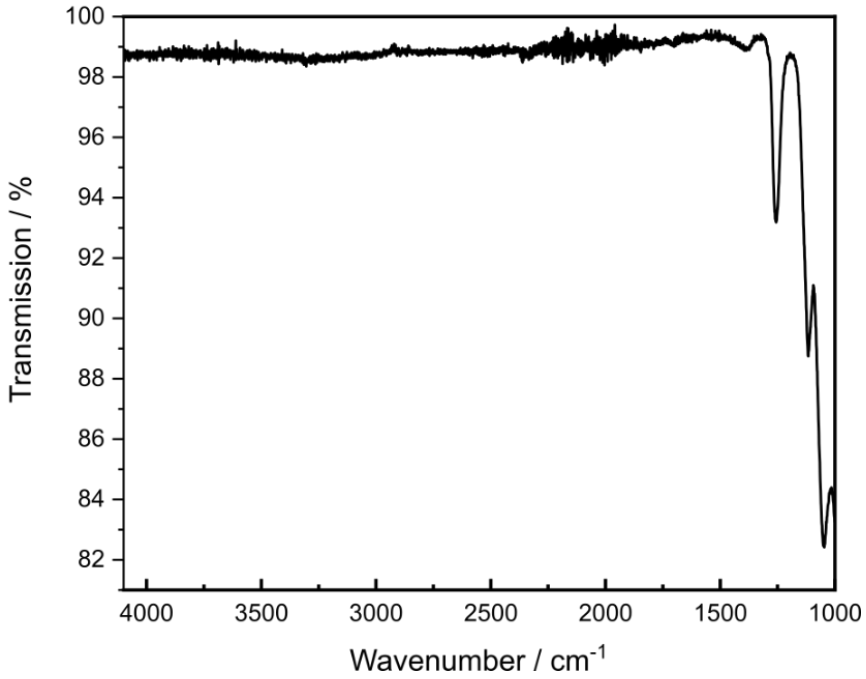

Figure S2.3. FTIR spectrum of β-$MgSrP_3N_5O_2$. No evidence of N−H valence modes (2700–3400 cm^{-1})

Additional crystallographic data:

Table S2.3. Atomic coordinates, crystallographic positions, and equivalent isotropic displacement parameters (Å^2) of β-$MgSrP_3N_5O_2$ (standard deviations in parentheses).

Atom	Wyckoff	*x*	*y*	*z*	U_{eq} [Å]
Sr1	4*e*	1/4	1/4	0	0.011
Mg1	4*c*	1/2	1/2	1	0.006
P1	8*m*	1/2	0.36509(6)	0.43983(15)	0.003
P2	4*b*	3/4	1/2	1/2	0.004
N1	4*g*	1/2	1/4	0.3112(8)	0.006
N2	16*o*	0.6466(2)	0.42538(14)	0.3016(4)	0.005
O1	8*m*	1/2	0.36424(19)	0.7539(4)	0.007

Table S2.4. Anisotropic displacement parameters of β-$MgSrP_3N_5O_2$ (Å^2) (standard deviations in parentheses).

Atom	U_{11}	U_{22}	U_{33}	U_{12}	U_{13}	U_{23}
Sr1	0.0137(2)	0.0091(2)	0.0116(2)	0.00000	-0.00766(16)	0.00000
Mg1	0.0083(7)	0.0056(6)	0.0055(6)	0.00000	0.00000	0.0008(6)
P1	0.0035(3)	0.0031(3)	0.0026(3)	0.00000	0.00000	-0.0001(2)
P2	0.0031(4)	0.0038(4)	0.0051(4)	0.00000	0.00000	0.00000
N1	0.0106(17)	0.0028(15)	0.0055(15)	0.00000	0.00000	0.00000
N2	0.0031(7)	0.0038(7)	0.0070(7)	-0.0018(7)	0.0006(6)	-0.0009(6)
O1	0.0089(10)	0.0068(10)	0.0068(9)	0.00000	0.00000	-0.0006(8)

Table S2.5. Interatomic distances (Å) and bond angles (°) in the structure of β-$MgSrP_3N_5O_2$, standard deviations in parentheses.

Sr1	N1	2.680(2)	P1	O1	N1	112.77(9)
Sr1	N1	2.680(2)	P1	O1	N2	114.47(7)
Sr1	N2	2.8402(18)	P1	O1	N2	114.47(7)
Sr1	N2	2.8402(18)	P1	O1	N2	67.30(4)
Sr1	N2	2.8402(18)	P1	O1	N2	67.30(4)
Sr1	N2	2.8402(18)	P1	O1	O1	61.92(9)
Sr1	O1	2.9071(15)	P1	O1	O1	179.41(9)
Sr1	O1	2.9071(15)	P1	O1	N2	68.52(3)
Sr1	O1	2.9071(15)	P1	O1	N2	68.52(3)
Sr1	O1	2.9071(15)	P1	N1	N2	105.57(6)
Mg1	O1	2.117(2)	P1	N1	N2	105.57(6)
Mg1	O1	2.117(2)	P1	N1	N2	156.40(3)
Mg1	N2	2.1845(19)	P1	N1	N2	156.40(3)
Mg1	N2	2.1845(19)	P1	N1	O1	50.86(5)
Mg1	N2	2.1845(19)	P1	N1	O1	66.64(5)
Mg1	N2	2.1845(19)	P1	N1	N2	110.52(3)
P1	O1	1.541(2)	P1	N1	N2	110.52(3)
P1	N1	1.6037(17)	P1	N2	N2	102.98(9)
P1	N2	1.6507(19)	P1	N2	N2	57.38(7)
P1	N2	1.6507(19)	P1	N2	N2	94.90(7)
P1	N2	3.2376(19)	P1	N2	O1	127.241()
P1	N2	3.2376(19)	P1	N2	O1	65.84(7)
P1	O1	3.317(3)	P1	N2	N2	48.71(7)
P1	O1	3.366(2)	P1	N2	N2	138.82(7)
P1	N2	3.4499(18)	P1	N2	N2	94.90(7)
P1	N2	3.4499(18)	P1	N2	N2	57.38(7)
P2	N2	1.6405(18)	P1	N2	O1	127.24(7)
P2	N2	1.6405(18)	P1	N2	O1	65.84(7)
P2	N2	1.6405(18)	P1	N2	N2	138.82(7)
P2	N2	1.6405(18)	P1	N2	N2	48.71(7)
P2	O1	3.0705(16)	P1	N2	N2	47.03(5)
P2	O1	3.0705(16)	P1	N2	O1	123.51(3)

P2	O1	3.0705(16)	P1	N2	O1	113.24(4)
P2	O1	3.0705(16)	P1	N2	N2	46.39(4)
			P1	N2	N2	91.74(4)
			P1	N2	O1	123.51(3)
			P1	N2	O1	113.24(4)
			P1	N2	N2	91.74(4)
			P1	N2	N2	46.39(4)
			P1	O1	O1	117.50(6)
			P1	O1	N2	91.57(3)
			P1	O1	N2	91.57(3)
			P1	O1	N2	111.62(3)
			P1	O1	N2	111.62(3)
			P1	N2	N2	129.00(4)
			P2	N2	N2	107.21(9)
			P2	N2	N2	112.53(9)
			P2	N2	N2	108.73(9)
			P2	N2	O1	165.73(6)
			P2	N2	O1	60.81(6)
			P2	N2	O1	80.08(6)
			P2	N2	O1	71.99(6)
			P2	N2	N2	108.73(9)
			P2	N2	N2	112.53(9)
			P2	N2	O1	60.81(6)
			P2	N2	O1	165.73(6)
			P2	N2	O1	71.99(6)
			P2	N2	O1	80.08(6)
			P2	N2	N2	107.21(9)
			P2	N2	O1	80.08(6)
			P2	N2	O1	71.99(6)
			P2	N2	O1	165.73(6)
			P2	N2	O1	60.81(6)
			P2	N2	O1	71.99(6)
			P2	N2	O1	80.08(6)
			P2	N2	O1	60.81(6)

	P2	N2	O1	165.73(6)
	P2	O1	O1	132.128(1)
	P2	O1	O1	88.323(1)
	P2	O1	O1	111.006(1)
	P2	O1	O1	111.006(1)
	P2	O1	O1	88.323(1)
	P2	O1	O1	132.128(1)

MAS NMR analysis

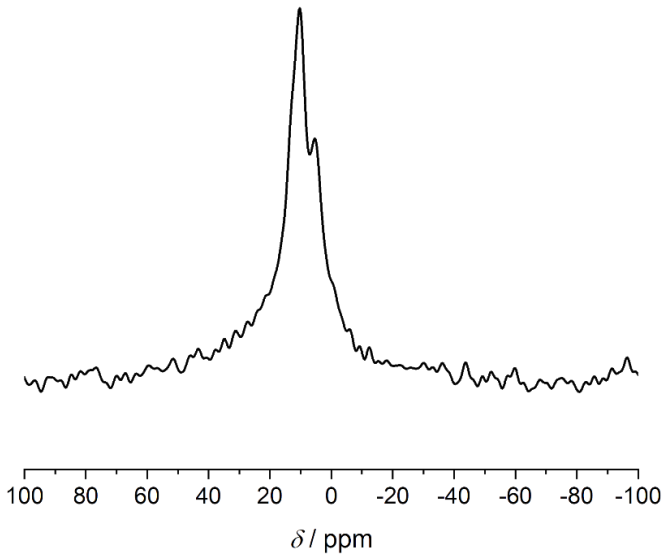

Figure S4. Solid-state ^{31}P MAS NMR spectrum of β-$MgSrP_3N_5O_2$ measured at a sample spinning frequency of 20 kHz.

Two overlaid bands can be identified with shifts of 5.4 and 10.4 ppm. These are in good agreement with the two crystallographic sites P1 and P2. The signal heights agree with the Wyckoff positions (8m and 4b) but a deconvolution of the spectrum was not possible.

Elemental analysis (CHNS)

Table S2.6. CHNS analyses of β-$MgSrP_3N_5O_2$.

Element	C	H	N	S
Measured weight %	-	0	23.66	-
Calculated weight %	-	0	22.82	-

Rietveld refinement of β-$MgSrP_3N_5O_2$

Table S2.7. Crystallographic data of the Rietveld refinement of β-$MgSrP_3N_5O_2$ (standard deviations in parentheses).

Formula	β-$MgSrP_3N_5O_2$
Formula weight / g·mol^{-1}	306.88
Crystal system; space group	hexagonal; $P6_3$ (no. 173)
Lattice parameters / Å	a = 8.8173(9)
	b = 12.8143(13)
	c = 4.9072(4)
Cell volume / Å^3	554.45(9)
Formula units per unit cell	4
Density / g·cm^{-3}	3.6761
μ / mm^{-1}	2.665
Diffractometer	Stoe Stadi P
Radiation	Cu-Kα_1 (λ = 1.5406 Å)
Detector	Mythen 1K
Monochromator	Ge(111)
2Θ-range / °	$5.0 \leq 2\Theta \leq 100.385$
Step width / °	0.015
Data points	6360
Total number of reflections	170
Refined parameters	63
Background function	Shifted Chebyshev
Number of background parameters	10
GooF(χ^2)	1.671
R_p; R_{wp}	0.044; 0.061
R_{exp}; R_{Bragg}	0.036; 0.033

Diffuse reflectance spectroscopy

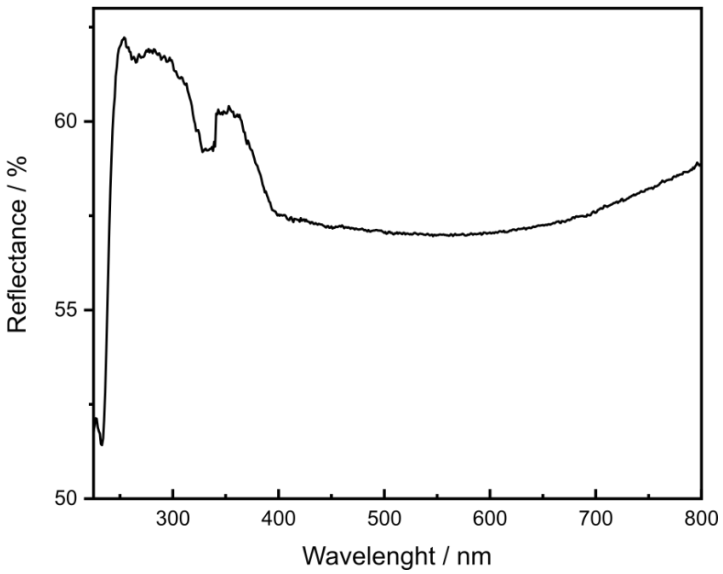

Figure S2.5. Diffuse reflectance spectrum of β-$MgSrP_3N_5O_2$.

Low-cost crystallographic calculations

Table S2.8. Results of MAPLE calculations [$kJ \cdot mol^{-1}$] for β-$MgSrP_3N_5O_2$. Total MAPLE values of binary ionic compounds forming β-$MgSrP_3N_5O_2$ in a hypothetical reaction.

MgO + SrO + γ-P_3N_5	
4632 + 3716 + 76830	**85178**
β-$MgSrP_3N_5O_2$	**84895**
Δ **≈ 0.33%**	

Table S2.9. Results of CHARDI calculations for β-$MgSrP_3N_5O_2$

site	**theoretical**	**CHARDI**	**BVS**
Sr1	2	1.94	1.84
Mg1	2	1.98	2.26
P1	5	4.88	4.85
P2	5	5.32	4.75
N1	−3	−3.12	−3.22
N2	−3	−2.82	−2.94
O1	−2	−2.30	−1.78

Weighed portions

Table S2.10. Weighed portions of the starting materials used for the synthesis of β-$MgSrP_3N_5O_2$.

Compound	Starting material	Amount [mg]
β-$MgSrP_3N_5O_2$	P_3N_5	15.2
	cri-PON	8.5
	$Sr(N_3)_2$	24.1
	MgO	5.6

10.3 Supporting Information for Chapter 3

Table S3.1. Crystallographic data of $AE_3[Mg_2P_{10}N_{20}]$ (*AE* = Sr, Ba) from single-crystal refinement. Standard deviations are given in parentheses.

Formula	**$Sr_3[Mg_2P_{10}N_{20}]$**	**$Ba_3[Mg_2P_{10}N_{20}]$**
Crystal system	monoclinic	
Molecular weight / $g \cdot mol^{-1}$	901.34	1050.46
Space group	$P2_1/c$ (no. 14)	
Lattice parameters	a = 4.8750(2)	a = 4.9116(1)
	b = 18.0568(6)	b = 18.4078(6)
	c = 9.7311(3)	c = 9.7422(3)
	β = 102.195(2)	β = 102.145(2)
Cell volume / $Å^3$	837.27(5)	861.08(4)
Formula units per cell	2	
Calculated density / $g \cdot cm^{-1}$	3.575	4.046
μ / mm^{-3}	10.611	7.834
T_{min} / T_{max}	0.8395 / 1.0000	0.9083 / 1.0000
Radiation	Mo-K_α (λ = 0.71073 Å)	
Temperature / K	293(2)	
F(000)	856	964
θ range / °	$2.256 < \theta < 29.574$	$2.406 < \theta < 27.873$
Total no. of reflections	9834	13453
Independent reflections (>2σ)	2347 (1702)	2059 (1732)
Refined parameters	110	112
R_{int}; R_σ	0.0790; 0.0771	0.0366; 0.0185
$R1$ (all data); $R1$ ($F^2>2\sigma(F^2)$)	0.0766; 0.0452	0.0404; 0.0385
$wR2$ (all data); $wR2$ ($F^2>2\sigma(F^2)$)	0.0915; 0.0825	0.0870; 0.0863
Goodness of fit	1.043	1.253
$\Delta\rho_{max}$; $\Delta\rho_{min}$ / $e \cdot Å^{-3}$	1.10; –0.89	4.19; –2.53

Table S3.2. Wyckoff position, coordinates, equivalent thermal displacement parameters and occupancy of $Sr_3[Mg_2P_{10}N_{20}]$ from single-crystal refinement. Standard deviations are given in parentheses.

Atom	***Wyck.***	***x***	***y***	***z***	U_{eq}	***SOF***
Sr1	2*a*	0	½	½	0.01158(19)	1
Sr2	4*e*	1.21068(13)	0.85962(3)	0.39249(6)	0.01166(15)	1
Mg1	4*e*	1.4258(4)	0.64476(12)	0.2885(2)	0.0112(4)	1
P1	4*e*	0.8843(3)	0.77508(8)	0.69115(15)	0.0054(3)	1
P2	4*e*	0.6084(3)	0.63520(8)	0.61239(15)	0.0054(3)	1
P3	4*e*	0.8136(3)	0.56987(8)	1.12003(15)	0.0052(3)	1
P4	4*e*	0.6642(3)	0.51244(8)	0.81684(15)	0.0053(3)	1
P5	4*e*	1.0474(3)	0.68755(8)	0.48693(15)	0.0048(3)	1
N1	4*e*	0.2718(10)	0.6261(3)	0.5630(5)	0.0071(10)	1
N2	4*e*	0.7084(11)	0.7033(3)	0.7210(5)	0.0085(10)	1
N3	4*e*	1.0626(11)	0.7642(3)	0.5706(5)	0.0070(10)	1
N4	4*e*	1.1184(10)	0.7097(3)	0.3362(5)	0.0063(9)	1
N5	4*e*	0.6883(10)	0.8486(2)	0.6527(5)	0.0052(9)	1
N6	4*e*	0.3315(11)	0.4912(3)	0.7946(5)	0.0093(10)	1
N7	4*e*	0.7421(10)	0.6456(3)	0.4699(5)	0.0059(9)	1
N8	4*e*	0.7256(10)	0.5565(3)	0.6809(5)	0.0057(9)	1
N9	4*e*	0.8409(11)	0.4344(3)	0.8242(5)	0.0073(10)	1
N10	4*e*	0.7502(11)	0.5666(3)	0.9506(5)	0.0105(10)	1

Table S3.3. Anisotropic displacement parameters (U_{ij} / Å^2) of $Sr_3[Mg_2P_{10}N_{20}]$ from single-crystal refinement. Standard deviations are given in parentheses.

Atom	U_{11}	U_{22}	U_{33}	U_{12}	U_{13}	U_{23}
Sr1	0.0117(4)	0.0082(4)	0.0169(4)	-0.0009(3)	0.0076(4)	-0.0026(3)
Sr2	0.0133(3)	0.0097(3)	0.0123(3)	-0.0029(2)	0.0035(2)	-0.0005(2)
Mg1	0.0067(10)	0.0164(11)	0.0108(10)	-0.0003(9)	0.0025(9)	-0.0040(8)
P1	0.0052(8)	0.0068(7)	0.0039(6)	0.0001(6)	0.0002(6)	0.0004(5)
P2	0.0053(7)	0.0060(7)	0.0042(6)	-0.0005(6)	-0.0007(6)	0.0002(5)
P3	0.0045(7)	0.0062(7)	0.0047(6)	-0.0002(6)	0.0007(6)	-0.0011(5)
P4	0.0048(7)	0.0069(7)	0.0034(6)	-0.0001(6)	-0.0006(6)	-0.0003(5)
P5	0.0050(7)	0.0061(7)	0.0033(6)	0.0001(6)	0.0013(6)	-0.0002(5)

Table S3.4. Interatomic distances (Å) of $Sr_3[Mg_2P_{10}N_{20}]$ from single-crystal refinement. Standard deviations are given in parentheses.

atom1–atom2	**distance [Å]**	**atom1–atom2**	**distance [Å]**	**atom1–atom2**	**distance [Å]**
Sr1—N1	2.641(5)	Sr2—N3	2.650(5)	Mg1—N4	2.032(5)
Sr1—N6	2.983(5)	Sr2—N5	3.063(5)	Mg1—N5	2.028(5)
Sr1—N7	2.901(5)	Sr2—N6	2.957(5)	Mg1—N7	2.084(5)
Sr1—N8	2.631(4)	Sr2—N8	3.174(5)	Mg1—N9	2.082(5)
Sr2—N1	2.641(5)	Sr2—N9	3.128(5)	P1—N2	1.614(5)
Sr2—N2	2.888(5)	Sr2—N10	2.896(5)	P1—N3	1.613(5)
P1—N4	1.641(5)	P2—N1	1.618(5)	P2—N7	1.663(5)
P1—N5	1.633(5)	P2—N2	1.627(5)	P2—N8	1.622(5)
P3—N5	1.650(5)	P3—N9	1.659(5)	P4—N6	1.636(5)
P3—N6	1.629(5)	P3—N10	1.613(5)	P4—N8	1.625(5)
P4—N9	1.645(5)	P5—N1	1.622(5)	P5—N4	1.626(5)
P4—N10	1.611(5)	P5—N3	1.599(5)	P5—N7	1.647(5)

Table S3.5. Wyckoff position, coordinates, equivalent thermal displacement parameters and occupancy of $Ba_3[Mg_2P_{10}N_{20}]$ from single-crystal refinement. Standard deviations are given in parentheses.

Atom	***Wyck.***	***x***	***y***	***z***	U_{eq}	***SOF***
Ba1	2a	½	0	0	0.00862(14)	1
Ba2	4e	0.27333(8)	0.64101(2)	0.11320(4)	0.00909(12)	1
Mg1	4e	0.0788(4)	0.85700(12)	0.2078(2)	0.0088(5)	1
P1	4e	0.1696(4)	0.01360(8)	0.31672(16)	0.0048(4)	1
P2	4e	0.1028(4)	0.14059(9)	0.11648(16)	0.0052(3)	1
P3	4e	0.3750(4)	0.27829(8)	0.19147(16)	0.0052(3)	1
P4	4e	0.3120(4)	0.43277(8)	0.12684(16)	0.0045(3)	1
P5	4e	0.5399(4)	0.31083(8)	0.48954(17)	0.0047(3)	1
N1	4e	0.5484(10)	0.2655(4)	0.0716(5)	0.0058(5)	1
N2	4e	0.1929(10)	0.2092(4)	0.2202(5)	0.0058(5)	1
N3	4e	0.2602(10)	0.0599(4)	0.4591(5)	0.0058(5)	1
N4	4e	0.2217(10)	0.0654(4)	0.1908(5)	0.0058(5)	1
N5	4e	0.7680(10)	0.1315(4)	0.0680(5)	0.0058(5)	1
N6	4e	0.1579(10)	0.4912(4)	0.2117(5)	0.0058(5)	1
N7	4e	0.6507(10)	0.4384(4)	0.1909(5)	0.0058(6)	1
N8	4e	0.2358(10)	0.3515(4)	0.4738(5)	0.0058(6)	1
N9	4e	0.1874(10)	0.3520(4)	0.1558(5)	0.0058(6)	1
N10	4e	0.6093(10)	0.2933(4)	0.3363(5)	0.0058(6)	1

Table S3.6. Anisotropic displacement parameters (U_{ij} / Å^2) of $Ba_3[Mg_2P_{10}N_{20}]$ from single-crystal refinement. Standard deviations are given in parentheses.

Atom	U_{11}	U_{22}	U_{33}	U_{12}	U_{13}	U_{23}
Ba1	0.0093(3)	0.0061(3)	0.0107(3)	0.0014(2)	0.0026(2)	-0.0002(2)
Ba2	0.0103(2)	0.0078(2)	0.0089(2)	-0.00056(17)	0.00143(16)	0.00224(17)
Mg1	0.0054(11)	0.0114(12)	0.0096(12)	0.0037(10)	0.0021(9)	0.0013(9)
P1	0.0056(8)	0.0050(9)	0.0039(9)	-0.0003(7)	0.0010(7)	-0.0006(6)
P2	0.0049(8)	0.0046(8)	0.0058(9)	-0.0008(7)	0.0008(7)	0.0007(7)
P3	0.0062(8)	0.0046(8)	0.0048(9)	-0.0007(7)	0.0010(7)	-0.0002(7)
P4	0.0027(8)	0.0046(8)	0.0059(9)	0.0002(7)	0.0004(7)	-0.0003(6)
P5	0.0049(8)	0.0043(8)	0.0050(8)	0.0000(7)	0.0010(7)	-0.0007(7)
N1	0.0061(11)	0.0051(11)	0.0062(12)	-0.0013(9)	0.0013(9)	0.0001(9)
N2	0.0061(11)	0.0051(11)	0.0062(12)	-0.0013(9)	0.0013(9)	0.0001(9)
N3	0.0061(11)	0.0051(11)	0.0062(12)	-0.0013(9)	0.0013(9)	0.0001(9)
N4	0.0061(11)	0.0051(11)	0.0062(12)	-0.0013(9)	0.0013(9)	0.0001(9)
N5	0.0061(11)	0.0051(11)	0.0062(12)	-0.0013(9)	0.0013(9)	0.0001(9)
N6	0.0061(11)	0.0051(11)	0.0062(12)	-0.0013(9)	0.0013(9)	0.0001(9)
N7	0.0037(13)	0.0053(14)	0.0089(15)	0.0001(12)	0.0028(11)	-0.0003(11)
N8	0.0037(13)	0.0053(14)	0.0089(15)	0.0001(12)	0.0028(11)	-0.0003(11)
N9	0.0037(13)	0.0053(14)	0.0089(15)	0.0001(12)	0.0028(11)	-0.0003(11)
N10	0.0037(13)	0.0053(14)	0.0089(15)	0.0001(12)	0.0028(11)	-0.0003(11)

Table S3.7. Interatomic distances (Å) of $Ba_3[Mg_2P_{10}N_{20}]$ from single-crystal refinement. Standard deviations are given in parentheses.

atom1–atom2	**distance [Å]**	**atom1–atom2**	**distance [Å]**	**atom1–atom2**	**distance [Å]**
Ba1—N5	2.768(5)	Ba2—N2	3.320(5)	Ba2—N9	3.087(5)
Ba1—N4	2.803(5)	Ba2—N3	2.944(5)	Ba2—N10	2.886(5)
Ba1—N6	2.962(5)	Ba2—N3	2.970(5)	Mg1—N7	2.105(6)
Ba1—N8	3.016(5)	Ba2—N4	3.121(5)	Mg1—N8	2.089(6)
Ba2—N1	2.766(5)	Ba2—N5	3.160(5)	Mg1—N9	2.052(6)
Ba2—N2	3.050(5)	Ba2—N6	3.014(5)	Mg1—N10	2.044(6)
P1—N3	1.609(6)	P2—N2	1.620(6)	P3—N1	1.604(5)
P1—N4	1.616(5)	P2—N4	1.613(5)	P3—N2	1.614(5)
P1—N6	1.628(5)	P2—N5	1.625(5)	P3—N9	1.631(5)
P1—N7	1.653(5)	P2—N8	1.664(5)	P3—N10	1.648(6)
P4—N3	1.606(6)	P4—N7	1.656(5)	P5—N1	1.610(5)
P4—N6	1.634(5)	P4—N9	1.661(5)	P5—N5	1.614(5)
P5—N8	1.651(5)	P5—N10	1.633(6)		

Charge distribution (CHARDI)

Table S3.8. CHARDI values for $Sr_3[Mg_2P_{10}N_{20}]$.

Sr1	**Sr2**	**Mg1**	**P1**	**P2**	**P3**	**P4**	**P5**
2.07	1.92	1.99	4.89	5.19	4.98	5.06	4.93

N1	**N2**	**N3**	**N4**	**N5**	**N6**	**N7**	**N8**	**N9**	**N10**
-2.91	-2.83	-3.09	-3.29	-3.11	-2.87	-2.89	-2.92	-2.79	-3.30

Table S3.9. CHARDI values for $Ba_3[Mg_2P_{10}N_{20}]$.

Ba1	**Ba2**	**Mg1**	**P1**	**P2**	**P3**	**P4**	**P5**
2.00	1.97	2.01	5.03	5.04	4.97	5.03	4.95

N1	**N2**	**N3**	**N4**	**N5**	**N6**	**N7**	**N8**	**N9**	**N10**
-2.99	-2.87	-3.18	-3.07	-3.05	-2.92	-2.77	-2.90	-3.07	-3.18

Bond-valence-sum (BVS)

Table S3.10. BVS values for $Sr_3[Mg_2P_{10}N_{20}]$ and $Ba_3[Mg_2P_{10}N_{20}]$.

	Sr1	**Sr2**	**Mg1**	**P1**	**P2**	**P3**	**P4**	**P5**
theo	2	2	2	5	5	5	5	5
Calc (Sr)	1.97	1.62	2.30	4.96	4.86	4.79	4.90	4.97
Calc (Ba)	2.70	2.45	2.18	4.93	4.89	4.96	4.79	4.92

	N1	**N2**	**N3**	**N4**	**N5**	**N6**	**N7**	**N8**	**N9**	**N10**
theo	-3	-3	-3	-3	-3	-3	-3	-3	-3	-3
Calc (Sr)	-2.89	-2.71	-2.93	-3.26	-3.09	-2.70	-2.98	-2.91	-2.95	-2.96
Calc (Ba)	-3.05	-2.84	-3.13	-3.12	-3.12	-2.93	-2.88	-3.02	-3.11	-3.29

Most charges are in good agreement with the theoretical values. The deviation of Ba1, Ba2 and Sr2 correlate with unusual coordination environments and bond lengths in the respective unregularly distorted polyhedral. The introduction of a new R_0 parameter for Ba–N (R_0=2.40) and Sr–N (R_0=2.285) provides charges with good agreement to the expected charges (Table S12).

Table S3.11. BVS values for $Sr_3[Mg_2P_{10}N_{20}]$ and $Ba_3[Mg_2P_{10}N_{20}]$ with redefined R_0 parameters.

	Sr1	**Sr2**	**Mg1**	**P1**	**P2**	**P3**	**P4**	**P5**
theo	2	2	2	5	5	5	5	5
Calc (Sr)	2.23	1.77	2.29	4.96	4.86	4.79	4.90	4.97
Calc (Ba)	2.23	2.03	2.18	4.94	4.90	4.96	4.79	4.92

	N1	**N2**	**N3**	**N4**	**N5**	**N6**	**N7**	**N8**	**N9**	**N10**
theo	-3	-3	-3	-3	-3	-3	-3	-3	-3	-3
Calc (Sr)	-2.89	-2.70	-2.98	-3.26	-3.11	-2.74	-3.01	-2.97	-2.94	-3.03
Calc (Ba)	-2.97	-2.79	-3.03	-3.02	-3.02	-2.84	-2.87	-2.98	-3.08	-3.24

Madelung Part of the lattice energy (MAPLE)

Table S3.12. Results of MAPLE calculations [kJ·mol^{-1}] for $Ba_3[Mg_2P_{10}N_{20}]$. Total MAPLE values of binary ionic compounds forming $Ba_3[Mg_2P_{10}N_{20}]$ in a hypothetical reaction $3\ BaP_2N_4 + Mg_2PN_3 + P_3N_5 \rightarrow Ba_3[Mg_2P_{10}N_{20}]$.

	MAPLE values [kJ·mol^{-1}]	
3 BaP_2N_4	167907.4	
Mg_2PN_3	36598.7	
α-P_3N_5	78531.1	
γ-P_3N_5		76829.6
∑	283037.2	281335.8
$Ba_3[Mg_2P_{10}N_{20}]$	285530.1	
Deviation *Δ* [%]	0.87	1.47

Solid-state MAS NMR spectra

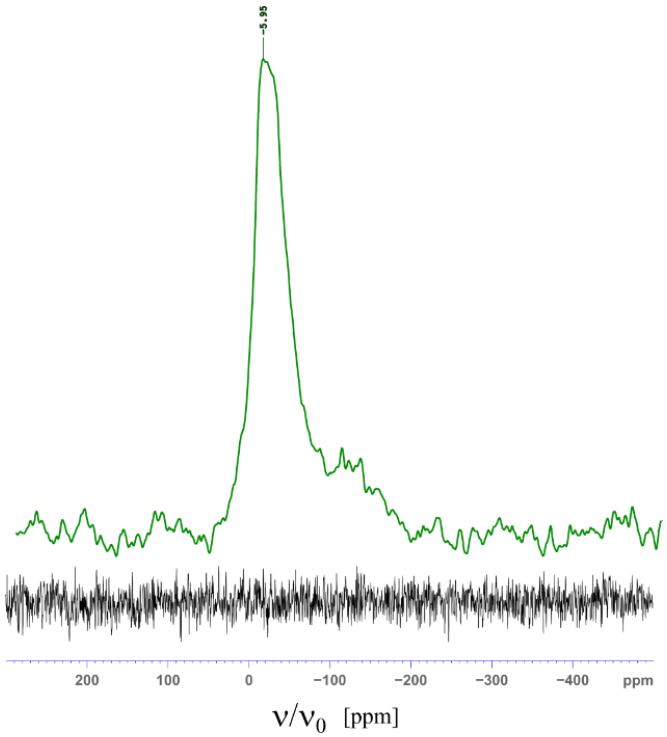

Figure S3.1. ^{31}P NMR spectrum (green) of $Ba_3[Mg_2P_{10}N_{20}]$ with one broad major signal at -5.95 ppm, which can be assigned to the five P positions in the crystal structure. $^{31}P\{^1H\}$ cross-polarization NMR spectrum (gray) indicates no H in direct environment of P in the structure.

Rietveld refinement

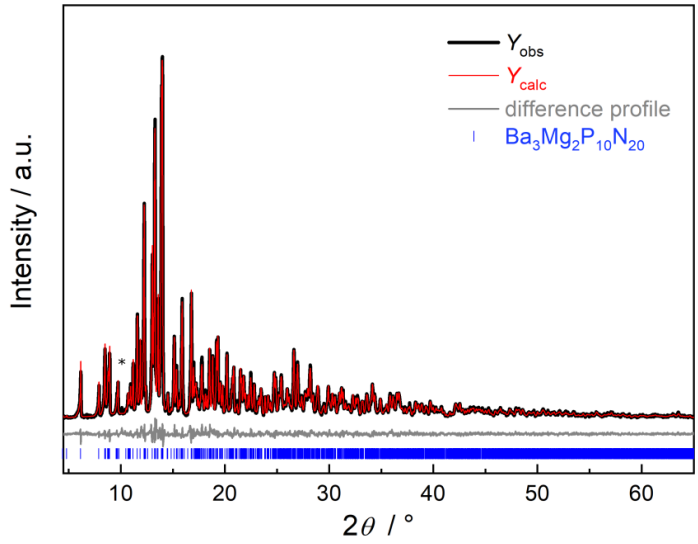

Figure S3.2. Rietveld refinement for $Ba_3[Mg_2P_{10}N_{20}]$. Observed (black) and calculated (red) powder X-ray diffraction patterns, difference plot (gray), positions of Bragg reflections of $Ba_3[Mg_2P_{10}N_{20}]$ (vertical blue bars), reflection marked with an asterisk can be assigned to agate from the agate mortar.

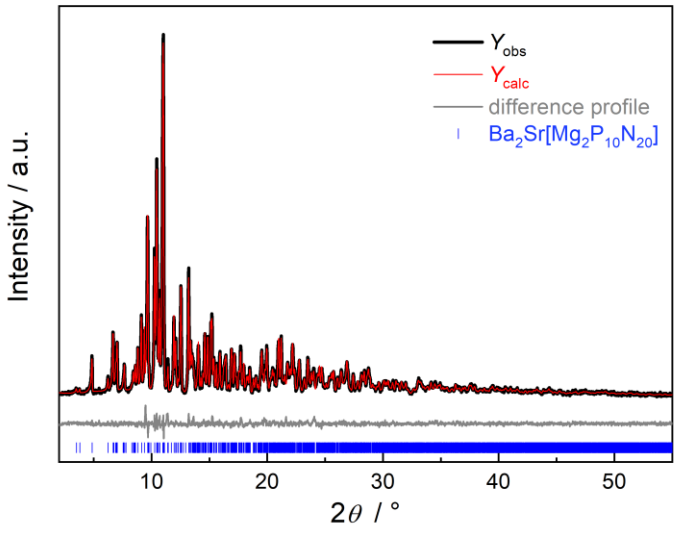

Figure S3.3. Rietveld refinement for $Ba_2Sr[Mg_2P_{10}N_{20}]$. Observed (black) and calculated (red) powder X-ray diffraction patterns, difference plot (gray), positions of Bragg reflections of Ba_2Sr $[Mg_2P_{10}N_{20}]$ (vertical blue bars).

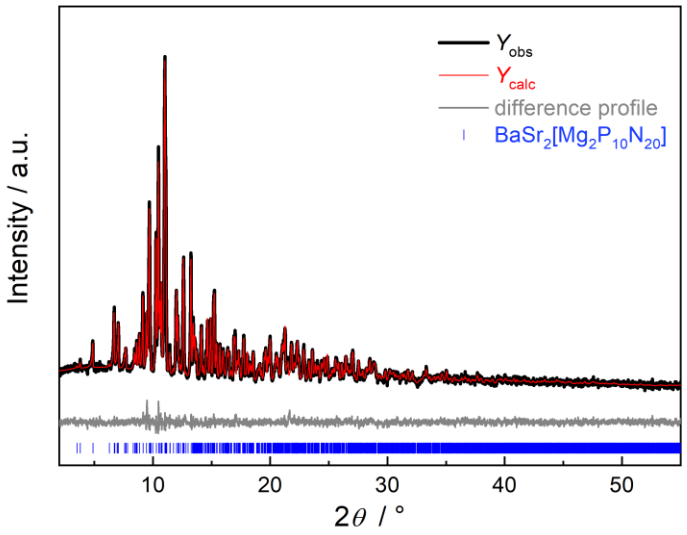

Figure S3.4. Rietveld refinement for $BaSr_2[Mg_2P_{10}N_{20}]$. Observed (black) and calculated (red) powder X-ray diffraction patterns, difference plot (gray), positions of Bragg reflections of $BaSr_2[Mg_2P_{10}N_{20}]$ (vertical blue bars).

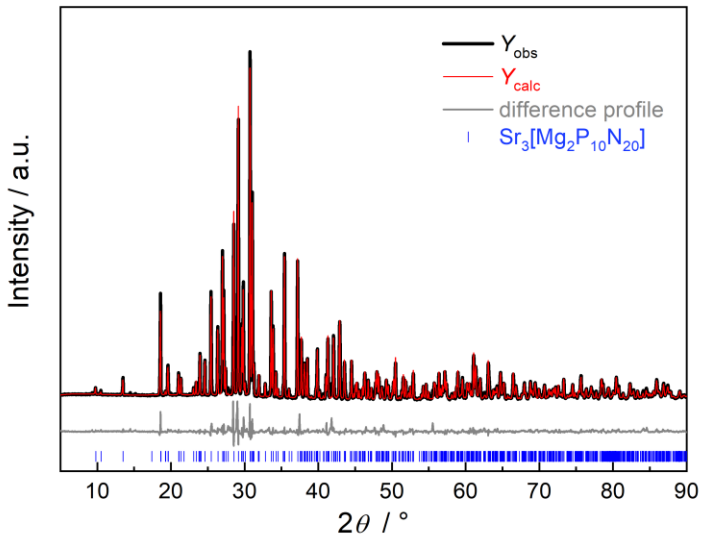

Figure S3.5. Rietveld refinement for $Sr_3[Mg_2P_{10}N_{20}]$. Observed (black) and calculated (red) powder X-ray diffraction patterns, difference plot (gray), positions of Bragg reflections of $Sr_3[Mg_2P_{10}N_{20}]$ (vertical blue bars).

Table S3.13. Wyckoff position, coordinates, isotropic thermal displacement parameters and occupancy of $Ba_3[Mg_2P_{10}N_{20}]$ from Rietveld refinement. Standard deviations are given in parentheses.

Atom	***Wyck.***	***x***	***y***	***z***	U_{eq}	***SOF.***
Ba1	2*b*	½	0	0	0.43(6)	1
Ba2	4*e*	0.2735(4)	0.64084(10)	0.11238(18)	0.66(4)	1
Mg1	4*e*	0.0790(17)	0.8543(5)	0.2121(8)	0.7	1
P1	4*e*	0.1712(15)	0.0142(4)	0.3160(7)	0.7	1
P2	4*e*	0.1028(13)	0.1427(4)	0.1158(7)	0.7	1
P3	4*e*	0.3060(17)	0.4335(4)	0.1272(8)	0.7	1
P4	4*e*	0.3762(16)	0.2789(4)	0.1905(7)	0.7	1
P5	4*e*	0.5439(17)	0.3120(4)	0.4877(9)	0.7	1
N1	4*e*	0.234(4)	0.3491(13)	0.4716(18)	0.7	1
N2	4*e*	0.188(3)	0.3565(13)	0.1575(16)	0.7	1
N3	4*e*	0.215(3)	0.6318(9)	0.4268(16)	0.7	1
N4	4*e*	0.266(3)	0.0597(10)	0.456(2)	0.7	1
N5	4*e*	0.190(3)	0.2061(9)	0.2141(16)	0.7	1
N6	4*e*	0.602(3)	0.2930(9)	0.3324(18)	0.7	1
N7	4*e*	0.645(4)	0.4388(11)	0.192(2)	0.7	1
N8	4*e*	0.550(3)	0.2657(8)	0.0734(15)	0.7	1
N9	4*e*	0.150(4)	0.4876(11)	0.210(2)	0.7	1
N10	4*e*	0.219(4)	0.0616(10)	0.196(2)	0.7	1

Table S3.14. Wyckoff position, coordinates, isotropic thermal displacement parameters and occupancy of $Ba_2Sr[Mg_2P_{10}N_{20}]$ from Rietveld refinement. Standard deviations are given in parentheses.

Atom	***Wyck.***	***x***	***y***	***z***	U_{iso}	***SOF.***
Ba1	2*b*	½	0	0	0.98(8)	0.5
Sr1	2*b*	½	0	0	0.98(8)	0.5
Ba2	4*e*	0.2748(4)	0.64054(11)	0.1118(2)	0.61(5)	0.627(11)
Sr2	4*e*	0.2748(4)	0.64054(11)	0.1118(2)	0.61(5)	0.373(11)
Mg1	4*e*	0.0715(18)	0.8559(6)	0.2138(9)	0.7	1
P1	4*e*	0.1733(15)	0.0122(4)	0.3158(8)	0.7	1
P2	4*e*	0.1159(14)	0.1399(5)	0.1177(7)	0.7	1
P3	4*e*	0.3789(17)	0.2755(4)	0.1939(8)	0.7)	1
P4	4*e*	0.3111(19)	0.4314(4)	0.1277(8)	0.7	1
P5	4*e*	0.5426(18)	0.3112(4)	0.4844(9)	0.7	1
N1	4*e*	0.561(4)	0.2620(10)	0.0595(19)	0.7	1
N2	4*e*	0.197(4)	0.2071(12)	0.214(2)	0.7	1
N3	4*e*	0.253(4)	0.0620(10)	0.458(2)	0.7	1
N4	4*e*	0.235(4)	0.0633(11)	0.195(2)	0.7	1
N5	4*e*	0.782(4)	0.1299(11)	0.0724(18)	0.7	1
N6	4*e*	0.171(4)	0.4929(12)	0.2075(19)	0.7	1
N7	4*e*	0.665(4)	0.4354(11)	0.182(2)	0.7	1
N8	4*e*	0.227(4)	0.3495(11)	0.4575(17)	0.7	1
N9	4*e*	0.208(4)	0.3507(12)	0.1532(19)	0.7	1
N10	4*e*	0.617(4)	0.2904(10)	0.331(2)	0.7	1

Table S3.15. Wyckoff position, coordinates, isotropic thermal displacement parameters and occupancy of $BaSr_2[Mg_2P_{10}N_{20}]$ from Rietveld refinement. Standard deviations are given in parentheses.

Atom	***Wyck.***	***x***	***y***	***z***	U_{iso}	***SOF.***
Ba1	2*b*	½	0	0	0.9(2)	0.13(3)
Sr1	2*b*	½	0	0	0.9(2)	0.87(3)
Ba2	4*e*	0.2809(7)	0.64042(18)	0.1101(3)	1.08(9)	0.35(2)
Sr2	4*e*	0.2809(7)	0.64042(18)	0.1101(3)	1.08(9)	0.64(2)
Mg1	4*e*	0.1126(18)	0.1371(6)	0.1121(10)	0.7	1
P1	4*e*	0.381(2)	0.2767(6)	0.1945(10)	0.7	1
P2	4*e*	0.317(3)	0.4293(5)	0.1217(12)	0.7	1
P3	4*e*	0.545(2)	0.3144(6)	0.4900(12)	0.7)	1
P4	4*e*	0.554(6)	0.2590(15)	0.067(3)	0.7	1
P5	4*e*	0.203(5)	0.2012(16)	0.221(3)	0.7	1
N1	4*e*	0.251(5)	0.0653(14)	0.447(3)	0.7	1
N2	4*e*	0.228(5)	0.0602(15)	0.186(3)	0.7	1
N3	4*e*	0.788(6)	0.1294(15)	0.065(2)	0.7	1
N4	4*e*	0.164(5)	0.4857(16)	0.206(3)	0.7	1
N5	4*e*	0.654(6)	0.4299(15)	0.174(3)	0.7	1
N6	4*e*	0.226(5)	0.3459(15)	0.457(3)	0.7	1
N7	4*e*	0.182(5)	0.3492(17)	0.152(3)	0.7	1
N8	4*e*	0.606(5)	0.2898(13)	0.334(3)	0.7	1
N9	4*e*	0.2809(7)	0.64042(18)	0.1101(3)	0.7	1
N10	4*e*	0.2809(7)	0.64042(18)	0.1101(3)	0.7	1

Table S3.16. Wyckoff position, coordinates, isotropic thermal displacement parameters and occupancy of $Sr_3[Mg_2P_{10}N_{20}]$ from Rietveld refinement. Standard deviations are given in parentheses.

Atom	***Wyck.***	***x***	***y***	***z***	U_{iso}	***SOF.***
Sr1	2b	½	0	0	2.41(5)	1
Sr2	2*b*	0.2909(4)	0.64031(12)	0.1076(2)	2.41(5)	1
Mg1	4*e*	0.0732(14)	0.8560(4)	0.2123(7)	0.7	1
P1	4*e*	0.1715(11)	0.0118(3)	0.3146(5)	0.7	1
P2	4*e*	0.1064(10)	0.1360(3)	0.1094(6)	0.7	1
P3	4*e*	0.3849(12)	0.2756(3)	0.1919(5)	0.7	1
P4	4*e*	0.3086(12)	0.4304(3)	0.1195(6)	0.7	1
P5	4*e*	0.5467(12)	0.3124(3)	0.4877(6)	0.7	1
N1	4*e*	0.557(3)	0.2648(8)	0.0644(14)	0.7	1
N2	4*e*	0.210(3)	0.2020(8)	0.2180(14)	0.7	1
N3	4*e*	0.241(3)	0.0667(7)	0.4502(14)	0.7	1
N4	4*e*	0.221(3)	0.0571(7)	0.1771(14)	0.7	1
N5	4*e*	0.779(3)	0.1254(7)	0.0638(14)	0.7	1
N6	4*e*	0.161(3)	0.4940(9)	0.2066(13)	0.7	1
N7	4*e*	0.655(3)	0.4326(8)	0.1774(14)	0.7	1
N8	4*e*	0.250(3)	0.3535(8)	0.4780(14)	0.7	1
N9	4*e*	0.204(3)	0.3501(8)	0.1547(14)	0.7	1
N10	4*e*	0.618(3)	0.2889(7)	0.3374(14)	0.7	1

Table S3.17. Comparison of the crystallographic data from Rietveld refinements of $Ba_{3-x}Sr_x[Mg_2P_{10}N_{20}]$ (x = 0–3). Standard deviations are given in parentheses.

Formula	$Ba_3[Mg_2P_{10}N_{20}]$	$Ba_2Sr_1[Mg_2P_{10}N_{20}]$	$BaSr_2[Mg_2P_{10}N_{20}]$	$Sr_3[Mg_2P_{10}N_{20}]$
Crystal system	monoclinic			
Space group	$P2_1/c$ (no. 14)			
Lattice parameters / Å,°	a = 4.9173(9) b = 18.398(4) c = 9.747(2) β = 102.16(2)	a = 4.91003(12) b = 18.3026(5) c = 9.7410(3) β = 102.238(2)	a = 4.89398(15) b = 18.1725(6) c = 9.7300(4) β = 102.271(3)	a = 4.87564(6) b = 18.0576(3) c = 9.73230(16) β = 102.1999(8)
Cell volume / Å^3	862.07(3)	855.50(4)	845.57(5)	837.50(2)
Radiation λ / Å	0.7093 (Mo-Kα_1)	0.5593 (Ag-Kα_1)		1.5406 (Cu-Kα_1)
2θ-range / °	$2 < 2\theta < 65$	$2 < 2\theta < 55$		$5 < 2\theta < 90$
Data points	4212	3535	3535	5668
Number of parameters (thereof back-ground)	99(16)	63 (12)	85(10)	84(12)
R values	R_{Bragg} = 0.0165 R_p = 0.0485 R_{wp} = 0.0660	R_{Bragg} = 0.0089 R_p = 0.0194 R_{wp} = 0.0265	R_{Bragg} = 0.0053 R_p = 0.0149 R_{wp} = 0.0193	R_{Bragg} = 0.0320 R_p = 0.0645 R_{wp} = 0.1009
GooF (χ^2)	1.327	1.293	0.991	4.292

SEM-EDX measurements

Several crystallites in samples of $Ba_{3-x}Sr_x[Mg_2P_{10}N_{20}]$ were used for EDX data collection. No other elements than *M*, P, N and O were detected. The presence of O may be explained by surface hydrolysis. Within the precision of EDX measurements, experimental and calculated values are in good agreement.

Table S3.18. Results of EDX measurements of $Sr_3[Mg_2P_{10}N_{20}]$. Results are given in atomic percent with standard deviations in parentheses.

	1	**2**	**3**	**4**	**5**	**6**	**7**	**Average**	**Normalized (Sr factor 3)**
Sr	9.2	9.1	8.4	9.0	8.6	8.9	8.4	9(1)	3
Mg	6.2	6.3	6.2	6.3	6.0	6.3	6.1	6(1)	2
P	33.6	34.3	32.8	33.2	31.2	32.9	32.8	33(1)	11
N	51.0	47.0	46.4	45.1	54.2	51.9	50.6	49(3)	17
O	0	3.3	6.1	6.4	0	0	2.1	3(3)	1

Table S3.19. Results of EDX measurements of $BaSr_2[Mg_2P_{10}N_{20}]$. Results are given in atomic percent with standard deviations in parentheses.

	1	**2**	**3**	**4**	**5**	**6**	**7**	**Average**	**Normalized (Ba)**
Sr	5.6	5.6	5.3	5.2	5.9	5.5	5.5	6(1)	2
Ba	2.6	3.2	3.1	3.3	3.8	2.6	2.7	3(1)	1
Mg	6.7	6.3	6.2	6.0	5.6	5.9	5.4	6(1)	2
P	28.4	29.8	29.1	29.1	30.7	28.7	28.2	29(1)	10
N	52.5	42.4	56.4	56.4	45.9	57.3	54.3	52(6)	17
O	4.2	12.7	0	0	8.1	0	4	4(4)	1

Table S3.20. Results of EDX measurements of $Ba_2Sr[Mg_2P_{10}N_{20}]$. Results are given in atomic percent with standard deviations in parentheses.

	1	2	3	4	5	6	Average	Normalized (Sr)
Sr	2.5	3.8	3.6	3.5	3.4	2.9	3(1)	1
Ba	5.6	5.8	6.3	6.1	5.9	5.7	6(1)	2
Mg	6.7	7.8	7.6	6.5	5.9	6.2	7(1)	2
P	29.7	36.0	36.0	33.0	31.3	30.2	32(3)	10
N	55.4	46.6	46.6	45.0	47.0	47.5	48(4)	15
O	0	0	0	5.9	6.5	7.5	3(3)	1

Table S3.21. Results of EDX measurements of $Ba_3[Mg_2P_{10}N_{20}]$. Results are given in atomic percent with standard deviations in parentheses.

	1	2	3	4	5	6	Average	Normalized (Ba factor 3)
Ba	9.9	9.4	9.1	9.0	9.6	9.8	10(1)	3
Mg	5.8	6.1	5.6	5.9	6.1	5.8	6(1)	2
P	32.0	31.1	30.0	30.6	31.9	32.1	32(1)	10
N	51.8	52.9	52.0	54.1	51.9	51.8	53(1)	17
O	0	0	3.0	0	0	0	1(1)	1

Table S3.22: Supplementary calculations for the mechanical properties literature known highly-condensed nitridophosphates.

Compound	Band gap lmbj / pbe [eV]	Debye Temperature [K]	Bulk modulus* [GPa] Voigt / Reuss / Hill	Shear Modulus [GPa] Voigt / Reuss / Hill	Poisson ratio Voigt / Reuss / Hill
CaP_2N_4	4.34 / 4.34	615.0	132.3 / 130.1 / 131.2	75.2 / 73.5 / 74.4	0.261 / 0.262 / 0.262
SrP_2N_4	4.36 / 4.36	621.0	135.4 / 134.5 / 134.9	75.1 / 73.8 / 74.4	0.266 / .268 / 0.267
BaP_2N_4	3.92 / 3.92	552.3	118.5 / 118.5 / 118.5	71.9 / 71.4 / 71.6	0.248 / 0.249 /0.248
CaP_8N_{14}	4.05 / 4.05	822.3	134.4 / 132.7 / 133.5	98.8 / 96.0 / 97.4	0.205 / 0.208 / 0.207
SrP_8N_{14}	4.12 / 4.12	779.6	144.5 / 140.5 / 142.5	96.0 / 93.1 / 94.5	0.228 | 0.229 | 0.228
BaP_8N_{14}	4.10 / 4.10	721.9	142.9 / 138.2 / 140.5	88.7 / 85.7 / 87.2	0.243 / 0.243 / 0.243
$Sr_3[Mg_2P_{10}N_{20}]$	4.23 / 4.22	653.5	136.7 / 135.0 / 135.9|	75.2 / 70.1 / 72.7	0.268 / 0.279 / 0.273
$Ba_3[Mg_2P_{10}N_{20}]$	3.85 / 3.85	640.8	143.3 / 142.2 / 142.8	82.2 / 79.3 / 80.7	0.259 / 0.265 / 0.262

Temperature dependent luminescence measurements

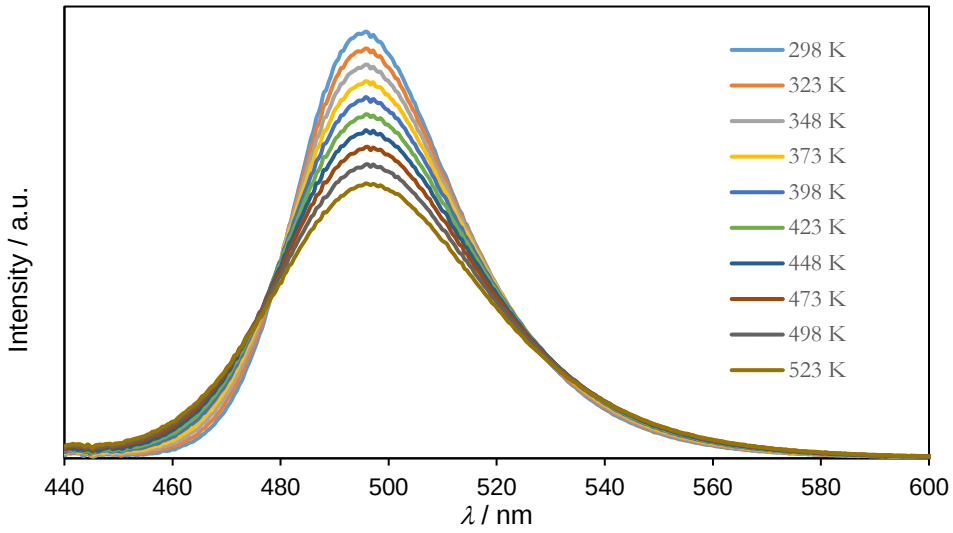

Figure S3.6. Temperature-dependent PL spectra of $Ba_3[Mg_2P_{10}N_{20}]:Eu^{2+}$ with 1 mol% Eu^{2+}.

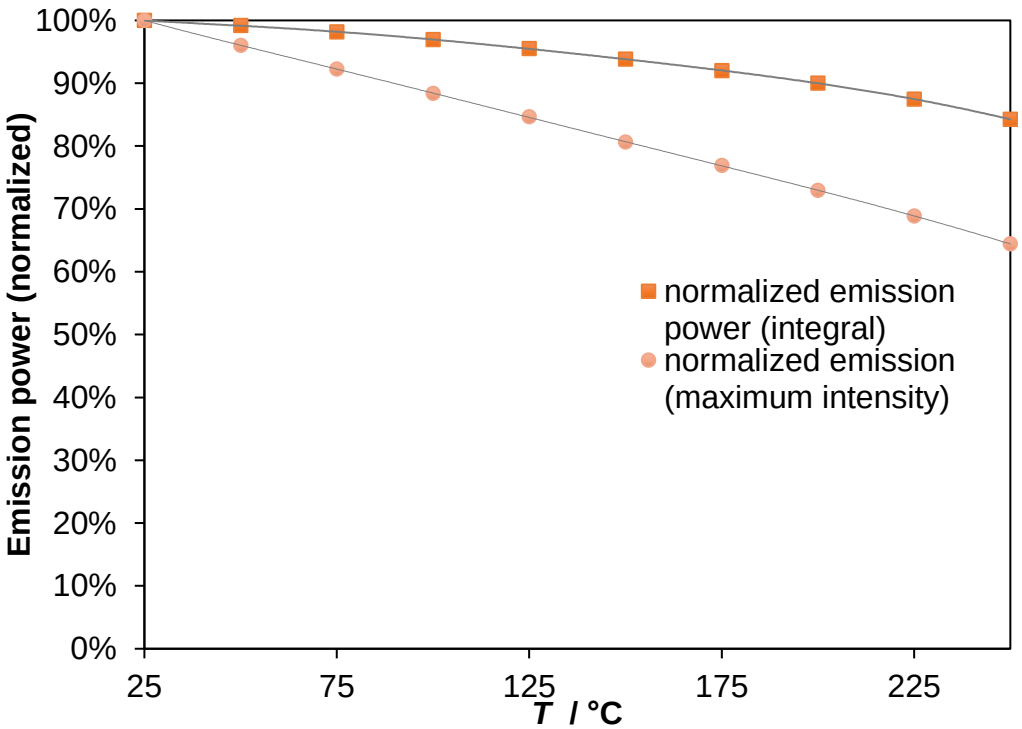

Figure S3.7. Temperature-dependent emission of $Ba_3[Mg_2P_{10}N_{20}]:Eu^{2+}$ with 1 mol% Eu^{2+} : Normalized emission intensities (maximum intensities; rose) and emission integrals (orange) for determination of the *TQ* behaviour.

HT- PXRD

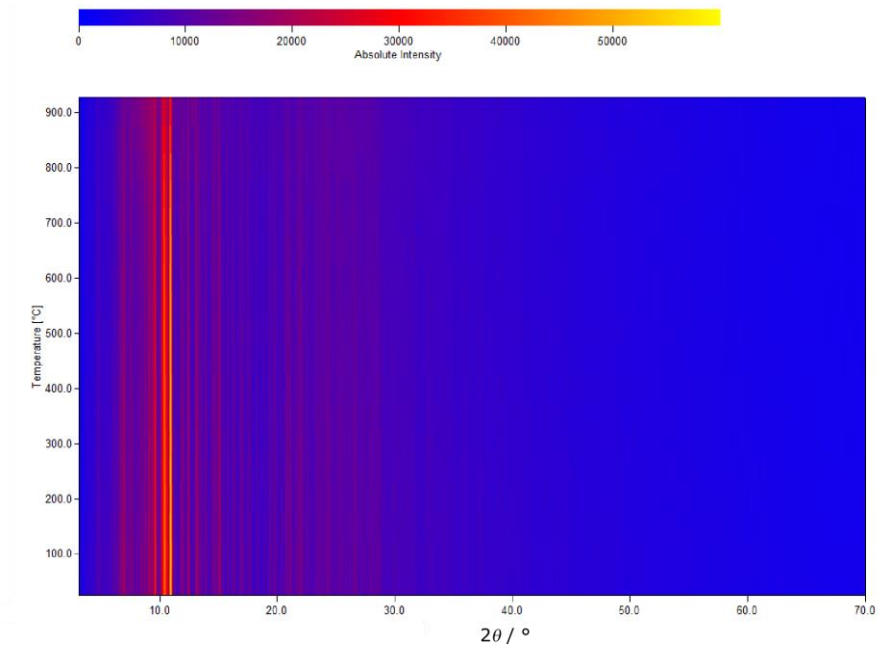

Figure S3.8. Temperature-dependent powder X-ray diffraction patterns (0.5593 Å (Ag-$K_{\alpha 1}$)) of $Ba_3[Mg_2P_{10}N_{20}]$ under argon atmosphere. Heating to 900 °C causes a shift of reflections to lower angles, corresponding to the thermal expansion of the unit cell. Cooling reverses this effect. Neither a phase transition nor thermal decomposition is observed.

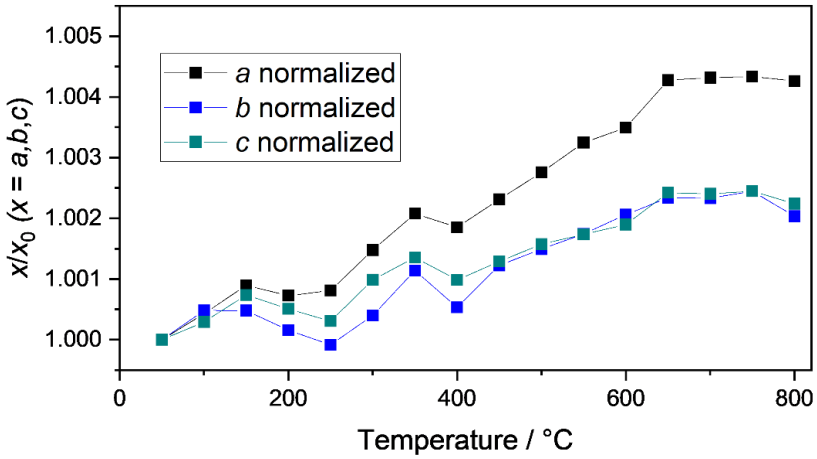

Figure S3.9. Temperature-dependent evolution of the lattice parameters of $Ba_3[Mg_2P_{10}N_{20}]$.

<u>Point symbol using TOPOS:</u>

without Mg as *NFC*: $\{3.6^2.7^2.8\}\{3.6^2.7^3\}\{3.6^3.7^2\}\{4^2.6^2.7^2\}\{4^2.6^4\}$

with Mg as *NFC*: $\{3^2.4^3.5.6^4\}\{3^3.4^2.5.6^4\}\{3^4.4^5.5^4.6^2\}\{3^5.4^2.5^2.6^6\}\{3^5.4^4.5^4.6^2\}\{3^8.4^8.5^9.6^3\}$

10.4 Supporting Information for Chapter 4

SEM-EDX

Table S4.1. SEM-EDX measurements of $Zn_xH_{4-2x}P_4N_8$ with $x \approx 1$ (nitride/azide direct reaction).

Measurement point	Zn / atom%	P / atom%	N / atom%	O / atom%
1	7.3	28.2	61.7	2.8
2	5.7	22.2	67.6	4.5
3	6.8	30.1	59.1	3.9
4	5.6	23.8	67.7	2.9
5	6.3	26.1	64.6	3.1
6	9.0	29.5	57.9	3.6
7	6.1	27.1	63.6	2.9
Average (standard deviation)	6.7(11)	27(3)	63(4)	3.4(1)
Theo.	8	31	62	0
Rel. formula (norm. to Zn)	1.0	4.0	9.4	0.5
Theo. (norm.)	1.0	4.0	8.0	0
P : Zn ratio exp.	4.0			
P : Zn ratio theo.	4.0			

Table S2. SEM-EDX measurements of $Zn_xH_{4-2x}P_4N_8$ with $x \approx 1$ (topochemical deprotonation).

Measurement point	Zn / atom%	P / atom%	N / atom%	O / atom%
1	6.3	26.8	63.9	3.0
2	7.2	28.1	61.7	2.9
3	6.6	26.6	66.8	0
4	6.6	26.2	64.0	3.2
5	8.1	30.3	58.6	3.1
6	7.8	29.2	60.0	2.9
7	7.1	27.4	62.6	2.6
Average (standard deviation)	7.1(6)	27.8(14)	63(3)	2.6(11)
Theo.	8	31	62	0
Rel. formula (norm. to Zn)	1.0	3.9	8.8	0.3
Theo. (norm.)	1.0	4.0	8.0	0
P : Zn ratio exp.	3.9			
P : Zn ratio theo.	4.0			

Table S4.3. SEM-EDX measurements of $Zn_xH_{4-2x}P_4N_8$ with $x \approx 0.85$ (topochemical deprotonation).

Measurement point	Zn / atom%	P / atom%	N / atom%	O / atom%
1	6.8	30.0	59.2	4.0
2	6.5	29.5	61.9	2.0
3	6.7	30.1	60.9	2.3
4	6.2	26.2	64.9	2.8
5	6.2	25.7	65.6	2.6
6	6.2	26.1	64.6	3.1
Average (standard deviation)	6.5(3)	28(3)	63(3)	2.8(6)
Theo.	6.6	31.1	62.3	0
Rel. formula (norm. to Zn)	1.0	4.3	9.7	0.4
Theo. (norm.)	1.0	4.7	9.4	0
P : Zn ratio exp.	4.3			
P : Zn ratio theo.	4.7			

Table S4.4. SEM-EDX measurements of $Zn_xH_{4-2x}P_4N_8$ with $x \approx 0.5$ (topochemical deprotonation).

Measurement point	Zn / atom%	P / atom%	N / atom%	O / atom%
1	4.7	33.5	56.0	5.8
2	4.4	31.9	56.7	7.0
3	3.7	29.3	58.5	6.8
4	3.7	29.6	59.6	7.1
5	3.4	28.1	60.4	8.1
6	4.7	33.5	56.0	5.8
Average (standard deviation)	4.1(5)	31.0(19)	57.9(17)	6.8(7)
Theo.	4.0	32.0	64.0	0
Rel. formula (norm. to Zn)	1.0	7.6	14.1	1.7
Theo. (norm.)	1.0	8	16	0
P : Zn ratio exp. (ratio)	7.6			
P : Zn ratio theo. l	8.0			

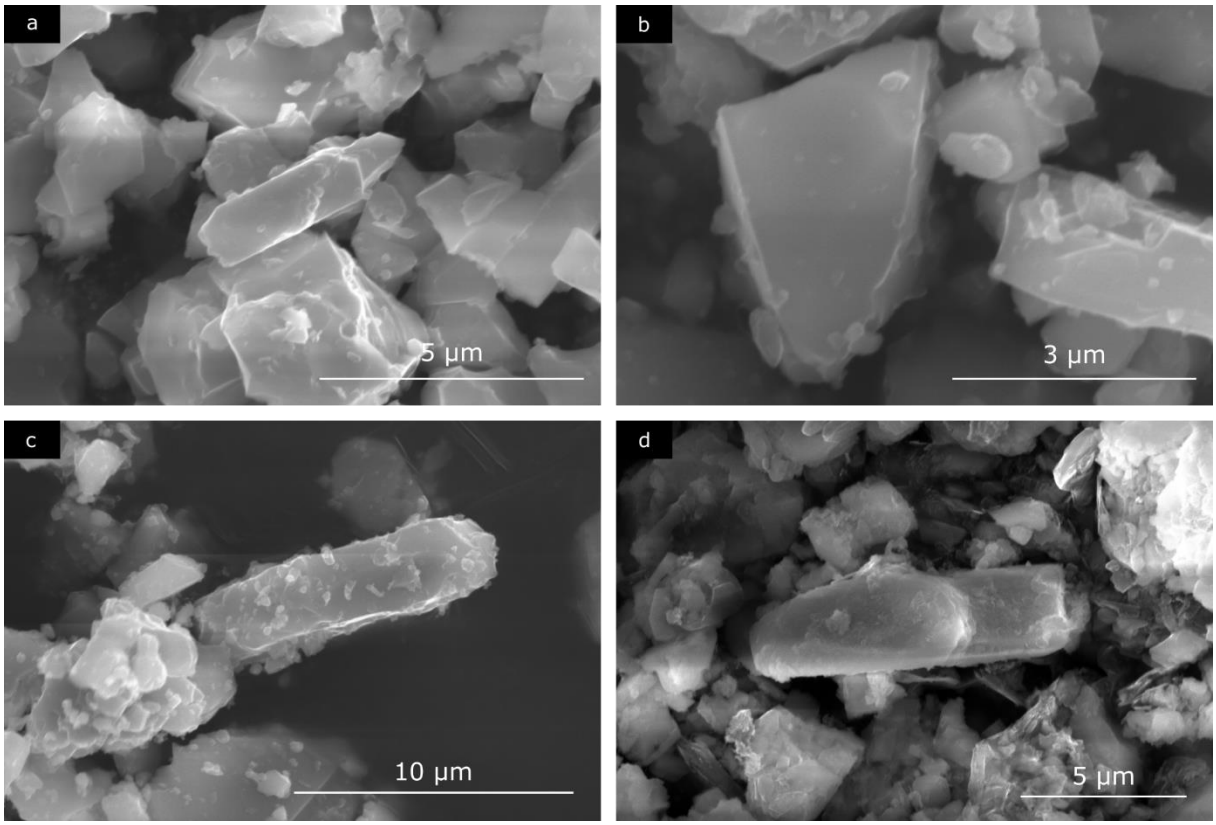

Figure S4.1. SEM images of $Zn_xH_{4-2x}P_4N_8$ ($x \approx$ 0, 0.5, 0.85, 1). a) $x \approx 1$ (nitride/azide direct reaction); b) $x \approx 1$ (topochemical deprotonation); c) $x \approx 0.85$ (topochemical deprotonation) and d) $x \approx 0.5$ (topochemical deprotonation).

Additional Crystallographic Data from single crystal X-ray diffraction data

Table S4.5. Atomic coordinates, crystallographic positions, and equivalent isotropic displacement parameters (Å^2) of $ZnH_2P_4N_8$ (standard deviations in parentheses).

Atom	Wyckoff	Occ.	*x*	*y*	*z*	U_{eq} [Å]
Zn1	4*g*	1/2	0.05586(8)	0.18398(11)	0.83550(8)	0.020
P1	4*g*	1	0.18358(8)	0.31216(12)	0.22644(8)	0.003
P2	4*g*	1	0.31421(8)	0.18614(12)	0.61680(7)	0.015
N1	4*g*	1	0.3329(4)	0.2828(4)	0.4237(4)	0.013
N2	4*g*	1	0.1625(4)	0.6277(4)	0.1638(4)	0.020
N3	4*g*	1	0.2466(4)	0.1274(4)	0.0909(4)	0.006
N4	2*e*	1	0	0.2035(7)	1/4	0.005
N5	2*f*	1	1/2	0.7564(7)	1/4	0.005
H1	4*g*	1	0.554(3)	0.314(10)	0.070(7)	0.063(17)

Table S4.6. Anisotropic displacement parameters of $ZnH_2P_4N_8$ ($Å^2$) (standard deviations in parentheses).

Atom	U_{11}	U_{22}	U_{33}	U_{12}	U_{13}	U_{23}
Zn1	0.0074(3)	0.0053(2)	0.0099(3)	0.0006(2)	0.0042(2)	0.0004(2)
P1	0.0039(2)	0.0039(2)	0.0044(2)	–0.0001(2)	0.0014(2)	0.0004(2)
P2	0.0032(2)	0.0038(2)	0.0035(3)	–0.00012(19)	0.0009(2)	0.0002(2)
N1	0.0039(8)	0.0074(8)	0.0048(8)	–0.0011(7)	0.0017(7)	0.0025(7)
N2	0.0051(8)	0.0036(8)	0.0091(9)	0.0007(7)	0.0029(7)	0.0020(7)
N3	0.0119(9)	0.0023(8)	0.0082(9)	0.0021(7)	0.0060(8)	–0.0002(7)
N4	0.0067(12)	0.0027(11)	0.0075(12)	0.00000	0.0029(10)	0.00000
N5	0.0045(12)	0.0170(15)	0.0062(13)	0.00000	–0.0021(11)	0.00000

Table S4.7. Interatomic distances (Å) in the structure $ZnH_2P_4N_8$ (standard deviations in parentheses).

Zn1	N2	1.962(4)		Zn1	N3	3.195(4)
Zn1	N4	2.020(4)		Zn1	N2	3.308(3)
Zn1	N2	2.035(4)		Zn1	N1	3.346(3)
Zn1	N3	2.152(3)		Zn1	N4	3.4657(7)
Zn1	N3	3.045(4)		Zn1	N3	3.523(3)
Zn1	N4	3.079(4)		Zn1	N2	3.694(3)
Zn1	N1	3.099(3)		P1	N1	3.592(3)
P1	N3	1.601(4)		P1	N5	3.667(3)
P1	N4	1.613(2)		P2	N5	1.5562(8)
P1	N2	1.617(3)		P2	N3	1.619(3)
P1	N1	1.661(3)		P2	N2	1.640(4)
P1	N5	3.282(3)		P2	N1	1.660(4)
P1	N2	3.387(3)		P2	N4	3.2126(5)
P1	N2	3.477(3)		P2	N1	3.326(3)
P1	N2	3.483(4)		P2	N3	3.402(23)
P1	N3	3.527(3)		P2	N1	3.543(3)
P1	N2	3.553(4)		P2	N4	3.547(2)

Table S4.8. P–N bond angles (°) in the structure of $ZnH_2P_4N_8$ (standard deviations in parentheses).

Zn1	N3	N1	97.54(8)	Zn1	N1	N3	112.81(8)
Zn1	N3	N3	115.13(9)	Zn1	N1	N2	45.68(6)
Zn1	N3	N2	101.73(7)	Zn1	N3	N2	137.93(7)
Zn1	N3	N1	148.77(7)	Zn1	N3	N1	95.69(7)
Zn1	N3	N4	59.58(7)	Zn1	N3	N4	144.73(7)
Zn1	N3	N3	78.60(8)	Zn1	N3	N3	71.51(8)
Zn1	N3	N2	61.15(6)	Zn1	N3	N2	91.80(7)
Zn1	N4	N1	144.45(7)	Zn1	N2	N1	47.74(6)
Zn1	N4	N3	113.15(7)	Zn1	N2	N4	45.87(7)

Zn1	N4	N2	61.28(7)		Zn1	N2	N3	138.58(7)
Zn1	N4	N1	47.67(7)		Zn1	N2	N2	88.63(6)
Zn1	N4	N4	97.62(6)		Zn1	N1	N4	92.53(7)
Zn1	N4	N3	81.57(7)		Zn1	N1	N3	118.30(7)
Zn1	N4	N2	149.58(7)		Zn1	N1	N2	115.67(6)
Zn1	N1	N3	49.61(7)		Zn1	N4	N3	132.46(6)
Zn1	N1	N2	108.23(6)		Zn1	N4	N2	54.06(6)
Zn1	N1	N1	98.88(6)		Zn1	N3	N2	124.55(7)
Zn1	N1	N4	95.24(7)		Zn1	N1	N3	112.81(8)
P1	N3	N4	111.69(13)		P1	N4	N2	46.40(9)
P1	N3	N2	110.86(14)		P1	N4	N3	66.99(9)
P1	N3	N1	108.13(15)		P1	N4	N2	66.40(9)
P1	N3	N5	91.36(12)		P1	N4	N1	138.93(9)
P1	N3	N2	49.64(9)		P1	N4	N5	112.07(9)
P1	N3	N2	76.54(13)		P1	N2	N1	110.60(13)
P1	N3	N2	148.35(12)		P1	N2	N5	52.35(11)
P1	N3	N3	102.45(11)		P1	N2	N2	154.81(9)
P1	N3	N2	145.76(12)		P1	N2	N2	70.34(11)
P1	N3	N1	67.97(12)		P1	N2	N2	68.79(10)
P1	N3	N5	42.79(11)		P1	N2	N3	144.40(10)
P1	N4	N2	109.84(13)		P1	N2	N2	101.09(12)
P1	N4	N1	105.60(13)		P1	N2	N1	44.66(9)
P1	N4	N5	155.87(9)		P1	N2	N5	136.90(11)
P1	N4	N2	71.62(9)		P1	N1	N5	72.05(11)
P1	N4	N2	68.81(9)		P1	N1	N2	92.45(9)
P1	N1	N2	174.00(13)		P1	N5	N2	98.75(6)
P1	N1	N2	100.89(12)		P1	N5	N1	43.10(6)
P1	N1	N3	44.46(11)		P1	N5	N5	89.49(5)
P1	N1	N2	46.46(12)		P1	N2	N2	87.82(7)
P1	N1	N1	113.48(11)		P1	N2	N2	117.98(6)
P1	N1	N5	66.95(11)		P1	N2	N3	60.35(6)
P1	N5	N2	131.88(6)		P1	N2	N2	102.23(7)
P1	N5	N2	112.07(7)		P1	N2	N1	117.36(6)
P1	N5	N2	109.72(7)		P1	N2	N5	43.51(6)
P1	N5	N3	116.33(7)		P1	N2	N2	73.76(8)
P1	N2	N3	131.60(7)		P1	N2	N2	56.01(7)
P1	N2	N2	127.66(8)		P1	N2	N1	111.66(8)
P1	N2	N1	71.55(7)		P1	N2	N5	153.48(6)
P1	N2	N5	116.71(6)		P1	N3	N2	43.92(7)
P1	N2	N3	89.37(7)		P1	N3	N1	153.85(7)
P1	N3	N5	65.25(6)		P2	N5	N1	64.16(9)
P1	N2	N1	137.48(7)		P2	N5	N4	119.84(9)
P1	N2	N5	104.30(6)		P2	N3	N2	108.64(13)
P1	N1	N5	94.86(6)		P2	N3	N1	105.78(13)
P2	N5	N3	117.78(13)		P2	N3	N4	76.97(11)
P2	N5	N2	110.51(13)		P2	N3	N1	51.50(9)
P2	N5	N1	104.37(13)		P2	N3	N3	152.91(9)
P2	N5	N4	157.83(9)		P2	N3	N1	136.66(9)
P2	N5	N1	78.59(9)		P2	N3	N4	44.96(11)

P2	N5	N3	87.79(9)		P2	N2	N1	109.37(16)
P2	N2	N4	76.97(11)		P2	N4	N1	122.43(7)
P2	N2	N1	95.03(10)		P2	N4	N3	81.64(7)
P2	N2	N3	49.57(9)		P2	N4	N1	117.83(7)
P2	N2	N1	46.66(10)		P2	N4	N4	82.33(5)
P2	N2	N4	66.48(11)		P2	N1	N3	134.30(6)
P2	N1	N4	53.96(11)		P2	N1	N1	90.93(6)
P2	N1	N1	151.96(11)		P2	N1	N4	44.46(6)
P2	N1	N3	73.65(9)		P2	N3	N1	44.66(5)
P2	N1	N1	115.72(11)		P2	N3	N4	116.00(7)
P2	N1	N4	134.45(11)		P2	N1	N4	94.25(6)

CHNS analysis

Table S4.9. Results of the elemental analysis of $Zn_xH_{4-2x}P_4N_8$ ($x \approx 0.5, 0.85, 1$) by CHNS analysis.

$Zn_xH_{4-2x}P_4N_8$	H_{exp} / H_{theo} [wt%]	N_{exp} / N_{theo} [wt%]
$x = 1$	1.1 / 0.7	35.5 / 36.9
$x = 0.85$	1.4 / 0.8	35.8 / 38.1
$x = 0.5$	1.8 / 1.1	35.9 / 41.2

**Deviation due the measurement method: 0.3 wt%*

FTIR analysis

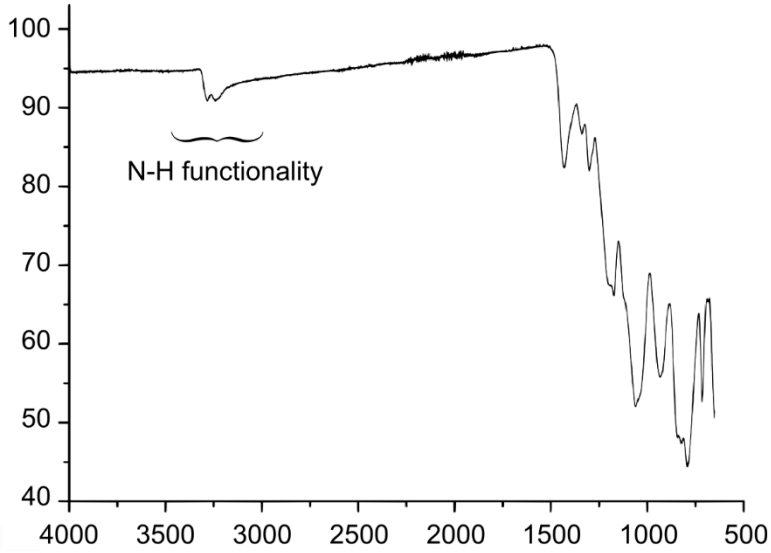

Figure S4.2. FTIR spectrum of $ZnH_2P_4N_8$. N–H vibrations in the range of 3500–3000 cm^{-1} are visible, P–N vibrational bands are visible in the fingerprint area (1500–500 cm^{-1}).

Rietveld Refinements

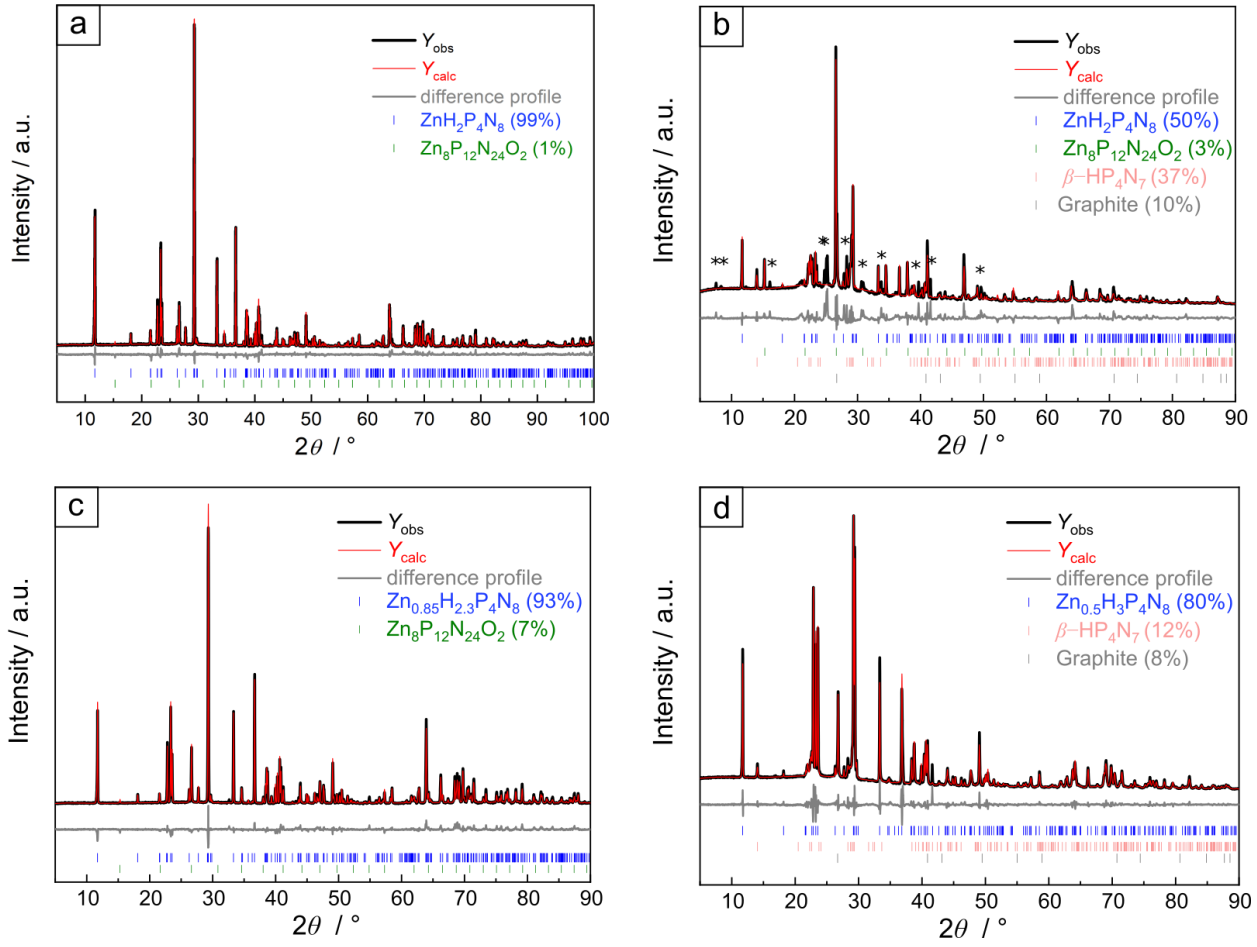

Figure S4.3. Rietveld refinements of $Zn_xH_{4-2x}P_4N_8$ with $x \approx 1$ (a, bottom-up approach), $x \approx 1$ (b, top-down approach), $x \approx 0.85$ (c, top-down approach), and x ≈ 0.5 (d, top-down approach). Observed (black) and calculated (red) powder X-ray diffraction patterns, difference plot (gray), positions of Bragg reflections of $Zn_xH_{4-2x}P_4N_8$ (vertical blue bars), $Zn_8P_{12}N_{24}O_2$ (vertical green bars), β-HP_4N_7 (vertical rose bars), graphite (carbon, vertical gray bars), reflections marked with an asterisk originate from an unknown side phase.

Table S4.10. Rietveld refinements for $Zn_xH_{4-2x}P_4N_8$ ($x \approx 0.5, 0.85, 1$).

	$ZnH_2P_4N_8$ bottom-up approach	**$ZnH_2P_4N_8$ top-down approach**	**$Zn_{0.85}H_{2.3}P_4N_8$ top-down approach**	**$Zn_{0.5}H_3P_4N_8$ top-down approach**
Formula	$ZnH_2P_4N_8$	$ZnH_2P_4N_8$	$Zn_{0.85}H_{2.3}P_4N_8$	$Zn_{0.5}H_3P_4N_8$
Crystal system		monoclinic		
Space group		*P*2/*c* (no. 13)		
Lattice parameters				
a / Å	7.92281(12)	7.9216(7)	7.92344(7)	7.91342(13)
b / Å	4.90420(8)	4.8939(3)	4.89919(5)	4.87689(8)
c / Å	7.98996(13)	7.9896(6)	8.00041(9)	8.02641(13)
β / °	107.7118(7)	107.718(6)	107.7211(8)	107.7255(11)
Cell volume / Å^3	295.741(8)	295.04(4)	295.04(4)	295.06(1)
Radiation *λ* / Å		1.540596 (Cu-Kα_1)		
Diffractometer		STOE Stadi P		
Monochromator		Ge(111)		
Detector		Mythen 1K		
2*θ*-range / °	$5 < 2\theta < 100$	$5 < 2\theta < 92$	$5 < 2\theta < 92$	$5 < 2\theta < 120$
Data points	6336	5808	5808	7788
Number of parameters (thereof background)	53(12)	88(16)	53(12)	80(16)
R values				
R_{Bragg}	0.5336	0.0531	0.07306	0.0230
R_p	0.7568	0.0837	0.0783	0.05193
R_{wp}	0.1003	0.1246	0.09887	0.07671
Goodness of fit	1.4524	7.118	1.9255	3.009

MAS NMR Spectroscopy

β-HPN_2

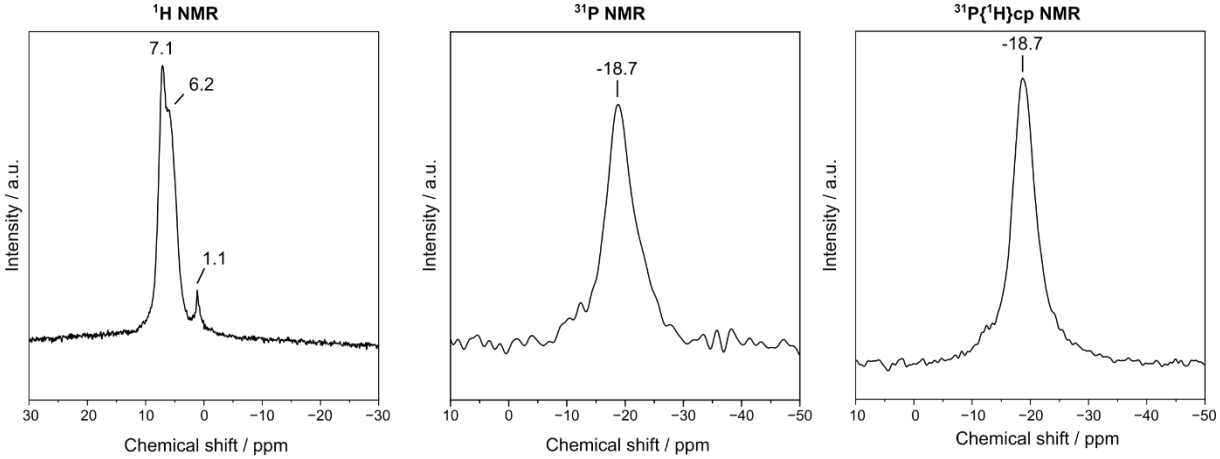

Figure S4.4. ^{1}H, ^{31}P and $^{31}P\{^{1}H\}$cp experiments of β-HPN_2.

$Zn_xH_{4-2x}P_4N_8$ ($x \approx 0.5$)

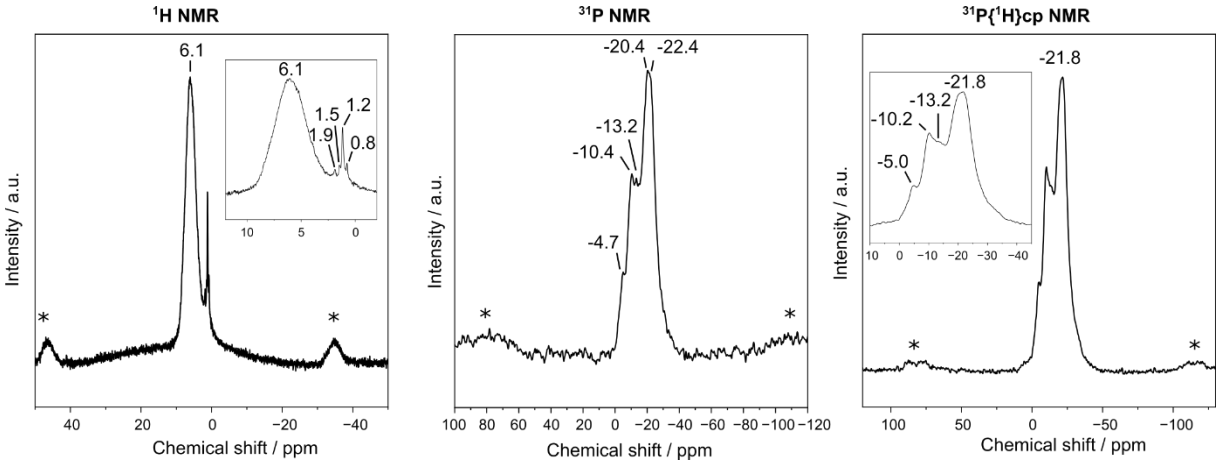

Figure S4.5. ^{1}H, ^{31}P and $^{31}P\{^{1}H\}$cp experiments of $Zn_xH_{4-2x}P_4N_8$ ($x \approx 0.5$).

$Zn_xH_{4-2x}P_4N_8$ ($x \approx 0.85$)

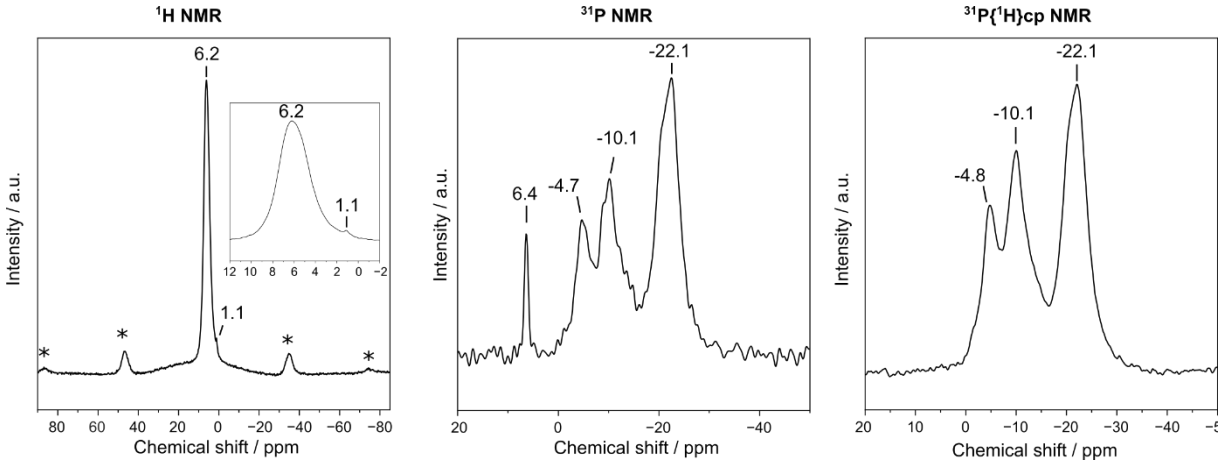

Figure S4.6. ^{1}H, ^{31}P and $^{31}P\{^{1}H\}$cp experiments of $Zn_xH_{4-2x}P_4N_8$ ($x \approx 0.85$).

$ZnH_2P_4N_8$

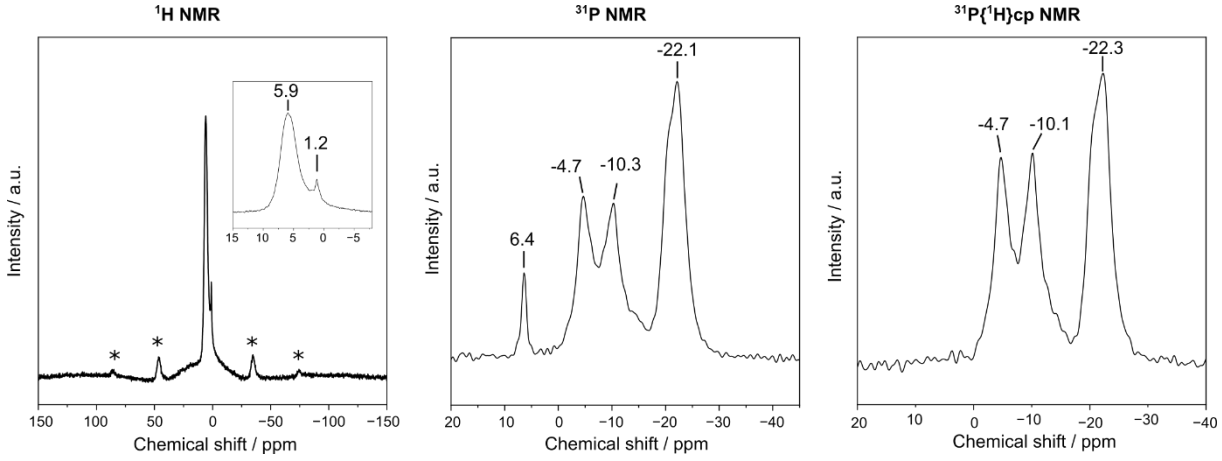

Figure S4.7. ^{1}H, ^{31}P and $^{31}P\{^{1}H\}$cp experiments of $ZnH_2P_4N_8$.

Local crystal structure of $ZnH_2P_4N_8$ in *Pc* (no. 7)

Table S4.11. Atomic coordinates of $ZnH_2P_4N_8$ in space group *Pc* for explanation of a possible local environment during synthesis.

Atom	Wyckoff	*x*	*y*	*z*
Zn1*	2*a*	0.38876	0.18398	0.75920
Zn2*	2*a*	0.27704	0.18398	0.58820
P1	2*a*	0.14932	0.31216	0.19726
P2	2*a*	0.51648	0.31216	0.15014
P3	2*a*	0.01869	0.18614	0.80690
P4	2*a*	0.64711	0.18614	0.54050
N1	2*a*	0.00000	0.28280	0.00000
N2	2*a*	0.66580	0.28280	0.34740
N3	2*a*	0.17040	0.62770	0.25990
N4	2*a*	0.49540	0.62770	0.08750
N5	2*a*	0.08630	0.12740	0.33280
N6	2*a*	0.57950	0.12740	0.01460
N7	2*a*	0.33290	0.20350	0.17370
N8	2*a*	0.83290	0.24360	0.67370
H1	2*a*	0.88690	0.68600	0.49370
H2	2*a*	0.77890	0.31400	0.35370

**occupation either Zn1 or Zn2 = 1, for reasons of electrostatic and charge neutrality never both at the same time.*

Schematic drawing of the octahedral pressure cell and Walker-type module used for multianvil press synthesis

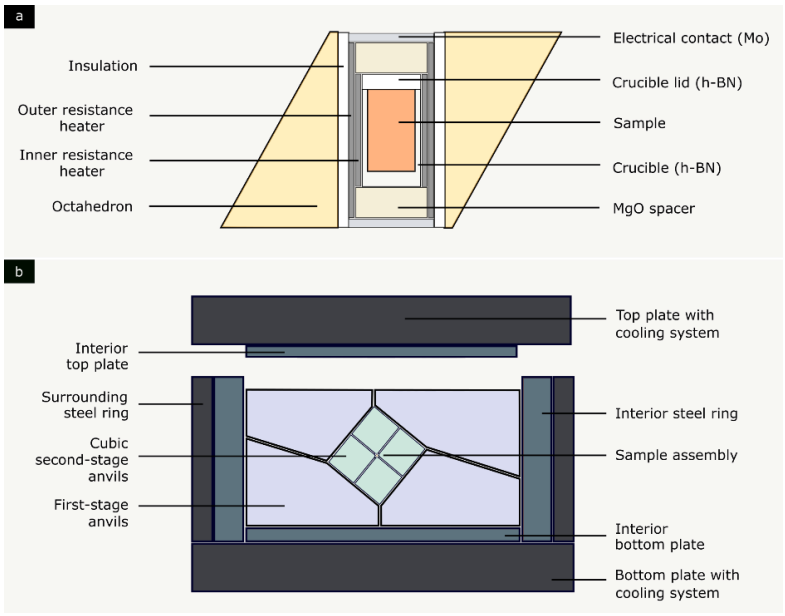

Figure S4.8. Schematic drawing of the octahedral pressure cell (a) and Walker-type module (b) used for high-pressure/high-temperature synthesis.

10.5. Supporting Information for Chapter 5

Rietveld refinement

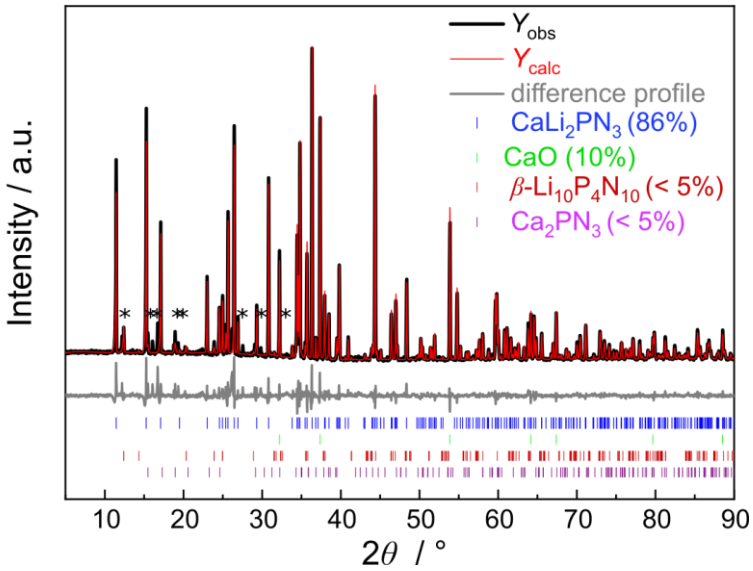

Figure S5.1. Rietveld refinement for $CaLi_2PN_3$ via bottom-up synthesis. Observed (black) and calculated (red) powder X-ray diffraction patterns, difference plot (gray), positions of Bragg reflections of $CaLi_2PN_3$ (vertical blue bars), CaO (vertical green bars), β-$Li_{10}PN_{10}$ (vertical red bars), Ca_2PN_3 (vertical purple bars), reflections marked with an asterisk originate from an unknown minor side phase.

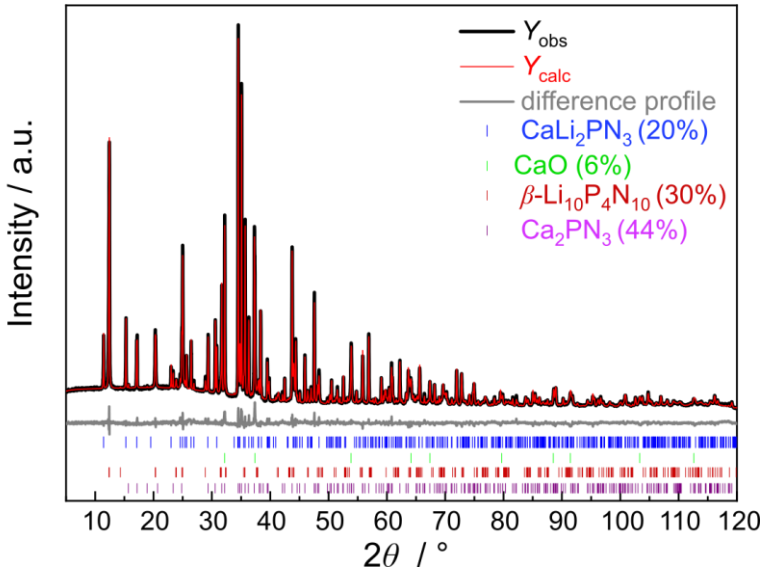

Figure S5.2. Rietveld refinement for $CaLi_2PN_3$ via top-down synthesis. Observed (black) and calculated (red) powder X-ray diffraction patterns, difference plot (gray), positions of Bragg reflections of $CaLi_2PN_3$ (vertical blue bars), CaO (vertical green bars), β-$Li_{10}PN_{10}$ (vertical red bars) and Ca_2PN_3 (vertical purple bars).

Table S5.1. Comparison of the crystallographic data from Rietveld refinements of $CaLi_2PN_3$. Standard deviations are given in parentheses.

	Bottom-up synthesis	**Top-down synthesis**
Formula	$CaLi_2PN_3$	
Crystal system	monoclinic	
Space group	*C*2/*c* (no. 15)	
Lattice parameters / Å,°	*a* = 11.3401(2) *b* = 11.5942(2) *c* = 4.9432(7) *β* = 113.9755(10)	*a* = 11.3422(2) *b* = 11.5944(2) *c* = 4.9444(10) *β* = 113.980(2)
Cell volume / $Å^3$	593.85(2)	594.10(2)
Radiation *λ* / Å	1.540596 (Cu-Kα_1)	
Diffractometer	STOE Stadi P	
Monochromator	Ge(111)	
Detector	Mythen 1K	
2*Θ*-range / °	$5 < 2\Theta < 90$	$5 < 2\Theta < 120$
Data points	5668	7668
Number of parameters (thereof background)	88(10)	90(12)
R values	R_{Bragg} = 0.0346 R_p = 0.0748 R_{wp} = 0.1116	R_{Bragg} = 0.0278 R_p = 0.0439 R_{wp} = 0.0593
Goodness of fit	2.5451	1.901

Additional crystallographic data:

Table S5.2. Atomic coordinates, crystallographic positions, and equivalent isotropic displacement parameters (Å^2) of $CaLi_2PN_3$ (standard deviations in parentheses).

Atom	Wyckoff	*x*	*y*	*z*	U_{eq} [Å]
Ca1	4*e*	0	0.4137	1/4	0.020
P1	8*f*	0.28562(3)	0.07576(3)	0.24149(7)	0.003
Li1	8*f*	0.1680(4)	0.2689(2)	0.2223(7)	0.015
Li2	4*e*	0	0.6378(4)	1/4	0.013
Li3	4*e*	0	0.4137(4)	1/4	0.020
N1	8*f*	0.36987(11)	0.18553(10)	0.4121(2)	0.006
N2	8*f*	0.13072(11)	0.09631(10)	0.1205(2)	0.005
N3	8*f*	0.16914(11)	0:45274(10)	0:0434(2)	0.005

Table S5.3. Anisotropic displacement parameters of $CaLi_2PN_3$ (Å^2) (standard deviations in parentheses).

Atom	U_{11}	U_{22}	U_{33}	U_{23}	U_{13}	U_{12}
Ca1	0.00599(14)	0.00513(14)	0.00595(14)	–0.00011(9)	0.00219(10)	–0.00008(9)
P1	0.0032(2)	00.0035(2)	0.0030(2)	–0.0003(1)	0.0013(1)	–0.0003(1)
Li1	0.0183(13)	0.0120(13)	0.0169(13)	–0.0018(10)	0.0085(10)	–0.0041(10)
Li2	0.0113(16)	0.0153(19)	0.0157(18)	0.000	0.0077(14)	0.000
Li3	0.024(2)	0.014(2)	0.0132(19)	0.000	–0.0025(16)	0.000
N1	0.0067(5)	0.0044(5)	0.0061(5)	–0.0014(4)	0.0024(4)	–0.0013(4)
N2	0.0045(5)	0.0063(5)	0.0053(5)	0.0005(4)	0.0021(4)	0.0005(4)
N3	0.0059(5)	0.0049(5)	0.0048(5)	–0.0016(4)	0.0029(4)	–0.0012(4)

Table S5.4. Interatomic distances (Å) in the structure of $CaLi_2PN_3$ (standard deviations in parentheses).

Ca1	N1	2.3468(12)		Li2	N1	2.0211(16)
Ca1	N2	2.3762(12)		Li2	N1	2.0211(16)
Ca1	N2	2.4692(12)		Li2	N3	2.150(2)
Ca1	N2	2.4740(11)		Li2	N3	2.150(2)
Ca1	N2	2.5323(12)		Li2	N3	3.303(3)
Ca1	N3	2.6367(10)		Li2	N3	3.303(3)
Ca1	N3	3.5303(13)		Li2	N2	3.583(3)
Ca1	N1	3.6467(14)		Li2	N2	3.583(4)
Li1	N2	2.064(3)		Li3	N1	2.070(3)
Li1	N1	2.0872(36)		Li3	N1	2.070(3)
Li1	N1	2.304(3)		Li3	N3	2.432(4)
Li1	N3	2.309(3)		Li3	N3	2.432(4)
Li1	N1	3.032(4)		Li3	N3	2.5526(16)
Li1	N1	3.138(4)		Li3	N3	2.5526(16)
Li1	N2	3.489(3)		Li3	N3	3.6252(11)
Li1	N3	3.592(3)		Li3	N3	3.6252(11)
Li1	N2	3.696(4)		P1	N3	1.7269(11)
P1	N1	1.6084(11)		P1	N3	3.3739(11)
P1	N2	1.6268(12)		P1	N2	3.478(1)
P1	N3	1.7147(13)		P1	N2	3.6387(13)

Table S5.5. P–N bond angles (°) in the structure of $CaLi_2PN_3$ (standard deviations in parentheses).

P1	N1	N2	113.56(6)		P1	N2	N2	66.07(5)
P1	N1	N3	105.69(5)		P1	N3	N3	103.48(5)
P1	N1	N3	111.44(6)		P1	N3	N3	150.68(5)
P1	N1	N3	73.94(4)		P1	N3	N2	51.52(4)
P1	N1	N2	153.55(5)		P1	N3	N2	133.22(4)
P1	N1	N2	118.15(5)		P1	N3	N3	52.69(4)
P1	N2	N3	111.41(6)		P1	N3	N2	89.25(4)
P1	N2	N3	110.70(6)		P1	N3	N2	46.82(4)
P1	N2	N3	94.67(4)		P1	N3	N2	132.47(3)
P1	N2	N2	71.14(4)		P1	N3	N2	46.15(3)
					P1	N2	N2	87.91(3)

MAS NMR Spectroscopy

^{31}P MAS NMR

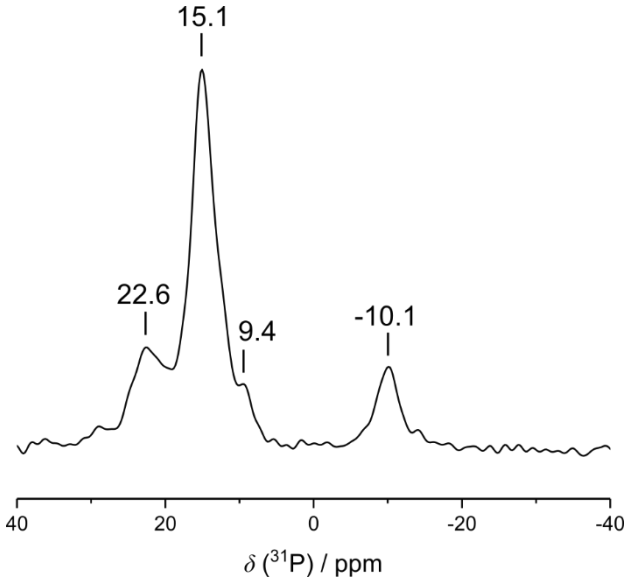

Figure S5.3. ^{31}P MAS NMR spectrum of the bulk according bottom-up synthesis via azide route. Signal at –10.1 ppm can be assigned to Ca_2PN_3 (see Figure S5.5; also in accordance to side phase of PXRD (Figure S5.1). The signals at 22.6 and 9.4 ppm results from unknown side phases.

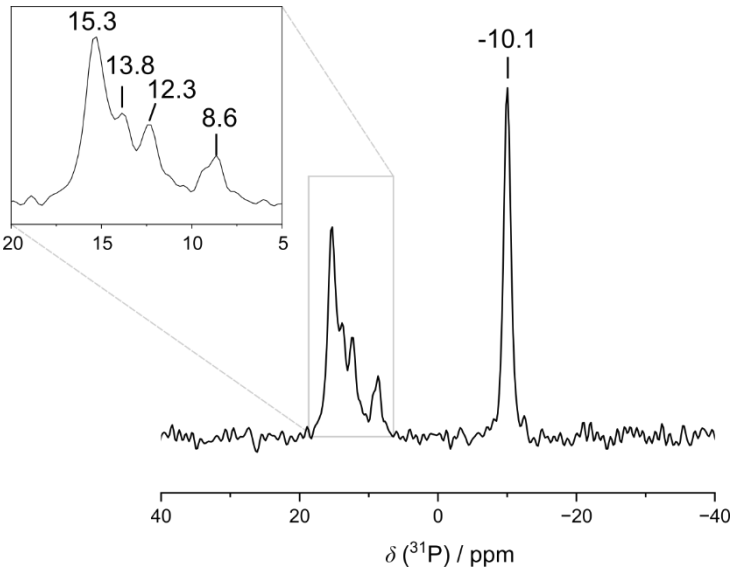

Figure S5.4. ^{31}P MAS NMR spectrum of the bulk according top-down synthesis via double salt synthesis. Signal at –10.1 ppm can be assigned to Ca_2PN_3 (see Figure S5; also in accordance to side phase of PXRD (Figure S2). Signals in enlarged section (gray box), can be assigned to β-$Li_{10}P_4N_{10}$ (15.4, 14.0, 12.4 and 9.0 ppm), with the ^{31}P signal of $CaLi_2PN_3$ superimposed at 15.3 ppm (derivable from reference by Bertschler et al.).[24]

Note: Since the signals at 22.6 and 9.4 ppm can only be observed in the bottom-up synthesis (Figure S3), it can be concluded from the comparison of both approaches that they can be assigned to the unknown minor phases.

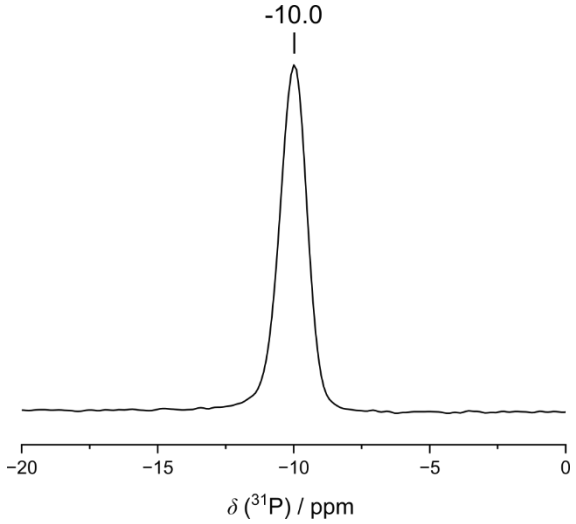

Figure S5.5. ^{31}P MAS NMR spectrum of Ca_2PN_3.

$^{6/7}$Li MAS NMR

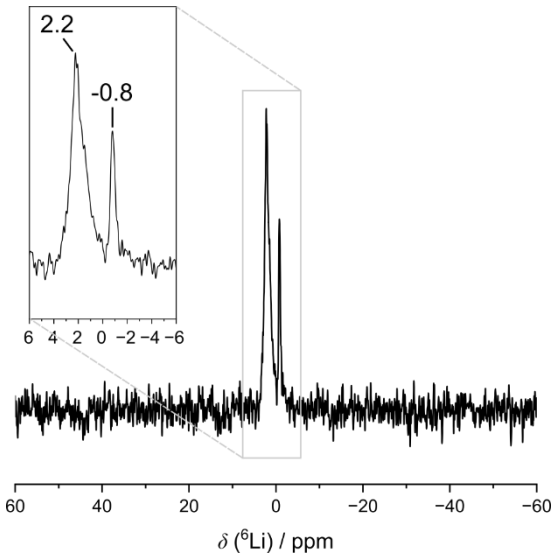

Figure S5.6. ^{6}Li MAS NMR spectrum of the bulk according bottom-up synthesis via azide route.

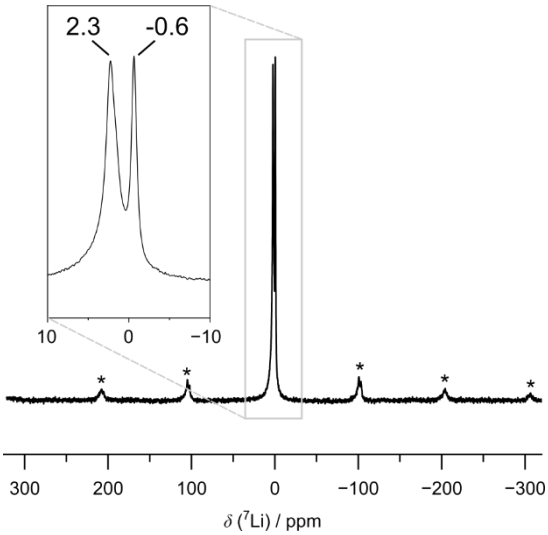

Figure S5.7. ^{7}Li MAS NMR spectrum of the bulk according bottom-up synthesis via azide route.

Note: The ^{6}Li and ^{7}Li MAS NMR spectra differ from pure α-/β-$Li_{10}P_4N_{10}$ (signal at 1.8 ppm not observable) suggesting that additional Li is present in one or more of the other phases in the bulk, superimposing this signal. In the double salt approach, where PXRD shows only $Li_{10}P_4N_{10}$, Ca_2PN_3 and CaO as minor phases, the signal is comparable, confirming Li in $CaLi_2PN_3$. Since the chemical environments of Li in $CaLi_2PN_3$ are similar to β-$Li_{10}P_4N_{10}$, a signal overlap is therefore not unexpected. However, it was not possible to make a more precise assignment.

^{1}H and ^{31}P{^{1}H} NMR

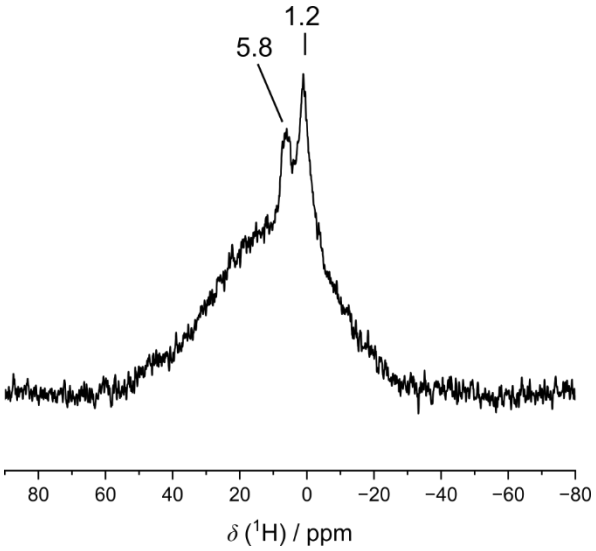

Figure S5.8. ^{1}H MAS NMR spectrum of the bulk according bottom-up synthesis via azide route.

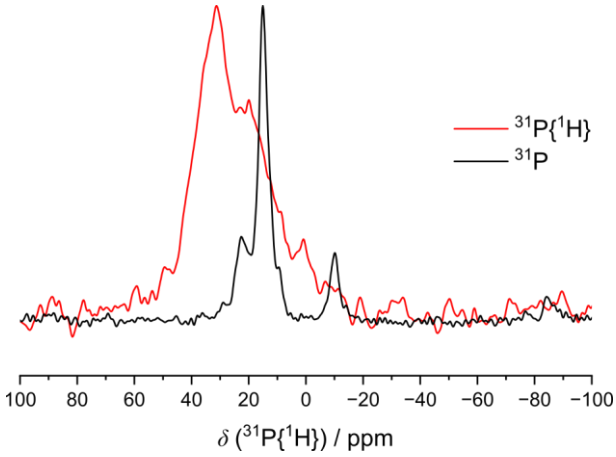

Figure S5.9. ^{31}P{^{1}H} MAS NMR spectrum of the bulk according bottom-up synthesis via azide route. The signals in the cp experiment do not match the ^{31}P direct experiment, which indicates no evidence of H in $CaLi_2PN_3$.

The signals in the cp experiment do not match the ^{31}P direct experiment, which indicates no evidence of H in $CaLi_2PN_3$. However, the agreement with the signal at 22.6 ppm means that the unknown minor phase contains H in the environment of P.

Table S5.6. SEM EDX measurements of $CaLi_2PN_3$

Meas. point	**Ca**	**P**	**N**	**O**	**standard. comp.**
measurement 1	19	21	30	30	$CaP_{1.1}N_{1.6}O_{1.5}$
measurement 2	16	18	33	33	$CaP_{1.1}N_{2.0}O_{2.0}$
measurement 3	17	18	51	15	$CaP_{1.2}N_{3.3}O_{1.0}$
measurement 4	19	16	48	18	$CaP_{0.8}N_{2.5}O_{0.9}$
measurement 5	24	21	39	17	$CaP_{0.9}N_{1.6}O_{0.7}$
measurement 6	19	16	48	18	$CaP_{0.8}N_{2.5}O_{0.9}$
Ø(SD)	**19(3)**	**18(2)**	**42(8)**	**22(7)**	**$CaP_{0.9}N_{2.5}O_{0.9}$**
calculated	20	20	60	0	$Ca_{1.0}P_{1.0}N_{3.0}$*

** Light atoms, such as lithium, are not detectable by EDX, and thus, may be excluded from the determination of the atomic ratio.*

Low-cost crystallographic calculations (*LCC*)

Table S5.7. Results of CHARDI calculations for $CaLi_2PN_3$.

Ca1	**P1**	**Li1**	**Li2**	**Li3**	**N1**	**N2**	**N3**
1.94	5.07	0.98	1.02	1.00	−3.12	−3.15	−2.73

Table S5.8. BVS values for $CaLi_2PN_3$.

atom	**Ca1**	**P1**	**Li1**	**Li2**	**Li3**	**N1**	**N2**	**N3**
theo.	2	5	1	1	1	−3	−3	−3
calc.	2.09	5.02	0.92	1.18	1.00	−3.04	−3.10	−2.98

Minimal bounding ellipsoid (MBE) analysis

$CaLi_2PN_3$

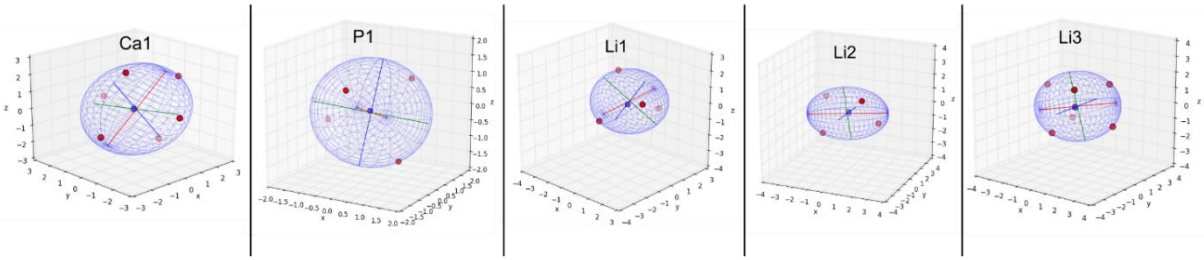

Figure S5.10. Graphical illustration of the minimal bounding ellipsoids of the cations in $CaLi_2PN_3$ calculated by PIEFACE (cations in blue, N in red).

Table S5.9. Results of the MBE calculation for $CaLi_2PN_3$. The values of Ca1 and Li3 describes typical octahedral coordination (axially stretched, prolate), P1 typical PN_4 tetrahedra; values of Li1 and 2 show tetrahedral coordination with minor (Li1) and major (Li2) distortion.

Atom	***R*1**	***R*2**	***R*3**	**<*R*>**	**Sigma (*R*)**	***S***	**Center Displacement**	***CN***
Ca1	2.6519	2.3677	2.3504	2.4567	0.1382	0.0998	0.1098	6
P1	1.7036	1.6889	1.6081	1.6669	0.0420	–0.0393	0.0932	4
Li1	2.7431	1.9906	1.5798	2.1045	0.4817	0.0680	0.3905	4
Li2	2.7605	1.8249	1.3876	1.9910	0.5727	0.0993	0.2480	4
Li3	2.8148	2.1905	1.9282	2.3112	0.3719	0.1020	0.2061	6

Ca_2PN_3

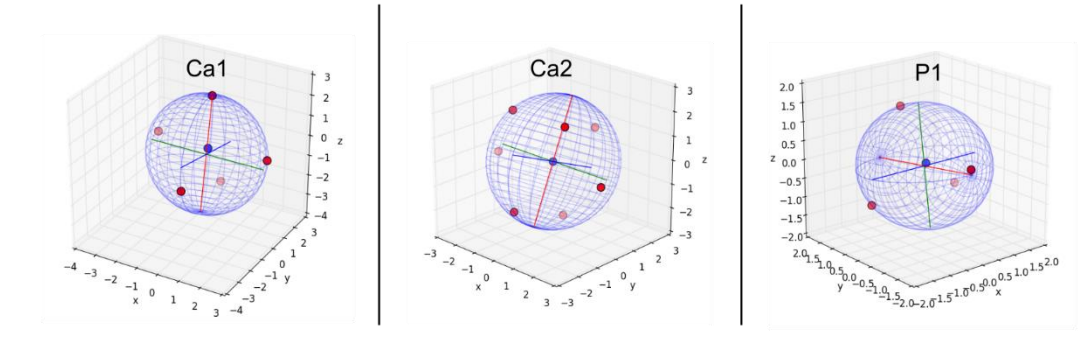

Figure S5.11. Graphical illustration of the minimal bounding ellipsoids of the cations in Ca_2PN_3 calculated by PIEFACE (cations in blue, N in red).

Table S5.10. Results of the MBE calculation for Ca_2PN_3. The values of Ca1 and Ca2 indicates axially compression (oblate) of fivefold, respectively sevenfold coordinated polyhedral. The values of P1 describe typical PN_4 tetrahedra.

Atom	***R*1**	***R*2**	***R*3**	**<*R*>**	**Sigma (*R*)**	***S***	**Center Displacement**	***CN***
Ca1	2.6944	2.6641	2.1098	2.4894	0.2687	–0.1968	0.2674	5
Ca2	2.6363	2.6191	2.2800	2.5118	0.1640	–0.1229	0.0016	7
P1	1.7425	1.6029	1.5895	1.6450	0.0692	0.0718	0.1107	4

Partial Topological Representation

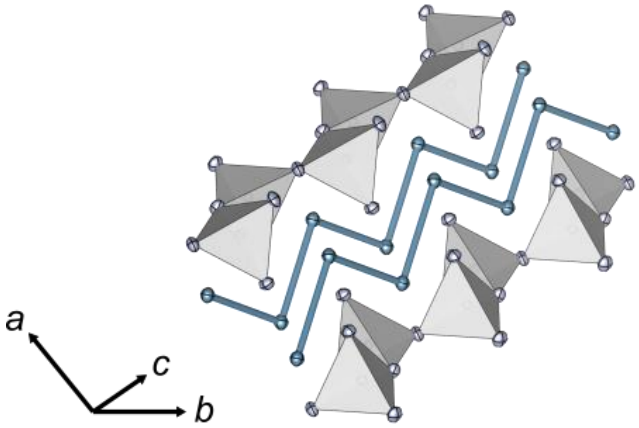

Figure S5.12. Partial topological representation: Shortest Ca–Ca distances connected via blue lines, PN_4 tetrahedra chains (gray). Atomic ellipsoids (N gray, Ca blue) are displayed with 95%.

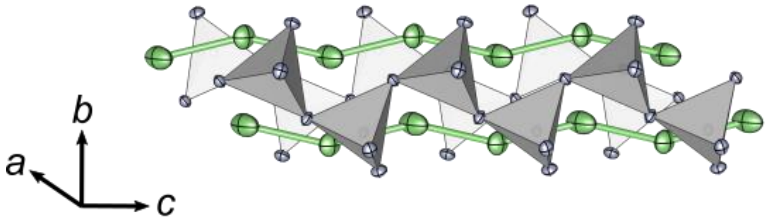

Figure S5.13. Partial topological representation: Shortest Li–Li distances connected via gree lines, PN_4 tetrahedra chains (gray). Atomic ellipsoids (N gray, Li green) are displayed with 95%.

Density Functional Theory (DFT) Calculations

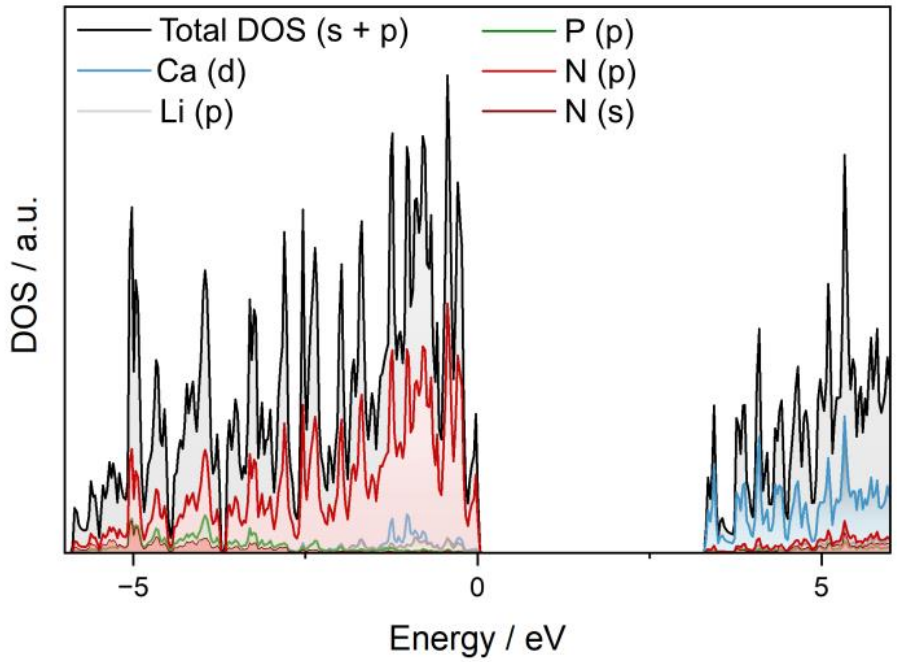

Figure S5.14. Partial and total contribution (N (s&p), P (p), Li (p) & Ca (d)) to the density of states of $CaLi_2PN_3$.

Formation Energy Calculations

Table S5.11. Total Energy Calculation of $CaLi_2PN_3$, Ca_2PN_3 and Li_4PN_3.

Compound	**Total Energy E_{tot} /eV**	***Z***	**Energy per form unit /eV**
$CaLi_2PN_3$	–170.51	2	–85.26
Ca_2PN_3	–163.85	4	–40.96
Li_4PN_3	–244.32	8	–30.54

$\Delta_f E = E_{tot}(CaLi_2PN_3) - E_{tot}(Li_4PN_3) - E_{tot}(Ca_2PN_3) = -13.75$ eV

Energy profit per atom ($n(CaLi_2PN_3) = 14$)

$\Delta_f E_{atom} = -13.75$ eV / 14 = –0.982 eV/atom (≙ –96.49 kJ/mol)

10.6. Supporting Information for Chapter 6

Structure determination

Table S6.1: Crystallographic data of $Ca_2Li_6P_4N_{10}$, $Ca_{2.7}Li_{4.6}P_4N_{10}$ and $Sr_3Li_4P_4N_{10}$ from single-crystal refinement. Standard deviations are given in parentheses.

Formula	**$Ca_2Li_6P_4N_{10}$***	**$Ca_{2.7}Li_{4.6}P_4N_{10}$**	**$Sr_3Li_4P_4N_{10}$**
Crystal system	tetragonal	triclinic	triclinic
Molecular weight /	385.78	404.12	554.60
Space group	$I\bar{4}2d$ (no. 122)	$P\bar{1}$ (no. 2)	$P\bar{1}$ (no. 2)
Lattice parameters / Å	a = 9.8906(2) c = 9.5917(2)	a = 7.6074(3) b = 8.0676(3) c = 8.4435(3) α = 101.5820(10) β = 93.937(2) γ = 113.888(2)	a = 7.6338(5) b = 7.8369(6) c = 8.5239(6) α = 106.076(3) β = 92.775(3) γ = 94.078(3)
Cell volume / Å^3	938.30(4)	457.62(3)	487.53(6)
Formula units per cell	4	2	2
Calculated density /	2.731	2.933	3.778
μ / mm^{-3}	1.888	2.329	17.002
T_{min} / T_{max}	0.9549 / 1.0000	0.9467 / 1.0000	0.9072 / 1.0000
Radiation		Mo-K$_\alpha$ (λ = 0.71073 Å)	
Temperature / K		293(2)	
F(000)	752	396	512
θ range / °	4.121 < θ < 33.109	3.115< θ < 29.129	2.715< θ < 30.998
Total no. of reflections	8726	16450	23080
Independent reflections	891 (863)	2471 (1947)	3108 (2692)
Refined parameters	48	130	193
Flack parameter	0.03(6)	-	-
BASF	0.02746	-	-
R_{int}; R_σ	0.0330; 0.0156	0.0967; 0.0657	0.0495; 0.0306
$R1$ (all data); $R1$	0.0155; 0.0144	0.0779; 0.0557	0.0407 / 0.0320
$wR2$ (all data); $wR2$	0.0388; 0.0383	0.1211; 0.1121	0.0785 / 0.0751
Goodness of fit	1.053	1.060	1.047

$\Delta\rho_{max}$; $\Delta\rho_{min}$ / e·Å^{-3}	0.328; –0.259	1.250; –0.896	1.386; –2.657

**refined as an inversion twin*

Note: Due to poor crystal quality of $Ca_{2.7}Li_{4.6}P_4N_{10}$ only the AE, P and N atoms were refined anisotropically. In the case of $Ca_4Li_2P_4N_{10}$ the structure solution was based on SCXRD data; the structure model was refined by Rietveld refinement based on PDXRD data.

Table S6.2. Wyckoff position, coordinates, equivalent thermal displacement parameters and occupancy of $Ca_2Li_6P_4N_{10}$ from single-crystal refinement. Standard deviations are given in parentheses.

Atom	***Wyck.***	***x***	***y***	***z***	U_{eq}	***SOF***
Ca1	8*d*	0.31853(4)	1/4	5/8	0.00640(9)	1
P1	16*e*	0.50284(4)	0.14089(4)	0.35889(4)	0.00437(8)	1
N1	8*c*	1/2	0	0.45299(17)	0.00586(17)	1
N2	16*e*	0.36931(14)	0.13824(14)	0.25025(15)	0.00586(17)	1
N3	16*e*	0.51337(14)	0.26728(13)	0.45828(13)	0.0070(2)	1
Li1	16*e*	0.3892(3)	0.4136(4)	0.3728(4)	0.0154(6)	1
Li2	8*d*	1/4	0.0101(5)	3/8	0.0208(9)	1

Table S6.3. Anisotropic displacement parameters (U_{ij} / Å^2) of $Ca_2Li_6P_4N_{10}$ from single-crystal refinement. Standard deviations are given in parentheses.

Atom	U_{11}	U_{22}	U_{33}	U_{12}	U_{13}	U_{23}
Ca1	0.00569(18)	0.00657(18)	0.00694(16)	0.00000	0.00000	0.00048(15)
P1	0.00491(15)	0.00448(16)	0.00371(14)	-0.00003(13)	-0.00017(15)	-0.00034(12)
N1	0.0073(5)	0.0051(4)	0.0052(4)	0.0002(4)	0.00000	0.00000
N2	0.0073(5)	0.0051(4)	0.0052(4)	0.0002(4)	0.00000	0.00000
N3	0.0073(5)	0.0072(6)	0.0063(5)	-0.0001(4)	0.0009(4)	-0.0017(4)
Li1	0.0153(15)	0.0174(15)	0.0136(13)	0.0028(10)	0.0001(13)	0.0039(13)
Li2	0.030(2)	0.014(2)	0.0185(19)	0.00000	0.018(2)	0.00000

Table S6.4. Wyckoff position, coordinates, equivalent thermal displacement parameters and occupancy of $Ca_{2.7}Li_{4.6}P_4N_{10}$ from single-crystal refinement. Standard deviations are given in parentheses.

Atom	***Wyck.***	***x***	***y***	***z***	U_{eq}	***SOF***
Ca1	2*i*	0.12333(15)	0.52270(13)	-0.26853(12)	0.0075(2)	1
Ca2	2*i*	-0.00231(15)	-0.16465(14)	0.09995(12)	0.0081(2)	1
Ca3	2*i*	0.4561(2)	0.1262(2)	0.20917(18)	0.0083(3)	0.7
P1	2*i*	0.63452(18)	0.71710(17)	0.30890(15)	0.0050(2)	1
P2	2*i*	0.30324(18)	0.71774(17)	0.43879(15)	0.0061(3)	1
P3	2*i*	0.26996(18)	0.39220(17)	0.21171(15)	0.0061(3)	1
P4	2*i*	0.32510(18)	0.71681(17)	0.10497(15)	0.0049(2)	1
N1	2*i*	0.5425(6)	0.7845(6)	0.4713(5)	0.0074(3)	1
N2	2*i*	0.2460(6)	0.7878(6)	0.2752(5)	0.0074(3)	1
N3	2*i*	0.2039(6)	0.4859(6)	0.3785(5)	0.0074(3)	1
N4	2*i*	0.2240(6)	0.4826(6)	0.0585(5)	0.0074(3)	1
N5	2*i*	0.5660(6)	0.7876(6)	0.1516(5)	0.0074(3)	1
N6	2*i*	0.5163(6)	0.4771(6)	0.2519(5)	0.0074(3)	1
N7	2*i*	0.2742(6)	0.8018(6)	-0.0338(5)	0.0087(4)	1
N8	2*i*	0.1574(6)	0.1710(6)	0.1707(5)	0.0087(4)	1
N9	2*i*	0.8616(6)	0.7939(6)	0.3529(5)	0.0087(4)	1
N10	2*i*	0.2258(6)	0.7876(6)	0.5933(5)	0.0087(4)	1
Li1	1*e*	1/2	1/2	0	0.012(3)	1
Li2	2*i*	0.0642(14)	0.2390(14)	0.4186(12)	0.0159(19)	1
Li3	2*i*	0.1736(14)	0.9727(13)	0.4625(12)	0.0140(19)	1
Li4	2*i*	0.2245(15)	0.9361(15)	0.8077(13)	0.021(2)	1
Li5	1*h*	1/2	1/2	1/2	0.016(3)	1
Li6	2*i*	0.419(5)	0.140(5)	0.076(4)	0.017(7)	0.3
Li7	2*i*	0.505(6)	0.018(6)	0.365(5)	0.036(10)	0.3

** The occupancy factors of Ca3 were initially refined freely based on charge neutrality constraints involving Li6 and Li7. Subsequently, these factors were fixed to the specified values, ensuring that they remained within the margin of error.*

Table S6.5. Anisotropic displacement parameters (U_{ij} / Å^2) of $Ca_{2.7}Li_{4.6}P_4N_{10}$ from single-crystal refinement. Standard deviations are given in parentheses.

Atom	U_{11}	U_{22}	U_{33}	U_{12}	U_{13}	U_{23}
Ca1	0.0103(5)	0.0036(4)	0.0084(5)	0.0050(4)	-0.0039(4)	-0.0012(4)
Ca2	0.0101(5)	0.0071(5)	0.0070(4)	0.0036(4)	0.0010(4)	0.0017(4)
Ca3	0.0057(6)	0.0071(7)	0.0109(7)	0.0022(5)	0.0011(5)	0.0006(5)
P1	0.0039(5)	0.0057(6)	0.0050(5)	0.0021(5)	0.0012(4)	0.0004(4)
P2	0.0059(6)	0.0064(6)	0.0067(6)	0.0032(5)	0.0028(5)	0.0013(5)
P3	0.0066(6)	0.0053(6)	0.0061(6)	0.0025(5)	0.0010(5)	0.0012(5)
P4	0.0051(5)	0.0043(6)	0.0058(5)	0.0025(5)	0.0013(4)	0.0012(4)
N1	0.0082(8)	0.0073(8)	0.0058(7)	0.0030(6)	0.0010(6)	0.0004(6)
N2	0.0082(8)	0.0073(8)	0.0058(7)	0.0030(6)	0.0010(6)	0.0004(6)
N3	0.0082(8)	0.0073(8)	0.0058(7)	0.0030(6)	0.0010(6)	0.0004(6)
N4	0.0082(8)	0.0073(8)	0.0058(7)	0.0030(6)	0.0010(6)	0.0004(6)
N5	0.0082(8)	0.0073(8)	0.0058(7)	0.0030(6)	0.0010(6)	0.0004(6)
N6	0.0082(8)	0.0073(8)	0.0058(7)	0.0030(6)	0.0010(6)	0.0004(6)
N7	0.0086(10)	0.007(1)	0.0096(10)	0.0032(8)	0.0010(8)	0.0008(8)
N8	0.0086(10)	0.007(1)	0.0096(10)	0.0032(8)	0.0010(8)	0.0008(8)
N9	0.0086(10)	0.007(1)	0.0096(10)	0.0032(8)	0.0010(8)	0.0008(8)
N10	0.0086(10)	0.007(1)	0.0096(10)	0.0032(8)	0.0010(8)	0.0008(8)

Table S6.6. Wyckoff position, coordinates, equivalent thermal displacement parameters and occupancy of $Sr_3Li_4P_4N_{10}$ from single-crystal refinement. Standard deviations are given in parentheses.

Atom	***Wyck.***	***x***	***y***	***z***	U_{eq}	***SOF***
Sr1	2*i*	0.10583(5)	0.48307(5)	0.25386(5)	0.00916(9)	1
Sr2	2*i*	0.25290(6)	0.88707(5)	0.58255(5)	0.01156(9)	1
Sr3	2*i*	0.63392(6)	0.89597(6)	0.87285(6)	0.01869(11)	1
P1	2*i*	0.18532(13)	0.26241(13)	0.83883(12)	0.00429(17)	1
P2	2*i*	0.31352(13)	0.58015(13)	0.76911(12)	0.00459(17)	1
P3	2*i*	0.21164(13)	0.27067(13)	0.50818(12)	0.00423(17)	1
P4	2*i*	0.51804(13)	0.28154(13)	0.71387(12)	0.00461(17)	1
N1	2*i*	0.2021(4)	0.4834(4)	0.8921(4)	0.0055(6)	1
N2	2*i*	0.5175(4)	0.5097(4)	0.7673(4)	0.0059(6)	1
N3	2*i*	0.3913(4)	0.2033(4)	0.8372(4)	0.0067(6)	1
N4	2*i*	0.1224(4)	0.1912(4)	0.3295(4)	0.0065(6)	1
N5	2*i*	0.2236(4)	0.4970(4)	0.5756(4)	0.0063(6)	1
N6	2*i*	0.3062(5)	0.7884(4)	0.8408(4)	0.0072(6)	1
N7	2*i*	0.4199(4)	0.2141(4)	0.5233(4)	0.0061(6)	1
N8	2*i*	0.0999(4)	0.1970(4)	0.6431(4)	0.0060(6)	1
N9	2*i*	0.0664(4)	0.1772(4)	0.9493(4)	0.0064(6)	1
N10	2*i*	0.7087(4)	0.2223(4)	0.7263(4)	0.0068(6)	1
Li1	2*i*	0.1903(10)	0.7225(10)	1.0387(9)	0.0113(14)	1
Li2	2*i*	0.9041(9)	0.0756(10)	0.7194(9)	0.0103(13)	1
Li3	2*i*	-0.0498(10)	0.1045(10)	1.1260(9)	0.0123(14)	1
Li4	1*h*	1/2	1/2	1/2	0.014(2)	1
Li5	1*e*	1/2	1/2	1	0.029(3)	1

Table S6.7. Anisotropic displacement parameters (U_{ij} / Å^2) of $Sr_3Li_4P_4N_{10}$ from single-crystal refinement. Standard deviations are given in parentheses.

Atom	U_{11}	U_{22}	U_{33}	U_{12}	U_{13}	U_{23}
Sr1	0.00702(17)	0.00673(16)	0.01441(18)	-0.00107(12)	-0.00305(13)	0.00518(13)
Sr2	0.0200(2)	0.00990(17)	0.00626(16)	0.00793(14)	0.00329(14)	0.00277(13)
Sr3	0.0124(2)	0.0204(2)	0.0214(2)	-0.00215(16)	0.00114(16)	0.00376(17)
P1	0.0040(4)	0.0044(4)	0.0043(4)	0.0002(3)	0.0005(3)	0.0010(3)
P2	0.0046(4)	0.0044(4)	0.0048(4)	0.0002(3)	0.0005(3)	0.0013(3)
P3	0.0045(4)	0.0044(4)	0.0035(4)	0.0002(3)	0.0000(3)	0.0008(3)
P4	0.0038(4)	0.0052(4)	0.0044(4)	0.0008(3)	0.0001(3)	0.0006(3)
N1	0.0050(14)	0.0052(13)	0.0058(14)	0.0003(11)	0.0022(11)	0.0005(11)
N2	0.0064(14)	0.0046(14)	0.0060(14)	0.0001(11)	0.0012(11)	0.0005(11)
N3	0.0048(14)	0.0077(14)	0.0085(14)	0.0021(11)	0.0008(11)	0.0034(12)
N4	0.0079(14)	0.0061(14)	0.0044(13)	-0.0008(11)	-0.0007(11)	0.0002(11)
N5	0.0074(14)	0.0054(14)	0.0049(13)	0.0000(11)	-0.0018(11)	0.0002(11)
N6	0.0086(15)	0.0051(14)	0.0084(14)	0.0006(12)	0.0005(12)	0.0026(11)
N7	0.0051(14)	0.0059(14)	0.0070(14)	0.0015(11)	0.0004(11)	0.0009(11)
N8	0.0074(14)	0.0049(14)	0.0050(14)	-0.0008(11)	-0.0012(11)	0.0009(11)
N9	0.0054(14)	0.0076(14)	0.0061(14)	-0.0005(11)	0.0021(11)	0.0021(11)
N10	0.0055(14)	0.0069(14)	0.0072(14)	0.0022(11)	0.0001(11)	0.0001(11)
Li1	0.016(4)	0.011(3)	0.006(3)	0.003(3)	0.000(3)	0.002(3)
Li2	0.007(3)	0.007(3)	0.015(3)	0.000(3)	0.001(3)	0.001(3)
Li3	0.013(3)	0.015(3)	0.011(3)	0.002(3)	0.001(3)	0.006(3)
Li4	0.007(5)	0.019(5)	0.015(5)	0.003(4)	0.002(4)	0.005(4)
Li5	0.042(8)	0.034(7)	0.014(6)	0.021(6)	0.005(6)	0.006(5)

Table S6.8. Interatomic distances (Å) of $Ca_2Li_6P_4N_{10}$ from single-crystal refinement. Standard deviations are given in parentheses.

atom1–	atom2	distance [Å]	atom1–	atom2	distance [Å]
Ca1	N2 2×	2.4732(14)	Li1	N3	2.145(4)
	N3 2×	2.5100(14)		N3	2.325(4)
	N3 2×	2.5244(13)		N2	2.973(4)
	N1 2×	3.4724(8)		N3	3.400(4)
P1	N3	1.5755(13)		N2	3.620(4)
	N1	1.6605(10)	Li2	N2 2×	2.105(4)
	N2	1.6825(15)		N2 2×	2.146(4)
	N2	1.7028(15)		N1 2×	2.5853(5)
Li1	N3	2.068(4)		N3 2×	3.2015(13)
	N1	2.141(4)		N3 2×	3.694(4)

Table S6.9. Interatomic distances (Å) of $Ca_{2.7}Li_{4.6}P_4N_{10}$ from single-crystal refinement. Standard deviations are given in parentheses.

atom1–	atom2	distance [Å]	atom1–	atom2	distance [Å]
Ca1	N7	2.474(4)	Li3	N9	2.310(12)
	N10	2.513(5)		N8	3.217(13)
	N9	2.562(5)	Li4	N10	1.963(12)
	N3	2.565(5)		N7	1.988(14)
	N6	2.735(5)		N5	2.090(11)
	N2	2.897(4)		N8	2.706(12)
	N4	2.930(5)		N9	3.039(15)
	N3	3.064(5)	Li5	N6	2.083(5)
	N4	3.273(5)		N6	2.083(5)
	N10	3.420(4)		N1	2.250(6)
Ca2	N8	2.398(4)		N1	2.250(6)
	N4	2.454(4)		N3	2.360(5)
	N9	2.461(5)		N3	2.360(5)
	N8	2.480(5)	Li6	N5	2.12(4)
	N2	2.517(5)		N7	2.26(4)
	N7	2.537(5)		N8	2.28(5)

	N5	3.219(5)		N7	2.44(4)
Ca3	N8	2.452(6)		N6	2.60(4)
	N7	2.557(5)	Li7	N10	1.97(3)
	N10	2.596(5)		N2	2.04(4)
	N6	2.621(6)		N1	2.06(5)
	N1	2.647(5)		N1	2.35(6)
	N7	2.738(4)		N5	2.53(5)
	N2	2.742(5)		N2	3.19(4)
	N5	3.126(6)		N10	3.24(5)
	N5	3.266(5)	P1	N9	1.568(5)
Li1	N4	2.146(5)		N1	1.675(5)
	N4	2.146(5)		N5	1.676(6)
	N6	2.171(5)		N6	1.716(5)
	N6	2.171(5)	P2	N10	1.564(5)
	N5	2.247(5)		N3	1.658(5)
	N5	2.247(5)		N1	1.660(5)
Li2	N3	1.954(12)		N2	1.687(5)
	N9	2.071(12)	P3	N8	1.585(5)
	N10	2.122(13)		N3	1.669(5)
	N8	2.290(12)		N4	1.688(6)
	N1	3.162(13)		N6	1.696(5)
	N9	3.190(11)	P4	N7	1.571(6)
Li3	N10	2.166(14)		N4	1.673(5)
	N1	2.187(9)		N5	1.674(5)
	N2	2.206(12)		N2	1.680(5)
	N9	2.227(9)			

Table S6.10. Interatomic distances (Å) of $Ca_4Li_2P_4N_{10}$ from Rietveld refinement. Standard deviations are given in parentheses.

atom1–	**atom2**	**distance [Å]**	**atom1–**	**atom2**	**distance [Å]**
Ca1	N5	2.38(2)	P2	N6	1.47(3)
	N6	2.41(2)		N1	1.69(3)
	N7	2.500(17)		N3 2×	1.82(2)
	N4	2.677(17)	P3	N2 2×	1.627(16)
	N2	2.698(16)		N1	1.70(3)
	N2	2.706(16)	Li1	N4	2.13(3)
	N3	3.122(15)		N4	2.14(3)
	N3	3.131(18)		N2 2×	2.184(14)
	N5	3.24(2)		N3 2×	2.423(17)
Ca2	N5	2.28(3)		N6	3.25(4)
	N5	2.31(3)	Li2	N7	1.87(3)
	N3	2.39(2)		N1	1.92(2)
	N7	2.602(16)		N6	2.28(3)
	N1	2.629(18)		N5 2×	2.580(17)
	N6	2.74(3)		N7	3.29(3)
	N2	3.242(15)			
	N3	3.250(14)			
P1	N2	1.646(16)			
	N4	1.676(14)			
	N5	1.70(2)			
	N3	1.733(16)			

Table S6.11. Interatomic distances (Å) of $Sr_3Li_4P_4N_{10}$ from single-crystal refinement. Standard deviations are given in parentheses.

atom1–	**atom2**	**distance [Å]**	**atom1–**	**atom2**	**distance [Å]**
Sr1	N4	2.552(4)	P2	N6	1.582(4)
	N10	2.581(4)		N1	1.683(4)
	N1	2.670(4)		N5	1.688(4)
	N5	2.815(4)		N2	1.688(4)
	N2	2.888(4)	P3	N4	1.577(4)
	N5	2.958(4)		N8	1.666(4)
	N9	2.992(3)		N7	1.689(4)
	N8	2.999(4)		N5	1.701(4)
	N1	3.205(4)	P4	N10	17566(4)
Sr2	N6	2.552(4)		N3	1.670(4)
	N10	2.572(4)		N7	1.682(4)
	N8	2.701(3)		N2	1.719(4)
	N7	2.790(3)	Li1	N1	1.954(8)
	N3	2.898(3)		N10	2.029(9)
	N7	2.960(4)		N6	2.111(9)
	N5	3.033(4)		N9	2.159(9)
	N4	3.059(4)	Li2	N10	1.940(9)
	N8	3.151(4)		N8	1.949(9)
Sr3	N6	2.559(4)		N4	2.009(9)
	N4	2.596(4)		N9	2.184(8)
	N3	2.800(4)	Li3	N9	1.978(9)
	N9	2.862(4)		N4	2.049(8)
	N6	2.945(3)		N9	2.114(9)
	N2	2.966(3)		N6	2.184(9)
	N10	3.171(4)	Li4	N2 2×	2.256(4)
	N3	3.211(4)		N2 2×	2.016(4)
	N7	3.243(4)		N7 2×	2.345(4)
P1	N9	1.582(4)		N1 2×	2.392(4)
	N1	1.658(4)		N3 2×	2.418(3)
	N3	1.670(4)		N5 2×	2.236(4)
	N8	1.687(4)			

Table S6.12. Interatomic angles (°) of $Ca_2Li_6P_4N_{10}$ from single-crystal refinement. Standard deviations are given in parentheses.

atom1	**atom2<**	**atom3**	**°**	**atom1**	**atom2<**	**atom3**	**°**
N2	Ca1	N2	82.61(5)	N1	Li1	N3	70.60(11)
N2		N3	148.85(5)	N1		N2	48.12(8)
N2		N3	107.32(5)	N3		N3	91.94(15)
N2		N3	96.31(5)	N3		N2	124.75(17)
N2		N3	65.70(5)	N3		N3	70.40(11)
N2		N1	80.75(4)	N3		N2	139.80(16)
N2		N1	159.61(4)	N3		N2	88.41(13)
N2		N3	107.32(5)	N3		N3	93.67(12)
N2		N3	148.85(5)	N3		N2	48.48(8)
N2		N3	65.70(5)	N2		N3	164.67(15)
N2		N3	96.31(5)	N2		N2	58.39(8)
N2		N1	159.61(4)	N3		N2	112.66(11)
N2		N1	80.75(4)	N2	Li2	N2	105.96(6)
N3		N3	79.69(5)	N2		N2	77.51(6)
N3		N3	114.77(5)	N2		N2	176.23(6)
N3		N3	83.65(5)	N2		N1	69.61(4)
N3		N1	81.80(3)	N2		N1	113.27(4)
N3		N1	49.38(3)	N2		N3	57.06(5)
N3		N3	83.65(5)	N2		N3	122.12(5)
N3		N3	114.77(5)	N2		N3	102.41(5)
N3		N1	49.38(3)	N2		N3	132.81(5)
N3		N1	81.80(3)	N2		N2	176.23(6)
N3		N3	156.83(5)	N2		N2	77.51(6)
N3		N1	127.85(3)	N2		N1	113.27(4)
N3		N1	66.04(4)	N2		N1	69.61(4)
N3		N1	66.04(4)	N2		N3	122.12(5)
N3		N1	127.85(4)	N2		N3	57.06(5)
N1		N1	117.752(0)	N2		N3	132.81(5)
N3	P1	N1	109.76(6)	N2		N3	102.41(5)
N3		N2	116.04(8)	N2		N2	99.07(6)
N3		N2	111.53(8)	N2		N1	69.16(4)

N3		N2	153.12(6)	N2	N1	107.80(3)
N3		N2	148.50(6)	N2	N3	58.332(5)
N3		N1	152.13(5)	N2	N3	122.56(5)
N1		N2	108.08(6)	N2	N3	46.58(4)
N1		N2	107.32(8)	N2	N3	73.94(5)
N1		N2	57.76(3)	N2	N1	107.80(4)
N1		N2	57.41(3)	N2	N1	69.16(4)
N1		N1	97.95(2)	N2	N3	122.56(5)
N2		N2	103.63(7)	N2	N3	58.33(5)
N2		N2	56.12(6)	N2	N3	73.94(5)
N2		N2	95.44(6)	N2	N3	46.58(5)
N2		N1	54.92(5)	N1	N1	175.571(0)
N2		N2	95.28(6)	N1	N3	109.90(3)
N2		N2	55.93(6)	N1	N3	70.15(3)
N2		N1	54.86(5)	N1	N3	45.79(3)
N2		N2	49.03(4)	N1	N3	129.79(4)
N2		N1	49.15(3)	N1	N3	70.15(3)
N2		N1	49.16(3)	N1	N3	109.90(3)
N3	Li1	N1	106.08(17)	N1	N3	129.79(3)
N3		N3	105.67(16)	N1	N3	45.79(3)
N3		N3	151.9(2)	N3	N3	178.84(4)
N3		N2	63.57(11)	N3	N3	104.91(3)
N3		N3	112.69(16)	N3	N3	75.98(3)
N3		N2	108.97(14)	N3	N3	75.98(3)
N1		N3	136.72(18)	N3	N3	104.91(3)
N1		N3	72.6(1)	N3	N3	84.06(3)
N1		N2	95.67(14)			

Table S6.13. Interatomic angles (°) of $Ca_{2.7}Li_{4.6}P_4N_{10}$ from single-crystal refinement. Standard deviations are given in parentheses.

atom1	**atom2<**	**atom3**	**°**	**atom1**	**atom2<**	**atom3**	**°**
N7	Ca1	N10	77.42(15)	N8	P3	N3	109.5(3)
7		N9	136.16(15)	N8		N4	113.2(3)
N7		N3	105.47(15)	N8		N6	114.7(3)
N7		N6	85.93(15)	N8		N2	147.9(2)
N7		N2	122.42(15)	N8		N1	149.6(2)
N7		N4	59.91(13)	N8		N5	154.9(2)
N7		N3	128.09(13)	N3		N4	107.8(3)
N7		N4	73.86(14)	N3		N6	106.4(3)
N10		N9	129.30(16)	N3		N2	55.8(2)
N10		N3	77.43(16)	N3		N1	54.89(17)
N10		N6	92.04(16)	N3		N5	95.7(2)
N10		N2	133.82(15)	N4		N6	105.2(3)
N10		N4	135.20(14)	N4		N2	57.1(2)
N10		N3	56.03(13)	N4		N1	97.2(2)
N10		N4	111.38(14)	N4		N5	55.9(2)
N9		N3	113.49(16)	N6		N2	97.4(2)
N9		N6	62.35(15)	N6		N1	57.1(2)
N9		N2	67.82(14)	N6		N5	56.3(2)
N9		N4	81.27(14)	N2		N1	49.96(12)
N9		N3	74.62(13)	N2		N5	49.77(12)
N9		N4	114.13(14)	N1		N5	49.81(12)
N3		N6	162.09(16)	N4	Li1	N4	180.1(2)
N3		N2	57.81(15)	N4		N6	102.99(17)
N3		N4	124.47(14)	N4		N6	77.01(17)
N3		N3	86.99(14)	N4		N5	75.3(2)
N3		N4	53.72(15)	N4		N5	104.8(2)
N6		N2	127.50(15)	N4		N6	77.01(17)
N6		N4	73.12(14)	N4		N6	102.99(17)
N6		N3	75.10(14)	N4		N5	104.8(2)
N6		N4	144.14(15)	N4		N5	75.3(2)
N2		N4	84.37(13)	N6		N6	180

N2		N3	107.04(13)	N6		N5	104.84(16)
N2		N4	51.32(13)	N6		N5	75.16(16)
N4		N3	146.43(12)	N6		N5	75.16(16)
N4		N4	71.13(12)	N6		N5	104.84(16)
N3		N4	140.47(12)	N5		N5	180
N8	Ca2	N4	158.26(16)	N3	Li2	N9	117.1(6)
N8		N9	98.23(16)	N3		N10	102.4(6)
N8		N8	91.26(15)	N3		N8	77.1(4)
N8		N2	96.68(16)	N3		N1	92.2(5)
N8		N7	93.50(16)	N3		N9	159.4(6)
N8		N5	98.00(15)	N9		N10	105.9(6)
N4		N9	93.75(15)	N9		N8	132.5(5)
N4		N8	67.24(15)	N9		N1	56.8(4)
N4		N2	103.84(16)	N9		N9	79.1(4)
N4		N7	89.39(16)	N10		N8	115.4(6)
N4		N5	74.29(15)	N10		N1	161.6(6)
N9		N8	130.26(15)	N10		N9	84.2(4)
N9		N2	75.80(15)	N8		N1	78.9(4)
N9		N7	138.50(16)	N8		N9	82.5(4)
N9		N5	54.85(14)	N1		N9	86.4(3)
N8		N2	151.37(15)	N10	Li3	N1	101.1(5)
N8		N7	88.82(15)	N10		N2	76(4)
N8		N5	75.54(15)	N10		N9	99.2(5)
N2		N7	63.33(16)	N10		N9	109.1(5)
N2		N5	129.93(15)	N10		N8	159.2(5)
N7		N5	160.71(15)	N1		N2	98.9(5)
N10	Ca3	N6	92.82(16)	N1		N9	159.8(6)
N10		N1	61.77(14)	N1		N9	72.8(4)
N10		N7	124.00(15)	N1		N8	79.0(4)
N10		N2	96.33(15)	N2		N9	87.3(5)
N10		N5	70.40(15)	N2		N9	170.6(6)
N10		N5	125.48(14)	N2		N8	83.1(4)
N6		N1	80.03(14)	N9		N9	99.4(5)
N6		N7	137.10(15)	N9		N8	82.8(4)

N6		N2	146.85(16)	N9		N8	91.0(4)
N6		N5	156.41(15)	N10	Li4	N7	104.3(6)
N6		N5	72.06(13)	N10		N5	110.3(6)
N1		N7	134.15(14)	N10		N8	104.9(6)
N1		N2	76.52(14)	N10		N9	91.0(5)
N1		N5	104.75(14)	N7		N5	113.8(6)
N1		N5	151.20(13)	N7		N8	95.7(5)
N7		N2	57.93(14)	N7		N9	164.8(6)
N7		N5	53.95(13)	N5		N8	125.6(6)
N7		N5	68.71(12)	N5		N9	60.3(4)
N2		N5	54.63(14)	N8		N9	79.3(4)
N2		N5	125.02(13)	N6	Li5	N6	180
N5		N5	103.68(13)	N6		N1	77.21(17)
N8		N7	127.05(17)	N6		N1	102.79(17)
N8		N10	145.82(17)	N6		N3	74.34(16)
N8		N6	65.86(16)	N6		N3	105.67(16)
N8		N1	87.41(16)	N6		N1	102.79(17)
N8		N7	87.55(16)	N6		N1	77.21(17)
N8		N2	89.84(16)	N6		N3	105.67(16)
N8		N5	136.57(16)	N6		N3	74.34(16)
N8		N5	74.98(14)	N1		N1	180.00(16)
N7		N10	74.48(16)	N1		N3	69.95(17)
N7		N6	86.71(16)	N1		N3	110.05(17)
N7		N1	133.22(15)	N1		N3	110.05(17)
N7		N7	83.54(15)	N1		N3	69.95(17)
N7		N2	126.44(16)	N3		N3	180
N7		N5	73.13(15)	N5	Li6	N7	75.6(13)
N7		N5	53.17(13)	N5		N8	107.2(16)
N9	P1	N1	110.6(3)	N5		N7	97.1(15)
N9		N5	112.7(3)	N5		N6	95.4(13)
N9		N6	113.4(3)	N7		N8	162(3)
N9		N3	150.7(3)	N7		N7	97.5(15)
N9		N2	150.1(3)	N7		N6	93.9(14)
N9		N4	152.6(3)	N8		N7	99.4(15)

N1		N5	108.7(3)	N8		N6	68.6(11)
N1		N6	105.9(3)	N7		N6	164.8(17)
N1		N3	55.3(2)	N10	Li7	N2	167(3)
N1		N2	57.2(2)	N10		N1	85(2)
N1		N4	96.9(2)	N10		N1	102(2)
N5		N6	105.3(3)	N10		N5	94.8(17)
N5		N3	96.6(2)	N10		N2	57.6(11)
N5		N2	57.1(2)	N10		N10	134(3)
N5		N4	55.8(2)	N2		N1	109(2)
N6		N3	57.0(2)	N2		N1	76.2(15)
N6		N2	96.2(2)	N2		N5	72.0(15)
N6		N4	56.0(2)	N2		N2	133(2)
N3		N2	48.68(13)	N2		N10	56.2(11)
N3		N4	49.71(13)	N1		N1	116(3)
N2		N4	49.16(13)	N1		N5	177(3)
N10	P2	N3	111.6(3)	N1		N10	55(1)
N10		N1	113.2(3)	N5		N2	124.3(15)
N10		N2	112.3(3)	N5		N10	108.1(15)
N10		N5	152.6(2)	N1		N2	57.7(11)
N10		N6	151.5(2)	N1		N10	75.1(14)
N10		N4	150.4(2)	N1		N5	67.8(11)
N3		N1	105.7(3)	N1		N2	72.4(12)
N3		N2	105.2(3)	N2		N10	76.5(11)
N3		N5	96.0(2)				
N3		N6	55.9(2)				
N3		N4	56.12(17)				
N1		N2	108.6(3)				
N1		N5	57.2(2)				
N1		N6	56.3(2)				
N1		N4	96.5(2)				
N2		N5	56.9(2)				
N2		N6	96.2(2)				
N2		N4	55.53(17)				
N5		N6	49.09(12)				

N5	N4	48.75(11)
N6	N4	48.77(11)

Table S6.14. Interatomic angles (°) of $Ca_4Li_2P_4N_{10}$ from Rietveld refinement. Standard deviations are given in parentheses.

atom1	**atom2**	**atom3**	**°**	**atom1**	**atom2**	**atom3**	**°**
N5	Ca1	N6	120.1(5)	N5	Ca2	N5	135(1)
N5		N7	148.9(5)	N5		N3	66.6(7)
N5		N4	65.9(5)	N5		N7	101.4(5)
N5		N2	91.6(6)	N5		N1	152.4(6)
N5		N2	89.6(7)	N5		N6	91.8(5)
N5		N3	73.7(7)	N5		N2	79.0(6)
N5		N3	91.7(6)	N5		N3	112.7(6)
N5		N5	136.1(6)	N5		N3	901.0(6)
N6		N7	69.48(12)	N5		N7	89.8(5)
N6		N4	71.99(12)	N5		N1	72.7(6)
N6		N2	132.9(4)	N5		N6	130.4(6)
N6		N2	124.2(4)	N5		N2	58.1(6)
N6		N3	53.4(3)	N5		N3	90.0(6)
N6		N3	85.7(4)	N3		N7	163.0(5)
N6		N5	78.3(4)	N3		N1	119.4(5)
N7		N4	92.88(14)	N3		N6	95.4(5)
N7		N2	102.06(4)	N3		N2	79.2(6)
N7		N2	63.9(4)	N3		N3	65.9(5)
N7		N3	122.8(4)	N7		N1	77.02(12)
N7		N3	119.3(4)	N7		N6	97.14(14)
N7		N5	73.1(4)	N7		N2	86.9(3)
N4		N2	154.4(4)	N7		N3	131.2(3)
N4		N2	81.4(4)	N1		N6	61.48(11)
N4		N3	71.8(3)	N1		N2	128.1(3)
N4		N3	131.5(4)	N1		N3	56.6(3)
N4		N5	150.0(4)	N6		N2	170.5(3)
N2		N2	86.6(5)	N6		N3	49.8(3)

N2		N3	115.2(5)	N2		N3	132.3(4)
N2		N3	57.3(5)	N2	P1	N4	110.1(6)
N2		N5	55.7(5)	N2		N5	115(1)
N2		N3	152.3(5)	N2		N3	113.0(8)
N2		N3	143.9(5)	N2		N2	55.0(6)
N2		N5	113.7(6)	N2		N1	60.0(5)
N3		N3	60.6(4)	N4		N5	109.8(7)
N3		N5	93.5(6)	N4		N3	112.4(7)
N3		N5	47.5(5)	N4		N2	61.9(4)
N4	Li01	N4	171(1)	N4		N1	102.0(3)
N4		N2	78(4)	N5		N3	97(1)
N4		N2	78(4)	N5		N2	155.1(8)
N4		N3	97.2(4)	N5		N1	147.1(7)
N4		N3	97.2(4)	N3		N2	108.2(7)
N4		N6	64.0(8)	N3		N1	62.2(5)
N4		N2	108.6(4)	N2		N1	52.4(3)
N4		N2	108.6(4)	N6	P2	N1	120.6(15)
N4		N3	76.5(4)	N6		N3	101.9(5)
N4		N3	76.5(4)	N6		N3	101.9(5)
N4		N6	107.6(8)	N6		N4	137.6(13)
N2		N2	70.5(5)	N6		N2	156.9(3)
N2		N3	173.8(6)	N6		N2	156.9(3)
N2		N3	104.7(5)	N1		N3	107.8(5)
N2		N6	128.5(4)	N1		N3	107.8(5)
N2		N3	104.7(5)	N1		N4	101.8(9)
N2		N3	173.8(6)	N1		N2	59.0(3)
N2		N6	128.5(4)	N1		N2	59.0(3)
N3		N3	80.0(5)	N3		N3	117.7(9)
N3		N6	51.4(4)	N3		N4	61.9(5)
N3		N6	51.4(4)	N3		N2	99.9(6)
N7	Li02	N1	119(1)	N3		N2	60.4(6)
N7		N6	85(1)	N3		N4	61.9(5)
N7		N5	101.4(5)	N3		N2	60.4(6)
N7		N5	101.4(5)	N3		N2	99.9(6)

N7		N7	174.4(9)	N4		N2	50.2(3)
N1		N6	157(1)	N4		N2	50.2(3)
N1		N5	80.1(5)	N2		N2	45.9(4)
N1		N5	80.1(5)	N2	P3	N2	101.5(8)
N1		N7	66.7(8)	N2		N1	112.9(5)
N6		N5	96.3(5)	N2		N7	104.1(5)
N6		N5	96.3(5)	N2		N4	56.4(5)
N6		N7	90.3(8)	N2		N1	112.9(5)
N5		N5	155.2(6)	N2		N7	104.1(5)
N5		N7	79.3(5)	N2		N4	56.4(5)
N5		N7	79.3(5)	N1		N7	119.7(13)
				N1		N4	99.0(9)
				N7		N4	141.4(9)

Table S6.15. Interatomic angles (°) of $Sr_3Li_4P_4N_{10}$ from single-crystal refinement. Standard deviations are given in parentheses.

atom1	**atom2<**	**atom2**	**°**	**atom1**	**atom2<**	**atom3**	**°**
N4	Sr1	N10	141.22(11)	N6	Sr2	N10	139.55(11)
N4		N1	114.63(10)	N6		N8	112.23(11)
N4		N5	61.30(1)	N6		N7	91.25(11)
N4		N2	87.11(1)	N6		N3	73.69(1)
N4		N5	83.81(1)	N6		N7	125.40(1)
N4		N9	70.47(1)	N6		N5	58.06(1)
N4		N8	135.85(1)	N6		N4	77.84(11)
N10		N1	104.15(1)	N6		N8	125.2(1)
N10		N5	90.98(1)	N10		N8	108.19(10)
N10		N2	59.38(1)	N10		N7	60.9(1)
N10		N5	117.91(1)	N10		N3	133.1(1)
N10		N9	122.57(1)	N10		N7	79.1(1)
N10		N8	67.25(1)	N10		N5	86.4(1)
N1		N5	134.75(1)	N10		N4	113.2(1)
N1		N2	145.84(1)	N10		N8	65.0(1)
N1		N5	58.04(9)	N8		N7	133.7(1)
N1		N9	75.78(1)	N8		N3	57.5(1)

N1		N8	55.71(9)	N8		N7	56.8(1)
N5		N2	78.22(9)	N8		N5	147.77(1)
N5		N5	77.09(9)	N8		N4	73.23(1)
N5		N9	130.28(1)	N8		N8	74.26(9)
N5		N8	94.33(1)	N7		N3	95.6(1)
N2		N5	155.11(9)	N7		N7	76.91(9)
N2		N9	88.42(9)	N7		N5	78.62(9)
N2		N8	125.77(9)	N7		N4	152.96(9)
N5		N9	110.06(9)	N7		N8	124.47(9)
N5		N8	53.68(9)	N3		N7	55.30(9)
N9		N8	130.52(9)	N3		N5	131.01(9)
N6	Sr3	N4	129.82(11)	N3		N4	104.72(9)
N6		N3	80.95(1)	N3		N8	131.34(9)
N6		N9	134.06(11)	N7		N5	155.33(9)
N6		N6	108.32(11)	N7		N4	129.49(9)
N6		N2	59.35(1)	N7		N8	104.11(9)
N6		N10	111.66(1)	N5		N4	74.61(9)
N4		N3	124.70(1)	N5		N8	87.20(9)
N4		N9	72.08(1)	N4		N8	50.99(8)
N4		N6	120.61(1)	N3	Sr3	N10	144.39(91)
N4		N2	84.67(1)	N9		N6	76.4(1)
N4		N10	73.75(1)	N9		N2	89.41(9)
N3		N9	57.29(1)	N9		N10	113.52(9)
N3		N6	69.56(1)	N6		N2	143.81(9)
N1	Li1	N10	118.9(4)	N5	Li4	N2	73.58(12)
N1		N6	80.3(4)	N5		N7	107.47(12)
N1		N9	115.8(4)	N5		N7	72.53(12)
N10		N6	127.9(4)	N2		N2	180
N10		N9	106.0(4)	N2		N7	71.24(12)
N6		N9	106.4(4)	N2		N7	108.76(12)
N10	Li2	N8	106.2(4)	N2		N7	108.76(12)
N10		N4	124.3(4)	N2		N7	71.24(12)
N10		N9	108.4(4)	N7		N7	180.00(12)
N8		N4	121.2(5)	N2	Li5	N2	180

N8		N9	80.7(3)	N2		N1	105.14(12)
N4		N9	106.8(4)	N2		N1	74.86(12)
N9	Li3	N4	106.2(4)	N2		N3	76.08(12)
N9		N9	104.7(4)	N2		N3	103.92(12)
N9		N6	110.5(4)	N2		N1	74.86(12)
N4		N9	107.9(3)	N2		N1	105.14(12)
N4		N6	113.8(4)	N2		N3	103.92(13)
N9		N6	113.3(4)	N2		N3	76.08(13)
N5	Li4	N5	180.00(12)	N1		N1	180
N5		N2	73.58(12)	N1		N3	112.89(11)
N5		N2	106.42(12)	N1		N3	67.11(11)
N5		N7	72.53(12)	N1		N3	67.11(11)
N5		N7	107.47(12)	N1		N3	112.89(11)
N5		N2	106.42(12)	N3		N3	180
N9	P4	N1	114.34(18)	N4	P6	N8	111.13(18)
N9		N3	113.20(17)	N4		N7	112.00(17)
N9		N8	110.16(18)	N4		N5	113.74(18)
N1		N3	106.06(17)	N8		N7	107.26(16)
N1		N8	105.65(17)	N8		N5	106.06(17)
N3		N8	106.89(17)	N7		N5	106.22(16)
N6	P5	N1	106.83(18)	N10	P7	N3	110.05(17)
N6		N5	113.96(18)	N10		N7	113.77(17)
N6		N2	114.9(2)	N10		N2	111.78(17)
N6		N8	147.33(15)	N10		N1	148.69(14)
N1		N5	108.86(17)	N3		N7	108.42(17)
N1		N2	106.23(16)	N3		N2	108.53(17)
N1		N8	56.63(13)	N3		N1	56.33(13)
N5		N2	105.67(16)	N7		N2	103.99(17)
N5		N8	57.48(13)	N7		N1	97.53(13)
N2		N8	97.40(13)	N2		N1	57.62(13)

Details on Rietveld refinement

Table S6.16. Wyckoff position, coordinates, isotropic thermal displacement parameters and occupancy of $Ca_2Li_6P_4N_{10}$ from Rietveld refinement. Standard deviations are given in parentheses.

Atom	***Wyck.***	***x***	***y***	***z***	U_{eq}	***SOF***
Ca1	8*d*	0.31810(13)	1/4	5/8	0.51(3)	1
P1	16*e*	0.50233(14)	0.141(12)	0.35905(12)	0.50(3)	1
N1	8*c*	1/2	0	0.4527(5)	0.45(10)	1
N2	16*e*	0.3694(4)	0.1383(4)	0.2504(4)	0.33(7)	1
N3	16*e*	0.5123(4)	0.2683(3)	0.4588(3)	0.25(6)	1
Li1	16*e*	0.3884(8)	0.4142(8)	0.3759(11)	0.93(15)	1
Li2	8*d*	1/4	0.014(14)	3/8	1.4(3)	1

Table S6.17. Wyckoff position, coordinates, isotropic thermal displacement parameters and occupancy of $Ca_{2.7}Li_{4.6}P_4N_{10}$ from Rietveld refinement. Standard deviations are given in parentheses.

Atom	***Wyck.***	***x***	***y***	***z***	U_{eq}	***SOF***
Ca1	2*i*	0.1235(10)	0.5200(9)	-0.2633(8)	0.82(7)	1
Ca2	2*i*	-0.0016(10)	-0.1662(10)	0.0963(10)	0.82(7)	1
Ca3	2*i*	0.4660(15)	0.1325(14)	0.2119(12)	0.82(7)	0.7
P1	2*i*	0.6491(15)	0.7137(14)	0.3086(11)	0.82(7)	1
P2	2*i*	0.3123(15)	0.7312(14)	0.4425(12)	0.82(7)	1
P3	2*i*	0.2662(14)	0.4011(13)	0.2143(12)	0.82(7)	1
P4	2*i*	0.3191(14)	0.7044(14)	0.0899(11)	0.82(7)	1
N1	2*i*	0.554(4)	0.798(3)	0.469(3)	0.82(7)	1
N2	2*i*	0.249(4)	0.816(3)	0.279(3)	0.82(7)	1
N3	2*i*	0.207(4)	0.494(4)	0.376(3)	0.82(7)	1
N4	2*i*	0.253(4)	0.498(4)	0.080(3)	0.82(7)	1
N5	2*i*	0.577(4)	0.794(3)	0.131(3)	0.82(7)	1
N6	2*i*	0.524(4)	0.451(3)	0.270(3)	0.82(7)	1
N7	2*i*	0.292(4)	0.795(3)	-0.055(3)	0.82(7)	1
N8	2*i*	0.135(4)	0.177(3)	0.182(3)	0.82(7)	1

N9	2*i*	0.885(4)	0.835(3)	0.376(3)	0.82(7)	1
N10	2*i*	0.237(4)	0.760(4)	0.583(3)	0.82(7)	1
Li1	1*e*	½	½	0	0.82(7)	1
Li2	2*i*	0.103(8)	0.259(7)	0.402(7)	0.82(7)	1
Li3	2*i*	0.131(8)	0.863(8)	0.449(6)	0.82(7)	1
Li4	2*i*	0.251(9)	0.958(8)	0.775(6)	0.82(7)	1
Li5	1*h*	½	½	½	0.82(7)	1
Li6	2*i*	0.419	0.14	0.076	0.82(7)	0.3
Li7	2*i*	0.505	0.018	0.365	0.82(7)	0.3

Note: The atomic positions of Li6 & 7 were not refined, due to the site occupancy deficiency and the local proximity to Ca3. A free refinement of site occupation of Ca3, dependent on the Li6 and Li7 sites, indicates a slightly higher occupation of the Ca3 site (~0.88); however, this was fixed at 0.7 based on the SCXRD data.

Table S6.18. Wyckoff position, coordinates, isotropic thermal displacement parameters and occupancy of $Ca_4Li_2P_4N_{10}$ from Rietveld refinement. Standard deviations are given in parentheses.

Atom	***Wyck.***	***x***	***y***	***z***	U_{eq}	***SOF***
Ca1	8*d*	0.2979(5)	0.5878(5)	0.0286(4)	1.30(9)	1
Ca2	8*d*	0.0145(6)	0.416(4)	0.2125(4)	1.30(9)	1
P1	8*d*	0.2603(8)	0.6212(5)	0.3195(6)	0.5(1)	1
P2	4*c*	0.4496(10)	¾	0.4922(9)	0.5(1)	1
P3	4*c*	0.1258(10)	¾	0.5202(10)	0.5(1)	1
N1	4*c*	0.291(3)	¾	0.614(3)	0.7(2)	1
N2	4*c*	0.112(2)	0.6261(15)	0.4157(13)	0.7(2)	1
N3	8*d*	0.444(2)	0.6267(16)	0.3961(14)	0.7(2)	1
N4	4*c*	0.260(3)	¾	0.234(2)	0.7(2)	1
N5	8*d*	0.260(3)	0.4933(15)	0.2315(16)	1.0(3)	1
N6	4*c*	0.610(3)	¾	0.563(3)	1.0(3)	1
N7	8*d*	-0.050(3)	¾	0.616(3)	1.0(3)	1
Li1	4*c*	0.434(7)	¾	0.219(6)	0.7	1
Li2	4*c*	0.784(7)	¾	0.661(6)	0.7	1

Table S6.19. Wyckoff position, coordinates, isotropic thermal displacement parameters and occupancy of $Sr_3Li_4P_4N_{10}$ from Rietveld refinement. Standard deviations are given in parentheses.

Atom	***Wyck.***	***x***	***y***	***z***	U_{eq}	***SOF***
Sr1	2*i*	0.1059(3)	0.4831(3)	0.2522(3)	0.43(4)	1
Sr2	2*i*	0.2544(3)	0.8856(3)	0.5815(3)	0.43(4)	1
Sr3	2*i*	0.6337(3)	0.8929(3)	0.8700(2)	0.43(4)	1
P1	2*i*	0.1858(9)	0.2582(9)	0.8372(7)	0.43(4)	1
P2	2*i*	0.3135(9)	0.5803(9)	0.7719(7)	0.43(4)	1
P3	2*i*	0.2149(8)	0.2701(9)	0.5068(8)	0.43(4)	1
P4	2*i*	0.5193(8)	0.2814(9)	0.7187(8)	0.43(4)	1
N1	2*i*	0.073(2)	0.175(2)	0.956(2)	0.43(4)	1
N2	2*i*	0.705(2)	0.210(2)	0.7242(19)	0.43(4)	1
N3	2*i*	0.209(2)	0.486(2)	0.8930(19)	0.43(4)	1
N4	2*i*	0.519(2)	0.511(2)	0.7648(19)	0.43(4)	1
N5	2*i*	0.385(2)	0.206(2)	0.8311(19)	0.43(4)	1
N6	2*i*	0.127(2)	0.194(2)	0.347(2)	0.43(4)	1
N7	2*i*	0.2198(19)	0.498(2)	0.5763(17)	0.43(4)	1
N8	2*i*	0.306(2)	0.787(2)	0.835(2)	0.43(4)	1
N9	2*i*	0.420(2)	0.210(2)	0.534(2)	0.43(4)	1
N10	2*i*	0.097(2)	0.208(2)	0.639(2)	0.43(4)	1
Li1	2*i*	0.205(5)	0.719(5)	1.062(4)	0.43(4)	1
Li2	2*i*	0.926(5)	0.098(5)	0.716(5)	0.43(4)	1
Li3	2*i*	-0.047(5)	0.125(5)	1.121(5)	0.43(4)	1
Li4	1*h*	½	½	½	0.43(4)	1
Li5	1*e*	½	½	1	0.43(4)	1

Table S6.20. Comparison of the crystallographic data from Rietveld refinements of $AE_xLi_{10-2x}P_4N_{10}$ (x (Ca) = 2, 2.7,4; x (Sr)= 3). Standard deviations are given in parentheses.

Formula	**$Ca_2Li_6P_4N_{10}$**	**$Ca_{2.7}Li_{4.6}P_4N_{10}$**	**$Ca_4Li_2P_4N_{10}$**	**$Sr_3Li_4P_4N_{10}$**
Crystal system	tetragonal	triclinic	orthorhombic	triclinic
Space group	*I*$\bar{4}$*2d* (no. 122)	*P*$\bar{1}$ (no. 2)	*Pnma* (no. 62)	*P*$\bar{1}$ (no. 2)
Lattice parameters / Å,°	a = 9.83060(7) c = 9.53541(11)	a = 7.5745(3) b = 8.0208(4) c = 8.3553(3) α = 101.343(4) β = 94.098(4) γ = 113.976(4)	a = 8.4420(4) b = 10.5528(6) c = 10.4118(7)	a = 7.63897(8) b = 7.82481(10) c = 8.51587(12) α = 105.9472(10) β = 92.8280(10) γ = 94.0696(10)
Cell volume / Å^3	921.508(17)	448.22(4)	927.57(9)	486.94
Radiation λ / Å	0.7093 (Mo-Kα_1)	0.7093 (Mo-Kα_1)	0.7093 (Mo-Kα_1)	1.5406 (Cu-Kα_1)
2θ-range / °	2 < 2θ < 55.625	2 < 2θ < 55.940	2 < 2θ < 56.435	5 < 2θ < 100.025
Data points	3576	3597	3630	6336
Number of parameters (thereof background)	47(14)	106 (14)	60(14)	103(12)
R values	R_{Bragg} = 0.0130 R_p = 0.0320 R_{wp} = 0.0422	R_{Bragg} = 0.0192 R_p = 0.0467 R_{wp} = 0.0618	R_{Bragg} = 0.0225 R_p = 0.0480 R_{wp} = 0.0633	R_{Bragg} = 0.0131 R_p = 0.0322 R_{wp} = 0.0423
Goodness of fit	1.140	1.698	1.549	1.217

MAS NMR experiments

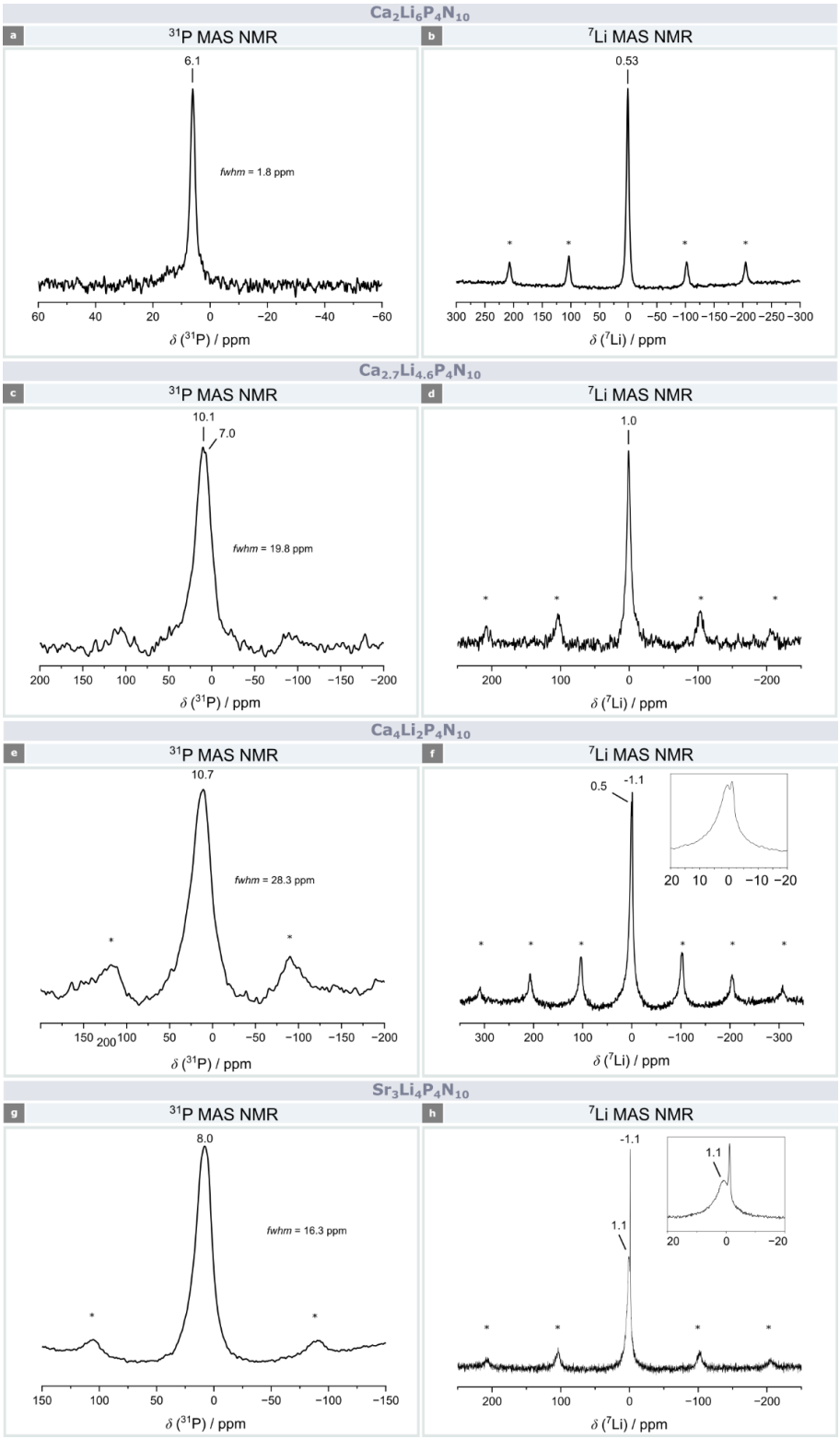

Figure S6.1. ^{31}P & ^{7}Li MAS NMR spectra of bulk samples of the title compounds $AE_xLi_{10-2x}P_4N_{10}$. Signals in small boxes show an enlarged range of the respective spectra. Rotational sidebands are marked with asterisks.

Infrared Spectroscopy (FTIR)

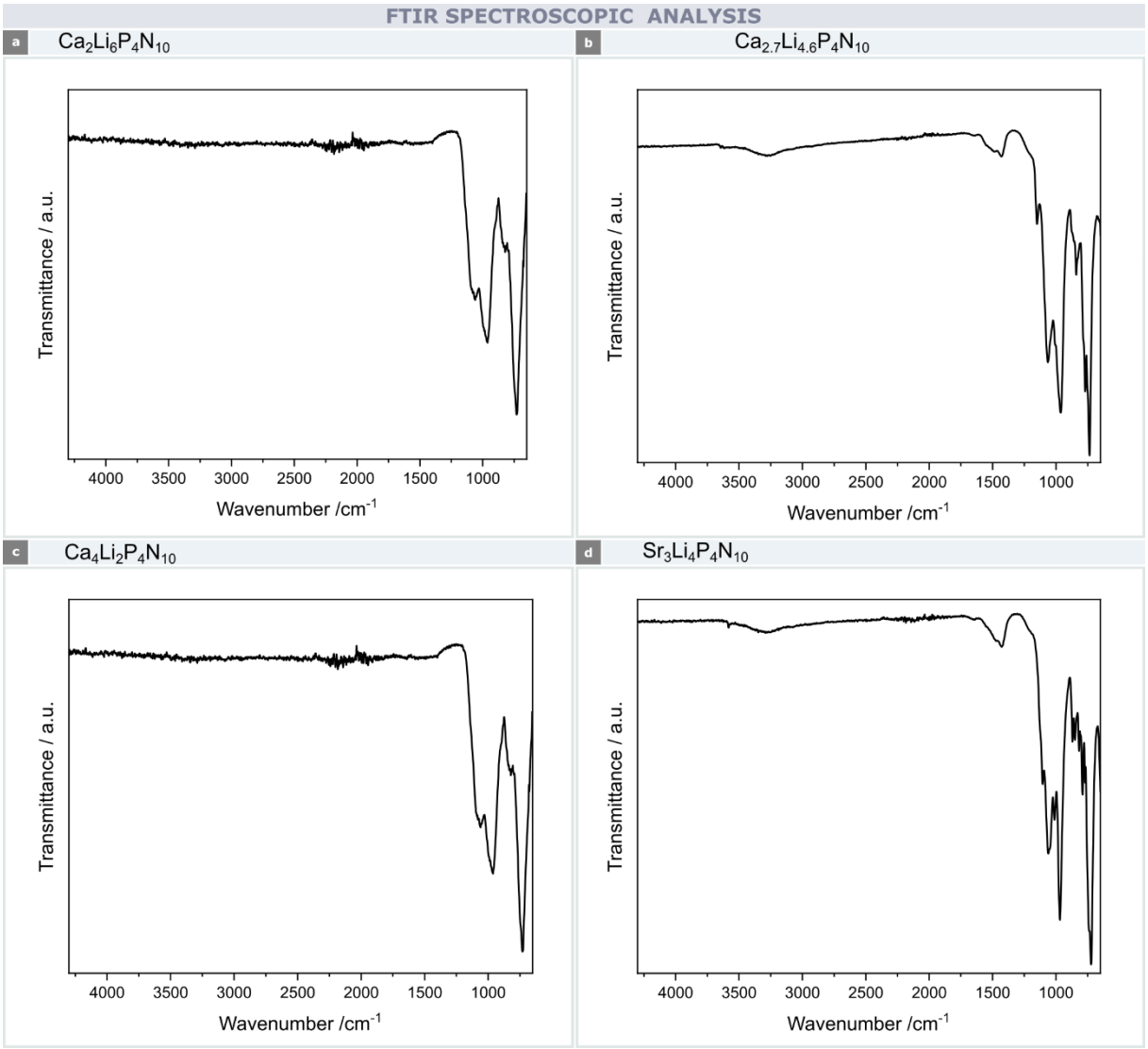

Figure S6.2. FTIR spectra of the title compounds: a) $Ca_2Li_6P_4N_{10}$, b) $Ca_{2.7}Li_{4.6}P_4N_{10}$, c) $Ca_4Li_2P_4N_{10}$ and d) $Sr_3Li_4P_4N_{10}$.

Note: In the samples of $Ca_{2.7}Li_{4.6}P_4N_{10}$ (b) & $Sr_3Li_4P_4N_{10}$ (d) small amounts of N–H functionality is observable (~3500 cm^{-1}); the broad signal at 3100–3450 cm^{-1} can be assigned to surface hydrolysis caused by the EtOH washing step (O–H-stretching vibrations). This is also consistent with the Rietveld refinements, according to which it was not possible to completely remove LiCl from these samples despite the washing steps (LiCl is extremely sensitive to hydrolysis). Further, these modes are not visible in $Ca_2Li_6P_4N_{10}$ (a) and $Ca_4Li_2P_4N_{10}$ (c), from which it can be concluded that there is no N–H and O–H functionality in this bulk samples.

Scanning Electron Microscopy (SEM) with Energy-Dispersive X-ray Spectroscopy (EDX)

Note: No other elements than AE, P, N and O were detected (Li is not detectable via EDX). The presence of O may be explained by surface hydrolysis resulting from the washing step with dry ethanol. As a result, the relative ratios AE : P were examined for the evaluation.

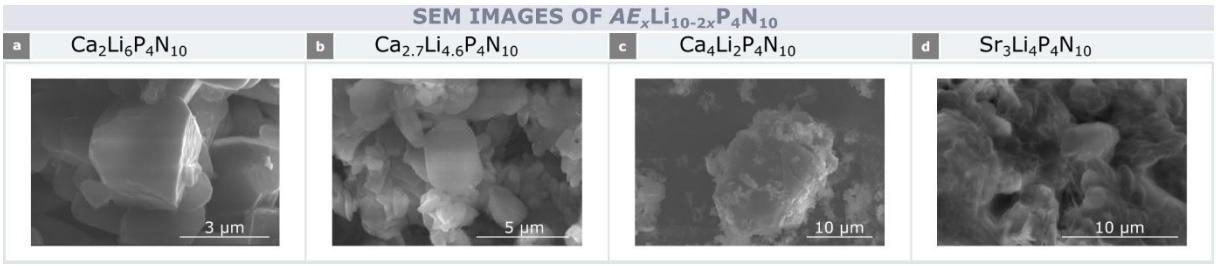

Figure S6.3. SEM images of $AE_xLi_{10-2x}P_4N_{10}$; a) $Ca_2Li_6P_4N_{10}$, b) $Ca_{2.7}Li_{4.6}P_4N_{10}$, c) $Ca_4Li_2P_4N_{10}$, and d) $Sr_3Li_4P_4N_{10}$.

Table S6.21. Results of EDX measurements of $Ca_2Li_6P_4N_{10}$; the results are given in atomic percent.

#	Ca	P	N	O	ratio theo Ca : P	ratio meas. Ca :P
1	11.1	22.7	50.6	15.6	0.5	0.49
2	10.7	21.7	52.9	14.7	0.5	0.49
3	11.1	22.8	48.8	17.3	0.5	0.49
4	12.8	25.8	47.2	14.2	0.5	0.50
5	13.5	26.8	46.2	13.5	0.5	0.50
6	11.4	23.0	47.7	17.9	0.5	0.50
7	11.0	22.7	48.6	17.6	0.5	0.48
average	11.7	23.7	48.9	15.8	0.5	0.49
standard deviation	1.0	1.7	2.1	1.6	-	0.01

Table S6.22. Results of EDX measurements of $Ca_{2.7}Li_{4.6}P_4N_{10}$; the results are given in atomic percent.

#	Ca	P	N	O	ratio theo Ca : P	ratio meas. Ca :P
1	10.3	14.4	61.4	13.8	0.68	0.72
2	10.4	15.1	64.9	9.7	0.68	0.69
3	10.5	15.7	63.9	10.5	0.68	0.67
4	10.6	15.2	65.2	8.9	0.68	0.70
5	10.7	15.3	66.2	7.8	0.68	0.70
6	10.0	14.3	64.2	11.4	0.68	0.70
7	9.4	13.6	65.8	11.3	0.68	0.69
average	10.3	14.8	64.5	10.5	0.68	0.70
standard deviation	0.4	0.7	1.5	1.8	-	0.02

Table S6.23. Results of EDX measurements of $Ca_4Li_2P_4N_{10}$; the results are given in atomic percent.

#	Ca	P	N	O	ratio theo Ca : P	ratio meas. Ca :P
1	20.4	18.9	52.7	8.0	1.00	1.08
2	18.6	17.1	56.8	7.5	1.00	1.09
3	19.6	17.2	56.3	6.9	1.00	1.14
4	19.9	17.7	54.9	7.5	1.00	1.13
5	20.9	18.3	55.5	5.3	1.00	1.14
6	20.2	17.9	56.3	5.5	1.00	1.13
7	20.5	18.3	54.8	6.4	1.00	1.12
average	20.0	17.9	55.3	6.7	1.00	1.12
standard deviation	0.7	0.6	1.3	1.0	-	0.02

Table S6.24. Results of EDX measurements of $Sr_3Li_4P_4N_{10}$; the results are given in atomic percent.

#	Sr	P	N	O	ratio theo Ca : P	ratio meas. Ca :P
1	10.1	14.6	22.0	53.4	0.75	0.69
2	10.5	14.8	21.0	53.7	0.75	0.71
3	9.8	13.8	18.5	57.9	0.75	0.71
4	10.8	15.2	19.2	54.8	0.75	0.71
5	9.5	13.7	17.9	58.9	0.75	0.69
6	10.4	14.8	18.4	59.5	0.75	0.70
7	9.6	13.8	18.7	57.9	0.75	0.69
average	10.1	14.4	19.4	56.6	0.75	0.70
standard deviation	0.5	0.6	1.4	2.4	-	0.01

Inductively Coupled Plasma Spectroscopy (ICP OES)

Table S6.25. Results of ICP-OES measurements of all title compounds; the results are given in mg/g (ppm).

compound	elements (theo) *AE* / Li / P	elements (measured) *AE* / Li / P	ratio theo. *AE*:Li:P	ratio meas. *AE*:Li:P
$Ca_2Li_6P_4N_{10}$	207.8 / 108.0 / 321.2	193.7 / 101.4 / 307.1	1 : 0.52 : 1.55	1 : 0.52 : 1.59
$Ca_{2.7}Li_{4.6}P_4N_{10}$	267.8 / 79.0 / 306.6	226.1 / 61.4 / 231.3	1 : 0.29 : 1.14	1 : 0.27 : 1.03
$Ca_4Li_2P_4N_{10}$	365.9 / 31.7 / 282.8	294.5 / 35.3 / 228.8	1: 0.09 : 0.77	1: 0.12 : 0.78
$Sr_3Li_4P_4N_{10}$	462.4 / 73.3 / 218.0	406.3 / 49.1 / 187.6	1 : 0.16 : 0.47	1 : 0.12 : 0.46

**The AE : Li : P ratios are normalized on the respective AE content.*

Additional representations of the FBU arrangements

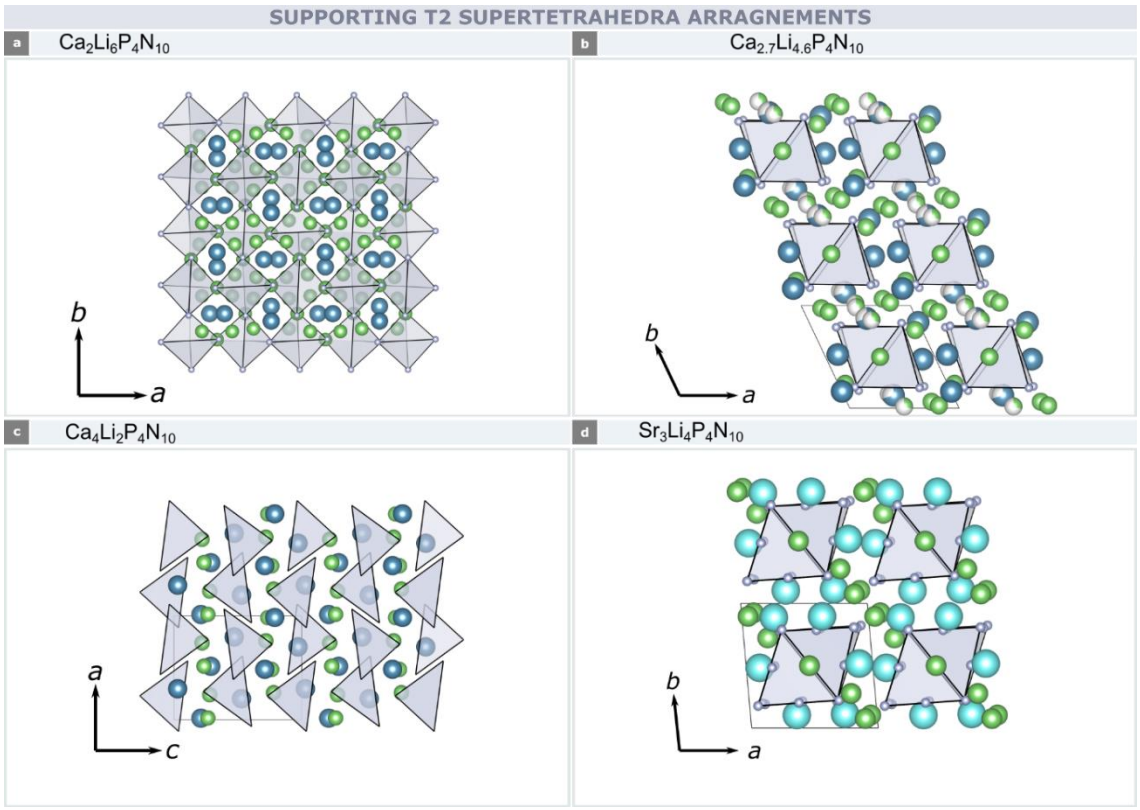

Figure S6.4. Additional representation of the T2 unit arrangement in all title compounds. Small boxes represent the unit cell. Color code: Ca atoms in blue, Sr atoms in cyan, Li atoms in green, and T2 units in gray.

Density Function Theory Calculations (DFT)

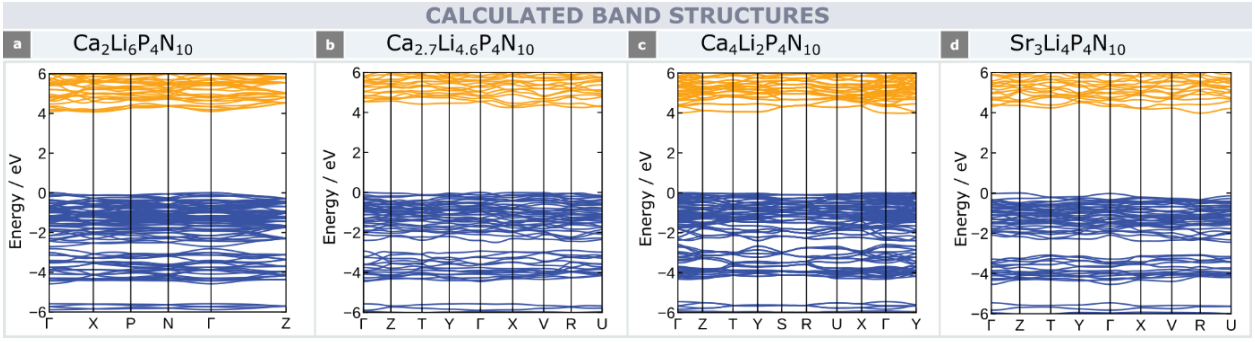

Figure S6.5. Calculated band structures of $Ca_2Li_6P_4N_{10}$ (a), $Ca_{2.7}Li_{4.6}P_4N_{10}$ (b), $Ca_4Li_2P_4N_{10}$ (c), and $Sr_3Li_4P_4N_{10}$ (d). Orange curves: conduction bands, blue curves: valence bands of the respective compounds.

Luminescence properties

Spectral Power Distribution (SPD)

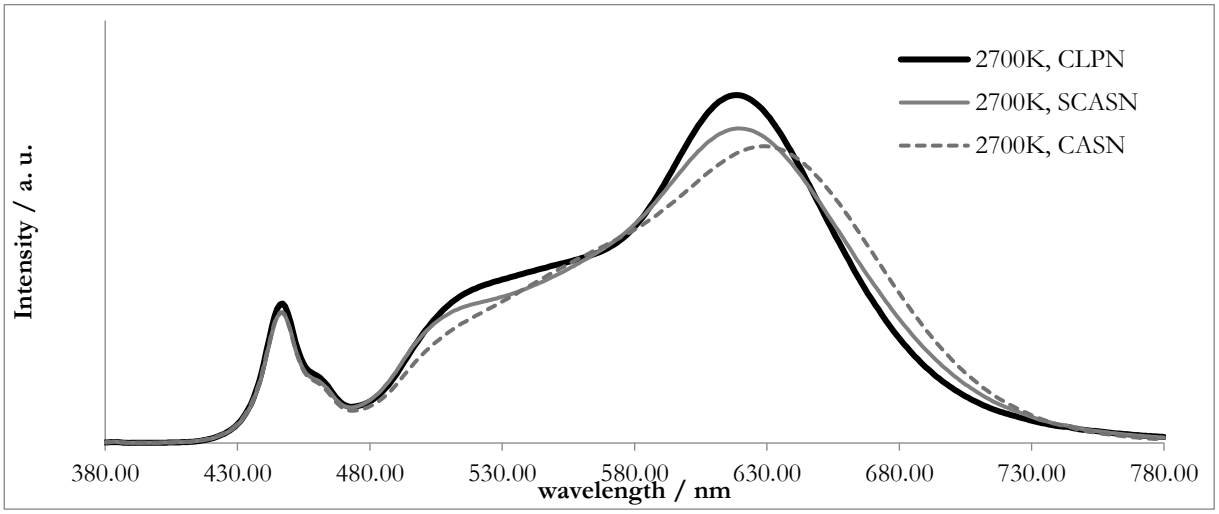

Figure S6.6. Spectral power distributions of white emitting pcLEDs (containing blue (InGaN), green (YAGG:Ce^{3+}) and respective red phosphors . SPD with CLPN (black curve), SCASN (gray solid curve) or CASN (gray dotted curve) with a correlated color temperature (*CCT*) of 2700K (*CIE x*, *y* color coordinates: $x = 0.458$, $y = 0.410$).

Color Rendering Indices (CRI) R8 and R9

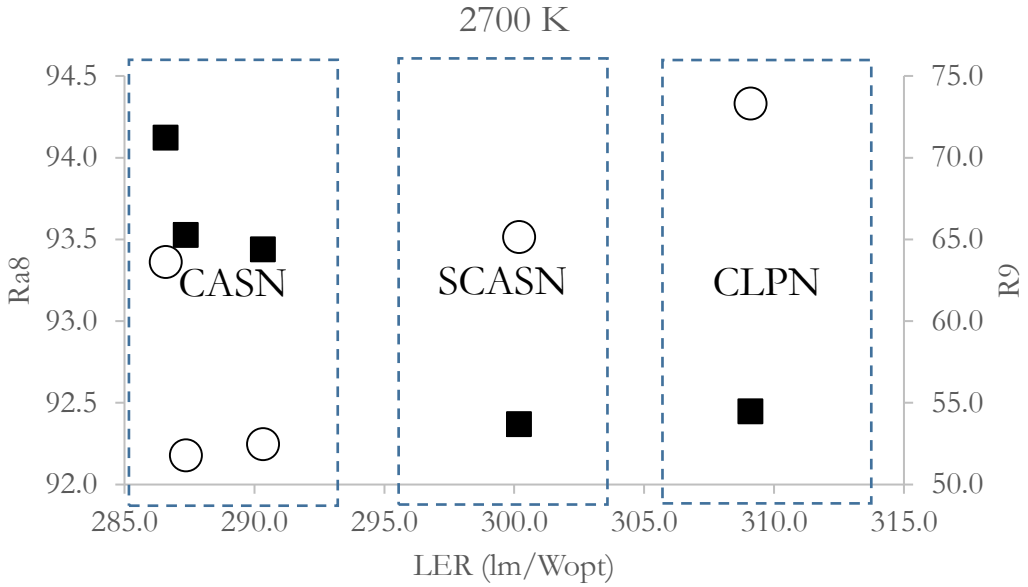

Figure S6.7. Ra8 (open circles) and R9 (filled squares) color rendering indices vs. lumen equivalent of radiation of 2700 K test pcLEDs (*CIE x*, *y* color coordinates for all parts: $x = 0.485$, $y = 0.410$) featuring *CASN* (left), *SCASN* (middle) or *CLPN* (right) as red phosphor.

10.7. Supporting Information for Chapter 7

Structure determination

Table S7.1. Crystallographic data of $Ba_3[PN_3]O$ from single crystal refinement. Standard deviations are given in parenthesis.

Formula	$Ba_3[PN_3]O$
Crystal system	trigonal
Space group	$R\bar{3}c$ (no. 167)
Lattice parameters / Å	a = 7.8315(3) c = 16.9865(5)
Cell volume / Å^3	902.24(7)
Formula units / unit cell	6
Calculated X-ray density / g·cm^{-3}	5.533
Molecular weight / g·mol^{-1}	500.974
Linear absorption coefficient / cm^{-1}	19.585
T_{min}/T_{max}	0.8579 / 1.000
Temperature / K	299(2)
Absorption correction	multi-scan
Radiation	Mo-Kα (λ = 0.71973 Å)
F(000)	1272
θ range / °	$3.845 \leq \theta \leq 33.124$
Total no. of reflections	5524
Independent reflections [$I \geq 2\sigma(I)$ / all]	387 (368)
R_{int}	0.0168
Refined parameters	15
Goodness of fit	1.197
R-values [$I \geq 2\sigma(I)$]	$R1$ = 0.0172; $wR2$ = 0.0319
R-values (all data)	$R1$ = 0.0186; $wR2$ = 0.0322
$\Delta\rho_{max}$, $\Delta\rho_{max}$ / e·Å^3	0.877; –2.391

Table S7.2. Wyckoff position, coordinates, isotropic thermal displacement parameters and occupancy of $Ba_3[PN_3]O$ from single-crystal refinement. Standard deviations are given in parenthesis.

Atom	**Wyck.**	***x***	***y***	***z***	U_{eq}	***occ.***
Ba01	18*e*	2/3	0.75732(3)	7/12	0.00872(7)	1
P01	6*a*	2/3	1/3	7/12	0.0075(3)	1
O01	6*b*	1	1	½	0.0111(9)	1
N01	18*e*	0.4640(4)	1/3	7/12	0.0113(6)	1

Table S7.3. Anisotropic displacement parameters (U_{ij} / Å^2) of $Ba_3[PN_3]O$ from single crystal refinement. Standard deviations are given in parenthesis.

Atom	U_{11} / Å^2	U_{22} / Å^2	U_{33} / Å^2	U_{12} / Å^2	U_{13} / Å^2	U_{23} / Å^2
Ba01	0.00869(11)	0.00777(9)	0.01000(11)	0.00092(4)	0.00184(7)	0.00434(6)
P01	0.0071(4)	0.0071(4)	0.0082(7)	0	0	0.0036(2)
O01	0.0092(13)	0.0092(13)	0.015(2)	0		0.0046(6)
N01	0.0064(10)	0.0105(14)	0.0184(17)	-0.0006(12)	-0.0003(6)	0.0053(7)

Table S7.4. Interatomic distances (Å) of $Ba_3[PN_3]O$ from single-crystal refinement. Standard deviations are given in parenthesis.

Atom1 – Atom2	**Distance / Å**	**Atom1 – Atom2**	**Distance / Å**
Ba01–O01	2.7330(1)	Ba01–N01	2.924(2)
Ba01–N01	2.8765(2)	P01–N01	1.5872(16)

Table S7.5. Interatomic angles (°) of $Ba_3[PN_3]O$ from single-crystal refinement. Standard deviations are given in parenthesis.

Atom1 – Atom2 – Atom 3	**Angle / °**	**Atom1 – Atom2 – Atom 3**	**Angle / °**	**Atom1 – Atom2 – Atom 3**	**Angle / °**
N01 – P01 – N01	120.000(2)	O01–Ba01–N01	77.419(1)	N01–Ba01–N01	172.352(0)
O01–Ba01–O01	154.838(1)	O01–Ba01–N01	76.579(0)	N01–Ba01–N01	93.824(1)
O01–Ba01–N01	78.233(1)	O01–Ba01–N01	105.139(0)	N01–Ba01–N01	151.455(6)
O01–Ba01–N01	125.918(1)	N01–Ba01–N01	57.090(3)	N01–Ba01–N01	94.810(1)
		N01–Ba01–N01	151.455(7)	N01–Ba01–N01	78.403(1)

SEM Analysis

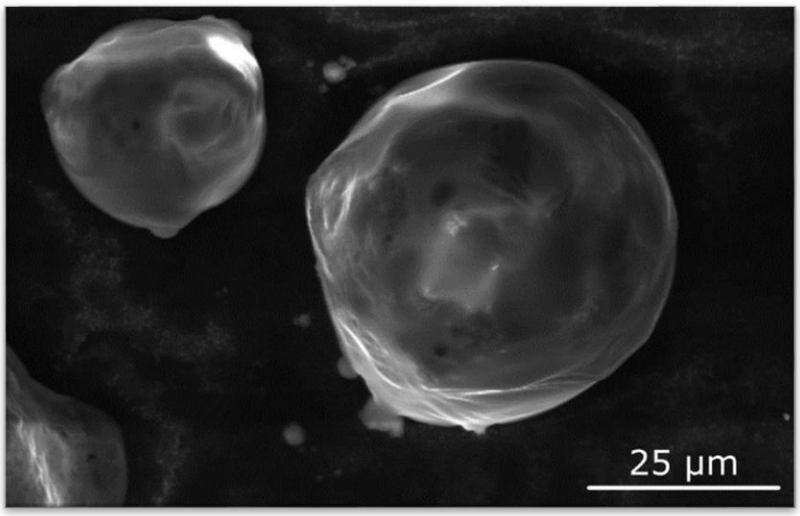

Figure S7.1. SEM image of $Ba_3[PN_3]O$ crystals up to 30 µm in size.

Rietveld refinement

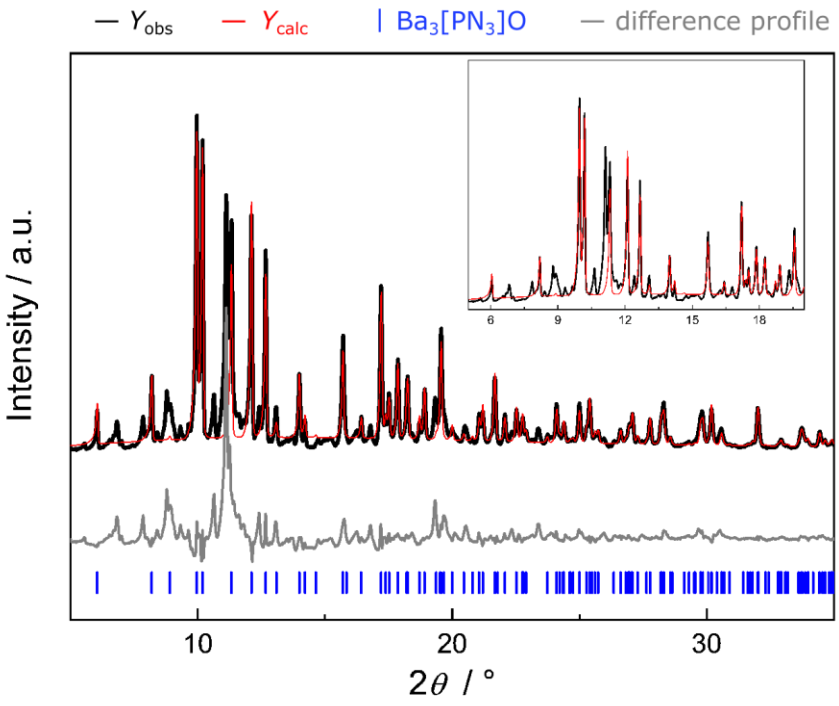

Figure S7.2. Result of the Rietveld refinement of $Ba_3[PN_3]O$. Observed (black), calculated (red) powder X-ray diffraction patterns (Ag-Kα_1 radiation, λ = 0.5594 Å) and difference plot (gray line). Positions of Bragg reflections are given as blue bars. Top right: Enlarged section of the range 5–20° (2Θ).

Table S7.6. Wyckoff position, coordinates, isotropic thermal displacement parameters and occupancy of $Ba_3[PN_3]O$ from Rietveld refinement. Standard deviations are given in parentheses.

Atom	***Wyck.***	***x***	***y***	***z***	U_{eq}	***SOF.***
Ba01	18*e*	2/3	0.7594(4)	7/12	0.75(6)	1
P01	6*a*	2/3	1/3	7/12	0.75(6)	1
O01	6*b*	1	1	½	0.75(6)	1
N01	18*e*	0.462(4)	1/3	7/12	0.75(6)	1

Table S7.7. Crystallographic data from Rietveld refinements of $Ba_3[PN_3]O$. Standard deviations are given in parentheses.

Formula	$Ba_3[PN_3]O$
Crystal system	trigonal
Space group	$R\bar{3}c$ (no. 167)
Lattice parameters / Å	a = 7.8320(6) c = 17.0118(17)
Cell volume / Å^3	903.8(2)
Formula units / unit cell	6
X-ray density / g·cm^{-3}	5.523(1)
diffractometer	STOE Stadi P
Radiation λ / Å	0.5593 (Ag-Kα_1)
monochromator	Ge(111)
detector	Mythen 1K
2θ-range / °	$2 \leq 2\theta \leq 81.155$
data points	5278
number of reflections	1353
refined parameters	21
background function	shifted Chebyshev, 10 polynomials
R values	R_p = 0.1223
	R_{wp} = 0.2092
	R_{exp} = 0.0176
	R_{Bragg} = 0.0229
GooF (χ^2)	11.78

Note on refinement: This Rietveld refinement only serves as proof of the presence in the bulk material due to the not inconsiderable proportion of unknown side phase.

EDX spectroscopy

EDX measurements were performed on various crystallites in the sample. No other elements than Ba, P, N and O were detected, whereby O can be attributed to surface hydrolysis due to the low degree of condensation. The normalized cationic ratio (Ba : P) is in good agreement to the theoretical values.

Table S7.8. Overview of EDX measurements of $Ba_3[PN_3]O$. Results are given in atomic percent. Standard deviations are given in parenthesis.

	1	**2**	**3**	**4**	**5**	**6**	**7**	**8**	**9**	**10**	**Ratio Ba:P**
Ba	16.9	15.6	17.3	15.5	15.2	26.6	24.3	16.2	26.9	22.4	2.9(2)
P	5.7	5.8	6.1	6.1	5.2	8.5	9.1	5.5	8.3	7.3	1
N	16.4	10.4	13.9	9.8	10.4	6.8	5.9	12.7	11.0	10.8	-
O	61.0	68.1	62.6	68.6	69.2	26.6	60.6	65.7	53.9	59.5	-

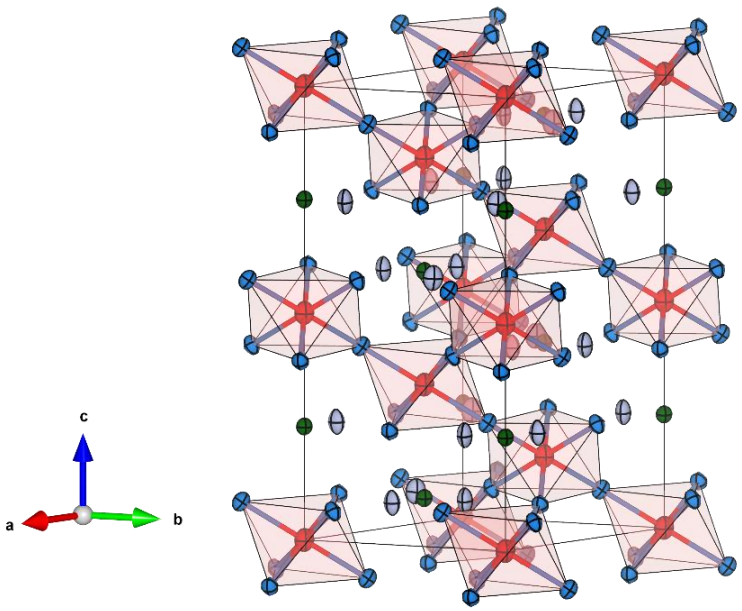

Figure S7.3. Reverse view on the coordination environment of O^{2-} ions (red), which are octahedrally coordinated by Ba^{2+}; P atoms (green), N atoms (gray). Displacement ellipsoids (probability): 95%

Solid-state MAS NMR spectra

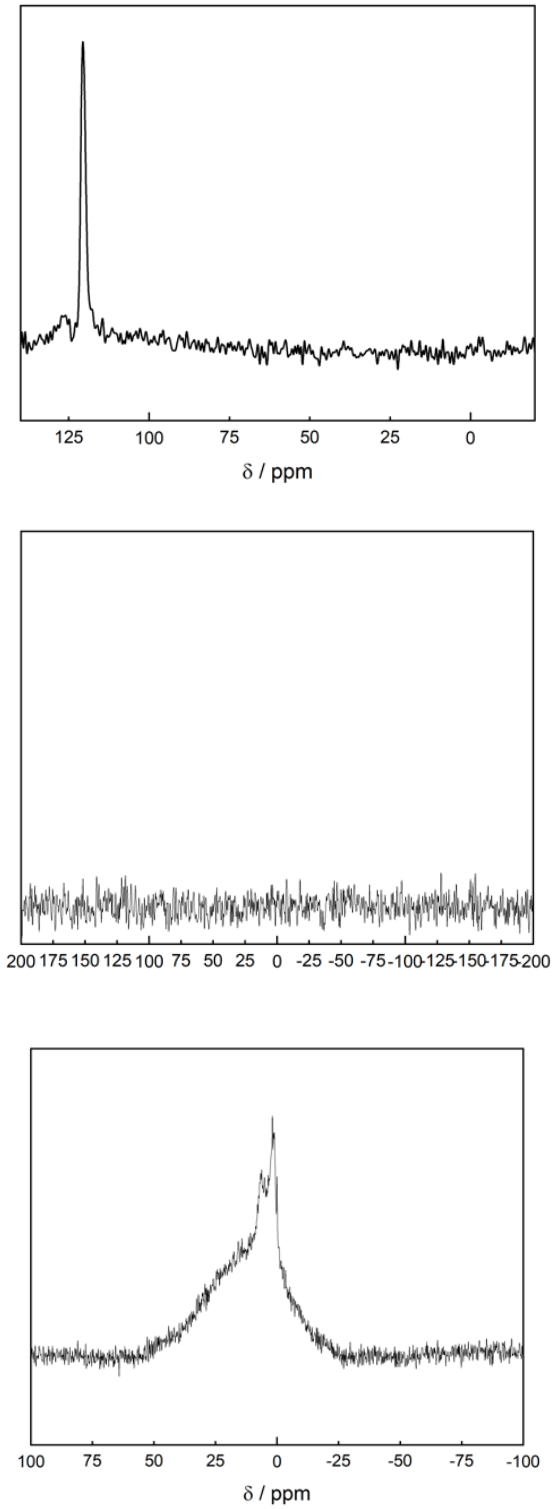

Figure S7.4. ^{31}P (top), $^{31}P\{^{1}H\}$ cross polarized (middle) and ^{1}H (bottom) solid-state MAS NMR spectra of $Ba_3[PN_3]O$. The ^{31}P spectrum shows one signals (δ = 120.5 ppm) with an *fwhm* of 1.7 ppm, which can be assigned to the one P site in $Ba_3[PN_3]O$. There is no evidence of hydrogen being present in $Ba_3[PN_3]O$ as the broad signal of the $^{31}P\{^{1}H\}$ cross polarized spectrum does not match with the ^{31}P peak.

FTIR spectrum

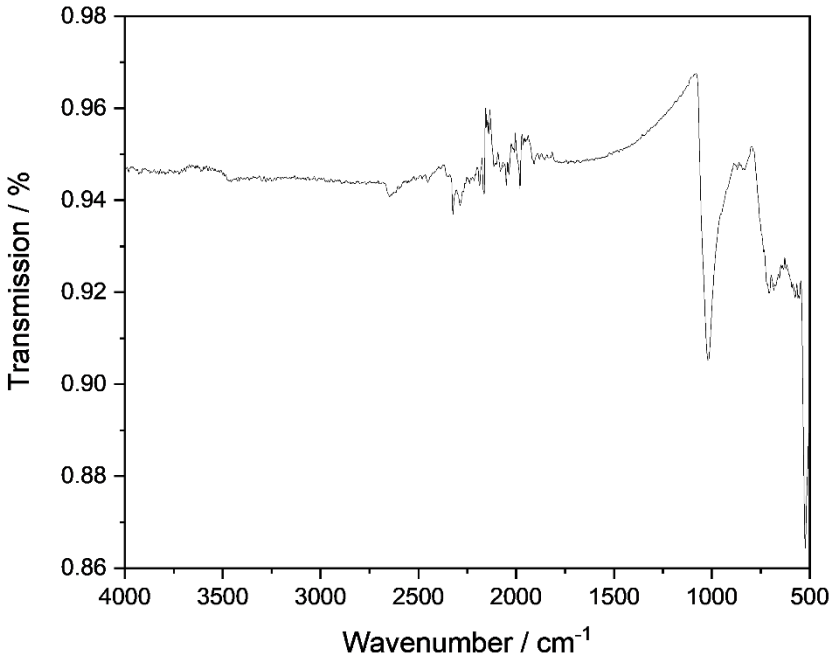

Figure S7.5. FTIR spectrum of $Ba_3[PN_3]O$. Absorption bands in the fingerprint region (< 1500 cm^{-1}) originate from modes of the $[PN_3]^{4-}$ anion as well as the lattice. Small signals at 3500 cm^{-1} indicate N–H modes in the sample. Noise signals from 2500–2000 can be attributed to the diamond window of the ATR unit.

Charge distribution (CHARDI)

Table S7.9. Results of the CHARDI analysis of $Ba_3[PN_3]O$. All effective coordination numbers and mean total charges are in good agreement with the theoretical values.

	Ba1	**P1**	**N1**	**O1**
Calculated	2.0	5.0	–3.0	–2.0
Theoretical	2	5	–3	–2

Ewald Summation (EwaldSum)

Table S7.10. Results of the EwaldSum analysis of $Ba_3[PN_3]O$.

	Ba1	**P1**	**N1**	**O1**
Calculated / MJ mol^{-1}	1.796	14.44	5.204	1.676

Bond-valence-sum (BVS)

Table S7.11. Results of the BVS analysis of $Ba_3[PN_3]O$. All charges are in good agreement with the theoretical values.

	Ba1	**P1**	**N1**	**O1**
Calculated	2.1	5.0	–3.1	–1.8
Theoretical	2	5	–3	–2

Table S7.12. ICSD collection codes for the references (Ba–N distances).

Collection code	**Sum formula**
81570	$Ba_5Si_2N_6$
130192	$BaBe_{20}N_{14}$
153060	BaP_2N_4
170265	$BaSiN_2$
187335	$Ba_4MgSi_2N_6$
187336	$Ba_3Ca_2Si_2N_6$
187337	$Ba_3Sr_2Si_2N_6$
235211	$CaBaLi_2Al_6N_8$
238968	$Ba_3P_5N_{10}Cl$
23869	$Ba_3P_5N_{10}I$
401501	$Ba_2Si_5N_8$
405772	$BaSi_7N_{10}$
410578	$Ba_3Al_2N_4$
415304	$BaBeN_2$
415715	$BaCa_2P_6N_{12}$
415716	$BaSr_2P_6N_{12}$
427065	$BaMg_2Al_2N_4$
428381	$Ba_3P_5N_{10}Br$
428510	$BaMg_3SiN_4$
429872	$BaLi_2Al_2Si_2N_6$

Table S7.13. ICSD collection codes for the references (Ba–O distances).

Collection code	**Sum formula**
1449	$Ba_3O(SiO_4)$
2394	$Ba(PO_3)_2$
6245	$BaSiO_3$
6246	Ba_2SiO_4
9339	$Ba_2Si_4O_{10}$
10036	$BaAl_2O_4$
10162	$Ba(Si_2O_5)$
15714	$Ba(PO_3)_2$
20038	$Ba_4Si_6O_{16}$
36172	$Ba_5Si_8O_{21}$
69450	$Ba_3(PO_4)_2$
79558	$Ba_3(Al_2O_6)$
100310	$Ba_4(Si_6O_{16})$
100312	$Ba_6(Si_{10}O_{26})$
280908	$Ba_3(P_4O_{13})$
424775	$BaAl_4O_7$

Table S7.14. ICSD collection codes for the references (P–N distances).

Collection code	**Sum formula**
12986	Mg_2PN_3
28375	Ca_2PN_3
40797	BeP_2N_4
51396	$Rb_3P_6N_{11}$
51397	$Cs_3P_6N_{11}$
153060	BaP_2N_4
241682	$Pr_2P_3N_7$
241683	$Ho_2P_3N_7$
411818	$NaPN_2$
415714	$BaCa_2P_6N_{12}$
415716	$BaSr_2P_6N_{12}$
425997	CaP_2N_4
429542	$LiNdP_4N_8$
434260	SrP_8N_{14}

11 Miscellaneous

11.1 List of Publications in this Thesis

1. **From Framework to Layers Driven by Pressure – The Monophyllo-Oxonitridophosphate β-$MgSrP_3N_5O_2$ and Comparison to its α-Polymorph**

   Reinhard M. Pritzl, Nina Prinz, Philipp Strobel, Peter J. Schmidt, Dirk Johrendt, and Wolfgang Schnick

   Chem. Eur. J. **2023**, *29*, e202301218

R.M.P.: Conceptualization: Lead; Formal analysis: Lead; Investigation: Lead; Validation: Equal; Visualization: Lead; Writing – original draft: Lead; Writing – review & editing: Equal

N.P.: Investigation: Supporting

P.S.: Formal analysis: Supporting; Investigation: Supporting; Writing – review & editing: Supporting

P.J.S.: Formal analysis: Supporting; Investigation: Supporting; Project administration: Supporting; Resources: Supporting; Supervision: Supporting; Validation: Supporting; Writing – review & editing: Supporting

D.J.: Investigation: Supporting**;** Supervision: Supporting**;** Writing – original draft: Supporting**;** Writing – review & editing: Supporting

W.S.: Conceptualization: Lead**;** Funding acquisition: Lead**;** Project administration: Lead**;** Resources: Lead**;** Supervision: Lead**;** Writing – original draft: Supporting**;** Writing – review & editing: Supporting

Synthesis and formal analyses were performed by Reinhard M. Pritzl and Nina Prinz over the course of her Bachelor thesis, which was supervised by Reinhard M. Pritzl and Wolfgang Schnick. Philipp Strobel carried out luminescence measurements. Philipp Strobel and Peter J. Schmidt helped with the interpretation of the luminescence data. The investigation of luminescence properties was supervised by Peter J. Schmidt. DFT calculations were performed and supervised by Dirk Johrendt. The manuscript was prepared by Reinhard M. Pritzl and Wolfgang Schnick supervised the project. All authors contribute to the discussion of the results and revised the manuscript.

2. Tunable Narrow-Band Cyan-Emission of Eu^{2+}-doped Nitridomagnesophosphates $Ba_{3-x}Sr_x[Mg_2P_{10}N_{20}]:Eu^{2+}$ (x = 0–3)

Reinhard M. Pritzl, Monika M. Pointner, Kristian Witthaut, Philipp Strobel, Peter J. Schmidt, and Wolfgang Schnick

Angew. Chem. Int. Ed. **2024**, *63*, e202403648; *Angew. Chem.* **2024**, *136*, e202403648

R.M.P.: Conceptualization: Lead; Formal analysis: Lead; Investigation: Lead; Validation: Equal; Visualization: Lead; Writing – original draft: Lead; Writing – review & editing: Equal

M.M.P.: Formal analysis: Supporting; Investigation: Supporting; Validation: Supporting; Visualization: Supporting; Writing – original draft: Supporting; Writing – review & editing: Supporting

K.W.: Formal analysis: Supporting; Investigation: Supporting; Validation: Supporting; Visualization: Supporting; Writing – original draft: Supporting; Writing – review & editing: Supporting
P.S.: Investigation: Supporting; Validation: Supporting; Writing – original draft: Supporting; Writing – review & editing: Supporting
P.J.S.: Formal analysis: Supporting; Funding acquisition: Supporting; Project administration: Supporting; Resources: Supporting; Supervision: Supporting; Validation: Supporting; Writing – review & editing: Supporting
W.S.: Conceptualization: Equal; Funding acquisition: Lead; Project administration: Lead; Resources: Lead; Supervision: Lead; Validation: Supporting; Writing – original draft: Supporting; Writing – review & editing: Supporting)

The Syntheses and formal analyses were performed by Reinhard M. Pritzl. Preparation and postprocessing of STEM measurements were done by Monika M. Pointner. DFT calculations were performed by Kristian Witthaut. Measurements of luminescence properties were carried out by Philipp Strobel. The investigation of luminescence properties was supervised by Peter J. Schmidt. Wolfgang Schnick supervised the project. Reinhard M. Pritzl wrote the manuscript and all authors contribute to the discussion of the results and revised the manuscript.

3. $ZnH_2P_4N_8$: Case Study on Topochemical Imidonitridophosphate High-Pressure Synthesis

Reinhard. M. Pritzl, Jennifer Steinadler, Amalina T. Buda, S. Wendl, and Wolfgang Schnick

Chem. Eur. J. **2024**, *30*, e202402741

R.M.P.: Conceptualization: Lead; Formal analysis: Lead; Investigation: Lead; Validation: Equal; Visualization: Lead; Writing – original draft: Lead; Writing – review & editing: Equal

J.S.: Formal analysis: Supporting; Investigation: Supporting; Validation: Supporting; Visualization: Supporting; Writing – original draft: Supporting; Writing – review & editing: Supporting

A.T.B.: Formal analysis: Supporting; Validation: Supporting; Writing – review & editing: Supporting

S.W.: Investigation: Supporting; Validation: Supporting; Writing – review & editing: Supporting

W.S.: Funding acquisition: Lead; Project administration: Lead; Resources: Lead; Supervision: Lead; Validation: Supporting; Writing – original draft: Supporting; Writing – review & editing: Supporting

The syntheses and formal analyses were performed by Reinhard M. Pritzl and supported by Sebastian Wendl. Jennifer Steinadler supported the interpretation of the results of the NMR experiments. The SEM-EDX measurements were performed by Amalina T. Buda. Reinhard M. Pritzl wrote the manuscript and Wolfgang Schnick supervised the project. All authors contribute to the discussion of the results and revised the manuscript.

4. $CaLi_2PN_3$ – A Quaternary Chain-Type Nitridophosphate by Medium-Pressure Synthesis

Reinhard. M. Pritzl, N. Fahle, K. Witthaut, S. Wendl, and Wolfgang Schnick

Chem. Eur. J. **2024**, *30*, e202402521

R.M.P.: Conceptualization: Lead; Formal analysis: Lead; Investigation: Lead; Validation: Equal; Visualization: Lead; Writing – original draft: Lead; Writing – review & editing: Equal

N.F: Investigation: Supporting

K.W.: Formal analysis: Supporting; Investigation: Supporting; Visualization: Supporting; Writing – review & editing: Supporting

S.W.: Conceptualization: Supporting; Formal analysis: Supporting; Investigation: Supporting; Validation: Supporting; Writing – review & editing: Supporting

W.S.: Conceptualization: Equal; Funding acquisition: Lead; Project administration: Lead; Resources: Lead; Supervision: Lead; Validation: Equal; Writing – original draft: Supporting; Writing – review & editing: Supporting

The synthesis and formal analyses were performed by Reinhard M. Pritzl and Nadine Fahle over the course of her Bachelor thesis that was supervised by Reinhard M. Pritzl and Wolfgang Schnick. DFT calculations were performed by Kristian Witthaut. Sebastian Wendl supported by the conceptionalization of the project. Reinhard M. Pritzl wrote the manuscript and Wolfgang Schnick supervised the project. All authors contribute to the discussion of the results and revised the manuscript.

5. Adamantane-Type Nitridophosphate Phosphors $AE_xLi_{10-2x}P_4N_{10}:Eu^{2+}$ via Medium-Pressure Ion-Exchange Reactions

Reinhard. M. Pritzl, Amalina T. Buda, K. Witthaut, Peter J. Schmidt, and Wolfgang Schnick

Angew. Chem. Int. Ed. **2024**, e202420565; *Angew. Chem.* **2024,** e202420565

R.M.P.: Data curation: Lead; Formal analysis: Lead; Investigation: Lead; Validation: Equal; Visualization: Lead; Writing – original draft: Lead; Writing – review & editing: Equal

A.T.B.: Data curation: Supporting; Formal analysis: Supporting; Investigation: Supporting; Writing – review & editing: Supporting

K.W: Data curation: Supporting; Formal analysis: Supporting; Investigation: Supporting

P.J.S.: Formal analysis: Supporting; Investigation: Supporting; Project administration: Supporting; Resources: Supporting; Supervision: Supporting; Validation: Supporting; Writing – review & editing: Equal

W.S.: Conceptualization: Lead; Funding acquisition: Lead; Project administration: Lead; Resources: Lead; Supervision: Lead; Validation: Equal; Writing – original draft: Supporting; Writing – review & editing: Equal

Synthesis, formal analyses and data evaluation were performed by Reinhard M. Pritzl. Amalina T. Buda performed SEM-EDX measurements. DFT calculations were performed by Kristian Witthaut. Peter J Schmidt performed luminescence measurements and helped with the interpretation of the luminescence data. Reinhard M. Pritzl wrote the manuscript and Wolfgang Schnick supervised the project. All authors contributed to the discussion of the results and revised the manuscript.

6. Trigonal Planar $[PN_3]^{4-}$ Anion in the Nitridophosphate Oxide $Ba_3[PN_3]O$

Reinhard. M. Pritzl, Kristian Witthaut, Marwin Dialer, Amalina.T. Buda, Victor Milman, Lkhamsuren Bayarjargal, Björn. Winkler, and Wolfgang Schnick

Angew. Chem. Int. Ed. **2024**, *63*, e202405849; *Angew. Chem.* **2024**, *136*, e202405849

R.M.P.: Formal analysis: Lead; Investigation: Lead; Validation: Equal; Visualization: Lead; Writing – original draft: Lead; Writing – review & editing: Equal

K.W.: Formal analysis: Supporting; Investigation: Supporting; Validation: Supporting; Visualization: Supporting; Writing – original draft: Supporting

M.D.: Formal analysis: Supporting; Investigation: Supporting; Visualization: Supporting; Writing – original draft: Supporting; Writing – review & editing: Supporting

A.T.B.: Investigation: Supporting; Writing – original draft: Supporting

V.M.: Formal analysis: Supporting; Investigation: Supporting; Writing – original draft: Supporting

L.B.: Formal analysis: Supporting; Investigation: Supporting; Writing – original draft: Supporting

B.W.: Formal analysis: Supporting; Funding acquisition: Supporting; Investigation: Supporting; Project administration: Supporting; Resources: Supporting; Supervision: Supporting; Writing – original draft: Supporting; Writing – review & editing: Supporting

W.S.: Conceptualization: Lead; Funding acquisition: Lead; Project administration: Lead; Resources: Lead; Supervision: Lead; Writing – original draft: Supporting; Writing – review & editing: Supporting)

The syntheses were performed by Reinhard M. Pritzl. The structure solution and formal data analysis was done by Reinhard M. Pritzl. LCC calculations were conducted by Marwin Dialer. DFT calculations were performed by Kristian Witthaut and Victor Milman. Lkhamsuren Bayarjargal conducted the Raman experiments and analyzed the data thereof. Reinhard M. Pritzl performed IR measurements. Amalina T. Buda carried out SEM-EDX measurements and supported the evaluation of the results. Björn Winkler supervised the Raman measurements and their calculations. Reinhard M. Pritzl wrote the major part of the manuscript. Supervision of the research project was headed by Wolfgang Schnick. All authors contributed to the discussion of the results and revised the manuscript.

11.2 List of Publications beyond this Thesis

1. **Nitride Synthesis Under High-pressure High-temperature Conditions: Unprecedented *in-situ* Insight into the Reaction**

   S.J. Ambach, R.M. Pritzl, S. Bhat, R. Farla, W. Schnick, *Inorg. Chem.* **2024**, *63*, 3535.

2. **Multicationic Tetrahedra Networks: Alkaline-Earth-Centered Polyhedra and Non-Condensed AlN_6-Octahedra in the Imido-nitridophosphates $AE_2AlP_8N_{15}(NH)$ (AE = Ca, Sr, Ba)**

   M.M. Pointner, R.M. Pritzl, J.M. Albrecht, L. Blahusch, J.P. Wright, E. Lawrence Bright, C. Giacobbe, O. Oeckler, W. Schnick, *Chem. Eur. J.* **2024**, *30*, e202400766.

3. **Super-Tunable $LaSi_3N_5$ Structure Type: Insights into the Structure and Luminescence of $SrSi_2PN_5:Eu^{2+}$**

   M. Dialer, R.M. Pritzl, S.L. Wandelt, D. Khalyavin, P.J. Schmidt, W. Schnick, *Chem. Mater.* **2024,** *36*, 3933.

4. **Ammonothermal Synthesis of Luminescent Imidonitridophosphate $Ba_4P_4N_8(NH)_2:Eu^{2+}$**

   F.M. Engelsberger, R.M. Pritzl, J. Steinadler, K. Witthaut, T. Bräuniger, P.J. Schmidt, W. Schnick, *Chem. Eur. J.* **2024**, e202402743; *accepted.*

5. **Scalable Bulk Synthesis of Pure γ-Sn_3N_4 as a Model for an Argon-Flow-Mediated Metathesis Reaction**

   M. Zipkat, S. S. Rudel, A. Koldemir, T. Block, C. Ceniza, T. D. Boyko, S. Kläger, R. M. Pritzl, A. Moewes, R. Pöttgen, W.Schnick, *submitted.*

11.3 Conference Contributions and Oral Presentations

1. **DESY, AlCaPONe und weitere angehende Celebrities?**

Reinhard M. Pritzl

Talk, Schnick Group Seminar

Munich (Germany), 30.06.2020

2. **A P/N Multiplayer Game**

Reinhard M. Pritzl

Talk, Schnick Group Seminar

Munich (Germany), 28.03.2021

3. **Von (PON)tius bis Nitridophosphatus**

Reinhard M. Pritzl

Talk, 6. Obergurgl-Festkörperchemie-Seminar

Obergurgl (Austria), 08.02.2022

4. **- Quid Valet Expectans – Nitridophosphate: Ein Einblick des Möglichen**

Reinhard M. Pritzl

Talk, Schnick Group Seminar

Munich (Germany), 27.07.2022

5. **- Under Pressure - Synthesis and Characterization of the Novel High Pressure Oxonitridophosphate β-$MgSrP_3N_5O_2$**

Reinhard M. Pritzl, Nina Prinz, Wolfgang Schnick

Poster, 21. Vortragstagung für Anorganische Chemie der Fachgruppen Wöhler-Vereinigung und Festkörperchemie und Materialforschung

Marburg (Germany), 27.09.2022

6. Revamping the Classics: Unleashing the Potential of Modified Nitridophosphates

Reinhard M. Pritzl

Talk, Schnick Group Seminar

Munich (Germany), 12.07.2023

7. [^{15}P]ermuda Triangle

Reinhard M. Pritzl

Talk, 7. Obergurgl-Festkörperchemie-Seminar

Obergurgl (Austria), 31.01.2024

11.4 Deposited Crystal Structures

The Crystallographic Information Files (CIF) of the investigated compounds are provided free of charge by the joint Cambridge Crystallographic Data Centre and Fachinformationszentrum Karlsruhe Access Structures service (http://www.ccdc.cam.ac.uk/structures) by quoting the corresponding deposition number.

compound	**CCDC-**
β-$MgSrP_3N_5O_2$	2236964
$Ba_3[Mg_2P_{10}N_{20}]$	2332859
$Sr_3[Mg_2P_{10}N_{20}]$	2332860
$Ba_3[PN_3]O$	2336088
$ZnH_2P_4N_8$	2300728 & 2379986
$CaLi_2PN_3$	2365190
$Ca_2Li_6P_4N_{10}$	2390824
$Ca_{2.7}Li_{4.6}P_4N_{10}$	2390554
$Ca_4Li_2P_4N_{10}$	2390555
$Sr_3Li_4P_4N_{10}$	2390556